Design of metal-oxide nanoparticles with the continuous hydrothermal synthesis (CHTS)

Zur Erlangung des akademischen Grades eines

DOKTORS DER INGENIEURWISSENSCHAFTEN (DR.-ING.)

von der KIT-Fakultät für Chemieingenieurwesen und Verfahrenstechnik des

Karlsruher Instituts für Technologie (KIT)

genehmigte

DISSERTATION

von

Christian Schüßler, M.Sc.

aus Marxzell

Tag der mündlichen Prüfung: 25.07.2023

Erstgutachter: Prof. Dr.-Ing. habil. Michael Türk

Zweitgutachterin: Prof. Dr. Silvia Gross

Danksagung:

Diese Arbeit entstand in meiner Zeit von Juli 2017 bis September 2022 als wissenschaftlicher Mitarbeiter am Institut für Technische Thermodynamik und Kältetechnik (ITTK) des Karlsruher Instituts für Technologie (KIT).

Mein besonderer Dank geht hierbei an Herrn Prof. Dr.-Ing. habil. Michael Türk, der mir immer unterstützend zur Seite stand. Die vielen fachlichen Diskussionen haben stets zu neuen Ideen und Denkanstößen geführt.

Des Weiteren möchte ich mich bei Frau Prof. Dr. Silvia Gross für die Übernahme des Korreferats bedanken.

Der Deutschen Forschungsgemeinschaft (DFG) danke ich für Ihre finanzielle Unterstützung im Rahmen des Forschungsvorhabens FOR 2383 (Tu 93/21-1, 21-2).

Ebenso gilt mein Dank Frau Dr.-Ing. Heike Störmer (LEM, KIT), die TEM-Aufnahmen mit hoher Präzision angefertigt hat und somit die Auszählung der Nanopartikel überhaupt erst möglich machte.

Insbesondere Frau Marlene Crone und allen Mitarbeitenden der Werkstätten danke ich für ihre tatkräftige Unterstützung beim Aufbau der Anlage, der Herstellung von Anlagenteilen und der steten guten Zusammenarbeit.

Meinen vier Masteranden Manuel Hohm, SathishKumar Ponusamy, Martin Zürn und Abhishek Goel und meiner Bachelorandin Esther Heil gilt ebenso mein Dank für ihre Unterstützung.

Ebenfalls danke ich dem Kollegium für spannende Gespräche und Diskussionen während des Institutsalltags.

Abschließend bedanke ich mich bei meiner Familie, die mich stets bei all meinen Vorhaben unterstützt hat.

Karlsruhe im April 2023 Christian Schüßler

Table of contents

Acronyms

2D	two dimensional
3D	three dimensional
ANSYS	analysis of systems
APS	average particle size
aq	aqueous
BSA	Bovine serum albumin
CAD	computer aided designs
CFD	computational fluid dynamics
CHTS	continuous hydrothermal synthesis
C.P.	critical point
Da	Damköhler number
DHD	Debye-Hückel-Davies
DI	deionized
EDX	energy dispersive X-ray analysis
eps	floating-point relative accuracy
GUI	graphical user interface
HKF	Helgeson-Kirkham-Flowers
hkl	symmetrical equivalent planes
HPLC	high performance liquid chromatography
IAPWS	international association for the properties of water and steam
ICEM	Integrated Computer-aided Engineering and Manufacturing
IS	impedance spectroscopy
L	liquid
LabVIEW	Laboratory Virtual Instrumentation Engineering Workbench
LES	linear equation system
LCEP	lower critical endpoint
L-N_2	liquid nitrogen
NS	Navier-Stokes
PSD	particle size distribution
PVP	Poly(N-vinyl-2-pyrrolidone)
PXRD	powder X-ray diffraction
QUICK	quadratic upwind interpolation
Re	Reynolds number
REFPROP	Reference Fluid Thermodynamic and Transport Properties
RESS	rapid expansion of supercritical solution
r-HKF	revised Helgeson-Kirkham-Flowers
RTD	residence time distribution
S	solid
SCF	supercritical fluid
SCWO	supercritical water oxidation
SAA	Sue-Arai-Adschiri

SIMPLE	Semi-Implicit Method for Pressure-Linked Equations
SLG	solid liquid gas
TEM	transmission electron microscopy
TP	triple point
UCEP	upper critical endpoint
UDF	user defined function
V	vapor
VOF	volume of fluid

Nomenclature

Latin:

symbol:	unit:	designation:
A_m	$\mathrm{m^2}$	average surface
A_M	-	Debeye-Hückel parameter
a	-	mixing ratio
a_i	-	calculation parameters
a_p	-	volume fraction of the primary phase
B^*_ca	-	temperature-dependent parameter
b_g	-	calculation parameters
C_i	-	constants
c_g	-	calculation parameters
c_p	$\mathrm{J\ kg^{-1}\ K^{-1}}$	specific isobaric heat capacity
c_product	$\mathrm{mol\ dm^{-3}}$	product concentration
c_s	$\mathrm{mol\ dm^{-3}}$	saturation concentration
c_salt	$\mathrm{mol\ dm^{-3}}$	salt concentration
c_i	-	different calculation parameters
d	m	diameter of the particle
d_m	m	diameter of the mixer
d_{hkl}	m	length between two planes
E	J	energy
E_x	-	electric fraction
e_r	$\mathrm{J\ mol^{-1}}$	activation energy
$\vec{F}$	N	external body force
F_a	-	parameter for the Bromley model for anions
F_c	-	parameter for the Bromley model for cations
G_b	-	parameters for k-ε model
G_k	-	
$\Delta\bar{G}^\circ_{j,i}$	$\mathrm{J\ mol^{-1}}$	difference of Gibbs free energy of formation for a species i and different interactions j
ΔG^*	J	Gibbs free energy of critical nucleus formation
g	Å	solvent function
$\vec{g}$	$\mathrm{m\ s^{-2}}$	gravitational acceleration
H	J	enthalpy
H_x	-	magnetic fraction
$\Delta\bar{H}^\circ_{j,i}$	$\mathrm{J\ mol^{-1}}$	difference of the standard enthalpy of a species i and different interactions j
h	$\mathrm{J\ kg^{-1}}$	specific enthalpy
i	-	species
I_m	$\mathrm{mol\ kg^{-1}}$	ionic strength
I	-	unit tensor

J	$cm^{-3}\ s^{-1}$	nucleation rate
J_j	kg m^2	diffusion flux
J_p^i	kg s^{-1}	mass transfer rate
K_w	-	ionic product of water
$K*$	-	frequency factor
K_{hkl}	-	scale factor
K_i	-	equilibrium constant
K_S	-	scale factor
k	s^{-1}	rate constant
k_B	J K^{-1}	Boltzmann constant
k_{HT}	W K^{-1}	heat transition coefficient
k_t	J kg^{-1}	turbulent kinetic energy
k_0	s^{-1}	frequency factor
k_x	-	direction vector of the wave
k_z	-	charge dependent constant
L_{hkl}	m	crystallite size
m_i	mol kg^{-1}	molality
$\dot{m}_1$	kg s^{-1}	mass flow of the cold stream
$\dot{m}_2$	kg s^{-1}	mass flow of the hot water stream
$\dot{m}_3$	kg s^{-1}	total mass flow
N_A	mol^{-1}	avogradro number
n	-	order of reflection
n_i	mol	amount of moles of species i
p_c	MPa	critical pressure
$\dot{Q}_v$	W	heat loss
R	J mol^{-1} K^{-1}	universal gas constant
R_h	s^{-1}	rate for heterogeneous reaction
R_i	s^{-1}	net production rate
R_p^i	s^{-1}	rate for homogeneous reaction
r_e	m	effective electrostatic radius
r_x	m	crystal ionic radius
r^*	m	critical radius of a nucleus
S	-	supersaturation
S_h	J	heat sources
S_i	s^{-1}	creation rate
S_{ε_t}	-	user-defined source terms
S_{k_t}	-	
S_m	J m^{-2} s^{-1}	external source term
t	s	time
T_a	K	ambient temperature
T_c	K	critical temperature
T_i	K	temperature of the different streams
T_r	K	reference temperature
T_{TP}	K	temperature at the triple point
T_0	K	reference temperature
T_1	K	temperature of the cold stream
T_2	K	temperature of the hot stream
T_3	K	temperature of the mixing stream
U	J	internal energy

$\dot{V}$	$m^3\ s^{-1}$	volume flow
v	$m^3\ kg^{-1}$	specific volume
$\vec{v}$	$m\ s^{-1}$	velocity vector
$v_{2,s}$	m^3	solute molecular volume in the solid phase
V	m^3	volume
X	-	conversion
Y_M	-	amount of fluctuating dilatation to the total dissipation rate
Y_{p_r,T_r}	K^{-1}	Born constant
z_i	-	electric charge

Greek:

symbol:	unit:	designation:
α	K^{-1}	fitting parameter
β	$J\ mol^{-1}$	fitting parameter
β_{hkl}	-	angular width
γ_i	-	activity coefficient of species i
$\gamma_i^{*,m}$	-	average activity coefficient of species i
Δ	-	width of the particle size distribution
Δ_λ	m	distance difference of two reflected waves
ε	-	dielectric constant
ε_t	$m^2\ s^{-3}$	turbulent dissipation rate
ε_r	-	dielectric constant at reference conditions
η	Pa s	dynamic viscosity
η_{HKF}	$J\ mol^{-1}$	parameter of the r-HKF model
Θ	°	angle
Θ_{hkf}	K	solvent-dependent parameter
Θ_{hkl}	°	angle of the unit cell
κ	$W\ m^{-2}\ K^{-1}$	thermal conductivity
λ	m	wavelength
λ_i	-	parameters for calculating β
μ	Pa s	dynamic viscosity
μ_t	$m^2\ s^{-1}$	turbulent viscosity
ρ_c	$kg\ m^{-3}$	critical density
ρ_{solv}	$kg\ dm^{-3}$	solvent density
ρ^*	-	normalized density
σ	$N\ m^{-1}$	surface tension
σ_{ε_t}	-	turbulent Prandtl number for k_t
σ_{k_t}	-	turbulent Prandtl number for ε_t
τ	s	residence time
τ_m	s	mixing time
τ_r	s	reaction time
$\bar{\bar{\tau}}$	Pa	stress tensor
Ψ	Pa	solvent-dependent parameter
Ψ_r	$J\ mol^{-1}$	species-dependent constant
ω	$J\ mol^{-1}$	Born coefficient

Zusammenfassung

Wasser (H_2O) wird als eines der wichtigsten Elemente für das irdische Leben gesehen. Es wird vermutet, dass das Leben vor Jahren durch überkritisches Wasser in den Tiefen des Meeres entstand. Überkritisches Wasser spielt eine entscheidende Rolle im Bereich der Nanotechnologie. Deren Einfluss und Wichtigkeit nahm in den letzten Jahrzehnten in der Wissenschaft stets zu. Nanopartikel kommen beispielsweise in Kosmetikprodukten und in der Katalyse zum Einsatz. Durch ihre geringe Größe verändern sich die physikalischen und chemischen Eigenschaften. Grund hierfür ist die stark vergrößerte spezifische Oberfläche verglichen mit größeren Partikeln. Insbesondere überkritische Fluide (SCFs) sind bei der Herstellung diverser Nanomaterialien von großer Bedeutung. Sie vereinen dabei die Eigenschaften sowohl einer Flüssigkeit als auch eines Gases. Dabei wird H_2O für die Herstellung metalloxidischer Nanopartikel aufgrund seiner außerordentlichen Eigenschaften als hervorragendes Reaktionsmedium gesehen. Die kontinuierliche hydrothermale Synthese (CHTS) wurde ausgehend vom Batch-Verfahren der hydrothermalen Synthese entwickelt. Der kontinuierliche Prozess wurde in den frühen 1990er Jahren von Adschiri et al. [1] in Japan entwickelt. Das Verfahren beruht auf der Vermischung eines kalten wässrigen Metallsalzstromes ($\dot{m}_1$) mit einem nahe- / überkritischen Wasserstrom ($\dot{m}_2$). Dies führt zum Ablauf zweier konsekutiver Reaktionen, gefolgt von der Partikelbildung durch Fällung. Die synthetisierten metalloxidischen Nanopartikel werden abgekühlt und in Form einer Nanopartikelsuspension aus der Anlage entnommen. Die in dieser vorliegenden Arbeit durchgeführten Arbeiten und Ergebnisse basieren auf diesem Prozess.

Die Löslichkeit von Metallsalzen in nahe- / überkritischem Wasser stellt einen wichtigen Parameter innerhalb des CHTS-Prozesses dar. Diese wurde mittels Modellierung angenähert. Dazu dienten zwei Löslichkeitsmodelle (r-HKF- und SAA-Modell) zur Berechnung der Gleichgewichtskonstanten K_i. In einem weiteren Schritt wurde die Löslichkeit durch ein iteratives Lösungsverfahren in Kombination mit unterschiedlichen Aktivitätskoeffizienten Modellen abgeschätzt. Hierzu wurde die Löslichkeit unterschiedlicher Metallsalze angenähert und die Ergebnisse mit Literaturdaten verglichen. Die Verwendung des SAA-Modells lieferte genauere Ergebnisse aufgrund der höheren Genauigkeit im nahekritischen Bereich.

Zuerst wurde eine Anlage zur CHTS ausgelegt, konstruiert und aufgebaut. Die Stabilität der Prozessparameter während des Betriebs wurde analysiert und gewährleistet. Anschließend wurde die Anlage durch Mischungsversuche von kaltem und heißem Wasser charakterisiert. Dabei wurden der Druck p und die Temperatur des heißen Wasserstromes T_2 variiert und der Einfluss dieser auf die Mischtemperatur T_3 untersucht. Nach der Charakterisierung lag der Fokus dieser Arbeit auf der Untersuchung von Ceroxid (CeO_2) Nanopartikeln. Dazu wurden erste Partikelbildungsversuche mit Cernitrat ($Ce(NO_3)_3$) durchgeführt. Dabei wurde der Druck p konstant gehalten. Die Mischtemperatur T_3, der Gesamtmassenstrom $\dot{m}_3$ und die Salzkonzentration c_{salt} wurden anschließend variiert. Die Partikelgröße und die resultierende Partikelgrößenverteilung (PGV) wurden mittels Transmissionselektronen-mikroskopischen (TEM) Aufnahmen ermittelt. Diese wurden mit Literaturdaten verglichen. Im Folgenden wurde

der Druck p variiert. Neben $Ce(NO_3)_3$ wurden zwei weitere Metallsalze Cersulfat $Ce_2(SO_4)_3$ und Ceracetat $Ce(CH_3COO)_3$ verwendet. Hierbei wurde der Einfluss des Anions auf die resultierende Partikelgröße untersucht. Die Prozessbedingungen wurden konstant gehalten, um die Ergebnisse der unterschiedlichen Metallsalze vergleichen zu können. Eine Erhöhung sowohl der Mischtemperatur als auch des Gesamtmassenstromes führte zu einer Reduzierung der Partikelgröße. Eine Erhöhung des Prozessdrucks und der Salzkonzentration führt hingegen zur Bildung größerer Nanopartikel. Die Verwendung von $Ce_2(SO_4)_3$ als auch $Ce(CH_3COO)_3$ führte zu einer Verringerung der Partikelgröße bei sonst konstanten Prozessbedingungen. Die Experimente wurden durch Strömungssimulationen (CFD) ergänzt. Hierzu wurde ein realistisches 3D CAD-Modell (computer aided design) des in der Anlage verwendeten Reaktors entwickelt. In der Anlage gemessene Temperaturen der unterschiedlichen Oberflächen dienten hierbei zur Implementierung der Randbedingungen. Zudem wurden Modelle mit weiteren Mischungsgeometrien entwickelt. Die Modelle wurden im Hinblick auf die Güte des verwendeten Netzes, der Konvergenz und der turbulenten Intensität getestet. Im Anschluss wurden die mit der Anlage durchgeführten Mischversuche simuliert. Die daraus erhaltenen Temperatur- und Geschwindigkeitsprofile wurden analysiert und das Modell mit experimentell ermittelten Mischtemperaturen validiert. Basierend auf diesen Simulationen wurden Verweilzeitverteilungen (RTD) simuliert. Abschließend wurde die Reaktion simuliert und ein optimales Mischungsverhältnis a ermittelt. Die simulierten Reaktionsprofile wurden anschließend dazu verwendet, um die Ergebnisse der durchgeführten Experimente zu erklären.

Abstract

Water (H_2O) is one of the most important substances for life on earth. It is suspected that life arose through supercritical water in the deep sea million years ago. Supercritical water is important in nanotechnology. The importance of nanotechnology in science increased within the last decades. Nanoparticles are applied, for example, in cosmetic products as well as in catalysis. Due to the drastically decreased size, the properties, such as the reactivity and the catalytic behavior, change. The reason for this is the strongly increased specific surface compared to larger particles. Especially supercritical fluids (SCFs) are of great interest in the synthesis of various nanomaterials. The SCFs combine the properties of both gas and liquid. H_2O is a suitable reaction medium for synthesizing metal-oxide nanoparticles due to its outstanding thermodynamic properties. The continuous hydrothermal synthesis (CHTS) emerged out of the batch process of the hydrothermal synthesis. The continuous process was developed by Adschiri et al. [1] in the early 1990s in Japan. It is based on the mixing of a cold aqueous metal salt solution stream ($\dot{m}_1$) with a hot near- / supercritical water stream ($\dot{m}_2$). Two consecutive reactions occur. This is followed by particle formation through precipitation. The synthesized nanoparticles are cooled down and recovered in a nanoparticle suspension ($\dot{m}_3$). The work and results presented in this thesis are based on this process.

The metal salt solubility in near- / supercritical water is an important parameter within the CHTS process. It was estimated through modeling. Therefore, two different solubility models, the r-HKF and the SAA model, were applied to determine the equilibrium constants K_i. Then, the metal salt solubility was estimated using an iterative calculation routine with different activity coefficient models. The solubility of different metal salts was estimated and compared to experimental literature data. The SAA-model showed a better accuracy in the nearcritical region.

Initially, a CHTS plant was designed, constructed, and set up. At first, the stability of the process parameters had to be guaranteed. The plant was then characterized by mixing experiments with a hot and cold water stream. The pressure p and temperature of the hot water stream T_2 were varied, and their influence on the mixing temperature T_3 was investigated. After characterizing the CHTS plant, the main focus of this work was the investigation of the cerium oxide (CeO_2) nanoparticles. Preliminary particle formation experiments were performed with cerium nitrate ($Ce(NO_3)_3$) as a precursor. Here, the pressure p was kept constant, whereas the mixing temperature T_3, the total mass flow $\dot{m}_3$ and the salt concentration c_{salt} were varied. The particle size and the particle size distribution (PSD) were determined by means of transmission electron microscopy (TEM) and compared to literature data. In the next step, the pressure p was changed. In addition to $Ce(NO_3)_3$, two other metal salts, namely cerium sulfate $Ce_2(SO_4)_3$ and cerium acetate $Ce(CH_3COO)_3$, were used for the investigation of the influence of the anion on the particle formation. Similar process conditions were selected to compare the assess role of the precursors. Increasing the mixing temperature and the total mass flow lead to a decrease of the particle size. An increase of the pressure and the salt concentration resulted in the formation of larger nanoparticles. The application of

$Ce_2(SO_4)_3$ and $Ce(CH_3COO)_3$ led to a decrease of the particle size with constant process conditions compared to $Ce(NO_3)_3$. The experimental work was supported through computational fluid dynamics (CFD) simulations. Therefore, a realistic 3D computer aided design (CAD) model of the reactor realized in the CHTS plant was developed. Surface temperatures measured during mixing experiments were applied for boundary conditions. Furthermore, models with other possible mixing setups were designed. The models were characterized in terms of mesh quality, convergence, and turbulent intensity. Then, the mixing experiments carried out with the CHTS plant were simulated. The resulting thermal and velocity fields were analyzed, and the model was validated with experimentally determined mixing temperatures. The residence time distribution (RTD) was simulated. In the next step, the reaction was simulated, and an optimal mixing ratio a was found. The simulated reaction profiles were applied to explain the results of the performed experiments.

1. Introduction

Water is a substance that humans need in their everyday life. It is essential for life on earth. Water is vital for the human body – internally for consumption and externally for showering or cooking. Very often, salt in terms of NaCl is mixed with boiling water for the preparation of noodles. At these process conditions of ambient pressure and a temperature around 373 K water has an excellent solubility behavior for inorganic metal salts.

In contrast to the ambient conditions where water has properties that enable life, supercritical water is a powerful reaction medium. In the supercritical state of water, life would not be possible. The water reaches its critical point at the critical pressure p_c of 22.1 MPa, the critical temperature T_c of 647.1 K, and the critical density ρ_c of 322 kg m^{-3}. The difference between gas and liquid is not observable. In nature, supercritical water occurs in regions with high pressures and temperatures. At the bottom of the sea, hot water exits through magma coming from the inner earth crust, with temperatures higher than the critical temperature. The high static pressure caused by seawater results in pressures above the critical pressure of water. In combination with dissolved metal salts in the seawater, hydrothermal synthesis occurs naturally. Water behaves like a polar solvent at ambient conditions with low solubility of organic solvents and high values of the dielectric constant [2]. With increasing temperature and pressure, it acts like a non-polar solvent with values of the dielectric constant like organic solvents (compare a value of 1.9 for hexane).

The absence of the phase boundary enables liquid-like densities and gas-like viscosities for a high capability of mass transport. The tunable properties depend on pressure and temperature, which favors near- / supercritical water for several technical applications. Especially the synthesis of metal-oxide nanoparticles is suitable with supercritical water. Metal-oxide nanoparticles are applied for example in food and cosmetic products as well as in catalysis. Due to the decreasing size, the physical and chemical properties like the reactivity and the catalytic behavior are changing. The reason for this is the strongly increased specific surface compared to larger particles as well as to the quantum confinement effect. The continuous hydrothermal synthesis (CHTS) emerged out of the supercritical water oxidation (SCWO). In combination with the hydrothermal synthesis in the batch setup, Adschiri et al. developed the CHTS process in the early 1990s [1]. The principle is based on mixing a cold aqueous metal salt solution stream ($\dot{m}_1$) with a hot near- / supercritical water stream ($\dot{m}_2$). The rapid heating results in two consecutive reactions with particle formation through precipitation. The low solubility of the metal salts in the near- / supercritical state compared to ambient conditions (due to the substantial variations of the dielectric constant) is the fundament of the CHTS process.

The solubility of the metal salts and the metal oxides is of great interest for the CHTS process, the simulation of the reaction, and the particle formation. Therefore, the modeling of the metal salt solubility was established. The degree of supersaturation at a given pressure and temperature, which directly affects the nucleation rate, depends on it. The modeling of the metal salt solubility was structured into two parts. First, the equilibrium constants of the

reactions were calculated. Therefore, two models were applied. The r-HKF model [3] and the SAA model [4] were implemented for the calculation. The SAA model was favored for further analyses. Both models were validated with experimental data of the equilibrium constant. To further estimate the metal salt solubility, an iterative calculation method with different activity coefficient models was chosen. The metal salts were classified according to their respective solubility in the near- / supercritical region. The estimated solubilities were validated with experimental data of different metal salts.

The exploration of the CHTS process lasts for nearly 30 years. In contrast to the batch process, the continuous process enables the production of a large number of nanoparticles. Furthermore, the recovery of the metal-oxide nanoparticles occurs at ambient conditions in a particle suspension which is save to handle. The mean particle size is easily tunable with the process conditions pressure, temperature, and total mass flow [1]. In addition to that, the used metal salt is also significant for the mean particle size and the resulting particle size distribution (PSD). After the development of the CHTS process, many metal-oxide nanoparticles of different materials were synthesized. The variety of the formed nanoparticles ranged from simple monometallic metal-oxide nanoparticles to complex nanoparticles consisting of several different metals. Simple metal-oxide nanoparticles were synthesized in terms of aluminum oxide Al_2O_3 [5], zinc oxide ZnO [6,7], copper oxide CuO and nickel oxide NiO [8], iron oxide Fe_2O_3 [8–11], cobalt oxide Co_3O_4 [9], ceria CeO_2 [12,13], titan dioxide TiO_2 [14], and complex mixed metal-oxide nanoparticles [15–17]. In addition to that, scale-ups to the large scale were performed successfully [18], as well as in situ experiments for further analysis of the particle formation [19]. Especially within the last years the research of the CHTS process with in situ analysis increased [20]. First experiments with in situ powder X-ray diffraction (PXRD) combined with high pressure capillaries were performed [21–24]. Regarding the high pressures and temperatures, it is challenging to implement known measuring techniques into the CHTS plants. Marre et al. implemented a glass capillary with HPLC fittings or a chip-sized microsystem consisting of Silicon and Pyrex operating at a pressure of 25 MPa and temperatures between 573 K and 673 K [25].

The stabilization of metal-oxide nanoparticles in organic solvents is realized with a surface modification for good dispersibility [26]. The precursor solution is mixed with an organic acid, and during the particle formation, the ligands of the organic acid attach to the surface of the formed metal-oxide nanoparticle. Depending on the amount of used organic acid, the shape of the metal-oxide nanoparticle is changed, or its growth inhibited.

In general, the hydrothermal synthesis of non-modified metal-oxide nanoparticles was investigated and is the subject of study of this thesis. The research on the CHTS process has already been carried out for many years. Especially in the work of Daschner de Tercero, a CHTS plant was constructed for total mass flows up to 12 kg h^{-1} [27]. The focus was on the synthesis of surface modified iron oxide nanoparticles with clickable anchors. In addition to that, only a few research groups are focusing on the construction of plants. However, the challenging part is still the construction of a lab-scale CHTS plant with a suitable reactor enabling even higher mass flows during the process. As mentioned above, there are only few in

situ measuring techniques established so far. For this reason, a newly designed ceramic reactor should be integrated into the CHTS plant to gather new information during the particle formation experiments with in situ impedance spectroscopy (IS). This allows a better and direct process control. This work was carried out within the framework of the research unit ProMiSe (Erfassung und Steuerung dynamischer lokaler Prozesszustände in Mikroreaktoren mittels neuer in situ-Sensorik) in subproject 4 (Elektrisches Monitoring der Fällung von Metalloxid-Nanopartikeln in keramischen Mikroreaktoren in nahe- und überkritischem Wasser) funded by the German Research Foundation (DFG). This work aims to investigate further the influence of the process conditions on the resulting mean particle size, shape, and the PSD. Therefore, a newly designed CHTS plant was constructed and set up. Optimization steps were ongoing continuously for future applications with modified metal-oxide nanoparticles. The used components allowed a flexible design of the CHTS plant what enabled easy optimization procedures. Special attention was taken to the extensive range of usable pressures, temperatures, total mass flows, and their respective constancy during the operation (low pulsation of the pumps).

Furthermore, the mixing geometry was designed for fast assembling and change. For the first characterization of the CHTS plant, mixing experiments with cold and hot water were carried out with near- and supercritical process conditions. The experiments were analyzed concerning constant process conditions. After the characterization experiments, experiments were carried out with $Ce(NO_3)_3$ as a precursor for the synthesis of ceria nanoparticles. This material was already investigated in literature, and it is of great interest for technical applications. The mean particle sizes of the produced ceria nanoparticles were compared to experimental results published in literature [13,27,28]. The properties of ceria are strongly dependent on the respective size of the nanoparticles. Therefore, the variation of the process conditions for tuning the mean particle size was investigated. After the analysis of the particle formation with $Ce(NO_3)_3$ as a precursor, the impact of the anion on the particle formation was determined.

Therefore, in addition to $Ce(NO_3)_3$, two cerium-containing metal salts were selected and used for the particle formation experiments $Ce_2(SO_4)_3$ and $Ce(CH_3COO)_3$. The process conditions were also varied for these metal salts, and the effect on the mean particle size and the PSD was investigated. The result of clogging was examined in the case of $Ce_2(SO_4)_3$, and thereafter the mixing geometry was optimized. For the benefit of $Ce(CH_3COO)_3$, clogging did not occur, and ceria nanoparticles were synthesized to compare to particles produced with the other metal salts. The resulting particle suspensions were either oven-dried or freeze-dried for the analysis with Powder X-ray diffraction (PXRD). PXRD assures if CeO_2 was produced during the particle formation experiments. For the analysis of the median particle size and PSD, images gathered with TEM were used. The structure of the ceria nanoparticles synthesized with $Ce(CH_3COO)_3$ was analyzed with energy-dispersive X-ray spectroscopy (EDX) to assure CeO_2 was formed.

The experimental work was supported through CFD simulations. 3D CAD models were designed with significant similarities to the mixing unit used in the CHTS plant. It is often the case that in literature, only 2D simulations were carried out. The heat transfer through the

wall to the surroundings is described with an adiabatic wall condition. This boundary condition represents the ideal case. The designed 3D model was applied with realistic boundary conditions. Experimentally determined surface temperatures were measured and correlated with depicting the mixing unit in the plant. The validation of the designed model with experimental mixing temperatures showed the potential of realistic boundary conditions. The thermal and velocity fields were simulated and analyzed depending on the used process conditions. All thermal and velocity fields were simulated for the designed models (Counter, Straight, Bending, and Y-30 model). Based on the results, the residence time distribution (RTD) was simulated and analyzed. The influence of the RTD on the resulting particle size was investigated as a function of the process conditions. It provided more information on the residence time of particles in the mixer and the hot reaction zone of the CHTS plant. The reaction of $Ce(NO_3)_3$ to CeO_2 was implemented in the simulation, and the relating concentration profiles of the educts and products were analyzed and compared. The simulation of the reaction was validated with the mass fraction. The simulation of the reaction was further utilized for the optimization of the CHTS process in terms of the process conditions for the improvement of the width of the resulting PSD.

2. Theoretical background

In this chapter, the basic principles and methods used in this work are presented. In particular, the physical properties of supercritical fluids and applications will be described. After that, the focus will be on the thermodynamic properties of water, water-salt mixtures, the basics of the continuous hydrothermal synthesis, and the fundamentals of the simulation.

2.1 Supercritical fluids

Depending on the pressure p, temperature T, and chemical structure, a pure substance occurs in different phase states. These are solid, liquid and gaseous. Figure 2-1 shows a phase diagram for a pure substance with the solid lines of the sublimation pressure curve (between solid and vapor), the vapor pressure curve (between liquid and vapor), and two different behaviors of the melting pressure curve (between solid and liquid) [29].

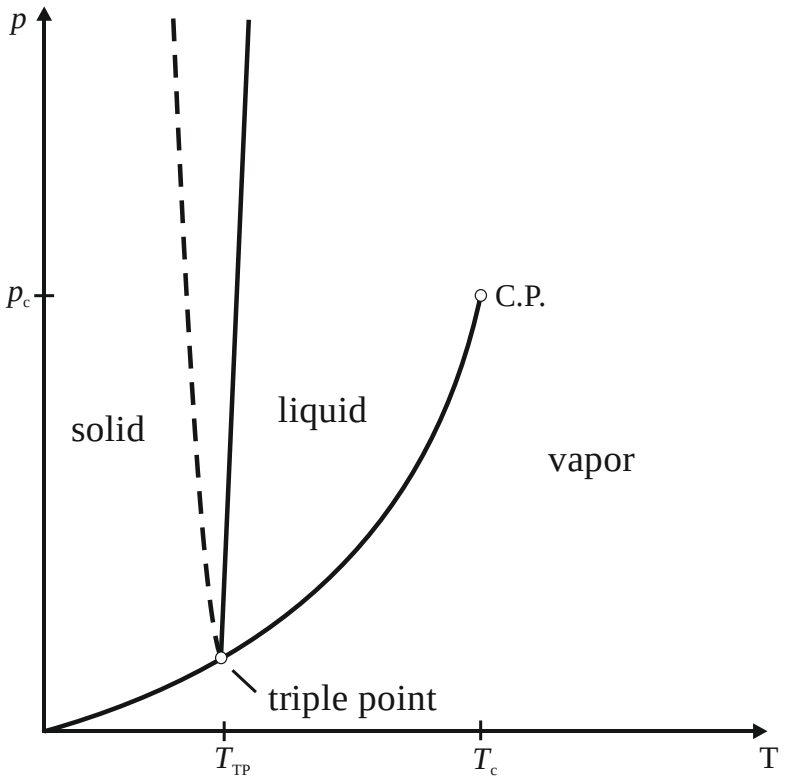

Figure 2-1: Phase diagram of a pure substance, the solid line with positive slope describes the trend of the melting pressure curve. The dashed line represents the trend of the melting pressure curve for water with a negative slope, according to [29].

Nearly all pure substances show a similar trend in the phase diagram. The solid lines show the transitions between the single-phase states. The dashed line of the melting pressure curve shows the behavior of water. Most of the other substances show a phase behavior like the solid line of the melting pressure curve. The phase transitions depend on pressure and temperature.

The critical point (C.P.) is defined as the inflection point of the critical isotherm. The first and the second derivation of pressure p by volume v at constant temperature T is equal to 0 (compare Figure 2-1). The relating pressure and temperature are named as the critical values of the substance. This is explained with an equation that looks like:

$$\left(\frac{\partial p}{\partial v}\right)_T = 0 \quad \left(\frac{\partial^2 p}{\partial v^2}\right)_T = 0 \tag{2-1}$$

The basis for this is the decrease in the volume difference between the gas and liquid phase during the evaporation process with increasing pressure and temperature. This fact results in a meeting of the curves in the critical point [29]. Here, two phenomena are taking place. While increasing the pressure, the molecules of a gas are compressed, which leads to an increase in the gas density. With increasing the temperature of the liquid phase, the molecules start to move faster. With this, the molar volume is rising, and the density is decreasing. Combining these effects leads to an approximation of both densities and results in the disappearing of the phase boundary between gas and liquid phase [30]. The critical point stands out for the assumption of the mixing of the properties of each phase. Based on that, the supercritical fluid has both of gaseous and liquid properties. For example, the supercritical fluid density is liquid-like, whereas the viscosity is similar to the gaseous phase. These effects affect the transport and material properties significantly. The high density favors the supercritical fluid's good dissolving behavior. The low viscosity leads to a high diffusivity and results then in a significant degree of mass transport [31]. Another property is the lack of surface tension increasing the permeation of tiny pores inside the materials.

As common supercritical fluids, carbon dioxide (CO_2), ethanol (C_2H_5OH), isopropanol (C_3H_7OH), hexane (C_6H_{14}) or water (H_2O) are applied. CO_2 is used in most supercritical fluid applications [32–35], followed by H_2O [15,36–38]. The most important application is the particle formation next to other important applications like the selective solubilization. Chattopadhyay et al. [33,34] describe a process for producing micro- and nanoparticles for the controlled release of drugs with supercritical CO_2. It decreases the solubility of the drugs within the mixture. Meziani et al. [35] also use supercritical CO_2 to synthesize silver nanoparticles with a modification of the Rapid Expansion of a Supercritical Solution (RESS) process. Within the modified RESS process, the formed particles are expanded into a liquid solvent. With this, a rapid reduction of the formed particles takes place with sodium borohydride or hydrazine. The resulting silver nanoparticles are then coated with a layer of either poly(N-vinyl-2-pyrrolidone) (PVP) or Bovine serum albumin (BSA).

Next to the previously described supercritical fluids, near- / supercritical water is also a suitable reaction medium. In particular, water shows the phase behavior in Figure 2-1 with a negative slope in the melting pressure curve. Increasing the pressure below 273 K leads to a liquefication of solid water. Water reaches the supercritical state at the critical point with $T_c = 647.1$ K, $p_c = 22.1$ MPa and $\rho_c = 322$ kg m^{-3}. Water is a green solvent due to its non-toxicity compared to classical organic solvents [39]. Supercritical water was already used in the past centuries and is naturally occurring on the sea ground. Hot gases pouring out of the sea ground are heating the high-pressure water rapidly to the supercritical state [40]. The demand for water as a solvent in the field of the chemical industry increased fast [41]. SCWO was developed as a process for wastewater treatment [42]. There, hazardous materials are split and broken. This kind of process is classified into a top-down process. Next to the SCWO, other methods using near- / supercritical water were developed, mainly to produce particles in a bottom-up approach.

For that, Hayashi et al. [36] describe a process of the formation of photocatalysts based on titanium dioxide (TiO_2). For this, water in the near- / supercritical state is used in an autoclave which is operated batch-wise. Through the variation of pressure and temperature, nanoparticles with a specific particle size distribution are synthesized. Wang et al. [37] investigate the phase behavior of aluminum nitrate in supercritical water. A metal salt solution of aluminum nitrate is filled in a reactor with a volume of 50 ml, and the phase behavior is determined at elevated pressure and temperature. Cote et al. [15] describe the process of the continuous hydrothermal synthesis (CHTS) of cobalt iron oxide hybrid nanoparticles ($CoFe_2O_4$). Viswanathan et al. [38] use this process for the production of zinc oxide nanoparticles.

The effort in developing new processes has intensified and is one of the potential future technologies as previously described. An important aspect of these particles' synthesis is the requirement of a defined size combined with a narrow particle size distribution and a specific shape [43–47]. Especially metal-oxide nanoparticles are of great interest in the field of catalysis, diagnostics, electronics and therapeutics [45]. These processes dealing with supercritical water as a reaction medium are complex due to the high C.P. of water and the resulting harsh operating conditions. The water properties and the behavior of water-salt mixtures and the application of supercritical water for the production of metal-oxide nanoparticles are shown in the following sections.

2.1.1 Water properties

At ambient conditions (0.1 MPa, 298 K), water is a polar solvent with a relatively high solubility for inorganic metal salts and a low solubility for non-polar organic substances. It has a high liquid density and dielectric constant, respectively [2]. Once reaching the C.P. (compare Figure 2-1) both, the properties of the liquid and the gaseous phase approach each other and become equally the same. The properties of water at ambient conditions are based on the strong hydrogen bonds between the atoms of the water molecule and their resulting arrangement in a tetrahedral shape [48]. Experimental measurements show that most of the

hydrogen bonds remain in the near- / supercritical range and especially a temperature over 673 K [49,50]. With increasing temperature up to 773 K, the hydrogen bonds become weaker, the length of the bond elongates, and the tetrahedral shape is softened [51]. With increasing temperature, the density decreases, which reduces the number of hydrogen bonds [48]. In the supercritical state, clusters of water molecules are formed. It results in differences in the local density what maximizes at the critical point of water. The weakness of the hydrogen bonds in the supercritical state leads to the destruction of the long-range order. A high heat transfer with a high self-diffusion due to lowered energy barriers is favored [52].

Figure 2-2 shows the drastic change in the water properties for a constant pressure of 30 MPa over the temperature:

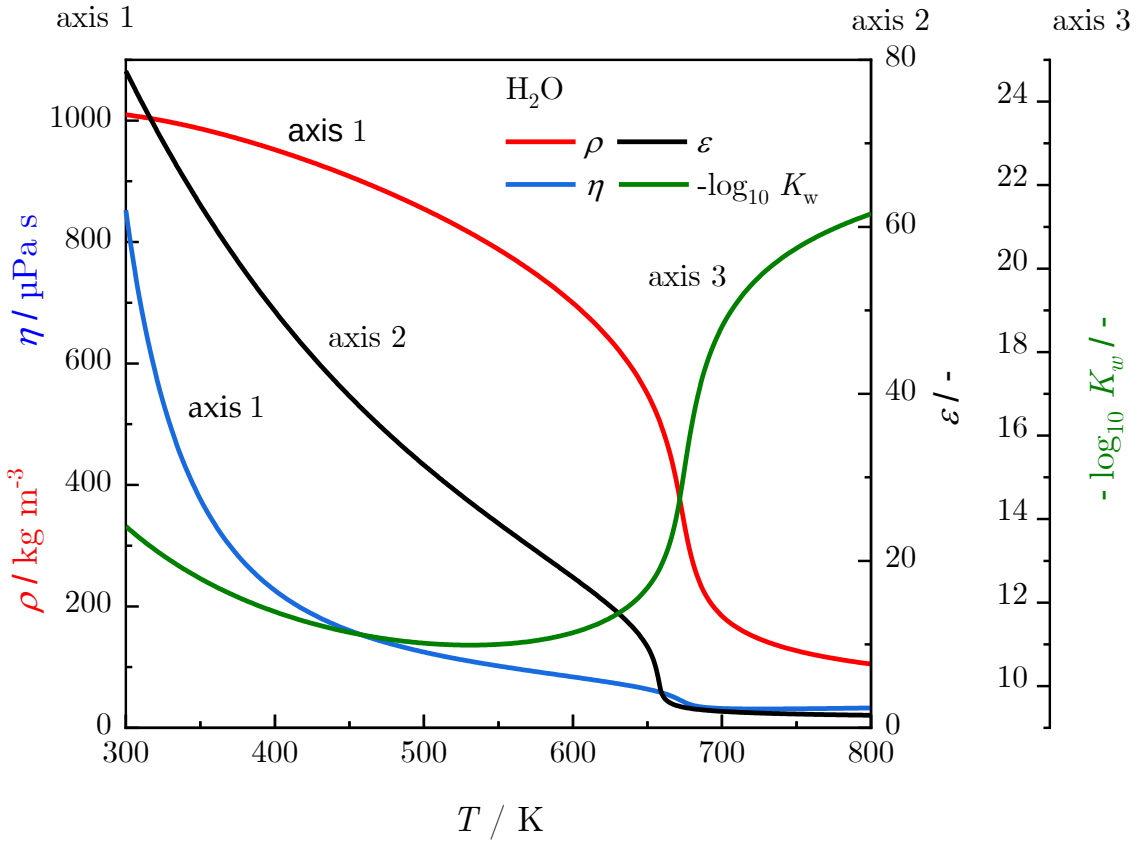

Figure 2-2: Selected water properties for a pressure p of 30 MPa over the temperature T, density ρ (red line, taken from [53] and calculated based on IAPWS 1995 from Wagner et al. [54]), dynamic viscosity η (blue line, taken from [53], based on IAPWS 1997 [55]), dielectric constant ε (black line, taken from [53], calculated according to Johnson et al. [56]) and logarithmic ion product K_w (green line, calculated according to Marshall et al. [57], according to[58].

Near the C.P., the water properties are changing rapidly. A variation of pressure and temperature allows the adjustment of the density, viscosity and dielectric constant over a wide range [46,48,59]. Both the density and the dielectric constant show a substantial decrease in

the near- / supercritical region. At 0.1 MPa and 300 K, the dielectric constant is around 80, whereas around the C.P., it is about 6. For 30 MPa and 800 K, the value decreases even more, down to 1.7. This value corresponds to the organic solvent n-hexane with a dielectric constant of 1.9 at ambient conditions [60]. The decreasing value of the dielectric constant changes the solubility behavior of water. A reason for this is the decrease of the density and the already explained weakening of the hydrogen bonds in the supercritical region. The high value of the dielectric constant at ambient conditions favors the dissociation of inorganic metal salts, whereas the low value in the near- / supercritical region favors the solvation of non-polar organic compounds.

The viscosity is decreasing in the subcritical region with increasing temperature from 300 K to 700 K. Compared to ambient conditions, the value for the viscosity is way lower at elevated temperatures. In the supercritical region, it is slightly increasing with increasing temperature. This behavior fits the temperature dependency of the viscosity of gases. The decrease in the viscosity leads to an increase either in the mass transport and the diffusivity.

Furthermore, the flow is affected for low viscosities, and the Reynolds number (Re) can increase from laminar to turbulent flows with the change of the thermodynamic properties of water. The thermal conductivity is also increasing. In combination with better mass transport, diffusion-controlled reactions are favored and accelerated [48]. The last important property described is the ionic product representing the self-dissociation of water (calculated according to Marshall et al. [57]). The rise in self-dissociation with increasing temperature is described with its endothermic behavior [52]. This affects chemical reactions, solubility and the chemical equilibrium [1]. Especially reactions catalyzed by acids are favored due to the higher amount of H^+ ions [52,61]. Table 2-1 summarizes the previously described water properties in the liquid, gaseous and supercritical state.

Table 2-1: Water properties as a function of pressure p and temperature T, according to [46,48,59].

	p / MPa T / K				
	0.1	25	25	50	0.1
	298	523	673	673	673
density ρ / kg m^{-3}	1000	820	170	570	0.3
viscosity μ / Pa s	$8.9 \cdot 10^{-4}$	$1.1 \cdot 10^{-4}$	$2.9 \cdot 10^{-5}$	$6.8 \cdot 10^{-5}$	$2.4 \cdot 10^{-5}$
ionic product K_w / -	10^{-14}	10^{-11}	10^{-20}	10^{-12}	-
dielectric constant ε / -	78	27	6	11	1

Next to the properties mentioned above, the specific isobaric heat capacity c_p is another essential property. It depends on the respective material's system, the pressure and temperature. The isobaric heat capacity of water is higher than for other liquids due to the strong hydrogen bonds. During the heating, energy is absorbed for the breakage of the hydrogen bonds [62].

The enthalpy H consists of the internal energy U and the pressure p and the volume V [29]:

$$H = U + pV \tag{2-2}$$

For constant pressures ($dp = 0$), the differential specific enthalpy dh is determined from the specific isobaric heat capacity c_p and the differential change of the temperature dT:

$$dh = c_p \, dT \tag{2-3}$$

The trends of c_p of water as a function of the temperature are shown in Figure 2-3. The trends are shown for different supercritical pressures as used in the CHTS process.

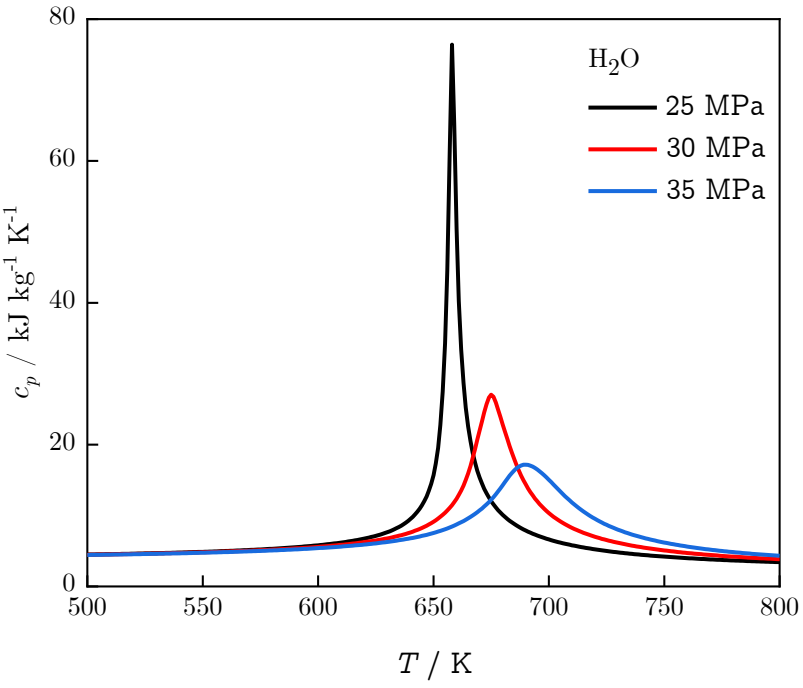

Figure 2-3: Specific isobaric heat capacity c_p of water as a function of temperature for different supercritical pressures – 25 MPa (black line), 30 MPa (red line) and 35 MPa (blue line), data taken from [53].

The deviation of the specific isobaric heat capacity from an ideal gas's behavior changes with pressure and temperature. Especially with approaching T_c, there is a drastic change. High

supercritical pressures ($p > p_c$) lead to lower maximum values of the specific isobaric heat capacity. From 25 MPa to 35 MPa, the value is decreasing from 77 kJ kg^{-1} K^{-1} to 18 kJ kg^{-1} K^{-1}. Furthermore, the maximum is shifting to higher temperatures in the supercritical region with increasing pressure. The respecting values change from 25 MPa to 35 MPa from 660 K to 690 K. It is essential to mention that the operating conditions of the CHTS process should not be close to the critical point of water due to the infinity of the specific isobaric heat capacity.

The adjustment of the water properties in terms of molecular and macroscopic scale greatly influences the solubility behavior. In the next section, the focus will be on the solubility of aqueous inorganic metal salt solutions.

2.1.2 Metal salt solubility and water – salt mixtures

Electrolyte solutions consist of a solvent and a solute. As already mentioned, the related solvent is water combined with inorganic metal salts as solutes. The electrolytes conduct electricity either in a solid or a liquid state [63]. Common examples of inorganic metal salts are sodium chloride (NaCl) or sodium sulfate (Na_2SO_4). At ambient conditions, metal salts are easily dissolvable in liquid water, whereas non-polar substances are only hard to dissolve. Metal salts can form different kinds of mixtures with water. Either symmetric or asymmetric mixtures are possible. Van Konynenburg and Scott defined different types of mixtures [64]. A symmetric mixture shows a critical line between the critical points of both pure substances. Most metal salts form asymmetric mixtures with water [48] with a broken critical line [47]. The behavior of both varieties is shown in Figure 2-4:

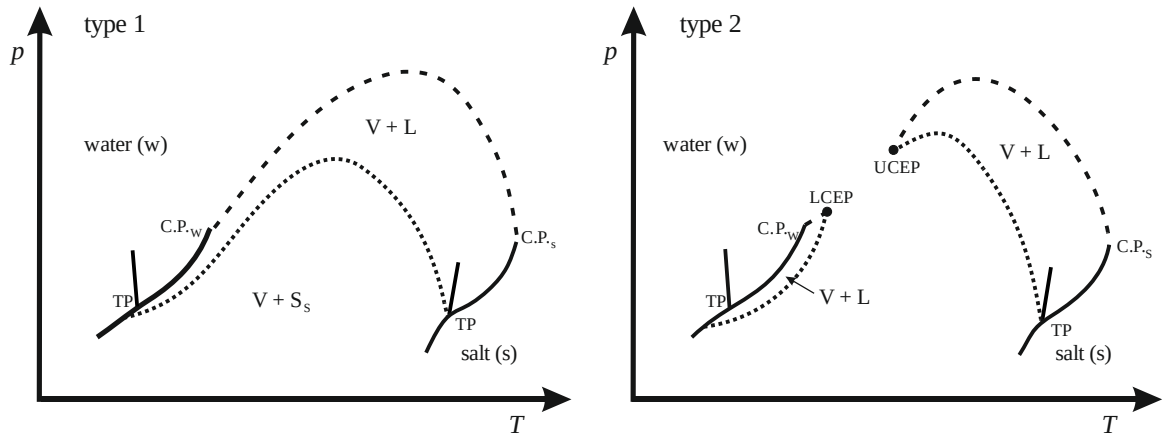

Figure 2-4: Pressure – temperature diagram for the salts categorized in type 1 and 2, with the critical points and the triple points (TP) of the pure substances, the lower critical endpoint (LCEP) and the upper critical endpoint (UCEP). The dotted line shows the solid-liquid-gas line (SLG), and the dashed line shows the critical line between both critical points. Reprinted with permission from Elsevier, according to [65].

The break in the critical line is based on the significant difference in the boiling and the critical temperature of the water and the metal salt as well as differences in the molar mass [60]. The critical point of metal salts is way higher than water, making water to the volatile compound within the mixture [48]. As already mentioned above, the metal salt solubility is low in supercritical water. Voisin et al. [60] published the classification of the metal salt solubility in supercritical water into two types according to either Marshall [66] or Valyashko [67]. Valyashko structured the metal salt solubility according to the melting temperature of the salts. Here, type 1 salts have a melting temperature between 800 °C and 1000 °C. Type 2 metal salts have a melting temperature between 700 °C and 800 °C. Marshall classifies the metal salt solubility with the solubility in the near- / supercritical region. Type 1 salts have a higher solubility in supercritical water compared to type 2 salts.

Furthermore, the metal salt solubility increases with increasing size of the corresponding anion / cation for a constant anion / cation [60]. For the type 2 metal salt, two characteristic points are visible in Figure 2-4. Both in the LCEP and the UCEP, the critical line hits the SLG line. Next to Van-der-Waals interactions for neutral molecules, long-range Coulomb interactions are present for electrolytes and significantly affect their phase behavior [48,63]. Coulomb-dipole interactions mainly influence water as a polar solvent in combination with electrolytes. This is reflected in high values of the dielectric constant. The hydrogen atoms, which show a positive partial charge, orient to the anions, whereas the oxygen atoms with negative partial charge orient to the cations [63]. This effect leads to the arrangement of water molecules between the ions on the surface of the metal salt. Due to that, ionic bonds and the crystal structure are destroyed. After breaking up, the ions are covered by water molecules. This step is the so-called hydration. This step is either endo- or exothermic. Once it is endothermic, the metal salt solubility increases with increasing temperature. If the hydration is exothermic, the metal salt solubility decreases with increasing temperature [68,69]. The dielectric constant affects the strength of the Coulomb forces leading to dissociation or association effects. These effects are hard to consider within an equation of state for describing electrolyte systems in the near- / supercritical region [48]. Examples for metal salts classified into type 1 or type 2 are shown in Table 2-2:

Table 2-2: Classification of metal salts into types 1 and types 2 according to their solubility in supercritical water, reprinted with permission from Wiley [39].

type 1	type 2
$BaBr_2$, $BaCl_2$, $Ba(NO_3)_2$	BaF_2, CaF_2
KBr, KCl, K_2CO_3	K_2SO_4
LiBr, LiCl	$LiPO_4$, $LiSO_4$
NaBr, NaCl, $NaNO_3$, Na_2SeO_4	Na_2CO_3, Na_3PO_4, Na_2SO_4

The metal salt solubility is estimated with different models. In the past decades, several models were developed to calculate the equilibrium constant K_i [3,4]. The equilibrium constant K_i compares the reactants of a reaction in terms of their activity or concentration correlated with stoichiometry. Once the difference between the forward and back reaction is 0 for a specific reaction, the system is in the equilibrium state [69]. If K_i is below values of 1, the back reaction is faster than the forward reaction, which results in the equilibrium location on the educt side. With values of K_i greater than 1, the equilibrium is on the product side. The equilibrium constant K_i describes the equilibrium location but does not give any information about the velocity of the reaction [69]. For this, approaches for the reaction kinetics need to be considered and is described in the later sections.

2.1.2.1 The Helgeson - Kirkham - Flowers (HKF model) and its revision (r-HKF model)

In 1981, Helgeson, Kirkham and Flowers developed the so called HKF model [3], which was revised by Tanger et al. as the r-HKF model in 1988 [70]. The models are semi-empirical equations of state which are based on the law of Debye and Hückel. Initially, the HKF model was developed within the framework of geochemistry. It was applied to calculate the equilibrium constants of more than 100 inorganic aqueous species in that field. High temperatures and pressures are present in the field of geochemistry. This requires a description of the equilibrium constant K_i over a wide range (298 K – 1273 K, 0.1 – 500 MPa) [71,72]. The calculation of K_i with the HKF model is based on the Gibbs free energy of formation at a given temperature and pressure for every single species. The advantage is the consideration of a large number of reactions based on a small number of required species. The Gibbs free energy of formation is calculated according to:

$$\Delta\bar{G}_i^\circ = \Delta\bar{G}_{\mathrm{r},i}^\circ + \Delta\bar{G}_{\mathrm{n},i}^\circ + \Delta\bar{G}_{\mathrm{s},i}^\circ \tag{2-4}$$

$\Delta\bar{G}_i^\circ$ consists out of the summation of three different terms of the Gibbs free energy. $\Delta G_{\mathrm{r},i}^\circ$ describes the Gibbs free energy at ambient conditions of 298.15 K and 0.1 MPa. $\Delta\bar{G}_{n,i}^\circ$ is defined as the difference in the Gibbs free energy through the interaction between the involved ions, whereas $\Delta\bar{G}_{\mathrm{s},i}^\circ$ describes the interactions between the ions and solvent. Both parts represent the

change of the aqueous species i from the reference state to elevated temperatures and pressures. The definitions of $\Delta\bar{G}^{\circ}_{\mathrm{n},i}$ and $\Delta\bar{G}^{\circ}_{\mathrm{s},i}$ are found in Appendix chapter 2 B: r-HKF model.

$\Delta\bar{G}^{\circ}_{n,i}$ contains the parameters a_1 – a_4, c_1, c_2 and ω. All of them depend on the species and are described more precisely in Appendix chapter 2 B: r-HKF model. The parameters Ψ, Θ and $Y_{p_\mathrm{r},T_\mathrm{r}}$ depend on each solvent. Concerning water used as a solvent, the values for these parameters result in 260 MPa, 228 K and -5.8 10^{-5} K^{-1}. The derivations of $\Delta\bar{G}^{\circ}_{n,i}$ and $\Delta\bar{G}^{\circ}_{\mathrm{s},i}$ are found more detailed in literature [3]. A modified Born type equation describes the electrostatic interactions between the involved ion and the solvent. The effective electrostatic ionic radius of the dissolved salt is pressure- and temperature-dependent.

This correlation is the so-called revised form of the HKF model, performed by Tanger et al. [70] and Shock et al. [71]. The coefficient related to the Born type equation is defined as follows and the parameters are found in Appendix chapter 2 B: r-HKF model.

$$\omega_{p;T} = \eta_{HKF}\left(\frac{z^2}{r_{e,p_\mathrm{r},T_\mathrm{r}} + |z|g} - \frac{z}{3.082 + g}\right) \tag{2-5}$$

The shown parameter g in equation (2-5) considers the density and temperature change of the effective electrostatic ionic radius. It is an empirical fit of the r-HKF model to experimental data of the equilibrium constant K_i. The g-function was defined by Tanger et al. [70]:

$$g = a_\mathrm{g}(1-\rho^*)^{b_\mathrm{g}} \tag{2-6}$$

The calculation of the parameters a_g and b_g is shown in Appendix chapter 2 B: r-HKF model. Within the HKF model, the g-function was adjusted to the supercritical region due to its historical background. Therefore, Shock et al. [72] structured it into three areas with different functions for calculating g what is found in Appendix chapter 2 B: r-HKF model. Both the HKF and the r-HKF model were developed based on geochemical processes where pressures above the critical point of water are present. Because of that, the application in the near-critical region was not focused while developing these models. For this reason, the model of Sue-Arai-Adschiri (SAA model) was developed. It will be described in detail in the next section.

2.1.2.2 Sue-Arai-Adschiri model (SAA model)

Next to the applicability of the r-HKF model for high system pressures, it requires different species-specific parameters. Most of them are only accessible through experiments. There is a need for a model for estimating the solubility behavior of metal salts in near- / supercritical water without requiring demanding experiments. In the early 2000's Sue, Arai and Adschiri developed the so-called Sue-Arai-Adschiri model (SAA model) for predicting the solubility behavior of metal salts [4]. The advantage of the model is the lower number of species-specific parameters compared to the r-HKF model. With the r-HKF model, the Gibbs free energy of formation for every species involved in a reaction is calculated. The Gibbs free energy of

formation for the reaction is then determined by a summation of the single amounts of the species. Within the SAA model, the Gibbs free energy of formation is calculated for the whole reaction. The model and its derivation will be described in the following.

For a reaction in the near- / supercritical region, the equilibrium constant of an aqueous system results in:

$$\ln K = -\frac{\sum_i n_i \Delta \bar{G}_i^\circ}{RT} = -\frac{\Delta \bar{G}_{T_\mathrm{r},\rho_\mathrm{r}}^\circ + \Delta \bar{G}^\circ}{RT} \tag{2-7}$$

For the temperature and the pressure, the reference state is considered with the reference temperature $T_\mathrm{r} = 298$ K, reference density $\rho_\mathrm{r} = 0.997$ g cm^{-3}, and a reference pressure $p_\mathrm{r} = 0.1$ MPa. The definitions of $\Delta \bar{G}_{T_\mathrm{r},\rho_\mathrm{r}}^\circ$ and $\Delta \bar{G}^\circ$ are found in Appendix chapter 2 C: SAA model.

The combination of equations (2-7-9) and (2-7-10) from Appendix chapter 2 C: SAA model show the calculation rule for the SAA model:

$$\ln K_{T,\rho} = \ln K_{T_\mathrm{r},\rho_\mathrm{r}} - \frac{\Delta \bar{H}_{T,\rho_\mathrm{r}}^\circ + \beta(1-\rho^*)^{\frac{2}{3}} + \alpha \Delta\omega_{T_\mathrm{r},\rho_\mathrm{r}} T_\mathrm{r}}{R}\left(\frac{1}{T} - \frac{1}{T_\mathrm{r}}\right)$$

$$- \frac{\Delta\omega_{T,\rho}}{RT}\left(\frac{1}{\varepsilon_{T,\rho}} - 1\right) + \frac{\Delta\omega_{T_\mathrm{r},\rho_\mathrm{r}}}{RT}\left(\frac{1}{\varepsilon_{T_\mathrm{r},\rho_\mathrm{r}}} - 1\right) \tag{2-8}$$

Typically, β is a fitting parameter for literature data and the calculated equilibrium constants. Sue et al. [4] re-evaluated the function of β for the SAA model. The values used in the calculation are shown in Table 2-3:

$$\beta = \lambda_1 \Delta \bar{C}_{P\,T_\mathrm{r},\rho_\mathrm{r}}^\circ + \lambda_2 \Delta\omega_{T_\mathrm{r},\rho_\mathrm{r}} + \lambda_3 \tag{2-9}$$

Table 2-3: Parameters used for calculating β [4].

parameter	
λ_1 / K	$9.737 \cdot 10^1$
λ_2 / –	$1.947 \cdot 10^{-2}$
λ_3 / J mol^{-1}	$-5.96 \cdot 10^2$

In the r-HKF model, the *g*-function is evaluated in the supercritical region in the pressure and density range of 50 MPa – 500 MPa and 0.35 g cm^{-3} – 1 g cm^{-3}. Its application is based in the field of geochemistry, which is unpracticable for process conditions near the critical point. For

this reason, the *g*-function was reevaluated from Sue et al. [4] with new experimental data in the near-critical region of the NaCl and KCl system. Data were published either by Gruszkiewicz et al. [73] and Ho et al. [74–76], and used for the adjustment of $f(p,T)$:

$$f(p,T) = c_{g1}(\rho^*) + c_{g2}(\rho^*)^2 + c_{g3}\ln(\rho^*) \tag{2-10}$$

with values for $c_{g1} = 0.18359$, $c_{g2} = -0.18632$ and $c_{g3} = 0.11531$. The function is valid for temperatures above 423 K and pressures up to 100 MPa [4].

2.1.2.3 Activity coefficient models

Once non-ideal effects of a water-salt mixture are dominating, activity coefficients need to be considered. For pure substances, the activity coefficient has a value of 1. This is the case for pure water. Once an electrolyte represented by a metal salt is added to the pure water, the activity coefficient decreases to values below 1. A reason for this is the long-term attractive Coulomb forces between the ions what increases the solubility. The trend of the activity coefficient as a function of the salt concentration reaches a minimum first and increases steadily afterwards. With increasing salt concentration, the short-term forces suppress the long-term attractive Coulomb forces, and the repulsive Coulomb forces are growing. Specific models were developed to describe the activity coefficients, and selected ones will be shown in the following [63].

The Debye-Hückel-Davies equation (DHD) is a modification of the classical Debye-Hückel equation. In general, the Debye-Hückel equation is valid for an infinite dilution of an electrolyte in a solvent. Here, only the repulsive Coulomb forces between the ions are considered. The own volume of the ions is neglected. The Debye–Hückel equation is valid for ionic strengths up to 0.005 mol kg^{-1} [69]. For more considerable ionic strengths up to 0.1 mol kg^{-1}, the Debye-Hückel-Davies equation was developed [63,77]. The activity coefficient is defined as follows:

$$\ln\gamma_i = -\frac{z_i^2 A_M \sqrt{I_m}}{1+\sqrt{I_m}} + 0.2 A_M z_i^2 \sqrt{I_m} \tag{2-11}$$

with A_M and I_m and z_i found in Appendix chapter 2 D: Activity coefficient models. To depict activity coefficients with higher ionic strengths than 0.1 mol kg^{-1}, another model, named as the Bromley equation, has to be considered. The limits of the Debye-Hückel equation are in the description of the long-term Coulomb interactions. With increasing salt concentration and thus an increase in the ionic strength, the amount of the short-term interactions is rising. For high concentrated salt solutions, this contribution needs to be considered. The Bromley model is based on the Debye-Hückel equation. Bromley modified the equation with a material-dependent parameter for the interactions. The limitation of the ionic strength results in

6 mol kg^{-1} [63]. The Bromley model is defined as follows. The parameters are described in Appendix chapter 2 D: Activity coefficient models.

$$\log_{10}\gamma_i = -z_i^2 A_{\mathrm{M}} \frac{\sqrt{I_{\mathrm{m}}}}{1+\sqrt{I_{\mathrm{m}}}} + F_i \tag{2-12}$$

The models for calculating the activity coefficients are used to estimate the metal salt solubility in the later sections.

2.2 The continuous hydrothermal synthesis (CHTS)

As described in section 2.1, the continuous hydrothermal synthesis (CHTS) emerged from previously developed processes with supercritical water. The SCWO process is an application in the field of wastewater treatment. Metal-oxide nanoparticles were already synthesized in batch-type reactors [78]. With these experiments, only a small number of metal-oxide nanoparticles was producible. The beginning of the formation of metal-oxide particles dates back to the middle of the 19th century. In 1900, the experiments of George Spezia changed the view on small synthesized particles [79]. Before, the formed particles were seen as insufficient because they were not visible without additional equipment, such as a microscope. The aim was to synthesize particles on the millimeter scale [80]. Up till 1920, it was not possible to examine and characterize nanosized particles. The discovery of the X-rays enabled the analysis of such small particles [81,82].

In contrast to the CHTS, in the batch-type hydrothermal synthesis, the metal salt solution is heated up in an autoclave. It is easy to realize and requires simple components. However, the heating process is slow and the temperature inside the reactor is not perfectly adjustable leading to a broad particle size distribution. Furthermore, the conduction of the experiment requires several hours what leads to long-duration experiments [83]. The density enormously depends on the mass of the liquid metal salt solution filled into the autoclave. The accuracy of the filled mass is necessary because the pressure is strongly influenced by the mass at near- / supercritical conditions. Compared to the batch process, in the continuous process, the cold aqueous metal salt solution is heated up rapidly by mixing with a hot near- / supercritical water stream in a simple T-shaped mixer [81]. In the early 1990's Adschiri et al. developed the CHTS process [1]. The advantage is the continuous production of metal-oxide nanoparticles in large quantities, combined with the precise control of the particle size. The continuous process enables a better scalability in comparison to the batch-type synthesis method. Next to the CHTS process, the RESS process in combination with hydrothermal treatment and a metal salt solution was used in the early 1990s to produce metal-oxide nanoparticles [84]. However, this process was not promising due to the challenging injection of the metal salt solution [81]. In the industrial field, first scale-ups have been realized. One example is the Hanwha Chemical company using the CHTS process since 2011. $LiFePO_4$ particles with an annual amount of 1000 tons are

produced [85,86]. On the lab-scale, certain studies have been performed on the synthesis of metal-oxide nanoparticles. Several review articles show an overview of the application and the formation of metal-oxide nanoparticles in the current state of the art:

Darr et al. reviewed these studies and summarize process conditions, and produced metal-oxide nanoparticles [81]. Aymonier et al. present the application of the formation of inorganic materials [44] and the influence of the chemistry in supercritical solvents [87]. Türk gives an overview of the particle formation with supercritical fluids and the respective limits [47]. Lester et al. describe the reaction engineering of the CHTS process [18]. Further review articles are found in literature [85,88–91].

As already mentioned, the particle formation is initialized through the mixing of a cold aqueous metal salt solution ($T_1 = 293$ K, $\dot{m}_1$, c_{salt}) with a hot near- / supercritical water stream ($T_2 = 573 - 673$ K, $\dot{m}_2$) in a resulting particle stream (T_3, $\dot{m}_3$) at pressures greater than the critical pressure (25 MPa – 35 MPa) of water. A significant value is the mixing ratio a which is defined as the follows:

$$a = \frac{\dot{m}_1}{\dot{m}_2} \tag{2-13}$$

After the particle formation, the product stream is cooled down to terminate the reaction and the further growth of the nanoparticles. A scheme of the process with important process parameters is shown in Figure 2-5:

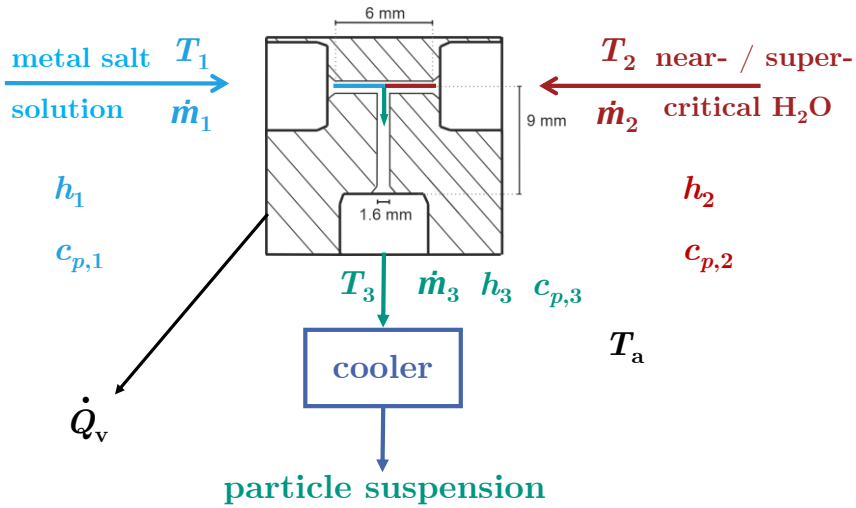

Figure 2-5: Scheme of the CHTS process with the used T-shaped mixing unit, dimensions and corresponding parameters for the energy and mass balance [47,85].

The shown T-shaped mixer in Figure 2-5 is used in three different setups [92]. The described mixing setup is the Counter setup. Other possible arrangements are the Straight and the Bending setup. All three mixing configurations of the T-shaped mixing unit are shown in

Figure 2-6. The streams of the cold aqueous metal salt solution, the hot water stream, and the product stream are equal to those shown in Figure 2-5.

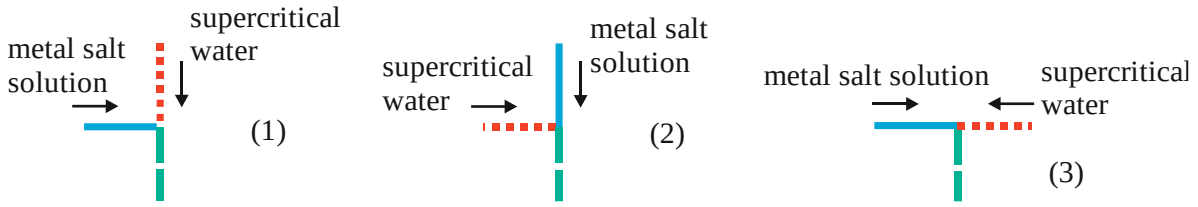

Figure 2-6: Mixing setups (1) Straight-, (2) Bending- and (3) Counter-setup in a T-shaped mixer, according to [92].

The mixing temperature T_3 of both streams has an important impact within the CHTS process. The mass, momentum, energy, and enthalpy balances are required for determining the theoretical mixing temperature [58]. The mass balance for the mass flows results in [29]:

$$\dot{m}_1 + \dot{m}_2 = \dot{m}_3 \tag{2-14}$$

In combination with the mixing ratio a, the mass flows are described in dependence on the total mass flow $\dot{m}_3$.

$$\dot{m}_1 = \frac{a}{a+1}\,\dot{m}_3$$
$$\dot{m}_2 = \frac{1}{a+1}\,\dot{m}_3 \tag{2-15}$$

Regarding the stationary energy balance (no change in enthalpy with time), equation (2-16) is valid with the specific enthalpy of each stream h_i and the heat loss $\dot{Q}_V$ [29]. Here, the unheated state of the mixing unit and the neglection of the kinetic and the potential energy is assumed:

$$\dot{m}_1\, h_1 + \dot{m}_2\, h_2 - \dot{m}_3\, h_3 - \dot{Q}_V = \cancel{\frac{dH}{dt}} = 0 \tag{2-16}$$

The heat loss $\dot{Q}_V$ is calculated with equation (2-17) [93]:

$$\dot{Q}_V = k_{\mathrm{HT}}\, A_{\mathrm{m}}\, (T_3 - T_{\mathrm{a}}) \tag{2-17}$$

It is calculated with the heat transition coefficient k_{HT} and the mean heat transition area A_{m} and the temperatures T_{i}. k_{HT} includes all specific heat transfer and transition coefficients. Combining the heat transition coefficient k_{HT} and the mean area A_{m} can either be determined experimentally or theoretically. The combination of the equations (2-16) and (2-17) results in:

$$k_{\mathrm{HT}}\, A_{\mathrm{m}} = \frac{\dot{m}_1\, h_1 + \dot{m}_2\, h_2 - \dot{m}_3\, h_3}{T_3 - T_{\mathrm{a}}} \tag{2-18}$$

Furthermore, equations (2-3), (2-17), and (2-18) lead to the equation for the theoretical mixing temperature depending on the values mentioned above and the reference temperature T_0:

$$T_3 = \frac{\dot{m}_1}{\dot{m}_3}\frac{c_p(T_1)}{c_p(T_3)}(T_1 - T_0) + \frac{\dot{m}_2}{\dot{m}_3}\frac{c_p(T_2)}{c_p(T_3)}(T_2 - T_0) - \frac{1}{\dot{m}_3}\frac{1}{c_p(T_3)}\, k_{\mathrm{HT}}\, A_{\mathrm{m}}\, (T_3 - T_{\mathrm{a}}) + T_0 \tag{2-19}$$

In combination with equation (2-15), equation (2-19) is rearranged to:

$$T_3 = \frac{a}{1+a}\frac{c_p(T_1)}{c_p(T_3)}(T_1 - T_0) + \frac{1}{1+a}\frac{c_p(T_2)}{c_p(T_3)}(T_2 - T_0)$$
$$- \frac{1}{\dot{m}_3}\frac{1}{c_p(T_3)}\, k_{\mathrm{HT}}\, A_{\mathrm{m}}\, (T_3 - T_{\mathrm{a}}) + T_0 \tag{2-20}$$

Concerning the temperatures used in the CHTS process, the first part of equation (2-20) is way smaller than the second part. In addition to that, the derivation of equation (2-20) for the mixing ratio a results in:

$$\left(\frac{\partial(T_3\, c_p(T_3) + \frac{1}{\dot{m}_3} k_{\mathrm{HT}} A_{\mathrm{m}} T_3)}{\partial a}\right)_{T_1,T_2} \approx \frac{1}{(1+a)^2} c_p(T_1)\, T_1 - \frac{1}{(1+a)^2} c_p(T_2)\, T_2 \tag{2-21}$$

The instantaneous heating of the metal salt solution leads to the drastic changes in the water properties mentioned above (compare section 2.1). It results in a homogeneous heat distribution inside the mixing unit and the reactor. These changes affect the solubility of the metal salts. In principle, three consecutive reactions occur during the CHTS process. They are structured into a hydrolysis reaction, a dehydration step and the precipitation reaction [1,85]. In the first step of the hydrolysis, the metal cation reacts with water to the metal hydroxide. With increasing temperature, the equilibrium shifts towards the product side of the metal hydroxides [1,83]. In the next step, the dehydration, the formed metal hydroxide reacts to the resulting metal oxide in the aqueous state (aq). The low solubility of the metal salt and the formed metal oxide at elevated temperatures and pressures results in a high degree of supersaturation occurring after hydrolysis and dehydration, which is thereafter reduced by particle formation [94]. This leads to the precipitation through homogenous nucleation of the aqueous metal oxide to the solid nanoparticles (s).

The occurrence of nucleation in real systems was described 1990 by Debenedetti [95] and extended by Türk in 2000 [96]. The classical nucleation theory was first expressed by Becker et al. [97] and later by Volmer [98]. The nucleation step during the particle formation can be split into primary and secondary nucleation. Crystals initiate secondary nucleation. The primary nucleation is either of homogeneous or heterogeneous nature. Here, the degree of supersaturation is the crucial parameter. The homogeneous nucleation is initialized spontaneously for high degrees of supersaturation. The heterogeneous nucleation occurs due to

foreign particles acting as seeds with a lower degree of supersaturation required [99]. The low solubility limit leads to a very high degree of supersaturation and results in the homogeneous nucleation of the formed metal oxides. The nucleation rate is defined as the follows [96]:

$$J = K^* \exp\left(-\frac{\Delta G^*}{k_B \cdot T}\right) \tag{2-22}$$

with K^* representing the number of hits between the nuclei per time and volume. It depends on the non-isothermal factor, the non-equilibrium factor according to Zeldovich, the condensation coefficient, the number of condensable molecules per volume, the thermal velocity and the mass of a solid molecule. ΔG^* and k_B are describing the Gibbs free energy of critical nucleus formation, and the Boltzmann's constant. The reciprocal nucleation rate is the which is the average time between the formation of nuclei in a unit volume and is defined as [96]:

$$J = \frac{1}{\Delta t\, V} \tag{2-23}$$

The Gibbs free energy of critical nucleus formation ΔG^* depends on the squared critical radius of a nucleus [47]:

$$\Delta G^* = \frac{4}{3}\,\pi\,\sigma\, r^{*2} \tag{2-24}$$

with

$$r^* = \frac{2\,\sigma\, v_{2,s}}{k_B\, T \ln S} \tag{2-25}$$

Here, σ, v_{2s} and S stand for the interfacial tension of the solute, solute molecular volume in the solid phase, and the supersaturation, respectively. Equation (2-24) combined with equation (2-25) leads to the following description of the Gibbs free energy of critical nucleus formation:

$$\Delta G^* = \frac{16}{3}\,\pi\,\frac{\sigma^3\, {v^2}_{2,s}}{(\ln S)^2\,(k_B\, T)^2} \tag{2-26}$$

There is a cubic proportionality of the Gibbs free energy of critical nucleus formation between the interfacial tension. In addition, a squared reciprocal proportionality between the supersaturation and the temperature is present. A slight change of either the supersaturation or the temperature results in drastic changes of the nucleation rate. The supersaturation is defined as the follows [100]:

$$S = \frac{c_{salt} - c_s(p,T)}{c_s(p,T)} \tag{2-27}$$

with c_{salt} and $c_s(p,T)$ describing the metal concentration used in the experiment and the estimated metal-oxide solubility at given pressure and temperature. Equation (2-27) is valid for values of $c_{salt} \geq c_S(T)$. Both values are affecting the supersaturation either by the salt concentration c_{salt} and the saturation concentration $c_s(p,T)$. This value is influenced by the mixing ratio a, the pressure, and temperature. At given near- / supercritical pressure and temperature within the CHTS process, $c_s(p,T)$ is low what leads in general to an exceptionally high value of the supersaturation. An increase in the supersaturation leads to a decrease in the critical radius of a nucleus. Once the critical radius is exceeded, the nucleus grows or is dissolved, respectively. Sue et al. [100] reported that the average particle size of different resulting metal-oxide nanoparticles (CuO, NiO, Al_2O_3, Fe_2O_3, and ZrO_2) is decreasing with increasing supersaturation. The pressure was varied between 25 MPa and 38 MPa for a temperature of 673 K and a residence time of 1 s. The resulting supersaturation depends on the metal-oxide system and increases from CuO (10^2) to ZrO_2 (10^{13} - 10^{14}). The size varied between 3.4 nm and 30.9 nm.

A variation of pressure and temperature allows the tunability of the formed particles in terms of size and shape. The already mentioned reactions are shown in more detail in the following [43,47,81,83,89,101–104]:

1. Hydrolysis: $Me^{z+}(\mathrm{aq}) + z\ H_2O \leftrightharpoons Me(OH)_z(\mathrm{aq}) + z\ H^+$ (2-28)

2. Dehydration: $Me(OH)_z(\mathrm{aq}) \leftrightharpoons MeO_{z/2}(\mathrm{aq}) + \frac{z}{2} H_2O$ (2-29)

3. Precipitation: $MeO_{z/2}(\mathrm{aq}) \leftrightharpoons MeO_{z/2}(\mathrm{s})$ (2-30)

The CHTS process has already widely been used to synthesize and study different metal salt systems, forming pure, mixed, doped metal-oxide nanoparticles and hybrid inorganic-metal-oxide materials [11,13,43,47,81,83,92,94,100–107].

Adschiri et al. [83] investigated the CHTS for different metal oxides and hydroxides as CeO_2, AlO(OH), Co_3O_4, and NiO for different temperatures. Aoki et al. [28] investigated the kinetic behavior of the cerium system using cerium nitrate ($Ce(NO_3)_3$) as a precursor. The general equations (2-28) - (2-30) for the cerium system are as follows [108]:

1. Hydrolysis: $2\,Ce(NO_3)_3 + 8\,H_2O \longrightarrow 2\,Ce(OH)_4(aq) + 6\,HNO_3(aq) + H_2(aq)$ (2-31)

2. Dehydration: $Ce(OH)_4(aq) \longrightarrow CeO_2(aq) + 2\,H_2O$ (2-32)

3. Precipitation: $CeO_2(aq) \longrightarrow CeO_2(s)$ (2-33)

Due to the fast hydrolysis reaction, the reactions are summarized to a global reaction assumed as a first-order reaction [108]:

$$2\,Ce(NO_3)_3 + 4\,H_2O \longrightarrow 2\,CeO_2 + 6\,HNO_3 + H_2 \tag{2-34}$$

Among the pressure and temperature, other process parameters like the total mass flow $\dot{m}_3$, the mixing ratio a, the salt concentration c_{salt}, and the mixing geometry affect the synthesized metal-oxide nanoparticles.

The reaction of the metal cation into the metal oxide and the resulting precipitation is strongly dependent on the pressure and temperature [28,45]. The reaction kinetics are, in addition to the mixing behavior, a major influence on particle formation. In general, the kinetic behavior of a hydrothermal reaction is explained by a Born type Arrhenius equation from Amis et al. [109] used by Adschiri et al. [83]:

$$ln\,k = ln\,k_0 - \frac{E_\mathrm{r}}{RT} + \frac{\psi_\mathrm{r}}{RT}\left(\frac{1}{\varepsilon} - \frac{1}{\varepsilon_\mathrm{r}}\right) \tag{2-35}$$

with k_0, E_r, R, ψ_r, ε and ε_r representing a frequency factor, the activation energy, the universal gas constant, a species-dependent constant, the solvent's dielectric constant, and the solvent's dielectric constant at a reference state. With increasing temperature, the rate constant is rising due to the decrease of the dielectric constant. The relation of the reciprocal dielectric constant at elevated pressures and temperatures and the reciprocal dielectric constant at reference state (T_r = 473 K at given high pressure) for water is shown in Figure 2-7:

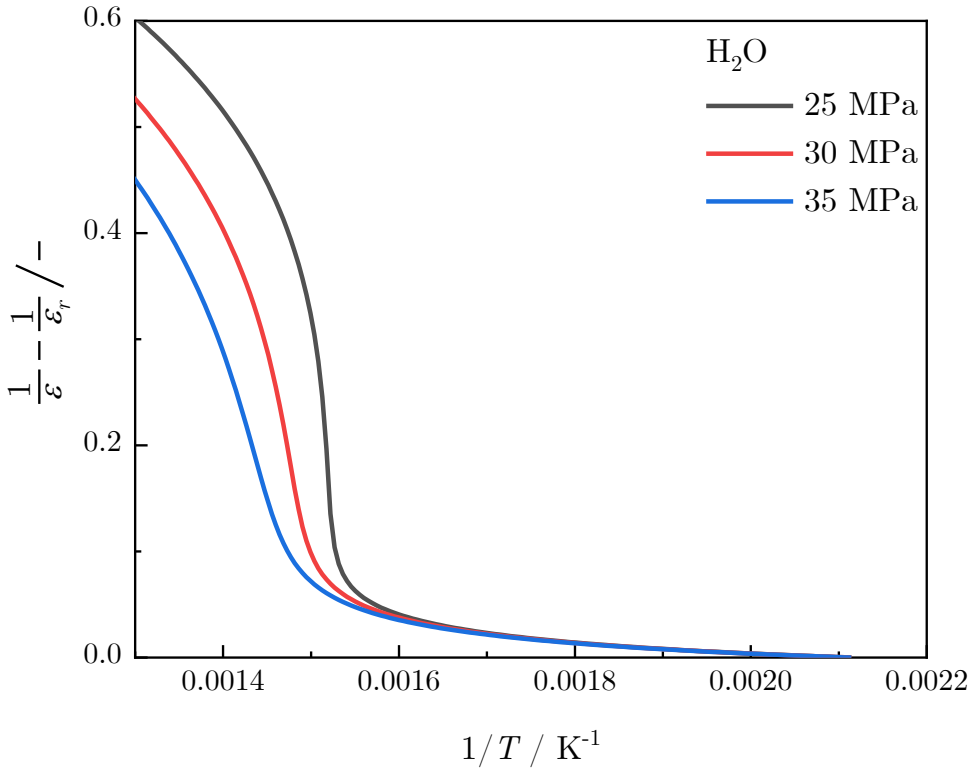

Figure 2-7: Behavior of $\frac{1}{\varepsilon} - \frac{1}{\varepsilon_r}$ for water as a function of the reciprocal temperature for different pressures, black line 25 MPa, red line 30 MPa, and blue line 35 MPa, data taken from [53].

For low temperatures, the dielectric factor is not pressure-dependent and slightly increasing with increasing temperature. Around the critical point, the factor is growing strongly. The influence of pressure is also visible. With increasing pressure, the substantial increase is depressed. The dielectric factor mainly influences the kinetic behavior during the CHTS process what is visualized in Figure 2-8.

Aoki et al. [28] determined the rate constant k in continuous flow type experiments. Here, $Ce(NO_3)_3$ was used as a precursor, and experiments with different process temperatures, mixing geometries, and residence times τ were carried out. The resulting conversion X of the reaction was determined and correlated with the residence time τ to get values for the rate constant. The above-shown parameters were fitted with a least square approach and result in $k_0 = 2.8 \cdot 10^7\ s^{-1}$, $E_r = 84\ kJ\ mol^{-1}$ and $\psi_r = 4.5 \cdot 10^2\ kJ\ mol^{-1}$ [28]. For the reference value of ε_r the value at 473 K was chosen (e.g. 35.93 at 30 MPa) [110]. With these values, the rate constant k was estimated as a function of $1/T$ and related to k_0. Figure 2-8 shows this trend for different pressures:

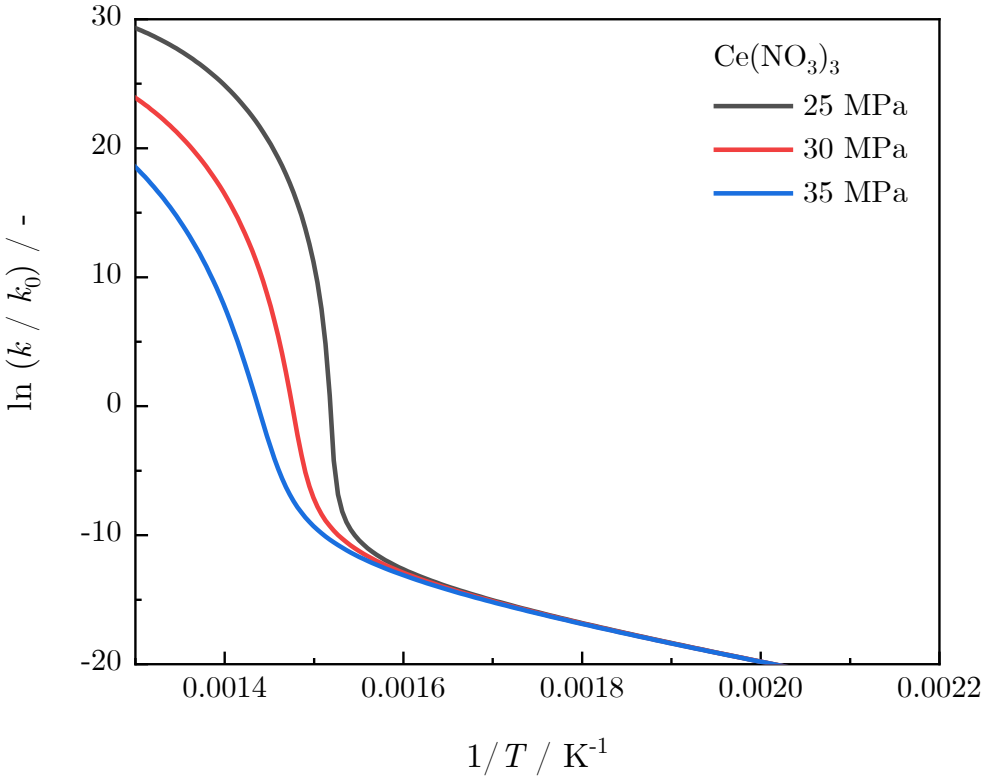

Figure 2-8: Arrhenius plot of the rate constant k related to k_0 as a function of the reciprocal temperature for different pressures, calculated with equation (2-35) and the parameters determined by Aoki et al. [28].

As already shown in Figure 2-7, the influence of the dielectric factor is significantly influencing the rate constant. Furthermore, the pressure dependency of the rate constant is visible for increasing pressures. It results in a decrease in the reaction rate with increasing pressure. The shown trend in Figure 2-8 was validated in the subcritical range with five experimentally determined values for the rate constant at different temperatures with the procedure shown above [28].

The synthesized particles grow within the hot reaction zone after the particle formation initialized by mixing up the cold aqueous metal salt solution with the hot near- / supercritical water stream. The growth of nanoparticles is initiated by coagulation where the growth occurs due to particle collisions. Additionally, growth can also occur through condensation where molecules are attached at the surface defects of nanoparticles. The supersaturation influences both, the nucleation and the growth rate. The supersaturation strongly influences the nucleation rate, whereas for the growth rate there is a linear dependence on the supersaturation [96].

The product suspension is then cooled down in the cooling unit where either the reaction and the growth are stopped. Cooling down the suspension leads to an immediate increase of the metal salt solubility. It leads to a degradation of the supersaturation. As long as aqueous metal

oxides remain in the reaction mixture, growth occurs due to condensation onto the metal-oxide nanoparticles. In addition to the growth due to condensation, other growth mechanisms potentially occur after cooling down the particle suspension. The particles can further agglomerate or coagulate to larger particles or accumulations.

Both, the occurring reaction within the process as well as the mixing quality of the streams are key factors. Within this frame, the mixing setup as well as the used mixing geometry affect the quality of the mixing and the resulting metal-oxide nanoparticles. For using the CHTS as a reliable process, mainly homogeneous mixing is required. Insufficient mixing of both streams leads to broad particle size distributions and potential clogging of the mixing unit [111]. The particle formation is very fast due to the fast reaction and nucleation (compare Figure 2-8). Once the resulting particles cannot be transferred out of the reaction zone in an adequate time, these agglomeration takes place leading to a blockage of the mixing unit or reactor. Another aspect is the remaining nanoparticles inside the hot reaction zone. Once the formed nanoparticles are not transferred directly outside the reaction zone, they interact further, resulting in non-uniform particle sizes and shapes [112]. The effect of clogging inside the mixing unit was of interest, and studies have been carried out to understand the basic principles during the mixing. It was investigated either by experiments (compare Sue et al. [113]) and CFD simulations. Sierra-Pallares et al. [114] characterized the mixing behavior with CFD simulations [111] and predicted the residence time distribution at low Reynolds numbers. Zhou et al. analyzed the mixing in combination with the precipitation of CuO nanoparticles with different mixing geometries [115]. In addition, in situ experiments have been conducted to visualize the mixing behavior. Tighe et al. [116] investigated the mixing of a counter-current mixing unit by in situ measurements of the temperature. Aizawa et al. [117] investigated the mixing with an optical flow cell combined with dye under supercritical conditions. Takami et al. [19,118] performed in situ neutron tomography experiments to visualize the mixing during the CHTS process. The studies have shown that mixing the cold aqueous metal salt solution with the hot near- / supercritical water stream is complex and crucial for the final PSD. Several mixing geometries next to the conventional T-shaped mixer have been developed. Possible mixing geometries are the Y-shaped mixer with different angles, a cross-section mixer, or a cyclone mixer. Further simulations need to be carried out to gain more information about the mixing quality and the effect on the resulting particles.

A simple scheme of a CHTS plant including the mixer and other used components is shown in Figure 2-9. The design of the CHTS plant with all the features and extensions is described in in more detail in the later sections.

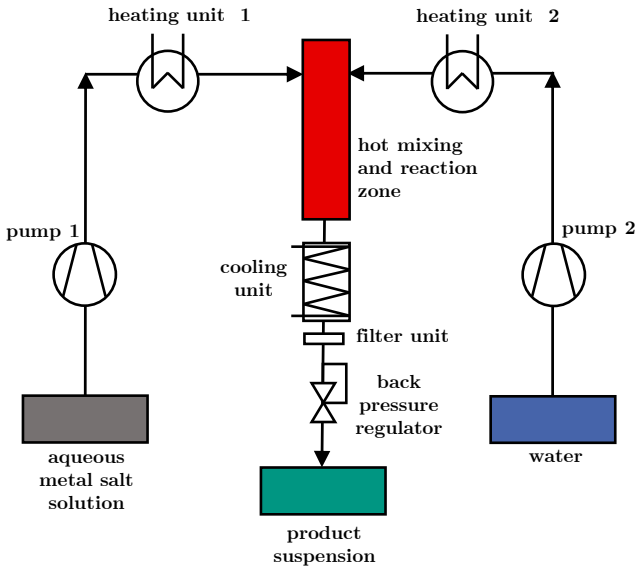

Figure 2-9: Simple scheme of a flow-type apparatus used for the CHTS [47,103].

The already mentioned theoretical studies of the CHTS process performed with CFD simulations, for example, have a great potential for gaining further knowledge concerning the process. In the next section, the simulation basics are described, along with the general equations of the CFD.

2.3 Simulation basics

In the past decades, the importance of simulations increased drastically. In terms of the increase in computational power over the last years and potential supercomputing, simulations will become even more critical. Supporting the experimental work with simulations leads to a better workflow and new insights into the process, which could typically not be performed [119]. In the following sections, the simulation software and the concerning simulation basics are described.

2.3.1 Simulation software and computational fluid dynamics (CFD)

Several simulation programs are available for the simulation of the single steps of the CHTS process. First of all, commercial software is applied in certain works. Nadimpalli et al. [108] are using ANSYS Fluent®, whereas gPROMS and M.DynaMix are applied by Chen et al. [120] and Lümmen et al. [121]. Next to that, open-source software like OpenFoam [122] is capable to simulate fluid dynamic problems. These programs are based on either the finite-element or finite-volume method or molecular dynamics. The development of the model and the simulations are all carried out within the CFD module of ANSYS Fluent® 17.2.

Mathematical equations describe the general fluid flow characterized by the velocity, temperature, and pressure fields. These properties are defined by partial differential equations [123]. Due to the complexity of the real model systems and the resulting equations, no analytical solutions are available. The problems have to be solved numerically. This complexity leads to the basic principle of CFD with the numerical estimation of the problem. Three different categories are named depending on the discretization method [123,124]. One of the most used categories in industry and science is the finite-volume method. This method is also integrated into ANSYS Fluent® and is well described by Ferziger et al. [124]. The single steps from the development of the model to the simulation are described in the following.

A two-dimensional (2D) or three-dimensional (3D) model needs to be designed at the beginning of the modeling process. It should be in the style of the real geometry that is simulated. The geometry of the model is realized with the integrated Workbench or CAD software, and then loaded into the working environment. The designed model is meshed afterwards. Different mesh generators like Gambit or Integrated Computer-aided Engineering and Manufacturing (ICEM) are common. In addition, the integrated ANSYS Mesher® is available [125]. A designed 3D model can be either meshed with tetrahedrons or hexahedrons. Using these hexahedrons for meshing requires longer meshing times and results in longer computational time. A hexahedral mesh could need fewer elements compared to a tetrahedron mesh, resulting in a faster simulation time [125]. The cell skewness is a crucial value for the mesh quality. Table 2-4 shows a description of the values of the cell skewness. A low value of the cell skewness between 0 and 0.25 shows an optimal value. Up to a value of 0.8, the mesh quality is still accurate enough to receive good results.

Table 2-4: Description of the quality of the cell skewness depending on its value [126].

value of the cell skewness / -	quality
0 – 0.25	excellent / equilateral
0.25 – 0.50	very good
0.50 – 0.80	good
0.80 – 0.94	acceptable
0.95 – 0.97	bad
0.98 – 1.00	unacceptable / degenerated

The designed and meshed model of the actual geometry is implemented into the graphical user interface (GUI) of ANSYS Fluent® to initialize the simulation. ANSYS Fluent® offers several different models and solvers. Both steady-state or transient solvers are available for finding the numerical solution of the Reynolds-Averaged-Navier-Stokes (RANS) equations. Before initializing the simulation, the boundary conditions need to be set according to the actual system. The required model equations for the respective simulations are set, and the convergence criteria are assigned before the simulation is started. When the convergence criteria

are lower than the set values for all the equations, the simulation is stopped. This indicates that improved residuals have no further effect on the resulting solution [125]. It is then transferred to the post-processing unit. Within that, the thermal and velocity fields and the reaction profiles are analyzed.

2.3.2 General equations

The simulation of the CHTS process from the analysis of the thermal and velocity fields, the reaction, and the particle formation require different models. For the simulation of particle formation, a multiphase approach is used. These approaches are generally based on the Euler-Euler approach named the volume of fluid (VOF) method and the Eulerian or the Mixture model, respectively [125]. The most favorable model of these three is the Eulerian model, which enables the modeling of the primary and secondary phases as continuum phases. A reason for this is the value of the Knudsen number of the metal-oxide nanoparticles less than 0.1 in supercritical water [108,127]. The volume fraction of the primary phase a_p is linked to the secondary phase. Especially the simulation of the secondary phase (metal-oxide nanoparticles) as a continuum is advantageous for the CHTS process. The volume fraction of the secondary phase is set to 0 for the other simulations of the thermal and the velocity field, the residence time distribution, and the homogeneous reaction. These simulations appear in the single-phase flow. The general equations for the Eulerian model are described more detailed in Appendix chapter 2 E: General equations [108,128]. The essential equations for the simulation are either the mass-, momentum- and energy conservation equations. They are combined with the Navier-Stokes equations (NS) for describing flow phenomena [124]. Next to these, other equations need to be solved. The mixing geometry combined with the process conditions during the CHTS process with elevated temperatures and pressures results in a turbulent flow pattern. For the simulation of the residence time distribution and the homogeneous reaction, the species transport equation also needs to be considered.

2.4 Ceria nanoparticles

In this work, ceria nanoparticles are synthesized with different cerium salts as precursor. Ceria is widely used in different applications like the medical sector, the technical field, and catalysis. It is known as cerium oxide, which is the oxide of the rare earth metal cerium and is named after the asteroid Ceres located in 1801. Cerium itself was discovered only two years later by Klaproth and Berzelius, and Hisinger. It is present in several minerals like allanite, monazite, and bastnasite. The latter is the largest source of cerium. Metallothermic reduction techniques produce pure metallic cerium. It is also an essential material due to its variability in the electronic structure [129]. The application of ceria within the sectors mentioned above has increased mainly throughout the last years [130]. Especially the use of ceria nanoparticles is of great interest. An important fact is the oxidation state of the cerium ion. Due to the crystal structure of ceria, the oxidation state is almost always +4. A decrease in the mean particle size leads to the presence of cerium ions with an oxidation state of +3 [131]. A further reduction below a mean particle size of 4 nm leads to an increase in the catalytic activity of ceria [132].

In addition, there is a high potential to bind free oxygen radicals of ceria nanoparticles. This happens due to an oxidation state transition +3 to +4 on the particle surface [133]. These properties favor ceria nanoparticles to use in the medical research of ischemic strokes [134]. The issue of ischemic stroke is the absence of essential oxygen for the nerve cells. Oxygen radicals like the superoxide anion are formed, which harm the brain cells [135]. By injecting the ultrasmall ceria nanoparticles, the consequences of the ischemic stroke can be mitigated, and doctors have more time to save human lifes [134].

Next to potential applications in the medical sector, ceria is used in several processes in the technical field. Ceria nanoparticles are deployed as abrasives in polishing slurries for glass surfaces. Heat treatment makes ceria softer than the glass surface to be polished. Due to this property and the faster polishing process, ceria mainly replaces the former rouge (iron oxide). The chemomechanical polishing (chemical and mechanical) shows the best results with ceria as a polishing additive [129,136].

The largest field of application for ceria nanoparticles is catalysis. Several applications have been developed and proposed over the last years and decades. Trovarelli shows that the number of published articles in literature about ceria used in catalysis increased steadily (for example, 29 articles in 1980 and 216 in 1994) [130]. In 2022, 399 articles were published according to a query in Web of Science. The redox potential of ceria-containing materials or nanoparticles is the crucial factor for catalytic research [137]. Ceria nanoparticles act themselves as a catalyst or are doped or coated with other materials to achieve a higher catalytic activity.

3. Materials and methods

For the synthesis of metal-oxide nanoparticles with the CHTS process, certain chemicals and materials were used. In addition, several techniques were applied for the analysis and characterization of the produced metal-oxide nanoparticles. The materials in combination with the experimental routines and methods are described in this chapter. Next to that, the theories of the analytical techniques are explained.

3.1 Chemicals

The synthesis of metal-oxide nanoparticles in terms of ceria was carried out with different cerium salts. The metal salts and other used chemicals with their formula, the grade, and the source of purchase are listed in the following table.

Table 3-1: Materials and chemicals for the CHTS experiments.

material / chemical	formula	purity / %	provider
acetone	C_3H_6O	> 99.5	Carl Roth
cerium(III)nitrate-hexahydrate	$Ce(NO_3)_3 \cdot 6\ H_2O$	99.999	Sigma Aldrich
cerium(III)sulfate-octahydrate	$Ce_2(SO_4)_3 \cdot 8\ H_2O$	99.995	Carl Roth
cerium(III)acetate-sesquihydrate	$Ce(CH_3COO)_3 \cdot 1.5\ H_2O$	99.99	ABCR
cerium(IV)oxide, $d_p < 50$ nm	CeO_2	99.95	Sigma-Aldrich
ethanol, embittered	C_2H_5OH	>99.8	Carl Roth
ethanol	C_2H_5OH	>99.8 p.a.	Carl Roth
deionized water	H_2O	double-distilled	Carl Roth
2-propanol	C_3H_8O	>99.5	Carl Roth

3.2 Analytical methods

For the characterization and the analysis of the synthesized metal-oxide ceria nanoparticles, specific methods were used. The methods applied in this thesis are described in the following. More details about these methods are found in Appendix chapter 3.

3.2.1 Powder X-ray diffraction (PXRD)

The basic principle of PXRD is the diffraction of the X-rays on ordered structures like crystals. The description of the related theory is based on Klug et al. [82] and Pecharsky et al. [138].

X-rays were already used in the past for the analysis of different structures of materials. The X-rays are absorbed differently (compare bones and tissues in the human body). In 1912 the origin of the X-rays was found out. In general, X-rays consist of perpendicular electric (E_x) and magnetic (H_x) fractions and the direction vector of the wave (k_x) (compare Figure 11-2 in Appendix chapter 3), generated by both an acceleration or deceleration of electric charges. Compared to the local image of the sample captured by electron microscopes, X-rays extract global information of the sample. From the diffraction pattern, 3D crystal structures are derived. The mean wavelengths are between 0.1 Å and 10 Å. For the analysis of crystallographic systems, wavelengths from 0.5 Å to 2.5 Å are required.

Preparation of the particles for the PXRD analysis

The analysis of the particles with PXRD requires dry particles. The particle suspension was centrifugated for low particles concentrations in the suspension, and the sediment was used. The drying of the particles was either performed in a drying oven or a freeze-drying unit. In the drying oven, the particle suspension was dried overnight at 363 K, and the dried particles were obtained. With the freeze-drying unit, the suspension had to be further prepared. The particles were concentrated with centrifugation or sedimentation beforehand. The concentrated particle suspension was collected in a glass bottle covered with a perforated lid of aluminum foil. It was then instantly frozen in a liquid nitrogen (L-N_2) bath. The cooling trap of the freeze-drying unit was filled up with L-N_2 and the particles dried after switching on the vacuum pump. Due to the pressure below the vapor pressure of water at ambient conditions, it evaporated, and dry particles could be recovered after finishing the drying process. For the powdered ceria nanoparticles analysis, the particles were portioned on a transparent rounded polymer carrier and fixed with an adhesive counterpart.

Characterization of the ceria nanoparticles with PXRD

For the characterization of the ceria nanoparticles after the examination with PXRD, the powder diffraction software WinXPOW (Version 3.07, STOE & Cie GmbH, Darmstadt, Germany) was used. The Raw Data Handling subprogram was applied to load the determined raw files from the diffractometer. The maximum peak was selected and further analyzed and all gathered values were inserted in the Scherrer equation (compare equation (3-3)) to determine the crystallite size. For the parameters of the wavelength λ a value of 1.540596 Å was considered, and for K_S, a value of 1.

3.2.2 Transmission electron microscopy (TEM)

TEM is used for the examination of synthesized nanoparticles regarding their size and shape. The theory of TEM is described according to Zuo et al. [139].

Compared to conventional optical microscopes, the TEM microscope enables a higher resolution for the analysis of nanostructured and thin materials. Inside the TEM microscope, an acceleration voltage is used to increase the energy of the electrons to 200 keV. This results in

an approach of the velocity of the electrons near the speed of light. Certain interactions of the electron beam with matter occur due to the Coulomb forces. The electrons interact with an electron transparent material as reflection, scattering, or passing through it.

In comparison to this, an inelastic scattering results in a measurable amount of electron loss. Elastic scattering does not affect a detectable energy loss. Furthermore, the elastic scattering is divided into low or high-angle scattering. The low angle scattering is caused by electrons and nuclei of the respected atoms. On the other hand, the high angle scattering is induced by nuclei, backscattering, or reflections. The elastically scattered electrons and transmitted ones are focused in the back of the examined sample.

The TEM images shown and analyzed in this work were recorded with the TEM systems Philips CM200 FEG/ST and a FEI Osiris ChemiStem operated at 200 kV. The measurements were performed at the Laboratory for Electron Microscopy (LEM, Karlsruhe Institute of Technology, KIT, Germany).

Preparation of the particles for imaging with TEM

For the imaging of the particles with TEM, the particles inside the suspension had to be prepared. Once the particle concentration inside the suspension was too high, a dilution was required. For a high concentration, 20 µl of suspension was filled up with 10 ml of deionized water. The diluted suspension was then put into an ultrasound bath for 30 minutes to ensure dispersion of the particles. Afterwards, one drop of the prepared diluted particle suspension was dropped on a TEM grid (carbon film on 3.05 mm copper grid, Plano GmbH, Wetzlar, Germany). The dropped particles dried overnight so that the whole water was able to evaporate. This had to be guaranteed for the examination with the TEM microscope. Another technique was the ultrasonic spraying of the particle suspension onto a TEM grid.

Characterization of ceria nanoparticles with TEM images

The images from both TEM systems were analyzed with the graphical software ImageJ (version 1.38). Therefore, an image taken with the TEM microscope was loaded. Before measuring the particles, the scale had to be adjusted to the scale bar of the image. Then 600 - 800 particles were measured with the diameter and collected. After finishing the measurement, the obtained data were saved in an and transferred into an evaluation program. The measured image was also saved. The respecting particle size distribution was obtained with the characteristic values of d_{10}, d_{50}, and d_{90}. Regarding these values, the width of the PSD, names as the span Δ was defined by: $\Delta = [(d_{90} - d_{10}) / d_{50}]$. It was used to describe the polydispersity of the various samples. d_{50} is defined as the diameter where 50% of the particles have a smaller diameter, and 50% have a larger diameter; d_{10} and d_{90} have defined accordingly with 10% or 90%, respectively.

3.3 Impedance spectroscopy (IS)

Impedance spectroscopy is a widely applied measuring technique using alternating current voltage. It is a non-destructive method using low amplitudes [140]. The theory of the impedance spectroscopy is well described by Barsoukov et al. [141]. Impedance spectroscopy is suitable for systems where the properties are characterized by electrical resistances. Main applications are in the fields of corrosion and battery technology. The partial resistances of the system components are combined to the impedance. The alternating current resistance of a system is defined as follows with a real and an imaginary part:

$$|Z| = \left[(Z_{\text{real}})^2 + (Z_{\text{imaginary}})^2\right]^{0.5} \tag{3-1}$$

Impedance spectroscopy is a sensitive measuring technique and small changes in the system result in large differences of the impedance. In order to compare single measurements, the experimental setup regarding the electrode's geometry and distance between them has to remain constant during the experiment. The advantage of the impedance spectroscopy is the transmission of the system into a physical model and to characterize the influence of the single components.

For the measuring of the impedance during the operation of the CHTS plant, an impedance analyzer Hioki IM 3570 was used in combination with 75 mm^2 aluminum electrodes. During the reaction, selected frequencies were adjusted to measure the temporal trend of the reaction from the metal salt to the metal oxide. The impedance is increasing after the reaction occurs. The application of the impedance spectroscopy enables the detection of changes in the reaction. The process parameters for the particle synthesis are then adjustable directly during the experiment. The conversion from the metal salt to the metal oxide is directly determined through the difference in the impedance of the metal salt solution and the product suspension. The correlation between the impedance and the salt concentration is established with a concentration dependent calibration curve.

4. Concept, construction, characterization of the CHTS plant

The CHTS plant for the synthesis of metal-oxide nanoparticles, based on mixing a cold compressed metal salt solution stream with a hot near- / supercritical water stream, was constructed within the framework of this thesis. Furthermore, the plant was set up, characterized, and optimized. The basic principle of the CHTS plant is based on academic research, e.g. [28,83,142]. These were used as indicators for the practical guide. In the following, the original concept of the CHTS plant is described in more detail. Selected work in this section was performed by Hohm [58].

4.1 Original concept of the CHTS plant

The constructed plant was dimensioned up to a total mass flow $\dot{m}_3$ of 4.8 kg h^{-1} (respective 80 g min^{-1}). The maximum pressure and temperature of 38 MPa and 773 K were applied for the design and construction of the new CHTS plant. During the construction, further modifications compared to the original scheme were carried out. Figure 4-1 shows a simple scheme of the constructed and set up CHTS plant with the positions of the pressure measurement (p_0, p_1, and p_2) and the temperatures to be controlled (TC 1, T_2, and TC 2, T_3):

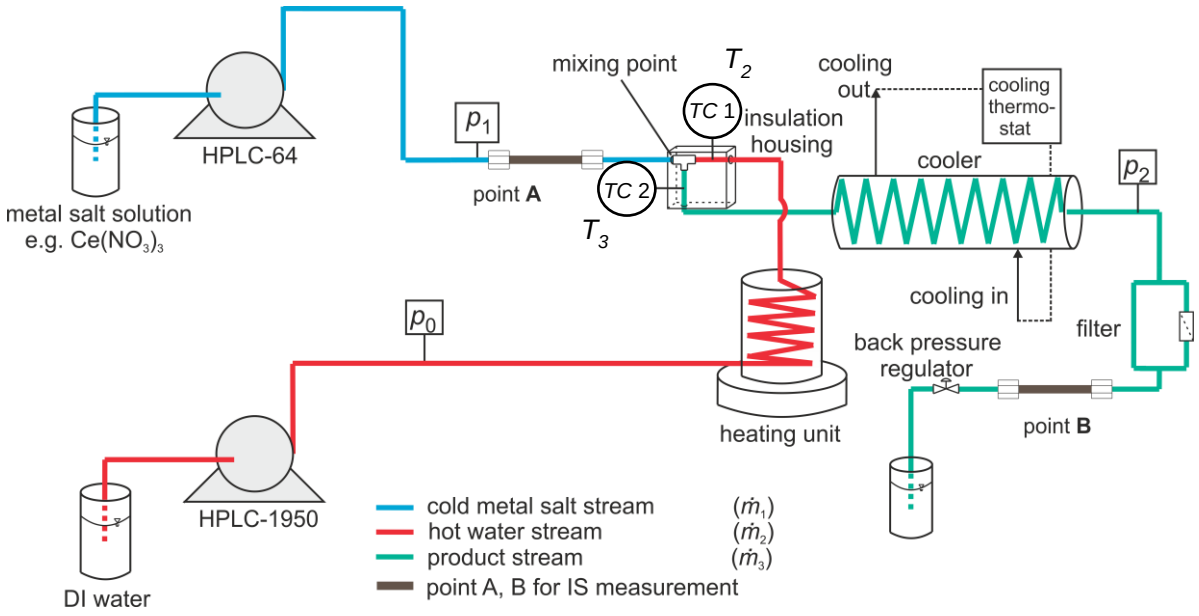

Figure 4-1: Simple flow scheme of the constructed and build up CHTS plant.

4.2 Construction of the CHTS plant

The pilot plant is constructed based on the scheme mentioned above. The general procedure is the pressurization and heating of a deionized water (DI) stream to the given pressure and temperature. Then the hot water stream is mixed up with a cold aqueous metal salt solution

stream. The resulting particle suspension is cooled down and collected at ambient pressure after the back pressure regulator. The most important parameters during the construction are the constant provision of either the hot and the cold streams combined with low pulsation and the easy assembling of different mixing units and different reaction tubes. These factors were important to study various phenomena during particle formation. The single components built in the plant are described in the following sections. A detailed list of all the parts is shown in Appendix chapter 4 A: Detailed list of the used components for the CHTS plant.

4.2.1 Tubing, valves, and fittings

The used stainless-steel tubes and valves for the CHTS plant were all purchased by SITEC-Sieber and Swagelok. All of these consist of an inner diameter between 1.6 mm and 5.4 mm. The components are valid for maximum pressures between 70 MPa and 700 MPa. The inner diameter of the tubes is 1.6 mm, 1.78 mm, 2.4 mm, and 5.4 mm and a respective outer diameter of either 3.18 mm, 6.35 mm, and 9.525 mm. The tube with an outer diameter of 3.18 mm withstands a maximum pressure of 70 MPa at ambient temperatures ($T = 293$ K) and unbent. The tubes with an outer diameter of 6.35 mm and 9.525 mm withstand a maximum pressure of 400 MPa and 240 MPa, respectively. The T-junctions and valves have an inner diameter of either 1.6 mm or 3 mm. They were either used inside the mixing unit or to integrate thermocouples or pressure sensors into the plant. The maximum pressure is 400 MPa and 700 MPa for the T-junctions and 100 MPa to 200 MPa for the valves. With increasing temperature (process temperatures of up to 773 K), the maximum pressure decreases up to 30%. However, for each element, the maximum pressure is still above 38 MPa. The tubes were bent at ambient temperatures and a maximum radius of 25 mm. This ensures that the maximum pressure is not exceeded. In order to guarantee the compatibility of the tubes with valves and fittings, the ends were cut cone-shaped and furnished with a thread. For the control of the plant, different valves and fittings were applied, e.g. stop valves, and a micrometer valve as a back pressure regulator. With the back pressure regulator, either the pressure p and the total mass flow $\dot{m}_3$ were controlled. To save sensitive components like pumps against backflow or pollution, check valves ensured the direction of the flow. These also withstand a maximum pressure of 400 MPa. In order to protect the other components against high pressure, two rupture discs with a pressure of 60 MPa at 293 K were integrated. The pulsation of the pumps, reduces the maximum pressure of the rupture discs. Therefore, rupture discs with the higher pressure of 60 MPa were chosen. Once the system's pressure exceeds the maximum pressure, the rupture discs are triggered. Before recovering the particle suspension and in terms of protecting the micrometer valve, a high-pressure filter unit with a maximum pressure of 400 MPa with a filter element and a related porosity of 10 µm was installed. For cleaning purposes, a filter cleaning unit was constructed. It is used to backflush the accumulated particles.

4.2.2 Pumps

For the pressurization of the hot, the cold, and the functionalization stream, three High Performance Liquid Chromatography (HPLC) pumps were applied. For the hot near- / supercritical water stream ($\dot{m}_2$) the pump HPLC-1950 and either for the cold water / aqueous metal salt solution stream ($\dot{m}_1$) and the functionalization stream ($\dot{m}_4$), the pump HPLC-64 were used. The pump HPLC-1950 is a pneumatic reciprocating pump (1.37 ml water per stroke) with a volume of the pump head of 250 ml and maximum pressure up to 67 MPa. Pressurized air with 0.7 MPa was required to provide the maximum pressure. The total mass flow provided by the pump was around 500 g min^{-1}. For the adjustment of the pressure, a rotary valve was used. The pump pressurizes the water as long as the set pressure is reached. Thus, it was not possible to set the total mass flow with this pump. Due to the strong influence of the pressure on the reaction kinetics, the consideration of the pulsation of the pump was important. The stroke of the pump induces pressure fluctuations. Therefore, an additional volume realized as a buffer tank was installed next to the pneumatic pump. This tank minimized the pulsation and enabled pressurization with constant pressure. The cold and the functionalization stream are pressurized with the isocratic single-piston pump HPLC-64. It is an electric pump with a maximum pressure of 40 MPa, and mass flows from 0.1 g min^{-1} to 9.9 g min^{-1}. It was possible to adjust either a minimum and a maximum pressure. Once the pressure was in between that range, the set volume flow was constant. With the total mass flow of 9.9 g min^{-1}, mixing ratios up to $a = 0.35$ were realizable depending on the total mass flow. It was possible to connect both isocratic pumps to increase the cold water or metal salt solution stream $\dot{m}_1$ up to 19.8 g min^{-1}. With this setup, even higher mixing ratios a were possible.

4.2.3 Heating and cooling units

For providing the hot near- / supercritical water stream at a given process temperature, an electrical heating unit was applied. Four heating cartridges provide the heat integrated into a brass cylinder. The 6 m high-pressure tube was coiled around the brass cylinder. In order to enhance the heat transfer, a thread was milled into the brass cylinder to enlarge the contact area. The heat loss was reduced by glass fiber around the high-pressure tube. A stainless-steel housing covered the heating unit. A second heating unit with a total power of 420 W was installed around the mixing unit (see section below). It provided a constant mixing temperature T_3 of the mixed hot and the cold water stream $\dot{m}_3$ and compensates the heat loss. For providing the heat, six heating cartridges were used. They were assembled in pairs in three U-shaped brass blocks surrounding three T-junctions. The fit of the heating cartridges inside the brass bodies and the brass bodies themselves was tight to provide an optimal heat transfer into the fluid. Furthermore, a thermocouple was integrated inside one brass body to measure the surface temperature of one heating cartridge.

The high-pressure cooling unit, valid for pressures up to 50 MPa, was set right after the mixing point and the reaction tube to cool down the particle suspension and stop either the reaction or particle growth. Inside the cooling unit, a 7 m coiled high-pressure tube was installed. The

cooling unit was realized in the counter-current flow. Cold water surrounded the high-pressure tube in order to cool the particle suspension down below 353 K. The cooling power was provided by two thermostats. Both provided a cooling power of 500 W and 200 W, respectively. The cooling temperature was set to 285 K. The maximum volume flow of the thermostats was 17 $dm^3\ min^{-1}$. Another cooling unit was realized around the high-pressure tubing of the cold water or aqueous metal salt solution stream. Four brass half shells with a thread at their surface were set around the tube with a tight fit. A copper tube was coiled around the half shells in the direction of the milled thread. In the counter flow setup, the cold stream was cooled down with water, cooled with a thermostat Lauda Alpha.

4.2.4 Mixing unit and reactor

The mixing unit was realized as a set of three T-junctions and a reaction tube afterwards. Two of these were used as measuring points of each hot water temperature in front of the mixer and the mixing temperature after mixing up the hot and the cold stream. The mixing unit is a conventional T-junction with a constant inner diameter of 1.6 mm. The scheme of the mixer was already shown in Figure 2-5.

The three components were connected with 65 mm tubes with an inner diameter of 1.6 mm. All the T-junctions were surrounded by the above-mentioned U-shaped brass heating units containing two heating cartridges each. The mixing unit was covered by 20 mm thick calcium silicate insulation plates. Next to that, the tubes between the heating and the mixing unit and the reaction tube were covered with half-shells of calcium silicate plates. Both the mixing unit setup and insulation housing are shown in Figure 4-2:

Figure 4-2: Mixing unit with opened insulation housing.

The setup of the mixing unit allows an easy assembling of different mixing units, geometries, and reaction tubes. However, the mixing unit with the insulation housing was designed to be easily changed or removed. This is mainly essential in case of clogging of the mixer. Enough space was planned to elongate the reaction tubes. This enables the investigation of the influence of the residence time on particle formation for future studies. Therefore, a longer reaction tube was already designed and constructed. Another insulation was realized to decrease the heat loss and guarantee a constant mixing temperature even in the reaction tube. It consisted of half-shells of 20 mm strong calcium silicate plates containing a recess of the contour of the reaction tube in combination with stainless steel plates. The elongated reaction tube was connected to the functionalization stream, described in the later section (see section 4.3).

4.2.5 Ceramic tubes

For future application of impedance spectroscopy (IS), two ceramic tubes made of alumina (Al_2O_3) were integrated into the CHTS plant (compare Figure 4-1). The measurement is located in the cold high pressure part of the plant. The ceramic tubes were installed in the line of the cold stream in front of the mixing unit and of the back pressure regulator. The integration into the plant was realized with straight reducing connectors from Swagelok and elastic Vespel® ferrules attaching to the high-pressure tube. For safety reasons, a check valve was installed in front of the ceramic tube. In case of a potential burst, the system's pressure remained constant during the operation of the plant. This aspect was necessary due to the phase change from the liquid to the gas phase and accompanied drastic water evaporation inside the system. Synthesized nanoparticles could then be spread as aerosols in the area around the CHTS plant. The ceramic tubes, in combination with the Vespel ferrules, withstand a pressure of up to 40 MPa.

4.2.6 Measuring, control, and logging of the process conditions

The three crucial process values to be adjusted accurately within the CHTS process were the pressure p, temperature T, and total mass flow $\dot{m}_3$. Therefore, a precise measurement of the values during the process was required.

The single measurement points of the process values and the before mentioned components in the complex flow scheme of the CHTS plant, including the Counter setup in the mixing unit, are shown in Appendix chapter 4.

To measure the different temperatures within the process, thermocouples of the type K were used. The thermocouples were arranged directly in the middle of the tubes inside the stream. They had an outer diameter of 1 mm in order not to influence the flow. These were compatible with high-pressure and high-temperature applications. They had an uncertainty of ± 2 K up to a temperature of 773 K. For the integration into the plant, the thermocouples were thread through blind plugs and soldered afterwards. All used thermocouples were calibrated beforehand (with a precise thermometer and a thermostat up to temperatures of 473 K) to

keep measuring uncertainties as low as possible. The thermocouples were arranged at the essential points inside the plant (for more detailed information see Appendix chapter 4).

The pressure was measured with two pressure transmitters located in front and at the back of the mixing unit. In addition, a manometer was installed in the cold part of the hot water stream in case either the pressure transmitters or the digital displays failed. Both pressures were indicated with the digital display for monitoring the pressure drop. Two Coriolis mass flow meters indicated $\dot{m}_1$ and $\dot{m}_2$ in combination with digital displays RHM. With these, the total mass flow $\dot{m}_3$ and the mixing ratio a were detectable through addition and division, respectively. $\dot{m}_3$ was also measured by a mass balance PM6100 and comparable to the total mass flow measured by the mass flow meters to double-check the measurement. Two PID process controllers, Eurotherm 3504, indicate and control both the hot water temperature and the mixing temperature. PID controllers consist of a proportional element (P), an integral element (I), and a differential element (D). A PID controller combines the advantages of each element, named as the speed, accuracy, and ability to react to a temporal change. The PID parameters were determined through the Autotune program of the controller at 673 K. The output value is the electric current heating up the heating cartridges. The control values are the fluid temperatures after running through the heating section. The control values' deviation was determined by the difference of the target temperature and the current temperature of fluid temperature after each heating unit. The controllers indicated an error during a sensor break or a broken heating cartridge. This resulted in a switch-off of the heating units. In addition to the two process controllers 3504, two other process controllers Eurotherm 2116, were used as overheat protection of the heating cartridges. The maximum temperature of the outer cover was, as already mentioned beforehand, 1023 K. The alarm temperature of this process controller was set to 973 K. Once this temperature was reached, the heating units were switched off automatically. As previously described in sections 4.2.1 and 4.2.2, the total mass flow and the pressure were controlled by the back pressure regulator and the pneumatic pump. The thermocouples, the pressure transmitters, and the mass flow meters were connected to a datalogger 34970A from Keysight. The datalogger was linked to a computer, and the signals were transferred through a RS-232 serial port. The mass balance was also connected to the computer via a RS-232 interface to determine the total mass flow rate. The different signals were collected and analyzed with the graphical programming software LabVIEW. Next to the RS-232 interface, the temperatures to be controlled (T_2, T_3) were linked via RS-485 to the computer and also analyzed by LabVIEW. During the experiments, the current values of the process parameters were shown on the Front Panel of the LabVIEW graphical surface. An output Excel file was generated containing each temperature, pressure, mass flow, and mixing ratio with the related time. The calibration of the thermocouples was considered in the LabVIEW program. The graphical surface of the LabVIEW routine is shown in Appendix chapter 4 C: Image of the graphical surface of the LabVIEW evaluation routine.

4.2.7 Process safety

The CHTS process requires high system pressures and temperatures, whereby potential overheating and overpressure need to be considered. Therefore, special safety devices had to be installed. The synthesized nanoparticles could be harmful if they were released into the environment. For these safety reasons, the CHTS plant was set up in an aluminum frame and covered by polycarbonate windows with a thickness of 5 mm. All components besides the pumps, valves for the product recovery, vales for the combination of the two HPLC pumps, a safety valve, and the back pressure regulator were located inside the polycarbonate housing. Two windows were furnished with hinges to reach essential components like the thermostats or the mass balance. In the case of a potential burst of high-pressure tubes or parts during the experiments and the possible uncontrolled release of nanoparticles, a draft with a controllable volume flow was installed and connected with the covering. Once a small leakage arose during the particle formation experiments, the streams were directly shifted from the aqueous metal salt or functionalization solution to pure water. This reduced the probability of the release of steam and nanoparticles blowing out of the leakage. Next to the mechanical safety equipment, electrical safety devices were installed. Both heating units were only operable in combination with running thermostats to protect the plant from overheating or an incorrect operation. The thermostats had to be switched on to operate the isocratic pumps HPLC-64. Once a thermostat broke down, the pressurization of the fluids stopped immediately. Beyond that, a thermal pill was installed after the cooling unit on the surface of the high-pressure tube. If the product stream flowing out of the cooling unit exceeded 353 K, the heating units were stopped. This was to prevent the outlet of the product stream as vapor. Concerning these potential risks and the related safety devices, an operation guide for the CHTS plant was prepared. The plant containing including all components after the setup is shown in Figure 4-3. The operation scheme of the pilot plant is shown in Appendix chapter 4.

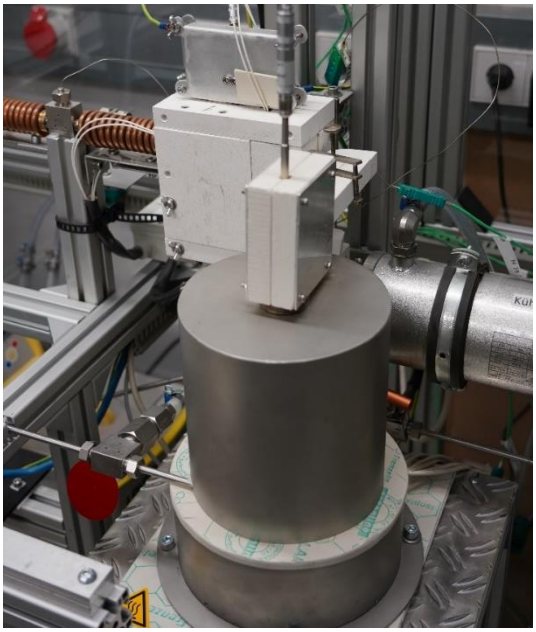

Figure 4-3: Image of the CHTS plant in the final setup and a detail image of the heating unit and the reactor covered by an insulation housing.

4.3 Change of the mixing geometries and elongation of the reaction tubes

For the construction, setup, and characterization of the CHTS plant the T-shaped mixer was assembled in the Counter setup (compare Figure 2-6). The mixing unit was followed by a short

reaction tube with a length of 0.22 m before entering the cooling unit. With this setup, the mixing experiments of the cold and the hot water stream were performed. Furthermore, the first experiments with cerium nitrate and cerium sulfate as a precursor were carried out with this setup. Due to the potential of clogging, the Counter setup was changed to the Straight setup (compare section 2.2, Figure 2-6). With this change, the hot water stream was redirected and mixed up from the top with the cold water or aqueous metal salt solution stream coming from the side. With this change, the probability of clogging was reduced.

Both mixing setups were used to study the influence of the process conditions on the resulting particle size and shape of the ceria nanoparticles. The straight setup was applied for the particle formation experiments with $Ce(CH_3COO)_3$ as a precursor.

The mean residence time was adjustable with the total mass flow. The Reynolds number (Re) increased with increasing total mass flow. For a constant Reynolds number, the reaction tube was elongated as previously described.

The elongation of the reaction tube allowed the realization of longer mean residence times. It was constructed out of larger tubes with an outer diameter of 9.52 mm, an inner diameter of 5.2 mm, and reducing connectors to change the tube diameter. Beyond that, the influence of the particles remaining longer in the hot reaction zone of the plant could be investigated. In addition, the functionalization line was connected to the elongated reaction tube. First experiments with the elongated reaction tube were performed to see the behavior of the plant. For a further investigation of the influence of longer residence times on the particle size, future experiments are required. The particle growth after particle formation needs to be evaluated.

5. Process modeling

Based on the theoretical background for the CFD simulation described in chapter 2, the design of the five different models of the mixing unit and the procedures, the simulation is described in the following sections.

5.1 Modeling of the mixers

The simulation of the CHTS process required the design of the mixing unit. With ANSYS Workbench®, a 2D model of the complete mixing unit was designed. Due to the complexity of the model, this approach was not suitable. It delivered inaccurate results for the simulation of the thermal and the velocity fields. A reason for this is the heat transfer from the hot near- / supercritical water stream to the air inside the mixing unit (compare chapter 4, Figure 4-2). There, the air was trapped through an L-shaped insulation component. Due to convection, the heated air affected the total heat transfer inside the mixing unit. This phenomenon could not be considered within the 2D simulation. A realistic 3D model of the mixing unit with all the used components was designed to remedy this problem. In general, five models with different mixing geometries were intended. Three were based on the T-junction as a mixer (Counter, Straight, and Bending setup).

Furthermore, a Y-shaped mixer with an angle of 30° was simulated. All models were designed with the symmetry condition, if possible. This reduced computational costs in terms of fewer cells, and saved computational time. The Counter and the Straight setup were designed based on the mixing units realized in the CHTS plant. These two setups were chosen to carry out all the experiments with the CHTS plant. Figure 5-1 shows the designed CAD models with the Counter and the Straight setup similar to the mixing unit in the CHTS plant. The other designed models are found in Appendix chapter 5 A: Designed 3D models with other mixing geometries used for the simulation.

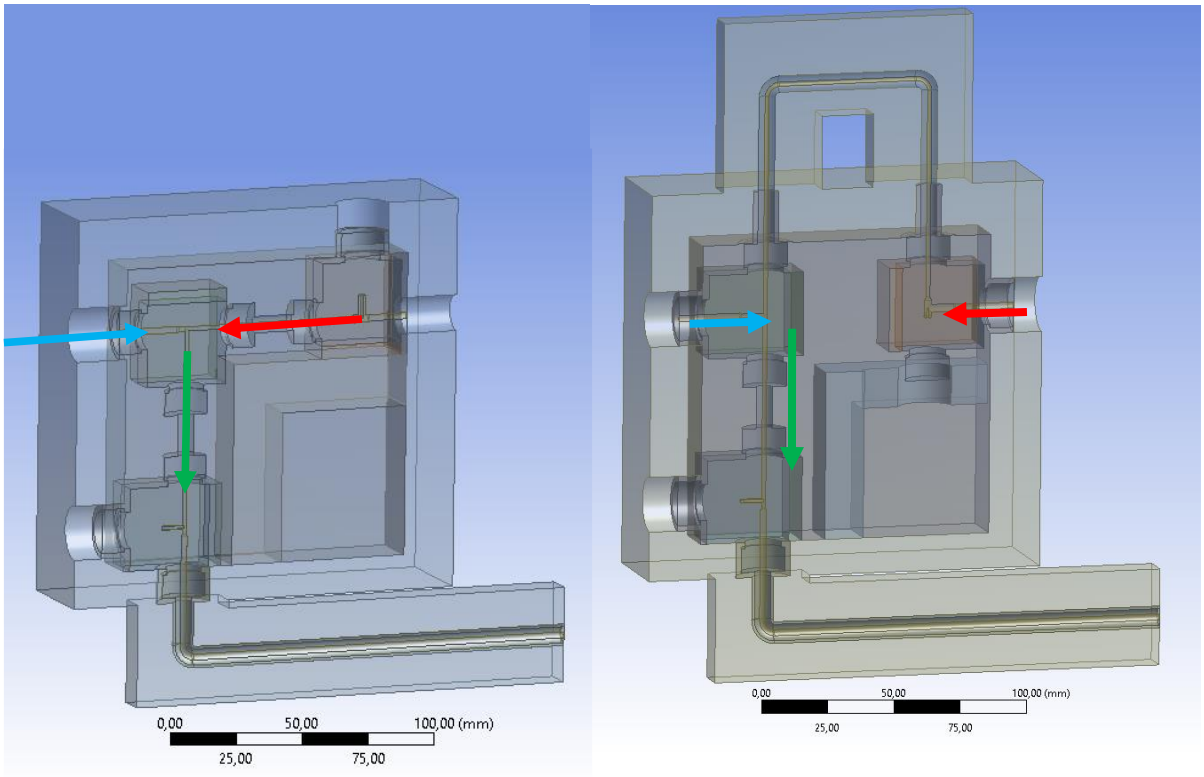

Figure 5-1: Designed CAD models of the mixing unit in the Counter setup (left side) and the Straight setup (right side) as used in the CHTS plant, created with ANSYS Workbench®, the blue arrow shows the direction of the cold stream, the red and green one the hot and the product stream, respectively.

Tetrahedron and hexagon elements define the meshing grid for the designed geometry (compare chapter 2, section 2.3.1). Here, tetrahedron elements were used instead of hexahedrons. The formation of the mesh with hexahedrons resulted in a smaller number of elements. More computational time was required to generate a mesh consisting of hexahedrons in comparison to tetrahedrons. This is the case in terms of complex geometries. The positive effects of using hexahedrons instead of other elements for creating a mesh were only marginal [125]. The mesh was designed for three different numbers of elements. The main difference was the variation of the element size of the tubes containing the fluid. In general, the diameter of the tubes varied between 1.6 mm (T-junction as a mixer) and 3 mm (places for measurement of the temperatures). The number of elements used for the Counter model with varying element size for the tubes resulted in $6.6 \cdot 10^6$ elements (for 0.1 mm) and $1.8 \cdot 10^6$ elements (for 0.2 mm).

The best mesh showed the most accurate results (temperature, velocity) with the smaller number of elements. For the determination of the best mesh to use, several tests were carried out. These were the mesh independency test, the convergence test, and the turbulent intensity test. The number of elements shown in Table 5-1 was in the same range for all designed meshed models. As an indicator for the quality of the created mesh, the cell skewness was concerned. The resulting cell skewness for a mesh of all the designed models was between 0.89 and 0.9.

These values were within the acceptable range, as indicated in Table 2-4. One reason for the relatively large values of the cell skewness was the complexity of the model. However, the simulation showed accurate results. Therefore, suitable model equations and related settings of the solver had to be chosen [125].

5.1.1 Mesh independency test, convergence test, and turbulent intensity test

After successfully meshing the models, three different tests were performed to find the most suitable mesh for the simulation. For the mesh independency test, three meshes with different element sizes were simulated. The resulting process conditions were kept constant at $p = 25$ MPa, $T_2 = 573$ K, $\dot{m}_3 = 35$ g min^{-1} and $a = 0.05$. The element size was decreased until the resulting solution showed no further changes. At this particular element size, the results are independent of the element size. Therefore, a further decrease results in higher computational costs but not in more resolution of the results. This mesh was chosen for the models and all the future simulations.

The convergence test was carried out with the mesh found with the mesh independency test. There, the meshed model was simulated. The simulation stopped as the convergence criteria were reached. The requirements were based on the root mean square residuals. For the simulation, standard convergence criteria were applied. For the pressure and the momenta (x, y, z) residuals, 10^{-3} was considered. For the residuals of the energy, 10^{-6} was set. After performing the simulation, the thermal and the velocity field results were saved to the computer. The simulation was then continued based on the received solution with lowered values of the residuals. As soon as the convergence was reached again, the results were saved and compared to those with higher residuals. As long as there were no discrepancies in the thermal and the velocity field, the convergence test was successful, and the residuals were found for future simulations. Once the differences were observable for the given grid size, the lower residuals were used.

After performing both the mesh independency and the convergence test, the turbulent intensity test was carried out. The turbulent intensity was increased from the standard value of 5% up to 10%. Thereby, either the solver settings and the boundary conditions were kept constant. The results of the simulations for both cases with the turbulent intensity of 5% and 10% were analyzed and compared. Once the simulation with a turbulent intensity of 10% showed more accurate results, this value was used for future simulations. This test was performed due to the high Reynolds number in the hot mixing stream inside the mixing unit.

5.2 Simulation of the mixing unit

After performing the three tests regarding the designed models and the meshes, these could be used for different simulations of the CHTS process. At first, simulations of the thermal and the velocity field were carried out, followed by simulations of the residence time distribution and the chemical reaction.

5.2.1 Method of the simulation of the thermal and velocity fields

At first, the method of the simulation is described. For the simulation of the thermal and the velocity fields, the mixing of the hot near- / supercritical water stream with a cold water stream was considered. The influence of different process and boundary conditions on the resulting mixing temperature T_3 was investigated. Therefore, no chemical reaction was concerned. Within the experiments, salt concentrations c_{salt} between 0.00125 mol dm^{-3} and 0.15 mol dm^{-3} were applied. The product stream with the particle suspension was very diluted. Due to the low concentration of the particles inside the suspension and the nanosized scale, the particles themselves did not affect the flow pattern and heat transfer phenomena largely, according to Ma et al. [143]. These aspects justify the analysis of the thermal and velocity fields without particle formation.

The designed and meshed models needed to be validated in the next step. For the validation, designed models with the Counter and the Straight setup could be installed for the application in the CHTS plant. Therefore, the experimental mixing temperature of the hot near- / supercritical water stream and the cold water stream T_3 was measured with the CHTS plant for these two mixing geometries. Here, only the heating unit for the hot near- / supercritical water stream was simulated. Experiments with variating process conditions were performed. Afterwards, the simulations were carried out with the same boundary conditions and the mixing temperature measured at the front part of the modeled thermocouple. Leybros et al. performed a validation method like this [127]. Based on the validation experiments and simulations of either the Counter and the Straight setup, the other designed models were seen as modeled correctly. In total, eleven mixing experiments for the Counter Setup and three for the Straight model were carried out to compare to the simulation results. The process conditions with the resulting mixing temperatures of the experiments are shown in Table 5-1:

Table 5-1: Mixing experiments with different process conditions and determined experimental mixing temperature to validate the designed model with the Counter and the Straight setup.

exp. no.	p / MPa	$\dot{m}_3$ / g min^{-1}	T_2 / K	a / -	T_3 / K
Counter					
1	25	35	573	0.05	544.1
2	25	35	573	0.20	517.8
3	25	35	573	0.35	495.2
4	25	35	673	0.05	660.8
5	25	35	673	0.35	647.1
6	35	35	583	0.05	552.3
7	30	35	583	0.05	555.2
8	35	35	583	0.35	502.4
9	35	35	673	0.05	647.0
10	30	35	673	0.35	607.4
11	35	35	673	0.35	588.0
Straight					
12	25	35	573	0.2	513.8
13	30	35	673	0.1	650.8
14	30	35	573	0.1	533.8

After the tests mentioned above, the designed and meshed models were implemented into ANSYS Fluent® for performing the simulations. The simulations were carried out in the steady-state setup with pressure-based solvers in the double-precision mode. The advantages of this solver were the robustness and less computational costs in terms of a low memory requirement [125]. For the solution of the energy equation, the associate solver was implemented. Regarding the turbulence, the realizable k-ε model was realized. There, the standard wall function was used. The realizable k-ε model showed the same robustness as the pressure-based solver. It was also suitable for the CHTS process due to its excellent fit to buoyancy-driven processes [104].

After implementing ANSYS Fluent®, the required thermodynamic properties of the used materials and the boundary conditions had to be set. The thermodynamic properties were estimated as a polynomial function of the temperature for the solid components made of either stainless steel, calcium silicate, or brass [93,144]. The densities were considered constant. On the other hand, for the description of the thermodynamic properties of water, user defined functions (UDFs) were used with a dependence on pressure and temperature. The UDFs are described in the later section.

Once the thermodynamic properties for all the materials were implemented, the solid material surfaces were connected to the fluid surfaces. This link enabled the simulation of the thermal fields in terms of heat transfer. Next to that, the process conditions were set according to the

experiments. The mass flow inlet condition was applied for both inlet streams of the hot and cold water stream. For the outlet of the mixing stream, the outflow condition was used. The operation pressure in terms of the system's pressure was adjusted.

Furthermore, the gravitational acceleration was also considered. Especially the boundary conditions of the wall temperatures were strongly dependent on the hot water temperature. The insulation wall surface temperatures around the hot and cold stream inlet and the outlet of the product stream changed drastically with the hot stream's temperature. This effect was neglected in other works published in literature. There, the tubes and fittings were perfectly covered with fiberglass and enabled the assumption of an adiabatic boundary condition was made [108].

The effects of the hot stream's temperature on the insulating walls' surface temperature were established to depict the realistic case within the simulation. Therefore, the wall temperatures were determined experimentally with a thermocouple at different points of the insulation housing. The temperatures were measured at both inlet points, at the outlet of the product stream, and the lateral wall. The measurement was carried out for different process conditions like changing the pressure p, the hot water temperature T_2, the total mass flow rate $\dot{m}_3$ and the mixing ratio a. The data were extrapolated to calculate the resulting boundary conditions for other process conditions.

After the experimental investigation of the boundary conditions, the convergence criteria were adjusted as found within the convergence test. These values were determined for each designed model. When the found values for the convergence criteria were not sufficient, the under-relaxation factor had to be adapted. This factor stabilized the iterative process of the pressure-based solvers. It was set as described in the Fluent User's Guide [125]. The convective term of the NS equations was discretized with the second-order upwind scheme instead of the first-order upwind method. An advantage of this scheme was its computational cheapness compared to higher-order discretization techniques. These were, for example, the power-law or the quadratic upwind interpolation (QUICK) [143]. Furthermore, it showed more accurate results compared to the first-order upwind method. Next to the convective term, the diffusive term of the NS equations was discretized with the Least Squares Cell-Based Gradient Method. It showed the same advantages as the second-order upwind method. For meshes consisting of tetrahedral elements, this method was favored [125]. For the pressure term of the NS equations, the standard discretization was applied.

For solving the NS equations, four algorithms were available in ANSYS Fluent®. For the simulation of the CHTS process, the Semi-Implicit Method for Pressure-Linked Equations (SIMPLE) was applied. It was appropriate for solving complex models. More details about the mentioned discretization methods can be found in [128]. For the initialization of the models, the standard initialization method was applied. In the beginning, all tetrahedral elements were initialized with the boundary condition of the cold stream. Once the initialization was successful, the simulation was started. After finishing, the results were implemented into the post-processing unit of ANSYS Fluent® and analyzed. The resulting temperatures at the measuring point of the hot water temperature T_2 and the mixing temperature T_3 at the front

part of the thermocouple were calculated and noted. After performing the simulations, the temperatures determined through the simulation were compared to the experimental temperatures shown in Table 5-1. The comparison of both temperatures showed the result of the validation test and the quality of the designed model. The other models without experimentally determined mixing temperatures (Bending and Y-30) in a total of 18 simulations with other process conditions were performed similarly. The different used process conditions are shown in Table 11-4 in Appendix chapter 5.

5.2.2 User defined functions (UDFs)

The properties of water, as described in section 2.1.1, had to be implemented into ANSYS Fluent®. The thermal conductivity, viscosity, density, and specific heat capacity are functions of pressure and temperature. These properties had to be provided precisely in ANSYS Fluent® over an extensive temperature range for different high pressures for an accurate simulation. Especially around the critical point of water, there is a drastic change in these properties [47]. For the implementation, different fit functions were tested. At first, polynomial temperature-dependent functions showed less accuracy in the nearcritical region. For this reason, piecewise polynomial temperature-dependent functions were applied for fitting the trend of the thermodynamic properties. The procedure could be split into single steps as shown in the following:

1. The properties of water were calculated using the software *REFPROP 9.1* (National Institute of Standards and Technology, Gaithersburg, USA) [53]. Besides the properties mentioned above, the dielectric constant of water was also of interest. The temperature range was between 300 K and 700 K for constant pressures of 25 MPa, 30 MPa, and 35 MPa.
2. Each property was then plotted using *Origin Pro 2018b* (OriginLab, Northampton, USA) for the constant pressures within the chosen temperature range. The resulting trend curves were split into single segments, and appropriate fit functions were chosen. The corresponding temperature ranges for each segment were noted. As far as the complexity of the trend curve was low, it was described by a single temperature-dependent function.
3. The simple trend curves, as well as the single segments, were fitted in *Origin Pro 2018b*. The best fit function regarding the smallest mean squared error was chosen within the segmented temperature range.
4. After finding the optimal fit functions for the trend curves, a C-file was created. It included all thermodynamic properties of water at the above-mentioned constant pressures. They were realized as piecewise fitted polynomials as a function of the temperature. For a better understanding, an example of a C-file including the fit functions of the thermodynamic properties at 30 MPa is shown in Appendix chapter 5 C: User-Defined Function (UDF) including water properties and kinetic approach.

5. The fitted thermodynamic properties of water could then be used within the simulations of the CHTS process as UDFs. Therefore, the written C-file was compiled in ANSYS Fluent® before the simulations were carried out. The UDF had to be changed once the used pressure was adapted. As previously mentioned, the initialization step was performed with constant values for each property and the boundary condition of the cold stream for each element. After the initialization, the compiled UDF was applied, and thereafter the properties of water could be selected in the material properties panel.

5.2.3 Simulation of the residence time distribution (RTD)

For the characterization of the CHTS plant, the knowledge of the residence time τ inside the mixing unit and in the whole plant was necessary. τ was determined through the volume of the tubing and fittings of the plant and the single mass flow rates dependent on either the pressure and the temperature. For the validation of these experiments, simulations of the residence time distribution inside the mixing unit could be carried out. Sierra-Pallares et al. [145] suggested a particle size distribution (PSD) dependence on the residence time distribution during the CHTS process. With this simulation, the quality of the mixing and the used mixer could be described and analyzed.

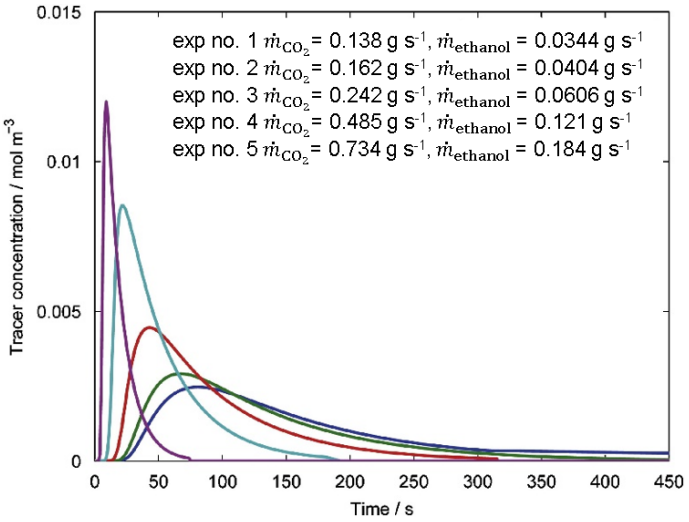

Figure 5-2: Simulations of the residence time distribution for 20 MPa and 573 K with different mass flows of CO_2 and ethanol, reprinted with permission from Elsevier [145].

By comparing the experimentally determined PSDs and simulated RTDs, it was found out that longer residence times affected a broader PSD and an enlargement in the average particle size (APS). The investigation of the RTD was necessary for the analysis of the influence of the process conditions on the PSD. RTDs with changing pressure, hot water temperature, total mass flow, and mixing ratio were simulated to examine this effect further. For the determination, the following steps were carried out:

1. After the successful simulation of both the thermal and the velocity field, a tracer substance was introduced. It showed the same thermodynamic properties as water. In addition to the models used to simulate the thermal and the velocity fields, the species-transport model was applied.
2. In the module of the species transport model, the mixture was specified. There, water was used as bulk material. Secondly, the mixture contained the tracer substance.
3. For the properties of the mixture, certain correlations for the mixture density, the specific heat capacity, the thermal conductivity, and the viscosity had to be chosen. Therefore, a volume-weighted mixing law was applied for the mixture density. A mixing law and mass-weighted mixing laws were used for the specific heat capacity, thermal conductivity, and viscosity. Secondly, the properties of water were set through the UDFs for the tracer. After the setup of the species transport model, it was first switched off. It was essential to switch the fluid type to liquid water again within the cell zone conditions panel.
4. The following steps were carried out as described in section 4.2.1 with the setup of the boundary conditions for the simulation of the thermal and the velocity field. The simulation was finished as the set convergence criteria were reached.
5. After finishing the simulation of the thermal and the velocity field, the type of solver was changed from a steady-state simulation to transient. The species transport model was reactivated. The air containing components air_chamber and air_outet had to be changed to air inside the cell zone conditions panel. Furthermore, the fluid type was changed to mixture again.
6. For the injection of the tracer at the hot water stream's inlet, the mass fraction of the tracer was set to a value of 1 in the boundary condition panel. The flow equation solver was disabled in the solution control panel due to the already successfully performed thermal and velocity field simulation.
7. Before simulating the RTD, a graph was initialized for plotting the respective curve. The plot and write options were located within the surface monitor panel. During the simulation, the area-weighted average of the injected tracer was plotted against the residence time. Additionally, the values were written in a text file.
8. The first time step was set to 0.05 s in the solution initialization panel. The number of time steps was adjusted to 1, whereas the number of iterations was set to 20.
9. After setting these values, the simulation was performed for one time step with the total amount of tracer as selected. For a time of 0.05 s, the tracer was injected at the inlet of the hot water stream.
10. Once the simulation for the time step of 0.05 s was finished, the mass fraction of tracer at the inlet of the hot water stream was set to 0 again. Then the simulation was carried out for another 100 time steps. Both the time step and the maximum number of iterations remained constant. With this setup, a total residence time of 5 s was reached.
11. The resulting RTDs were analyzed using both the post-processing tool of ANSYS® and *Origin Pro 2018b* to plot and fit the RTD curves.

5.2.4 Simulation of the chemical reaction

Once the thermal and velocity fields simulation and the RTDs were carried out, the reaction was simulated in the next step. As previously mentioned, the global reaction of cerium nitrate with water to ceria was concerned. This step provided new insights into the concentration profiles of both the educts and the products during the reaction inside the mixer. Next, it could be obtained how the reaction took place depending on the used process conditions. In the style of the performed experiments with the CHTS plant, the molar concentration of cerium nitrate was adjustable within the simulation. Later, the obtained results of the simulation were compared with the experimental ones.

The previously described UDFs were supplemented with a function describing the kinetic behavior of the reaction (compare section 2.2). The extended UDFs had to be recompiled in ANSYS Fluent® to apply the reaction kinetics in the later simulations. The following steps of the simulation of the reaction are shown in detail:

1. Once the thermal and the velocity fields were simulated, the species transport model was reactivated. In addition to the simulation of the RTDs, the species transport model had to be adapted. The volumetric reaction was chosen and activated in the panel.
2. For the realization of the reaction, the involved educts and products had to be defined in the materials panel. Some of them were partially available within the materials database of ANSYS Fluent®. Cerium nitrate and ceria had to be created manually with the thermodynamic properties found in literature [146]. For the thermodynamic properties of cerium nitrate, the properties of water were chosen. Due to the low concentration of the cerium nitrate salt in water, this assumption was valid.
3. For the reaction model, the Finite-Rate / Eddy-Dissipation model was applied. After setting up both the thermodynamic and the kinetic properties, the reaction equation (compare section 2.1) was defined. The stoichiometric coefficients for the species involved were chosen according to the reaction equation. The exponent of the reaction rate of the educts was set to 1. The parameters of the kinetic approach (pre-exponential factor and activation energy) were used from Nadimpalli et al. [108] for the given reaction system with cerium nitrate as a precursor.
4. The salt concentration at the inlet of the cold stream was initialized accordingly to the experiments. This was realized in the species panel of the species transport model. The concentration was defined as a mole fraction. The flow equation solver was switched off in the solution control panel. As for the simulation of the RTD, the thermal and the velocity fields were already successfully simulated, and the convergence criteria were reached.
5. The UDF of the kinetic approach was chosen in the User-defined panel as the rate of the volumetric reaction. Before starting the simulation, specific values could be selected in the data quantity files panel. The molar concentration of the species and heat of the reaction were set for analyzing the reaction.

6. The simulation was carried out until the convergence criteria were reached. After that, the results were checked and analyzed. The main focus was on the analysis of the concentration profiles as a function of time and position.

5.3 Estimation of the metal salt solubility

Estimating the metal salt solubility at elevated pressures p and temperatures T was performed stepwise in different programs. First, the equilibrium constants K_i of the single reactions were calculated with *Origin Pro 2018b*. The r-HKF model, as well as the SAA model, were implemented into a LabTalk routine. The equilibrium constants K_i were calculated assuming a constant pressure p and a variation of the temperature T. For both models, different parameters were required to calculate K_i. For the r-HKF model, specific parameters were needed (compare section 2.1.2.1) for the calculation, whereas the SAA model only requires the water density ρ and the respective dielectric constant ε. Both parameters were calculated using *REFPROP 9.1* (water density) and the equation of Johnson et al. (dielectric constant) [56]. The standard molar Gibbs free energy of formation, the standard reaction enthalpy, and the heat capacity of the reaction at standard conditions available in literature were further used for the calculation of K_i. In addition, the crystal ionic radius and the ion charge of each species were required values. The analysis of the equilibrium constants K_i is the basis of the estimation of the metal salt solubility using a *MATLAB* solver. A flow scheme representing the single steps is shown in the following image:

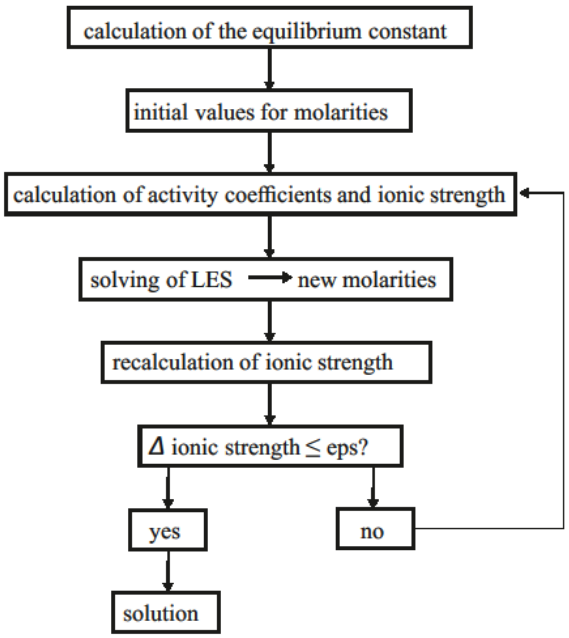

Figure 5-3: Scheme of the involved steps of the estimation of the metal salt solubility [147].

For the initial step, a linear equation system (LES) was set up for each metal salt. The equation system contained all reactions taking place during the solvation process. The structure itself was taken from Adschiri et al. [83] and Masoodiyeh et al. [77]. The total number of reactions was simplified and shown for NaCl in the following equations:

$$0 = a_{\mathrm{Na^+}} a_{\mathrm{Cl^-}} - K_1 a_{\mathrm{NaCl_{aq}}} \tag{5-1}$$

$$0 = a_{\mathrm{NaCl_s}} - K_2 a_{\mathrm{NaCl_{aq}}} \tag{5-2}$$

$$0 = m_{\mathrm{Na^+}} - m_{\mathrm{Cl^-}} \tag{5-3}$$

$$0 = m_{\mathrm{NaCl_{aq}}} + m_{\mathrm{NaCl_s}} - m_{\mathrm{Na^+}} \tag{5-4}$$

The first equation (5-1) describes the dissociation of dissolved NaCl into ionic Na^+ and Cl^-. Equation (5-2) represents the precipitation of dissolved NaCl to the solid form. Equations (5-3) and (5-4) show the electroneutrality condition and the material balance. Those complete the linear equation system with four equations for four unknown parameters. In order to estimate the metal salt solubility and the solution of the linear equation system, the calculated equilibrium constants K_i (r-HKF or SAA model), the temperature T, the density ρ and the dielectric constant ε were implemented into the *MATLAB* routine. The first step was the generation of a matrix for the initial solution of each species. The activity coefficients and the ionic strength were calculated with the initial values of the molalities. Due to the ionic strength, they depend on the molalities. The above-shown calculation scheme was then used to solve the linear equation system iteratively. The calculation was continued until the difference of the old and newly calculated ionic strength I was smaller than *eps* (floating-point relative accuracy). If not, the calculation was continued in a while loop until *eps* was reached.

6. Estimation of the metal salt solubility

The metal salt solubility was estimated with different models. As previously described in section 2.1.2, the metal salt solubility is high in H_2O at ambient conditions where water acts as a polar solvent. On the other hand, in the near- / supercritical region, the metal salt solubility is low and H_2O acts like a non-polar solvent. This is due to the dependence of the dielectric constant ε on the pressure p and the temperature T. The solubility is dependent on the used metal salt. Depending on their respective solubility in the supercritical region, they are structured into type 1 or type 2 metal salts. According to the definition of Marshall and Valyashko [66,67], type 1 metal salts show either a higher melting temperature or a higher solubility in the near- / supercritical region.

In this chapter, the modeling results structured into the calculation of the equilibrium constants K_i and the estimation of the metal salt solubility at elevated pressures p and temperatures T are shown. The equilibrium constants K_i were calculated using the r-HKF and the SAA model. The solubility was estimated with an iterative method (compare section 5.3). Main parts of this chapter were performed by Zürn [147].

6.1 Calculation of the equilibrium constants K_i

As described in section 2.1.2, the equilibrium constants K_i were calculated with the r-HKF and the SAA model. At first, the implemented models had to be validated with data from literature. Here, the SAA model was applied to calculate the equilibrium constants K_i for the NaCl dissociation in H_2O. K_i was calculated for different constant pressures p as a function of the temperature T. Both models were validated with data from Shock et al. [72]. Figure 6-1 shows the validation results for K_i different pressures p between 25 MPa and 100 MPa, as a function of the temperature T:

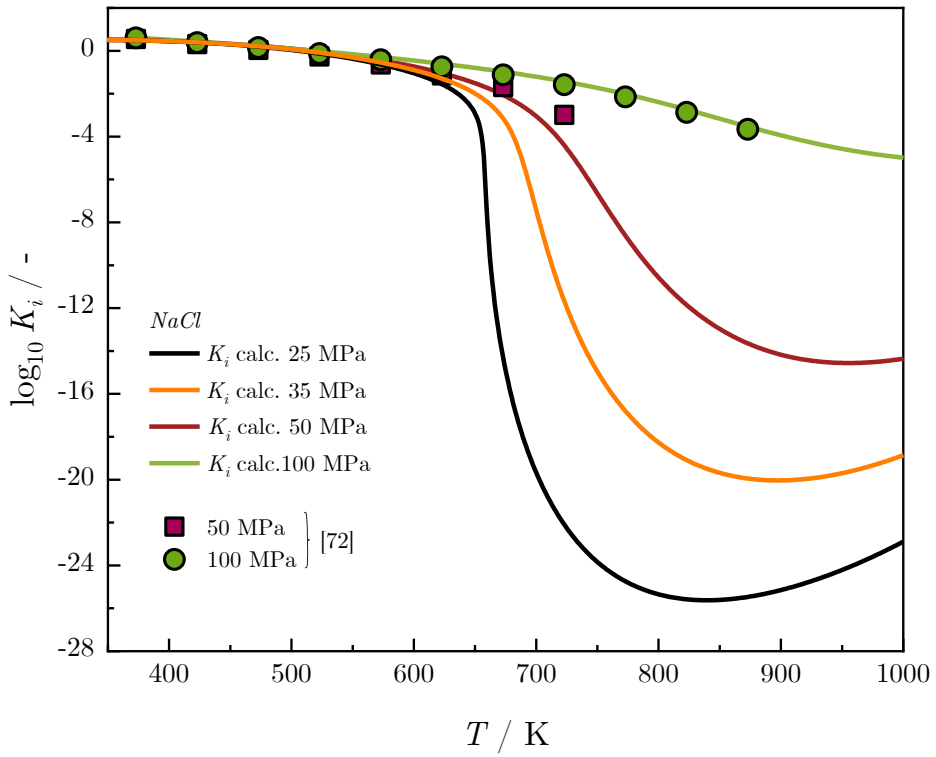

Figure 6-1: Validation results for the logarithmic equilibrium constant K_i of the dissociation reaction of NaCl calculated with the SAA model with data taken from Shock et al. [72] as a function of temperature. The pressure p was varied between 25 MPa and 100 MPa [147].

The calculated trends of the equilibrium constant K_i data agree with data taken from literature. The high pressures of 50 MPa, 100 MPa were selected due to the presence of literature data for K_i and the original background of the r-HKF model. The deviation between the calculated and literature data is increasing with decreasing pressure p, especially in the subcritical range. However, the validation shows a high accuracy (for $p = 50$ MPa and $T = 723$ K, the deviation is about 10^{-3}). For a pressure of 100 MPa, the deviation between the calculated and literature data is neglectable up to a temperature of 873 K. With increasing temperature, the values calculated with the SAA model are lower than the literature data, and the model underestimates the equilibrium constant. The validation with high pressures of 50 MPa and 100 MPa shows that equilibrium constants K_i are obtainable with the SAA model for lower pressures used in the CHTS process (25 MPa – 35 MPa). The lack of data in that region is explained by the history of both the r-HKF model. The r-HKF model was originally developed in geochemistry with specific higher pressures than the CHTS process (compare section 2.1.2.1). It was fitted to experimental values of NaCl and KCl in the supercritical region. This leads to the assumption that there is a deviation in the nearcritical region between experimental data and the model. The SAA model was validated with the r-HKF model. This could also lead to deviations. Furthermore, there is a drastic decrease of K_i for nearcritical pressures and

temperatures. This is due to the fast reduction of density and the dielectric constant around the critical point of water.

After validating the SAA model with literature data of NaCl, both models were compared with data of NaCl taken from Shock et al. [72] for a pressure of 50 MPa. This is illustrated in Figure 6-2:

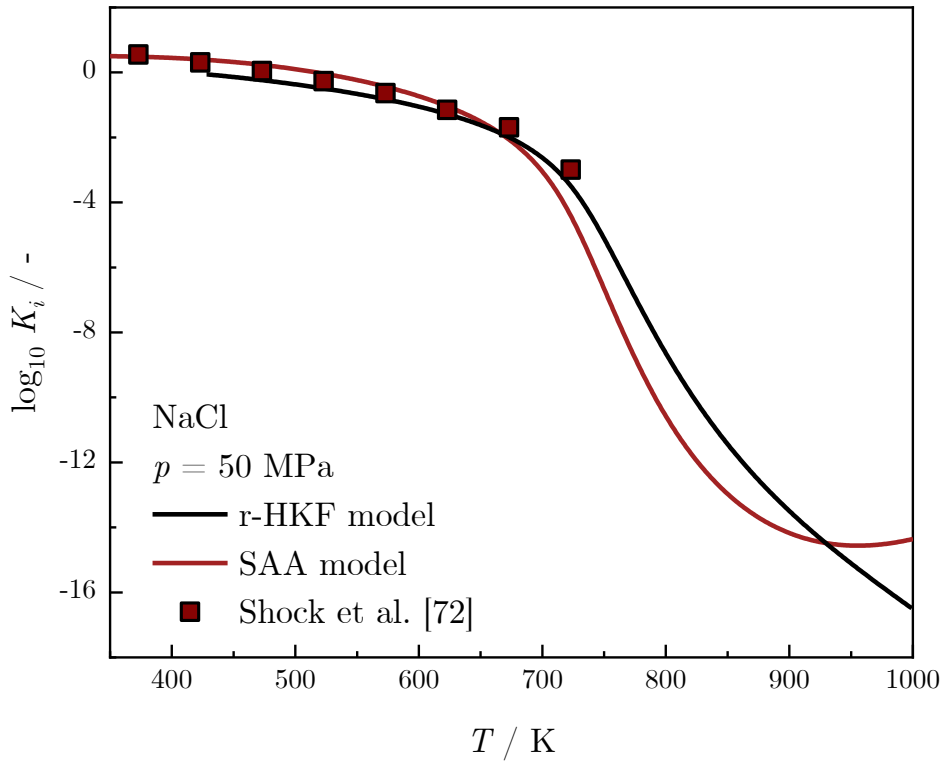

Figure 6-2: Trend of the logarithmic equilibrium constants of the dissociation reaction of NaCl calculated with the r-HKF and the SAA model for a pressure of 50 MPa as a function of temperature [147]. The trends are compared to data taken from Shock et al. [72].

For low process temperatures, there is a slight deviation between the literature data and both models. The r-HKF model fits to the experimental data up to a temperature above 700 K. The SAA model shows a slightly larger deviation in this region. Both models show a similar trend up to 700 K. Beyond this temperature, the similar trend is changed, and the deviation increases steadily. The reason for this is the difference in the calculation of the g-function for each model. This results in a steady decrease of the equilibrium constant K_i up to temperatures of 1000 K for the r-HKF model. The SAA model results in increasing values for K_i at around 900 K. The r-HKF model predicts a further decrease of the metal salt solubility with decreasing equilibrium constant K_i. In contrast, the SAA model shows more realistic non-infinite values of K_i in the supercritical region. In this region, differences in temperature, density, and the dielectric constant are concurring increasing K_i. Concerning equation (2-8), both the density and the dielectric constant are decreasing with increasing temperature at constant pressure.

Furthermore, the temperature difference is increasing. This increases the second part of equation (2-8) and an increase of K_i for higher process temperatures.

The calculation method of the g-function has a particular effect on the effective electrostatic radius. It describes its pressure and temperature dependence. The trend of the g-function as a function of temperature for the r-HKF and SAA model is shown in Figure 6-3:

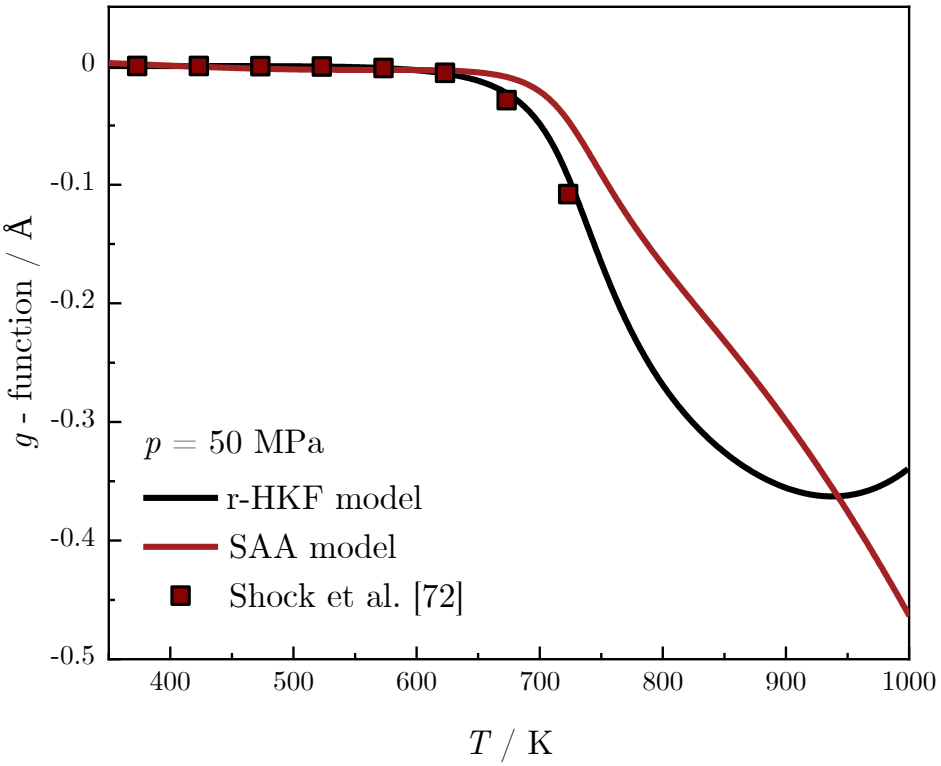

Figure 6-3: Trend of the g-function calculated with the r-HKF and SAA model for a pressure of 50 MPa as a function of temperature [147]. The calculation methods were proposed by Shock et al. [72] and Sue et al. [4].

The calculations of the g-function with the r-HKF model agree with the data from Shock et al. [72]. For low temperatures up to 650 K, the SAA model is also in good accordance with the experimental values. At a temperature of 630 K, the deviation between both models is increasing. The SAA model underestimates the influence of pressure and temperature on the effective electrostatic radius. This is the validation of the g-function in area II (compare Figure 11-1 Appendix chapter 2) with nearcritical values. Sue et al. [4] tried to increase the performance of the SAA model in that region. This deviation is the reason for the difference between both models for high process temperatures. The advantage of the SAA model compared to the r-HKF model is the use of less experimental data to calculate K_i. For this reason, the SAA model is used for all the calculations in the following.

6.2 Influencing parameters of the equilibrium constants K_i

The above-shown results are based on the dissociation reaction from the aqueous metal salt to the respective ions. In the following, the precipitation reaction is combined with the dissociation reaction for both salt types (compare section 2.1.2). In the next step, the influence of the parameter β is investigated.

6.2.1 Influence of the salt type on the equilibrium constant K_i

The previously-mentioned classification of the metal salts in type 1 or type 2 (compare Figure 2-4) has a specific influence on the equilibrium constant K_i. Both the values of K_i and the respective trends are used to divide the metal salts into type 1 or type 2. According to the definition, NaCl is a type 1 metal salt. The trend of the dissociation and precipitation reaction for NaCl as a function of temperature and constant pressure is shown and illustrated in Figure 6-4:

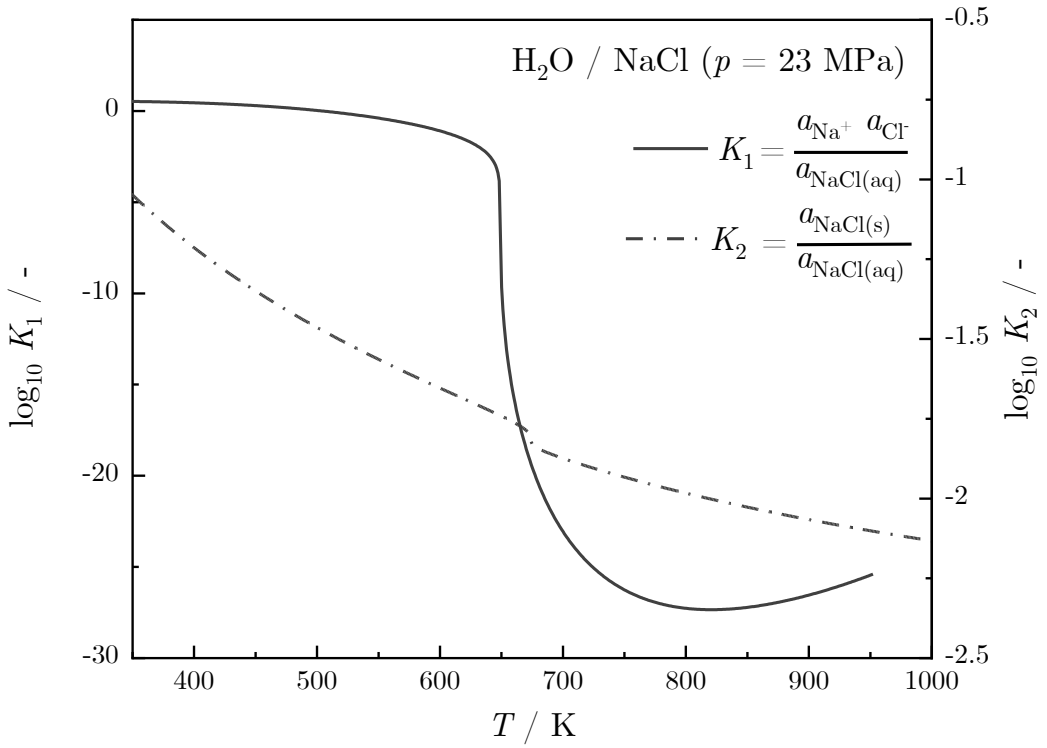

Figure 6-4: Trend of the calculated logarithmic equilibrium constants K_1 for the dissociation reaction and K_2 for the precipitation reaction of NaCl for a pressure of 23 MPa as a function of temperature. The trends were calculated with the SAA model.

The equilibrium constant K_1 stands for the dissociation reaction from the aqueous form of NaCl to the respective ions, whereas K_2 represents the precipitation reaction from the aqueous NaCl to the solid form. Both equilibrium constants are defined as a function of the activity of the related species. Figure 6-4 illustrates the trend of both equilibrium constants. Concerning K_1,

there is only a slight decrease between 300 K and 600 K. The value of K_1 is more significant than 1. The equilibrium is on the product side (Na^+ and Cl^-). In the vicinity of the critical point of water at around 630 K, the value of K_1 is decreasing. It reaches its minimum at 800 K. A further increase of the temperature leads to a slight rise up to 950 K. The precipitation reaction is described with the trend of K_2. The values of K_2 are decreasing steadily with increasing temperature. At the critical point, there is a characteristic kink. In general, the values of K_2 are below 1, resulting in the location of the equilibrium on the side of the dissolved NaCl. Furthermore, the density and the dielectric constant show relatively high values that favor the respective solubility. According to the trend of both equilibrium constants, the solubility should decrease with increasing temperature. The minimum reached near the critical point, and in the supercritical region, the solubility rises again. In addition to that, it is assumed that a low amount of NaCl is dissolvable at high process temperatures. This trend is according to the structure of type 1 salts and the respective solubility behavior. These metal salts are even soluble in the supercritical range. Beyond the trend of the equilibrium constants of NaCl representing a type 1 metal salt, the equilibrium constants of Na_2SO_4 are shown in the following image:

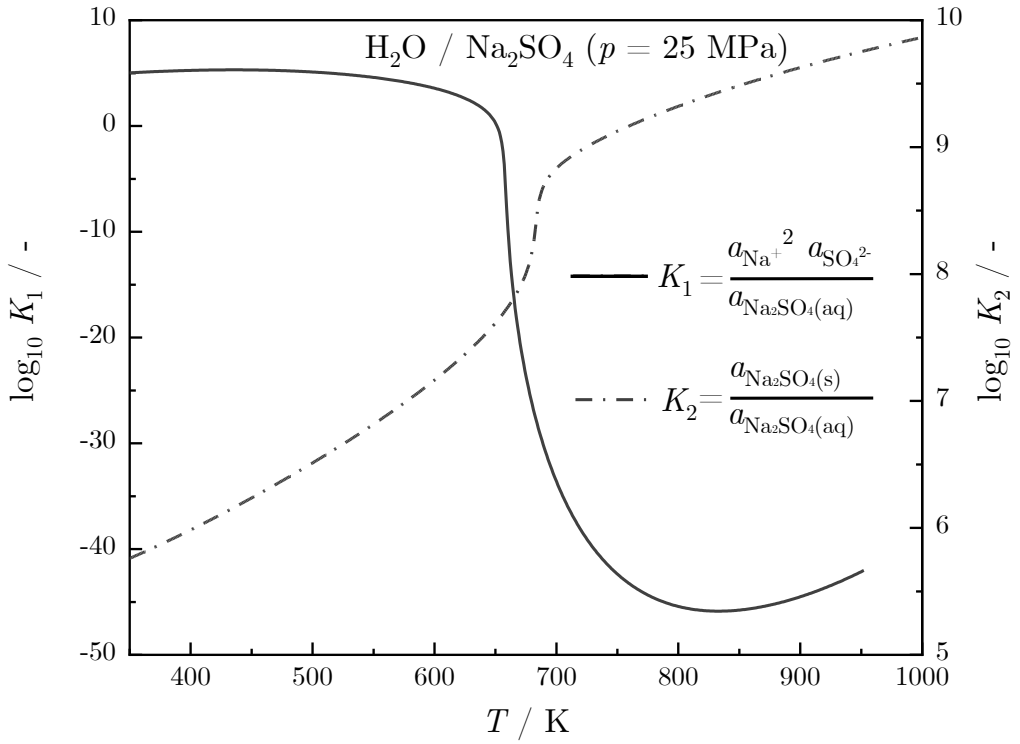

Figure 6-5: Trend of the calculated logarithmic equilibrium constants K_1 for the dissociation and K_2 for the precipitation reaction for Na_2SO_4 (p = 25 MPa) as a function of temperature. The trends were calculated with the SAA model.

For this metal salt, the significant difference of the equilibrium constant of the dissociation reaction in the nearcritical range is also visible. The reason for this is the already-mentioned

decrease in density. At around 800 K, there is a slight increase of K_1. The comparison of the absolute values shows lower values for Na_2SO_4. The minimum value of Na_2SO_4 is around 1.6 times smaller compared to NaCl. This leads to the fact that the dissociation will probably not occur for high process temperatures. On the other hand, the equilibrium constant of the precipitation reaction shows a different trend compared to NaCl, with values larger than 1. The equilibrium is shifted to the side of the solid Na_2SO_4 with increasing temperature. The values of K_2 are steadily rising with increasing process temperature. Around the critical point of water, there is a substantial increase of K_2. Comparing both trend curves assumes that Na_2SO_4 shows a lower solubility than NaCl at given pressure and temperature. This fits to the definition of a type 2 metal salt. The estimation of the metal salt solubility based on the equilibrium constants is described in the next section.

6.2.2 Variation of the parameter β

Since the SAA model was developed as a semi-empirical model, it is based on several parameters. According to equation (2-7-10) in Appendix chapter 2, β is used as a fitting parameter. Here, the equilibrium constant is fitted with literature data of the reciprocal temperature and the density. Figure 6-6 shows the influence of β on the logarithmic equilibrium constant as a function of temperature:

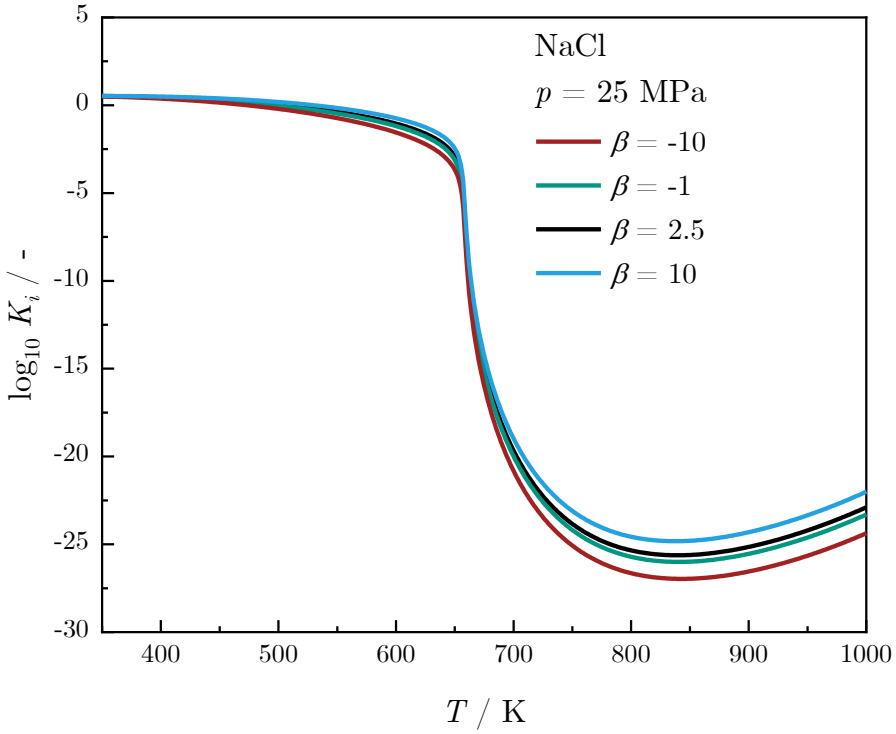

Figure 6-6: Trend of the logarithmic equilibrium constant for the dissociation reaction of NaCl as a function of temperature at a pressure of 25 MPa. The fit parameter β was varied between values of -10 and 10 [147].

The above-shown trends show the influence of the fit parameter β on the equilibrium constant. Up to temperatures of 650 K, the trends are similar, and no effect of β is visible. In the supercritical region, β has a specific impact on the equilibrium constants. Especially at around 800 K, the effect is noticeable. The deviations between the trend curves are based on fitting the equilibrium constant on the temperature and density. The values of β (2.5 kJ mol^{-1} and -1 kJ mol^{-1}) were investigated by Sue et al. [4] using equation (2-9). Here, -1 represents the fitted value with equation (2-8) for NaCl. The values of β = -10 and β = 10 were chosen to see the influence of β at the borders. A difference of β = 20 kJ mol^{-1} is not neglectable for high process temperatures. The slight deviation between the fit and the model shows that the SAA model is helpful for a predictive calculation of the equilibrium constants. β does not influence the values of the equilibrium constant the most. This enables the prediction of the equilibrium constants for new metal salts with unknown standard molar heat capacity values. For this case, a study of β with similar metal salts is assumed.

6.3 Solubility estimation for different types of metal salts

In this section, pressure influences on the solubility of both type 1 and type 2 metal salts are analyzed. The solubility estimation is based on the determination of the equilibrium constants with the SAA model combined with the iterative calculation of the molalities. In this calculation method, only the dissociation and the precipitation reaction were concerned. This enables the estimation even without the knowledge of the thermodynamic properties of the other species. Estimating the solubility allows the classification of the metal salts either into type 1 or type 2. For the analysis of the estimated solubility, the metal salts of type 1, NaCl, $CaCl_2$, and of type 2, Na_2SO_4 are described. The classification of typical metal salts into type 1 or 2 are found in Appendix chapter 6. Figure 6-7 images the trend of the estimated solubility of NaCl, Na_2SO_4, and $CaCl_2$ as a function of temperature for a pressure of 25 MPa.

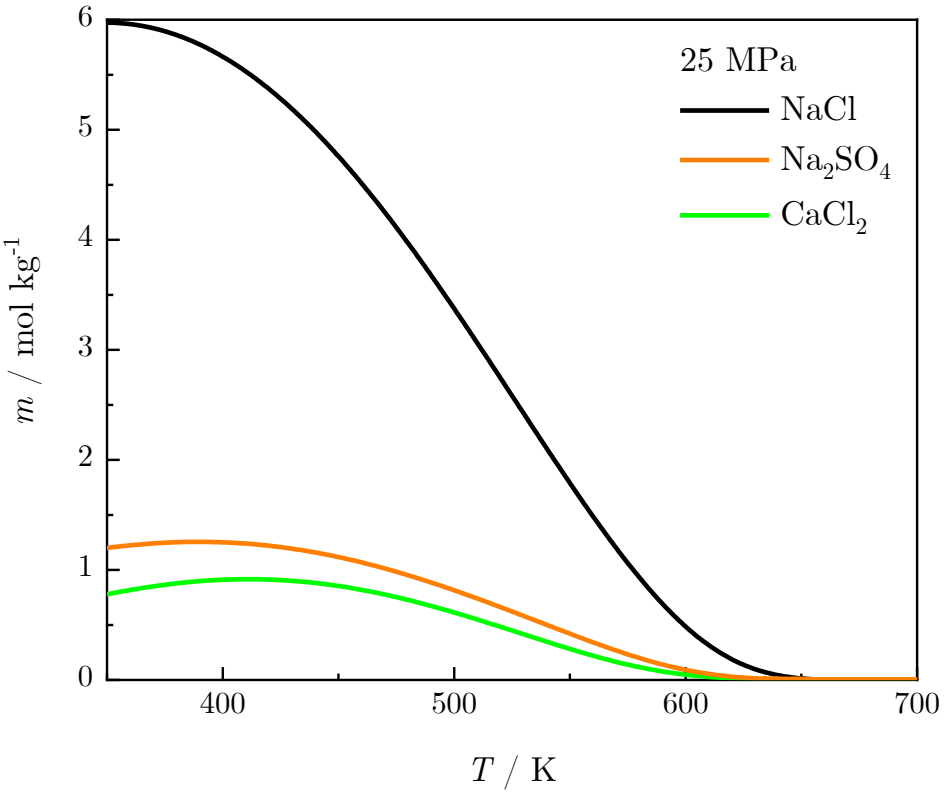

Figure 6-7: Estimated molality of NaCl, Na_2SO_4, and $CaCl_2$ as a function of temperature for a pressure of 25 MPa. The equilibrium constants were calculated with the SAA model.

In the field of the research of metal salts, NaCl is one of the most popular ones. Due to this reason, experimental data are available in literature. The dissociation reaction of NaCl takes place in a 1:1 ratio to Na^+ and Cl^-. NaCl is a so-called 1:1 electrolyte. In general, the solubility at a temperature of 300 K is around 6 mol kg^{-1}. The high values of the density and the dielectric constant result in a high value of the solubility. At a temperature of 650 K, the solubility drops down to low values which continues till 800 K. This result is evident for the solubility behavior of metal salts in near- / supercritical water. The calculation of the equilibrium constants is carried out with a normalized density of 0.997 g cm^{-3} leading to the beginning of the solubility estimation at around 350 K. With NaCl representing a 1:1 electrolyte, $CaCl_2$ represents a 2:1 electrolyte. In contrast to NaCl, the solubility of $CaCl_2$ is increasing for low temperatures up to a maximum at 420 K (0.91 mol kg^{-1}). After reaching the maximum, the solubility decreases with increasing temperature. In general, the estimated solubility for $CaCl_2$ is lower compared to NaCl. The decrease of the solubility is less drastic than for NaCl. The minimum solubility is also reached at temperatures around 650 K. Beyond the analysis of the type 1 metal salts, the type 2 metal salts were also analyzed.

The metal salt Na_2SO_4 shows a low solubility in the near- / supercritical region. As already mentioned, according to Marshall and Valyashko, it is structured into type 2 metal salts. Beyond that, it is categorized into 2:1 electrolytes due to the dissociation reaction into two

parts of Na^+ and one of SO_4^{-2}. The increase of the solubility at low temperatures up to 620 K is similar as for $CaCl_2$. The decrease of the solubility is drastic around the critical point, and the lowest value of the solubility is reached at around 620 K.

All solubility trends fit the definition of the classification of the metal salts into type 1 and type 2. The estimation of the solubility based on the calculation of the equilibrium constants with the SAA model agrees with the theory. The activity coefficient models used for the iterative calculation of the molalities are limited in the description of the maximum ionic strength. In order to optimize the calculation method, the activity coefficient models and a combination of them depending on the temperature range were further analyzed. Figure 6-8 shows the trends of the estimated solubility of NaCl as a function of temperature for different activity coefficient models used for the iterative calculations:

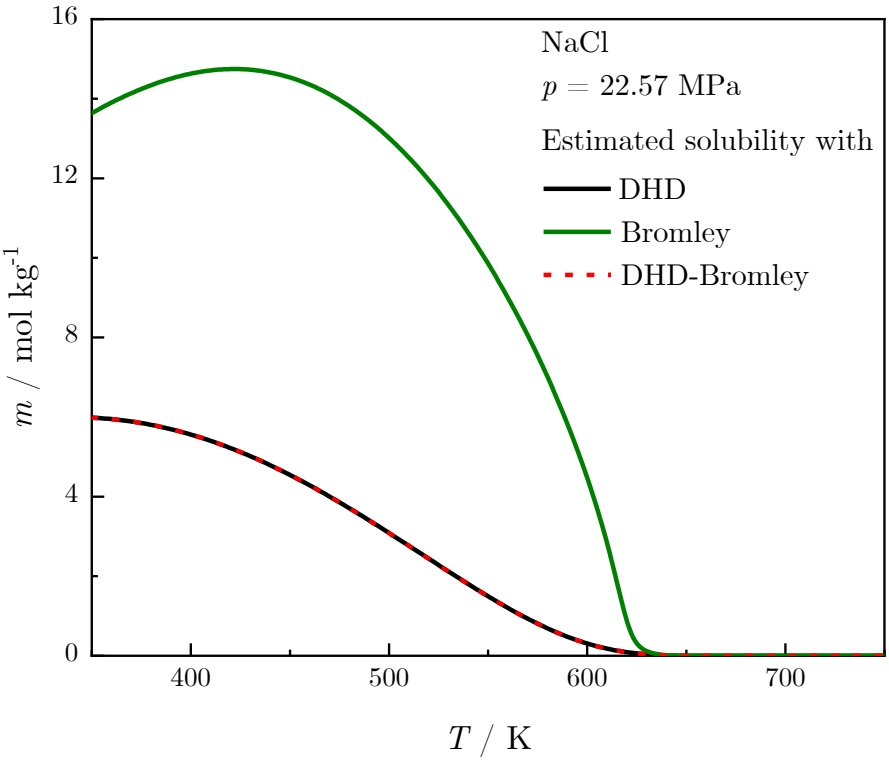

Figure 6-8: Estimated molality of NaCl as a function of temperature for a pressure of 22.57 MPa with different activity coefficient models. The solid black line shows the estimated solubility with the use of the Debye-Hückel-Davies (DHD) equation, the green line with the Bromley model, and the orange dashed line the combination out of the DHD model and the Bromley model. The equilibrium constants were calculated with the SAA model [147].

The black and the green line represent the DHD and the Bromley model. The orange dashed line shows the combination of both models. Especially in the sub- and nearcritical region, the difference between both models is significant. The Bromley model's estimated solubility increases up to temperatures of 420 K and then decreases drastically. The use of the DHD model shows a decreasing solubility of NaCl with increasing temperature. Up to a temperature

of 620 K, both models result in a substantial difference in the estimated solubility. The values for the solubility are two times larger for the Bromley model than for the DHD model. The valid range of the model leads to these differences. The DHD model is accurate up to an ionic strength of 0.1 mol kg^1. In contrast to that, the Bromley model is valid up to ionic strengths of 6 mol kg^{-1}. For the estimation of the solubility presented in this work, both models exceed their valid range. The limitations for both models were set for low pressures. This results in uncertainties for the near- / supercritical region. According to Figure 6-8, the solubility trend estimated with the DHD model results in values fitting to literature in the sub- / nearcritical area. The Bromley model shows good accordance in the supercritical region. This leads to the combination of both models for the estimation of the metal salt solubility. As already mentioned, the green dotted line shows the trend of the estimated solubility with both activity coefficient models. The DHD model is applied up to temperatures of 630 K, whereas the Bromley model is used for elevated temperatures up to 900 K.

6.3.1 Comparison of the estimated metal salt solubility with literature data

The estimated solubilities of the investigated metal salts NaCl, $CaCl_2$, and Na_2SO_4 were compared to data published in literature. The published solubility data are often found as a function of density. In comparison to that, published solubilities as a function of pressure and temperature are available. For higher pressures, some experimental data are published. Therefore, the trends of the solubility were estimated for higher pressures and then compared. First, the estimated solubility of NaCl is compared with higher pressures of 50 MPa and 100 MPa. As already mentioned, NaCl is a well-investigated metal salt, and specific experimental data are available for near- / supercritical temperatures and high pressures. Figure 6-9 shows the trends of the estimated solubility of NaCl as a function of temperature for different pressures and data published in literature:

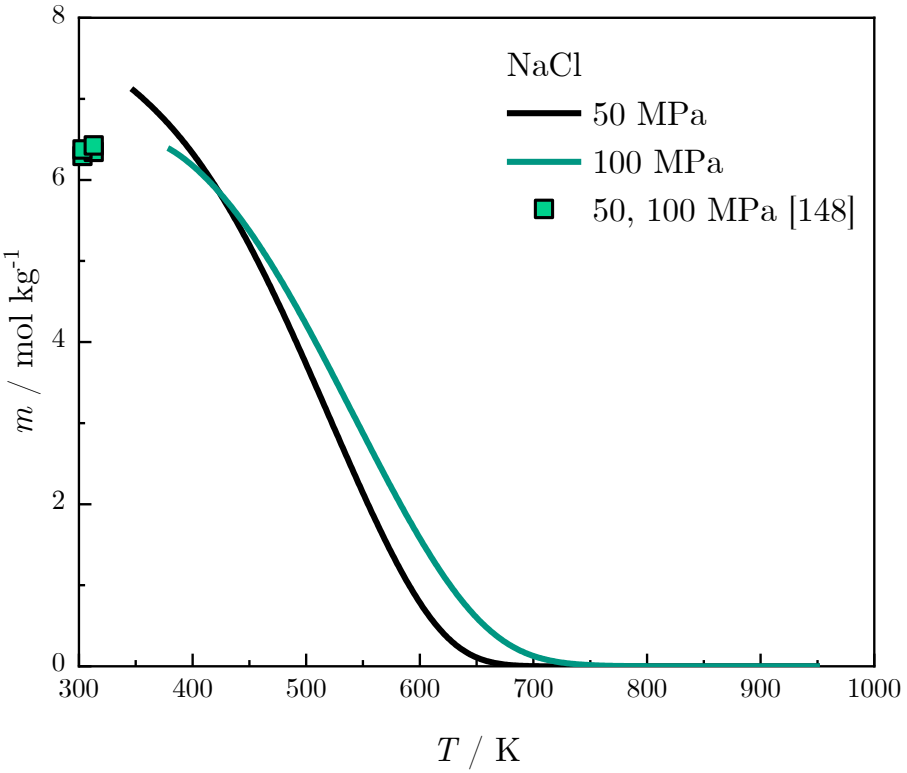

Figure 6-9: Estimated molality of NaCl as a function of temperature for different pressures with experimental data taken from [148]. The equilibrium constants were calculated with the SAA model [147].

Due to the normalized density of 0.997 g cm^{-3}, the estimation of the solubility starts at temperatures around 350 K. In contrast to that, literature data were determined for lower temperatures of 300 K – 310 K and pressures of 50 MPa and 100 MPa, respectively. The figure reflects the accuracy of the model. The solubility was estimated using the DHD model. The model overestimates the solubility for low temperatures and pressures of 50 MPa and 100 MPa. Nevertheless, the comparison of the estimated solubility with the experimental data is used for a first evaluation due to the correct tendency of the estimated solubility. The deviation between the values decreases with increasing pressure. Beyond that, the estimated solubility was compared with experimental data in the relevant region of the CHTS process:

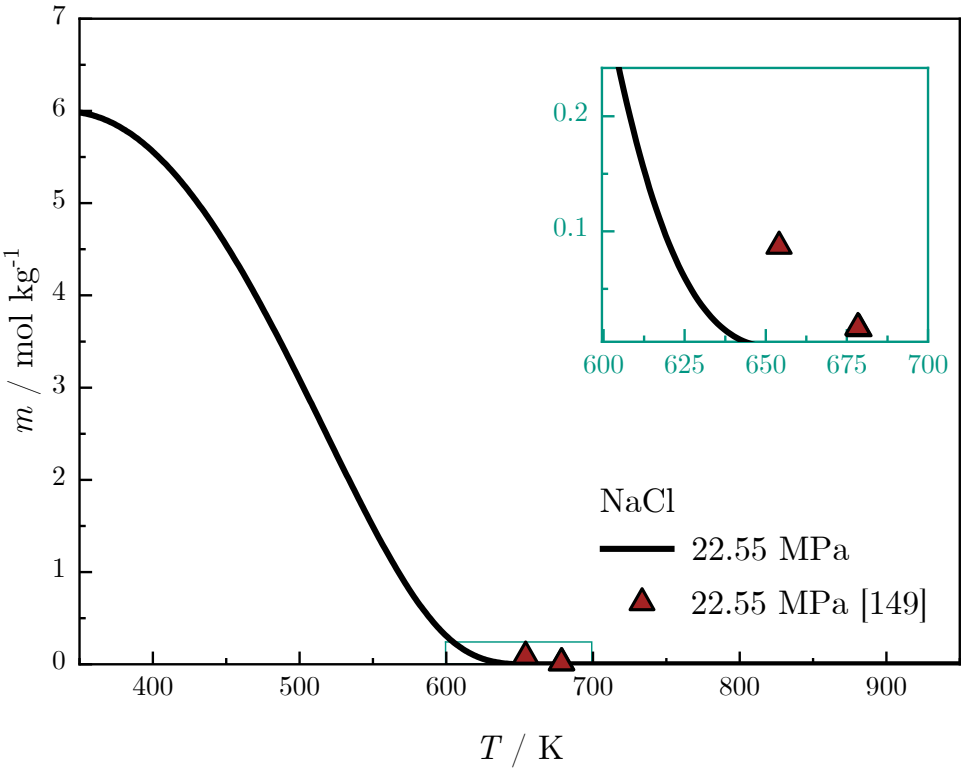

Figure 6-10: Estimated molality of NaCl as a function of temperature for a pressure of 22.55 MPa compared with experimental data taken from Leusbrock et al. [149]. The equilibrium constants were calculated with the SAA model [147].

The experimental data were determined for supercritical conditions for a pressure of 22.55 MPa and temperatures between 654 K and 679 K. The error for these values is 0.02 MPa and 0.45 K – 0.65 K, according to Leusbrock et al. [149]. The deviation between the estimated solubility and the experimental data (zoom in the top right corner of Figure 6-10) is significant. The error of the calculated solubility exceeds the experimental uncertainty. The solubility is underestimated in that region. There are three possible reasons for this problem. The calculated equilibrium constants are close to zero in that region (10^{-14}). In addition to that, the DHD model only considers the short-term Coulomb interactions. The long-term interactions are just implemented with an empirical extension. Another explanation is the assumption of an ideal behavior of the neutral species (activity coefficient equals to 1 for the dissolved and the solid NaCl). The use of the Bromley model (compare the combination of both activity coefficient models) leads to an improvement. Nevertheless, the deviation is still significant.

After comparing the estimated solubility of NaCl with literature data, the trends of $CaCl_2$ and Na_2SO_4 are validated:

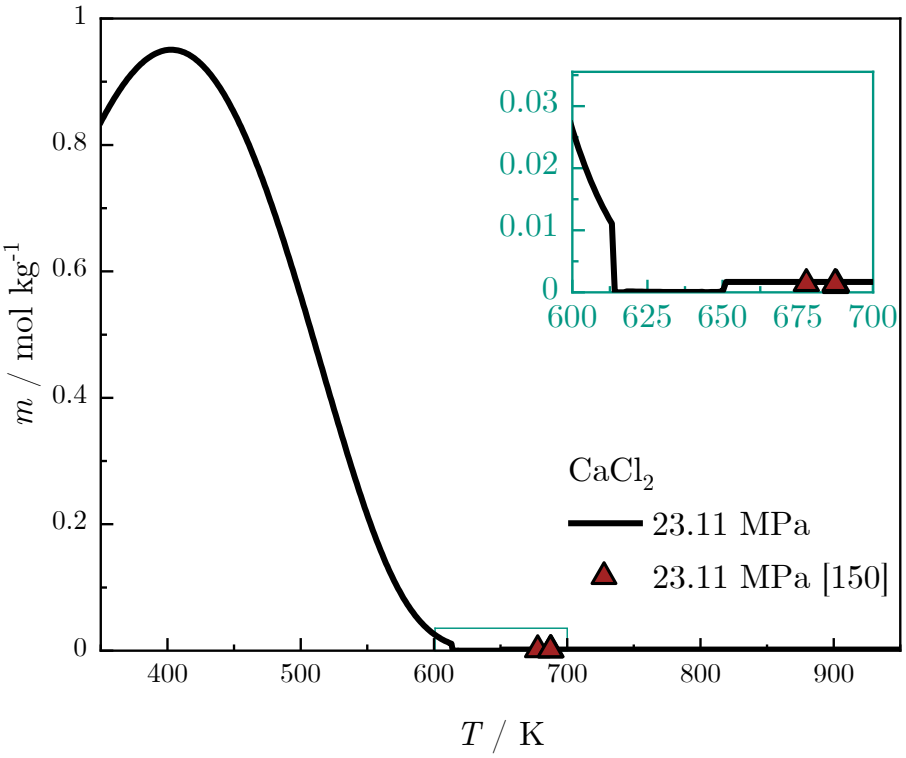

Figure 6-11: Estimated molality of $CaCl_2$ as a function of temperature for a pressure of 23.11 MPa compared with experimental data taken from Leusbrock et al. [150]. The equilibrium constants were calculated with the SAA model [147].

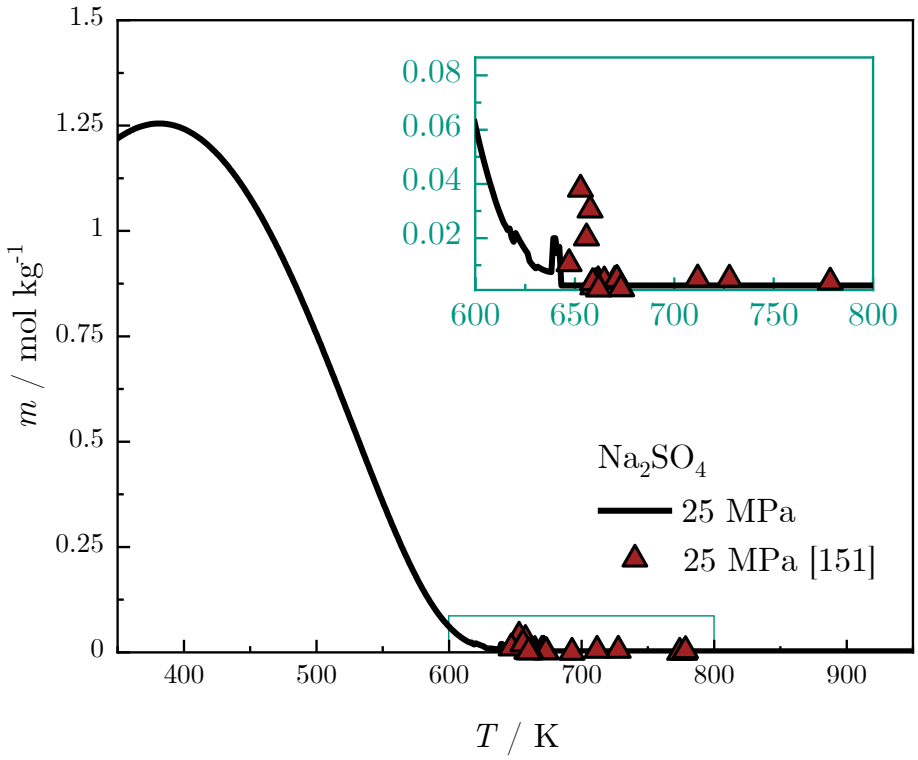

Figure 6-12: Estimated molality of Na_2SO_4 as a function of temperature for a pressure of 25 MPa compared with experimental data taken from Rogak et al. [151]. The equilibrium constants were calculated with the SAA model [147].

The $CaCl_2$ and Na_2SO_4 solubility were estimated with the DHD model as a function of temperature and a pressure of 23.11 MPa and 25 MPa. Both trends fit to the experimental data in the supercritical region. In both images, the trends show kinks due to density fluctuations around the critical point of H_2O.

After the validation of the equilibrium constants calculated with the r-HKF and the SAA model and the trends of the solubilities, other metal salts were investigated. The results are summarized in Table 6-1 for pressures of 25 MPa and 35 MPa and temperatures of 573 K and 673 K.

Table 6-1: Estimated molality for different types of metal salts.

type 1	m / mol kg^{-1}		m / mol kg^{-1}	
	573 K		673 K	
	25 MPa	35 MPa	25 MPa	35 MPa
NaBr	1.22	1.41	$2.20 \cdot 10^{-5}$	0.01
KBr	1.45	1.63	$4.38 \cdot 10^{-5}$	0.01
KCl	1.59	1.79	$8.63 \cdot 10^{-5}$	0.01
KNO_3	1.64	1.80	$4.41 \cdot 10^{-5}$	0.03

$NaNO_3$	1.34	1.50	$1.49\ 10^{-8}$	0.01

type 2	m / mol kg^{-1}		m / mol kg^{-1}	
	573 K		673 K	
	25 MPa	35 MPa	25 MPa	35 MPa
K_2SO_4	0.47	0.56	0.005	0.01
NaF	0.03	0.04	$2.64 \cdot 10^{-10}$	$6.02 \cdot 10^{-5}$

The results show the difference between type 1 and type 2 metal salts and their respective solubility in the near- / supercritical region. The metal salt solubilities are lower in the supercritical state (673 K) compared to the nearcritical state (573 K). An increase in the pressure leads to a rise in the metal salt solubility. These results enable the calculation of the supersaturation with pressure and temperature dependency and a further prediction of the particle size during the particle formation through precipitation.

The modeling of the metal salt solubility was carried out with a developed model. First, the equilibrium constants were calculated using the r-HKF and the SAA model. These values were further used in combination with the activity coefficient models in an iterative calculation of the molalities. The classification of the metal salts into either type 1 or type 2 was validated with the estimated metal salt solubility. Every step was validated with experimental data. In a final step, the routine was applied to estimate different metal salts for other pressures as a function of temperature.

7. Experimental results – Synthesis of ceria nanoparticles

In the following, the experimental results are described and discussed. After the setup of the CHTS plant, it was characterized with specific stability tests of the process conditions. After that, mixing experiments were carried out. Then three cerium salts were used for the particle formation and the investigation of the process conditions on the resulting particle size and shape.

Once the CHTS plant was characterized and the stability tests carried out, particle formation experiments were performed. The results for the characterization of the CHTS plant is shown in Appendix chapter 7 A: Characterization of the CHTS plant. First, preliminary experiments were carried out to compare the size of the synthesized nanoparticles with particle sizes published in literature. Then, further experiments with $Ce(NO_3)_3 \cdot 6\ H_2O$ (in the following $Ce(NO_3)_3$) as precursor were carried out to investigate the influence of the process parameters on the resulting particle size, shape, and the relating particle size distribution. Beyond that, the metal salt was changed from $Ce(NO_3)_3$ to $Ce_2(SO_4)_3 \cdot 8\ H_2O$ (next $Ce_2(SO_4)$). The influence of the change in the ion on the particle size and shape should be obtained. Specific experiments were then performed also to study the impact of the process conditions. As a last metal salt, $Ce(CH_3COO)_3 \cdot 1.5\ H_2O$ (next $Ce(CH_3COO)_3$) was used for the synthesis of ceria nanoparticles. In the following, the mentioned experiments concerning the different metal salts will be described in more detail. Table 7-1 – Table 7-3 represent an overview of all performed experiments.

Table 7-1: Overview of the performed experiments with $Ce(NO_3)_3$ as precursors and process conditions.

$Ce(NO_3)_3$	exp. no.	p / MPa	T_3 / K	$\dot{m}_3$ / g min^{-1}	a / -	c_{salt} / mol dm^{-3}
	1	30	673	35	0.1	0.005
	2	30	673	35	0.1	0.05
	3	30	673	35	0.1	0.15
	4	30	673	45	0.1	0.05
	5	30	673	55	0.1	0.05
	6	30	573	35	0.1	0.1
	7	30	573	35	0.1	0.15
	30	25	673	35	0.1	0.05
	31	25	673	35	0.1	0.005
	33	25	673	45	0.1	0.05
	34	25	673	35	0.1	0.15

Table 7-2: Overview of the performed experiments with $Ce_2(SO_4)_3$ as precursors and process conditions.

$Ce_2(SO_4)_3$	exp. no.	p / MPa	T_3 / K	$\dot{m}_3$ / g min^{-1}	a / -	c_{salt} / mol dm^{-3}
	17	30	523	35	0.1	0.0125
	24	30	523	45	0.1	0.0125
	25	30	523	55	0.1	0.0125
	40	30	573	35	0.1	0.00625
	41	30	573	45	0.1	0.00625
	54	30	523	35	0.1	0.00625

Table 7-3: Overview of the performed experiments with $Ce(CH_3COO)_3$ as precursors and process conditions.

$Ce(CH_3COO)_3$	exp. no.	p / MPa	T_3 / K	$\dot{m}_3$ / g min^{-1}	a / -	c_{salt} / mol dm^{-3}
	57	30	673	35	0.1	0.05
	58	30	673	35	0.1	0.005
	59	30	673	45	0.1	0.05
	60	30	673	55	0.1	0.05
	61	30	573	35	0.1	0.05
	62	30	573	45	0.1	0.05
	64	30	573	55	0.1	0.05
	65	30	523	35	0.1	0.05
	66	30	473	35	0.1	0.05
	67	30	423	35	0.1	0.05
	69	30	523	45	0.1	0.05
	71	30	523	55	0.1	0.05
	72	30	473	45	0.1	0.05
	73	30	473	55	0.1	0.05
	74	30	423	45	0.1	0.05
	75	30	423	55	0.1	0.05

7.1 Preliminary experiments

At first, experimental results from literature were considered. The process conditions in these experiments were applied in the CHTS plant. Three different preliminary experiments were carried out with a variation in the metal salt concentration. It was varied between 0.005 mol dm^{-3}, 0.05 mol dm^{-3}, and 0.15 mol dm^{-3}. Table 7-4 shows the process conditions and their respective standard deviation:

Table 7-4: Process conditions with respective standard deviation for the duration of the particle formation experiment of ceria nanoparticles wit $Ce(NO_3)_3$ as precursor [58].

	exp. no. 1	exp. no. 2	exp. no. 3
p / MPa	30.1 ± 0.2	30.1 ± 0.1	30 ± 0.1
T_3 / K	673.0 ± 0.2	673.0 ± 0.2	673.0 ± 0.2
$\dot{m}_3$ / g min^{-1}	35.1 ± 0.6	35.6 ± 0.6	35.1 ± 1.0
a / -	0.1	0.1	0.1
c_{salt} / mol dm^{-3}	0.005	0.05	0.15
$c_{product}$ / mol dm^{-3}	$4.5 \cdot 10^{-4}$	$4.5 \cdot 10^{-3}$	$1.4 \cdot 10^{-2}$

As previously shown in the characterization of the pilot plant (compare Appendix chapter 7A: Characterization of the CHTS plant), the process conditions remained constant, and a stable process was guaranteed. The product concentration $c_{product}$ was estimated by a complete conversion from $Ce(NO_3)_3$ to CeO_2 with the reaction's stoichiometry (compare equation (2-34)). The results of these experiments analyzed with TEM images are illustrated in Figure 7-1:

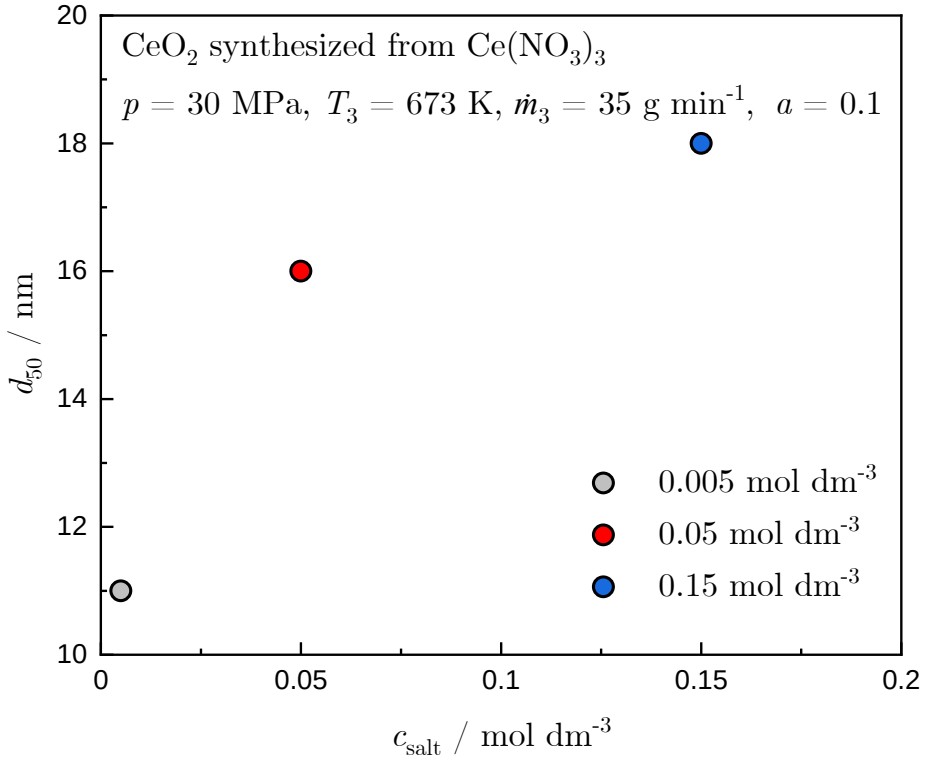

Figure 7-1: Experiments after the setup of the CHTS plant, variation of the metal salt concentration (p = 30 MPa, T_3 = 673 K, $\dot{m}_3$ = 35 g min^{-1} and a = 0.1).

As previously mentioned in section 2.2, the Reynolds number (Re) is a dimensionless number used to describe different flow situations. Beyond that, it is practicable for the scaling of flow phenomena for other sized models.

$$\mathrm{Re} = \left(\frac{\rho\ u\ d_\mathrm{m}}{\eta}\right) = \left(\frac{4\ \dot{m}_3}{\pi\ d^2\ \nu}\right) \tag{7-1}$$

For the process conditions pressure p of 30 MPa, the mixing temperature T_3 of 673 K, the total mass flow $\dot{m}_3$ of 35 g min^{-1}, the mixing ratio a of 0.1, and a respective inner diameter of the mixer of 1.6 mm, Re results in 10522 and the mean residence time τ of 0.73 s for all three experiments. In general, the mean particle size increases with increasing salt concentration c_{salt}. Concerning the nucleation theory (compare section 2.2, equations (2-22), (2-26) and (2-27)), the supersaturation S rises with increasing salt concentration c_{salt}. Due to this, the Gibbs free energy of formation ΔG^* and the critical radius r^* of the nucleus are decreasing. These effects increase the nucleation rate J. This generally leads to a decrease of the critical radius r^* with increasing salt concentration c_{salt}. For equation (2-22), the number of formed particles as a function of time and volume rises with increasing salt concentration c_{salt}. Due to the static T-shaped mixer with a constant volume V, the mean distance between the produced particles decreases with the increasing number of particles. The particle interaction is enforced, and particle growth is preferred. These effects lead to an increase in the median particle size d_{50} with increasing salt concentration c_{salt}.

With increasing salt concentration c_{salt}, the number of particles in the suspension is expanding. The increasing turbidity of the suspension expresses this effect. The particle concentration in the suspension is crucial for the further analysis of the particles. As described in section 3.2.1 the study with PXRD requires a certain amount of dry ceria nanoparticles. For the low salt concentration c_{salt} of 0.005 mol dm^{-3}, the suspension was very dilute. It was not possible to dry enough ceria nanoparticles for the analysis with PXRD. For the higher concentrations of 0.05 mol dm^{-3} and 0.15 mol dm^{-3}, the particles suspension was centrifuged, oven-dried, and then analyzed with PXRD. Figure 7-2 shows the results for these two experiments and commercial CeO_2:

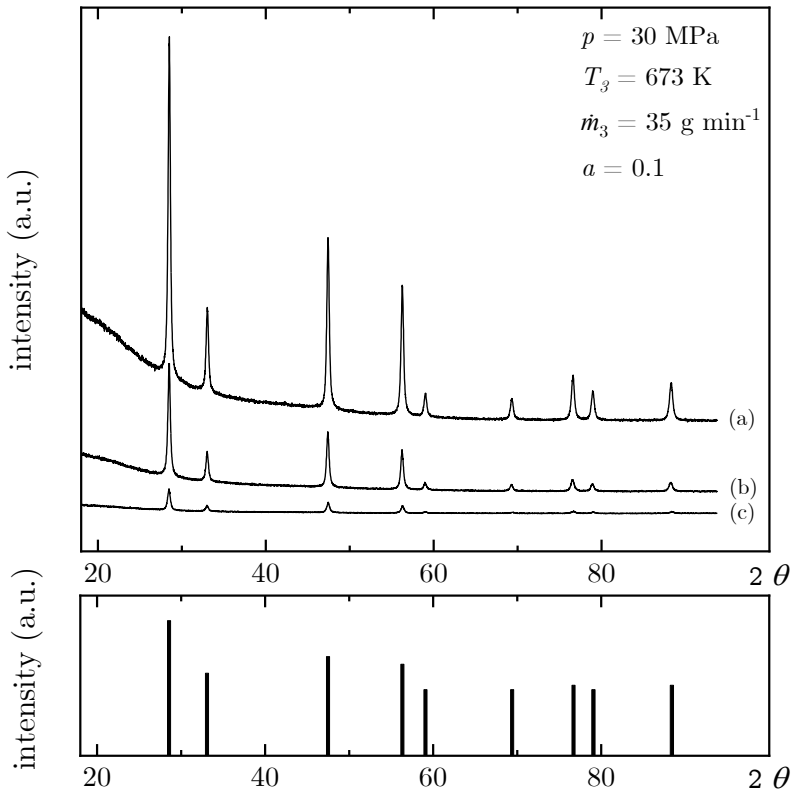

Figure 7-2: Image of the PXRD pattern of dry particles with the salt concentration c_{salt} of 0.05 mol dm^{-3} (a), 0.15 mol dm^{-3} (b), and commercial CeO_2 (c). The peaks detected with phase reference data are from the International Center for Diffraction Data (below).

Both PXRD patterns of the dried particles with the concentration of 0.05 mol dm^{-3} (a) and 0.15 mol dm^{-3} (b) are in good agreement with the reference data peaks. The commercial ceria nanoparticles are also showing a good agreement. These results indicate that ceria nanoparticles were formed during the experiments. Based on the highest intensity peaks, the Scherrer-equation (compare equation (3-2) in Appendix chapter 3) was applied to determine the crystallite size of the particles.

In addition to the PXRD analysis, the nanoparticles were analyzed with TEM images and the previously described routine (compare section 3.2.2). TEM and the PXRD analysis prove the possibility to synthesize ceria nanoparticles with the setup CHTS plant in the range between 10 nm and 20 nm. The related TEM images of the first experiments are illustrated in the following:

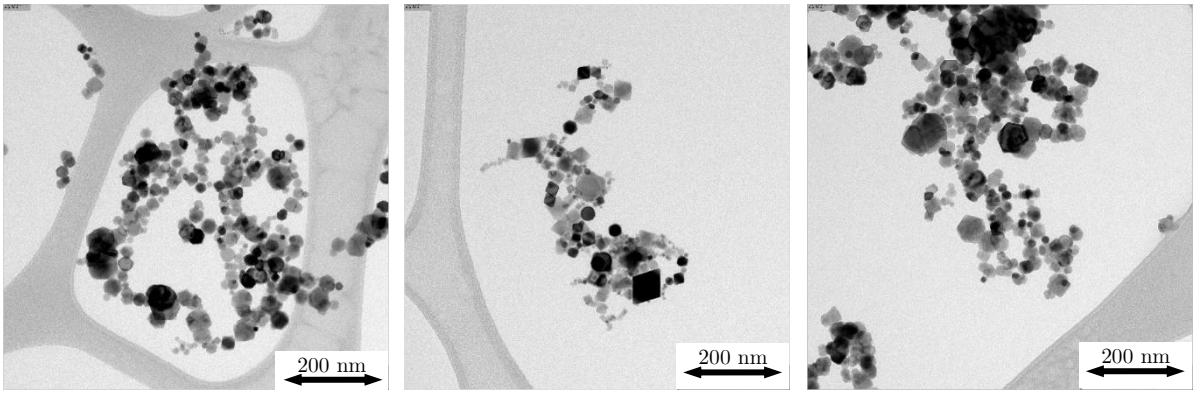

Figure 7-3: TEM images of the validation experiments with ceria nanoparticles synthesized with $Ce(NO_3)_3$ for three different salt concentrations c_{salt} 0.005 mol dm^{-3} (d_{50} = 11 nm, top left), 0.05 mol dm^{-3} (d_{50} = 16 nm, top right), and 0.15 mol dm^{-3} (d_{50} = 18 nm, bottom centered) with a scale bar of 200 nm. The process conditions were set to a pressure p of 30 MPa, a temperature of 673 K, a total mass flow $\dot{m}_3$ of 35 g min^{-1}, and a mixing ratio a of 0.1.

In literature, Daschner de Tercero [27], Aoki et al. [28], and Hakuta et al. [13] synthesized ceria nanoparticles with related process conditions. The mixing geometry applied in the CHTS plant was the Counter setup (compare section 2.2, Figure 2-6). In contrast to that, Daschner de Tercero used a T-mixer with the Straight-setup. The process conditions pressure p, mixing temperature T_3, and mixing ratio a remained the same in both experiments. The residence time τ was equal below 1 s. Next to the constant process conditions, the mass flows $\dot{m}_1$, $\dot{m}_2$ and $\dot{m}_3$ and the inner diameter of the tubes showed different values within the experiments. For the comparison of the experiments, Re at the mixing point was evaluated. The mean diameter of the particles for a salt concentration c_{salt} of 0.05 mol dm^{-3} and Re of 16700 was between 33 nm and 42 nm. Aoki et al. synthesized ceria nanoparticles with different process conditions [28]. The experiments with a mixing temperature T_3 of 653 K and a T-shaped mixer with an inner diameter of 1.3 mm are comparable. For these experiments, the Bending setup was applied. The pressure p was set to 30 MPa, the mixing ratio a to 0.36, and the salt concentration to 2 mol dm^{-3}. For Re of 5500, the mean particle diameter resulted in 18 nm. Hakuta et al. carried out particle formation experiments for CeO_2 with a pressure p of 30 MPa, a mixing temperature T_3 of 673 K, and a mixing ratio a of 0.33 [13]. The median particle size resulted in 20 nm. As a summary of the preliminary experiments, the synthesized particles with the CHTS plant showed a similar size to those mentioned in literature.

7.2 Experiments with cerium(III)nitrate-hexahydrate

After performing experiments with the constructed and setup CHTS plant, and the comparison with literature data [13,27,28], further experiments with $Ce(NO_3)_3$ as a precursor were carried out. The focus of the investigations was on the examination of the influence of the process conditions pressure p, mixing temperature T_3, and total mass flow $\dot{m}_3$ on the resulting particle size and shape. As previously described, increasing the salt concentration c_{salt} lead to an increase

in the median particle size d_{50}. In the following, the single influence of the previously mentioned process conditions is described. The variation of the salt concentration leads to changes in the supersaturation and the nucleation rate. The pressure p and the mixing temperature T_3 affect the reaction kinetics. As described in section 2.2, two consecutive reactions occur during the CHTS (equation (2-31) and (2-32)). Due to the low solubility of metal salts in the near- / supercritical region and the related high temperatures, the reactions occur. The reaction rate is described with an Arrhenius Born type equation (2-35), a function of temperature and dielectric constant. The dielectric constant itself is a function of pressure and temperature, and it is not affected by the pressure in the subcritical region (compare Figure 2-7). Especially in the near- / supercritical region, the rate constant is increasing drastically, which leads to very high reaction rates for a mixing temperature T_3, for example of 673 K. Here, a pressure decrease leads to an increased reaction rate. This deals with the critical pressure. The closer the pressure to the critical pressure of water, the lower the dielectric constant value. With increasing pressure, the dielectric constant increases for a constant temperature due to the rise in the density (compare Figure 2-7). Figure 7-4 shows the results for a decrease of the pressure p from 30 MPa to 25 MPa with the same variation of the salt concentration c_{salt} as previously described for a pressure p of 30 MPa. The mixing temperature T_3, the total mass flow $\dot{m}_3$ and the mixing ratio a remained constant.

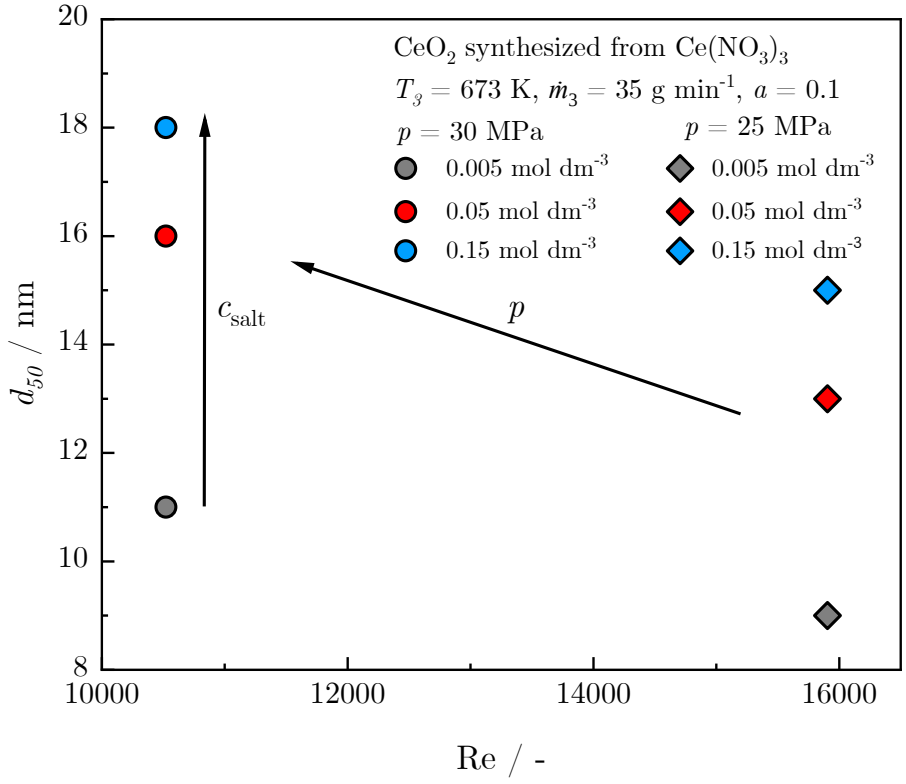

Figure 7-4: Median particle size d_{50} as a function of Re for the given constant process conditions. The pressure p was lowered from 30 MPa to 25 MPa, and the salt concentration

c_{salt} was varied according to the previous experiments for 0.005 mol dm^{-3}, 0.05 mol dm$^{-3,}$ and 0.15 mol dm^{-3}.

The dependence of the median particle size d_{50} on the used salt concentration c_{salt} is the same for a lower pressure p of 25 MPa. In general, the particle size d_{50} is decreasing with decreasing pressure p. This is caused by an increase in the rate constant due to a decrease in the dielectric constant. Another effect caused by the reduction of the pressure p is the decrease of the water density ρ. This increases the flow velocity v_3 of the mixing stream.

$$v_3 = \frac{4\,\dot{m}_3}{\pi {d_m}^2 \rho} \tag{7-2}$$

$$\tau = \frac{V}{\dot{V}} = \frac{V}{\dot{m}}\,\rho(p,T) \tag{7-3}$$

The increase of v_3 results in a decrease in the mean residence time τ of 0.34 s (compare equation (7-3)), and an increase of Re of 15900 (compare equation (7-1)). Both effects lead to the decrease in the median particle size d_{50} for a lower pressure p of 25 MPa. With this pressure and the salt concentration c_{salt} of 0.005 mol dm^{-3}, it is possible to synthesize ceria nanoparticles with a size below 10 nm.

Besides the variation of the salt concentration c_{salt} and the pressure p, the change of the mixing temperature T_3 has another particular effect on the median particle size d_{50}. In the same way, as the pressure p (pressure dependence of the rate constant at temperatures $> T_c$), the mixing temperature T_3 affects the rate constant k over the whole temperature range, as visible in equation (2-35) and Figure 2-8. As previously described, the rate constant is slightly increasing linearly with increasing temperature in the subcritical range. Approaching the critical point, both the density and the dielectric constant decrease drastically (compare Figure 2-2), leading to a rapid increase of the rate constant. Figure 7-5 images the effect of the mixing temperature T_3 on the median particle size d_{50}.

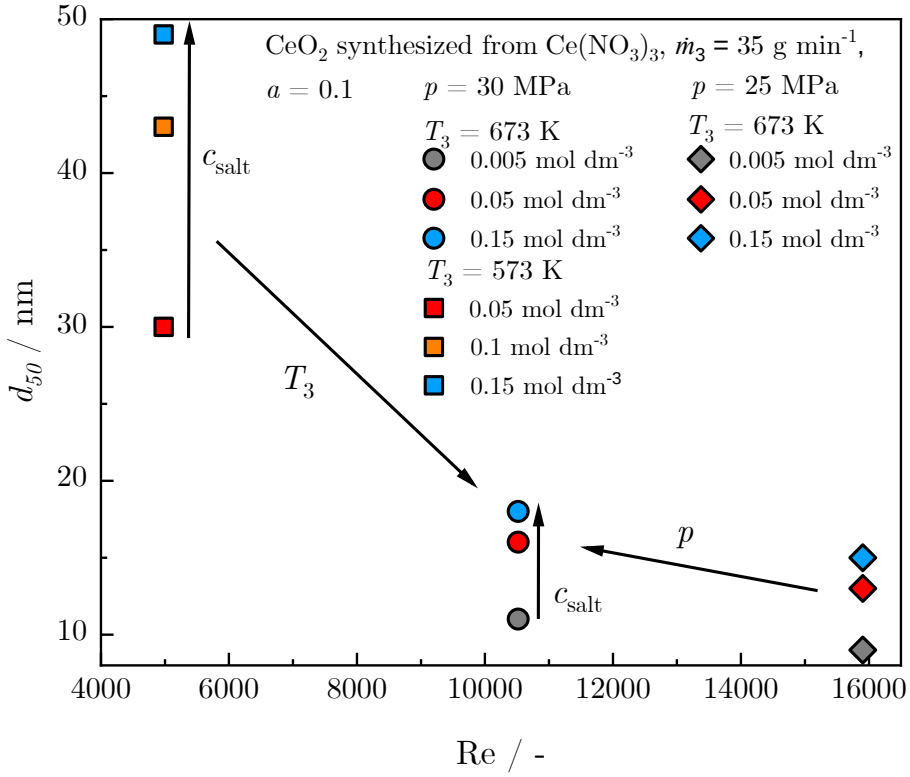

Figure 7-5: Median particle diameter d_{50} as a function of Re with the process conditions of p = 25 MPa and 30 MPa, T_3 = 573 K and 673 K, a total mass flow $\dot{m}_3$ = 35 g min^{-1}, a mixing ratio a = 0.1 and a variating salt concentration c_{salt} between 0.005 mol dm^{-3} and 0.15 mol dm^{-3}.

For the decrease of the mixing temperature T_3 from 673 K to 573 K, the rate constant decreases and the density increases for a constant pressure p of 30 MPa. The increase of the density leads to a decrease in the flow velocity v_3 resulting in lower values of Re (4980) and longer mean residence times τ (1.53 s). In addition to these effects, the salt solubility is higher at 573 K compared to mixing temperatures of 673 K. The combination of all these effects leads to lower supersaturation values, a lower nucleation rate, longer time in the hot reaction zone for particle growth and results in larger particle sizes. As already mentioned, the particle size increases with decreasing mixing temperature T_3 from 673 K to 573 K from 18 nm to 49 nm (c_{salt} = 0.15 mol dm^{-3}). Next to the median particle size, the particle size distribution (PSD) is also essential for the quality of the synthesized nanoparticles. Figure 7-6 shows the PSD for the two different mixing temperatures T_3 of 573 K and 673 K:

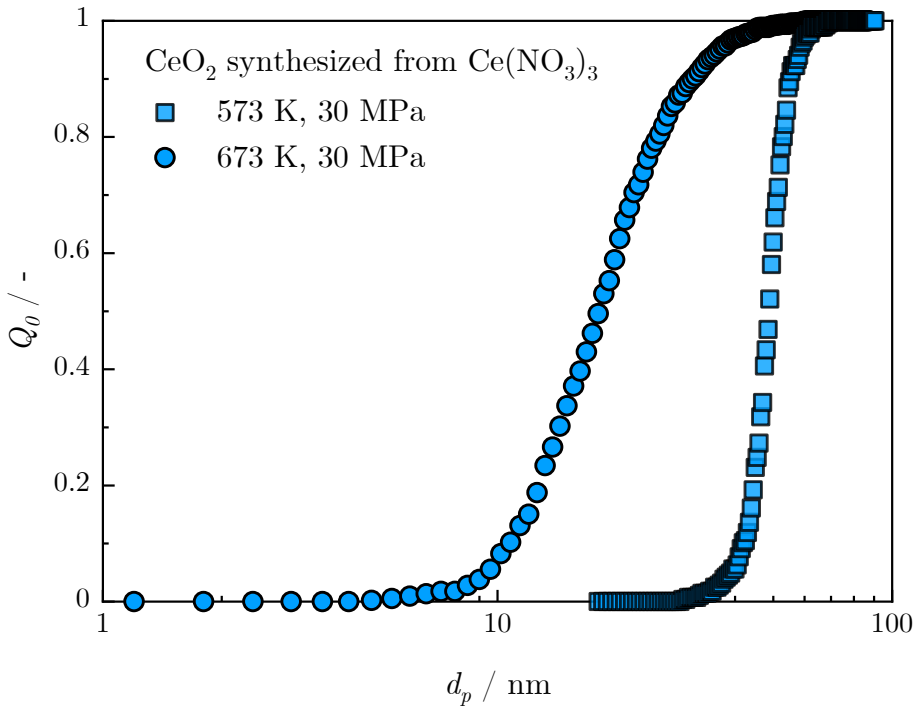

Figure 7-6: Trend of the number density Q_0 as a function of the mean particle size d_p for two different mixing temperatures and constant process conditions of $p = 30$ MPa, $\dot{m}_3 = 35$ g min^{-1}, $a = 0.1$ and $c_{salt} = 0.15$ mol dm^{-3}.

The PSD is different next to the fact that the particle size decreases with increasing mixing temperature T_3. For the near-critical mixing temperature T_3 of 573 K, the PSD is narrower than for the supercritical temperature of 673 K. The ceria nanoparticles show a larger variation in the particle size for the higher temperature for the smaller particle size. This is caused by the high amount of energy provided through the high temperature, the increased flow velocity, and the low mean residence time compared to 573 K. On the one hand, many particles are formed simultaneously due to the high nucleation rate. Collisions occur inside the mixer and the hot reaction zone through the decrease in the mean distance between the formed particles. These forced particle interactions lead to the formation of different-sized particles. The high rate constant, the high nucleation rate, and the short mean residence time lead to less time for particle growth. In the near-critical region (573 K), the metal salt solubility is higher compared to the supercritical region (673 K). This results in lower values for the supersaturation and a lower nucleation rate. Furthermore, the higher density leads to a decrease of the flow velocity v_3 and an increase of the mean residence time τ. The formed particles remain longer in the hot reaction zone where particle growth occurs. These effects result in the formation of larger, and narrow distributed particles. The width of the PSD is defined as follows:

$$\Delta = \frac{d_{90} - d_{10}}{d_{50}} \tag{7-4}$$

In this equation, the characteristic values of the PSD d_{10}, d_{50}, and d_{90} are correlated. The respecting values for Δ are 1.11 (673 K) and 0.27 (573 K). The results of the difference in the PSD are further directly visible from TEM images.

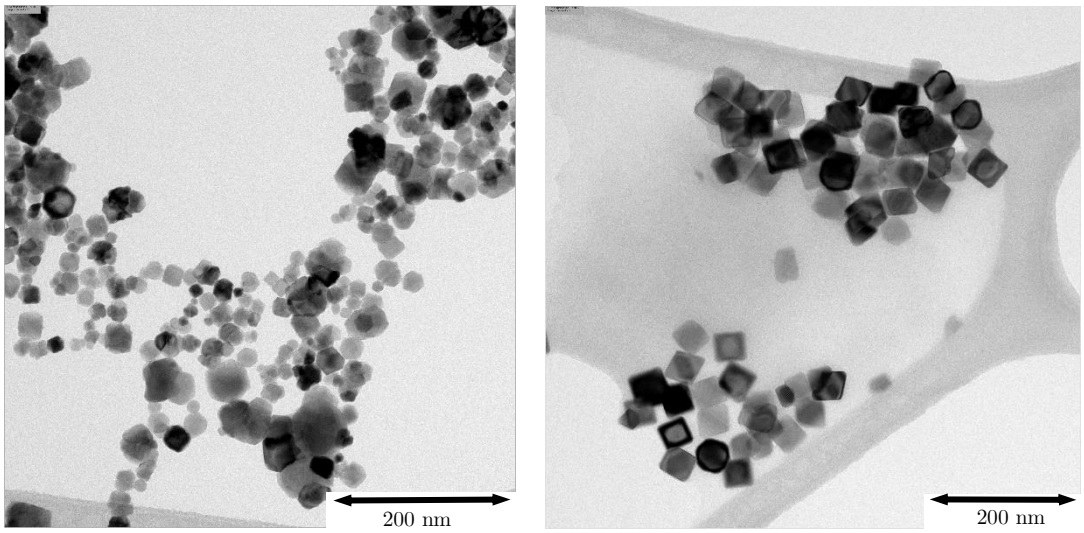

Figure 7-7: TEM images of ceria nanoparticles synthesized with $Ce(NO_3)_3$ for two different mixing temperatures T_3 of 673 K (d_{50} = 18 nm, left) and 573 K (d_{50} = 49 nm, right) with a scale bar of 200 nm. The process conditions were set to a pressure p of 30 MPa, a total mass flow $\dot{m}_3$ of 35 g min^{-1}, a mixing ratio a of 0.1, and a salt concentration c_{salt} of 0.15 mol dm^{-3}.

The TEM images are the basis of the previously shown results. The analysis of these for the particle diameter results in the determination of d_{10}, d_{50}, and d_{90}. The images clarify the two main differences between the synthesized ceria nanoparticles. The nanoparticles show differences in size and their relating distribution. On the left image, small-sized nanoparticles are surrounded by larger nanoparticles leading to a broad PSD. Especially in the nanoscale region, the properties of the particles strongly depend on their related size. Therefore, homogeneous particles with a narrow PSD are required. On the right image, the homogeneously distributed particles with a defined size are obtainable, which can be used for further applications. Ideally, the synthesis of small-sized homogenous ceria nanoparticles (10 nm – 20 nm) with a supercritical mixing temperature T_3 is favorable. This aspect will be further discussed in the later sections.

Beyond the process conditions mentioned above, the total mass flow $\dot{m}_3$ is also affecting the mean particle size in combination with the mean residence time τ. Figure 7-8 shows the results for the variation of the total mass flow $\dot{m}_3$ for the different pressures p of 25 MPa and 30 MPa.

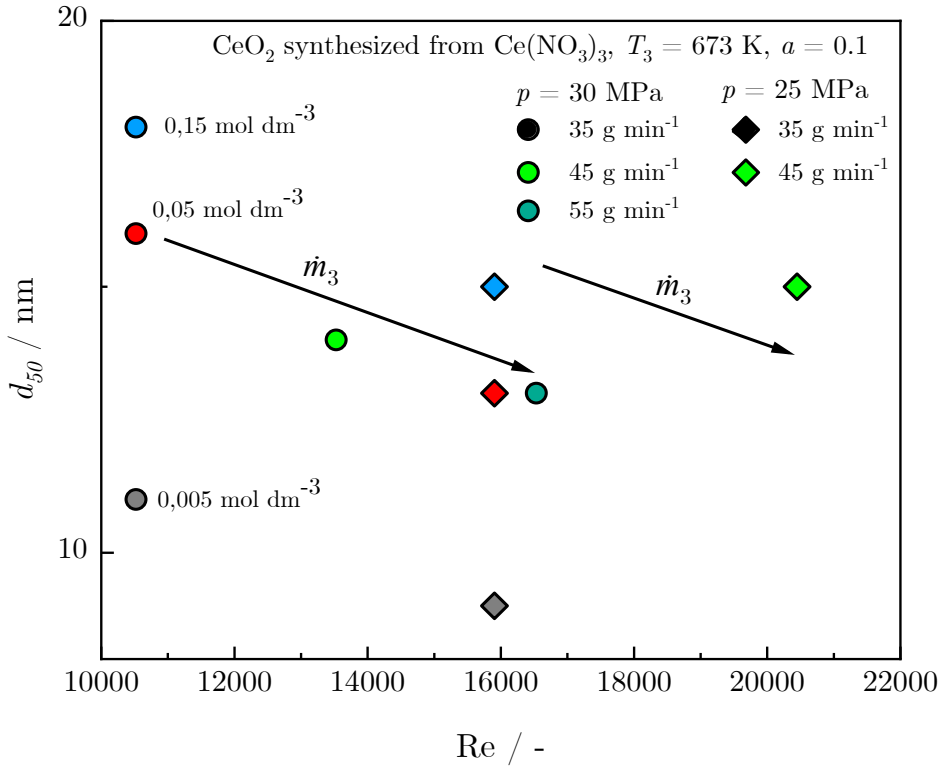

Figure 7-8: Trend of the median particle size as a function of Re for different pressures p of 25 MPa and 30 MPa and a mixing temperature T_3 of 673 K with a variation in the total mass flow $\dot{m}_3$. The grey, red, and blue colored symbols represent the different salt concentrations c_{salt} with 0.005 mol dm^{-3}, 0.05 mol dm$^{-3,}$ and 0.15 mol dm^{-3}, respectively. The green-colored symbols representing a total mass flow $\dot{m}_3$ of both 45 g min^{-1} and 55 g min^{-1} were carried out with the salt concentration c_{salt} of 0.05 mol dm^{-3}.

The increase of the total mass flow $\dot{m}_3$ leads to a decrease in the mean residence time τ (according to equation (7-3) and higher values for Re (compare equation (7-1). Due to the lower mean residence time τ, the particles have less time in the hot reaction zone. The median particle size for a pressure p of 30 MPa is decreasing for an increasing total mass flow of 45 g min^{-1} to 14 nm and 55 g min^{-1} to 13 nm, respectively. For a pressure p of 25 MPa and an increase to 45 g min^{-1}, the further increase does not affect the median particle size anymore due to the exceptionally high value of the rate constant for the lower pressure and values for Re over 20000. Experiments with a pressure p of 25 MPa and a total mass flow $\dot{m}_3$ of 55 g min^{-1} were not possible to conduct due to the high requirement of energy to heat the hot water stream $\dot{m}_2$ (compare equation (2-3). The heating unit could not provide the required heating power to heat the hot water stream $\dot{m}_2$ to 673 K for the higher total mass flow $\dot{m}_3$.

In total, the performed experiments with $Ce(NO_3)_3$ as a precursor were carried out to determine the influence of the single process parameters on the resulting particle size d_{50} and the respecting PSD.

As already explained Figure 7-6, the variation of the mixing temperature T_3 is affecting the PSD. The results of the PSDs with the variation of the salt concentration c_{salt} as well as the total mass flow $\dot{m}_3$ are discussed in the following images. Figure 7-9 shows the trend of the number density Q_0 as a function of the mean particle size d_p for a salt concentration c_{salt} between 0.005 mol dm^{-3} and 0.15 mol dm^{-3}:

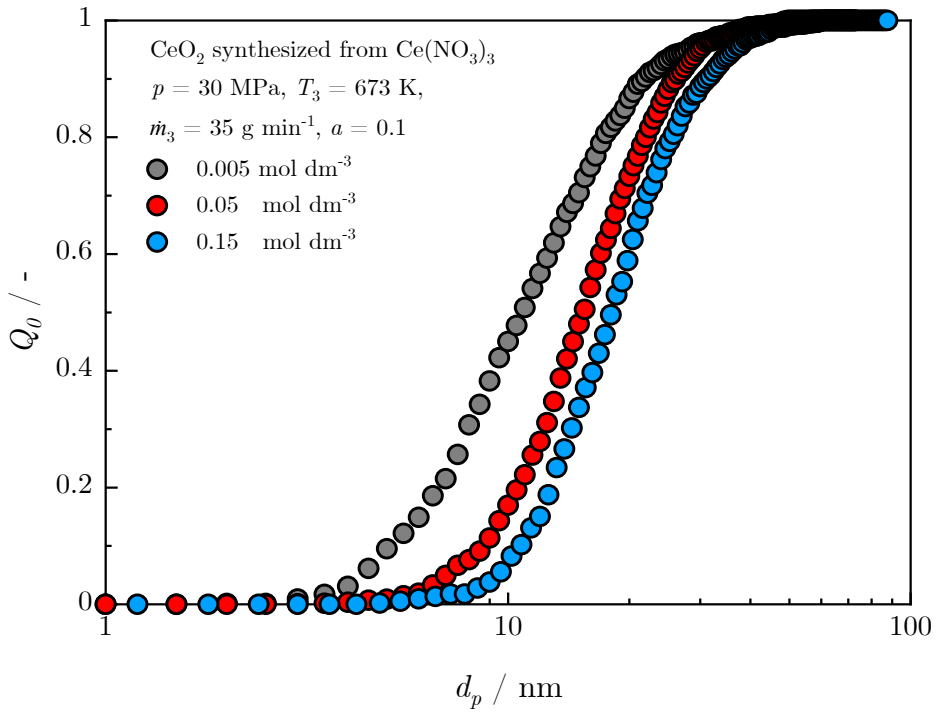

Figure 7-9: Trend of the number density Q_0 as a function of the mean particle size d_p for different metal salt concentrations c_{salt} and constant process conditions of $p = 30$ MPa, $T_3 = 673$ K, $\dot{m}_3 = 35$ g min^{-1}, and $a = 0.1$.

The width of the PSD Δ (compare equation (7-4)) is decreasing with increasing salt concentration c_{salt} from 1.50 ($c_{salt} = 0.005$ mol dm^{-3}) to 1.11 ($c_{salt} = 0.05$ mol dm^{-3} and 0.15 mol dm^{-3}). For higher salt concentration of 0.05 mol dm^{-3} and 0.15 mol dm^{-3}, respectively, the nanoparticles are more uniform compared to the lower salt concentration of 0.005 mol dm^{-3}. One reason for this could be the fast nucleation and low amount of metal salt for particle growth. This leads to the formation of different sized nanoparticles. Figure 7-10 shows the PSDs for three different total mass flow $\dot{m}_3$ between 35 g min^{-1} and 55 g min^{-1}:

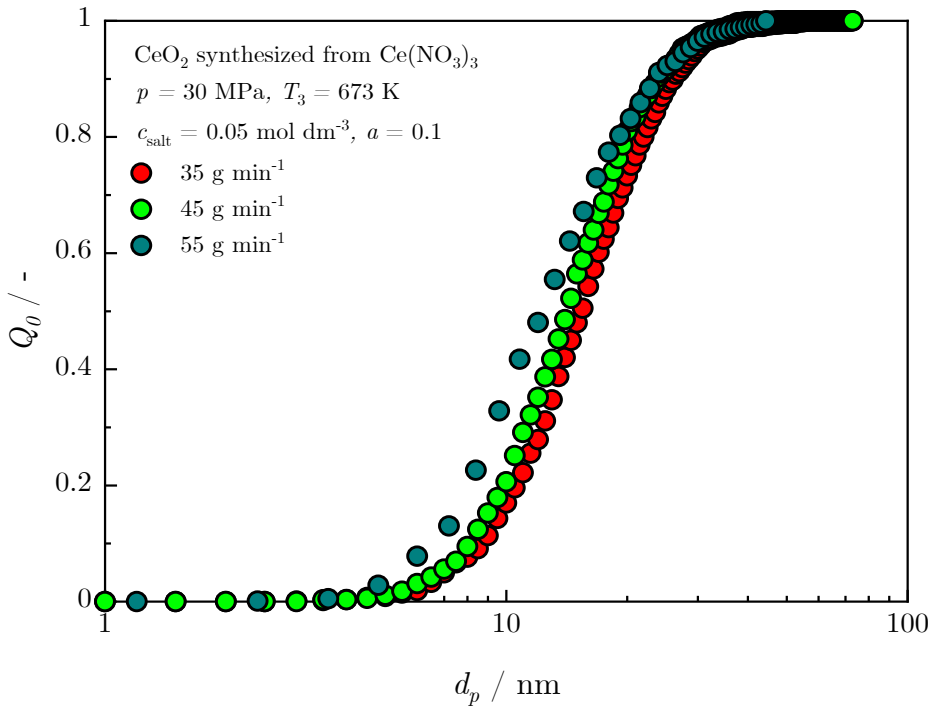

Figure 7-10: Trend of the number density Q_0 as a function of the mean particle size d_p for three different total mass flows $\dot{m}_3$ and constant process conditions of $p = 30$ MPa, $T_3 = 673$ K, $c_{salt} = 0.05$ mol dm^{-3}, and $a = 0.1$.

The width of the PSD is slightly increasing with increasing total mass flow $\dot{m}_3$ from 1.11 (35 g min^{-1}) and 1.09 (45 g min^{-1}) to 1.32 (55 g min^{-1}). The increasing total mass flow leads to a decrease of the mean residence time τ. Due to this fact, the time for particle growth and the formation of uniform particles is reduced. The consideration of the PSD is mainly important to evaluate the quality of the nanoparticles. Their usage in technical applications requires uniform particle sizes due to the size-dependence of their catalytic properties for example.

As shown above, the median particle size d_{50} is mainly influenced by the pressure p and the mixing temperature T_3, the total mass flow $\dot{m}_3$ and the salt concentration c_{salt}. Here, the pressure and the mixing temperature affect the rate constant of the reaction resulting in a change in the reaction time τ_r. An increase of the total mass flow $\dot{m}_3$ decreases the mean residence time τ while increasing the mixing time τ_m. The salt concentration c_{salt} is proportional to the supersaturation S what is relevant for the later particle formation. Both the reaction time τ_r and the mixing time τ_m are essential values for predicting the median particle size d_{50}. For the correlation of both values, the Damköhler number Da was implemented. In general, it is defined as the follows:

$$\mathrm{Da} = \frac{\tau_r}{\tau_m} \tag{7-5}$$

The reactions taking place during the CHTS process are assumed as first-order reactions. This enables to equalize the reaction time τ_r to the rate constant k. For the mixing time τ_m, a simple

correlation between the diameter of the mixer d_m and the flow velocity v_3 is used. τ_m is defined as the flow velocity v_3 divided by the diameter of the mixer d_m. Using both values for the respecting characteristic times equals in:

$$\mathrm{Da} = \frac{\tau_r}{\tau_m} = \frac{k d_m}{v_3} = \frac{\frac{\pi}{4}\, {d_m}^3 \rho(T,p)\, k(T,p)}{\dot{m}_3} \tag{7-6}$$

The rate constant k is calculated with the given constants and the dielectric constant at pressure p and temperature T with equation (2-35). The diameter of the mixer d_m is set constant to 1.6 mm. The flow velocity v_3 is calculated using equation (7-2) depending on the total mass flow $\dot{m}_3$ and density ρ at given pressure p and temperature T. Aoki et al. performed specific experiments regarding the kinetic behavior of the particle formation of CeO_2 with $Ce(NO_3)_3$ as a precursor [28]. The results shown in their work are correlated with the results shown in this work. Figure 7-11 images the comparison of the results of the experiments carried out:

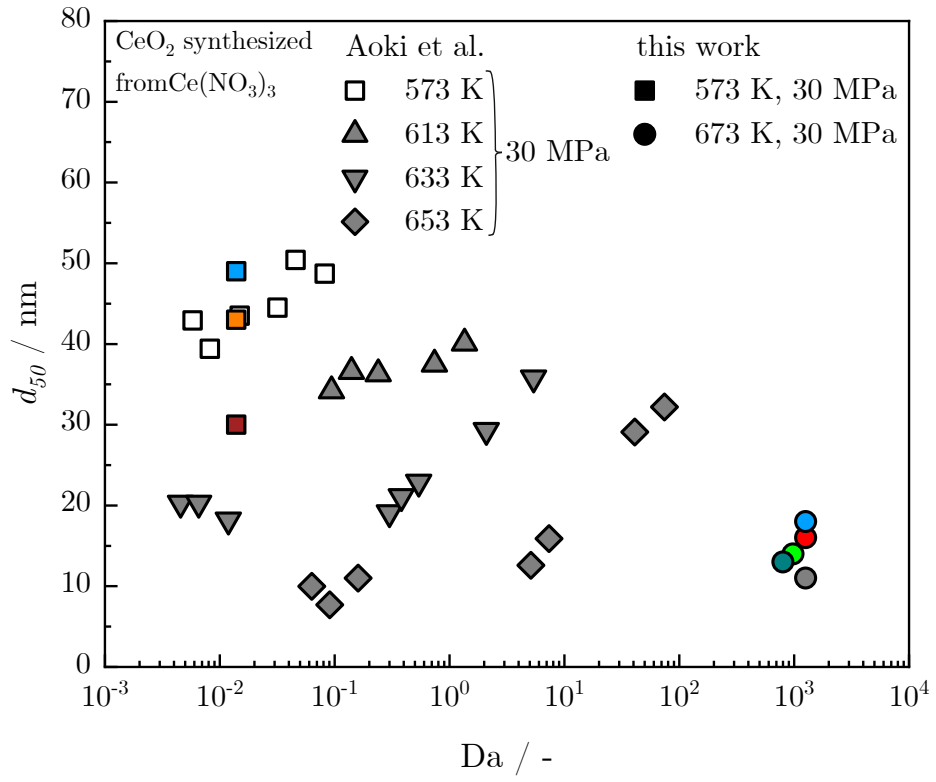

Figure 7-11: Median particle size d_{50} as a function of Da for experiments performed by Aoki et al. [28] with different process conditions and variating mixing temperatures T_3 (white and grey colored symbols, triangles and squares) and carried out in this work (colors and symbols according to the previously shown diagrams).

In general, Da is decreasing with increasing total mass flow $\dot{m}_3$ and with decreasing diameter d_m of the used mixing geometry. As previously mentioned, the experiments in this work were all performed with a constant diameter d_m of the mixing unit of 1.6 mm. In the work of Aoki et al.,

diameters d_m between 0.3 mm and 2.3 mm were applied for the particle formation experiments. For each constant temperature, experiments were carried out with a variation in the total mass flow $\dot{m}_3$. The median size of the synthesized particles with process temperatures of 613 K, 633 K and maximum 653 K is not further decreasing after reaching Da = 0.1. Below this value of Da, the particle size is not depending on the total mass flow $\dot{m}_3$. The reaction limits the particle formation within the process with $Ce(NO_3)_3$ as a precursor. The median particle sizes for the subcritical mixing temperature T_3 fit to the results presented from Aoki et al. In this work, the mixing temperature T_3 reached up to 673 K, resulting in higher values of Da. For 673 K and a constant pressure p of 30 MPa, Da reaches values up to 1250 for a total mass flow $\dot{m}_3$ of 35 g min^{-1}. It decreases with increasing total mass flow $\dot{m}_3$ down to 800 for 55 g min^{-1}. For 573 K, Da equals to a value of 3.4. The smaller the value of Da, the lower the reaction time due to the lower rate constant. The trend of the median particle size d_{50} as a function of Da of the results from Aoki et al. equals to the results presented in this work regarding the slope. The salt concentration c_{salt} does not affect the values of Da. With decreasing pressure from 30 MPa to 25 MPa, Da is increasing up to values of 10^{10}. For better comparability, the results for a pressure p of 25 MPa are shown in Figure 7-12:

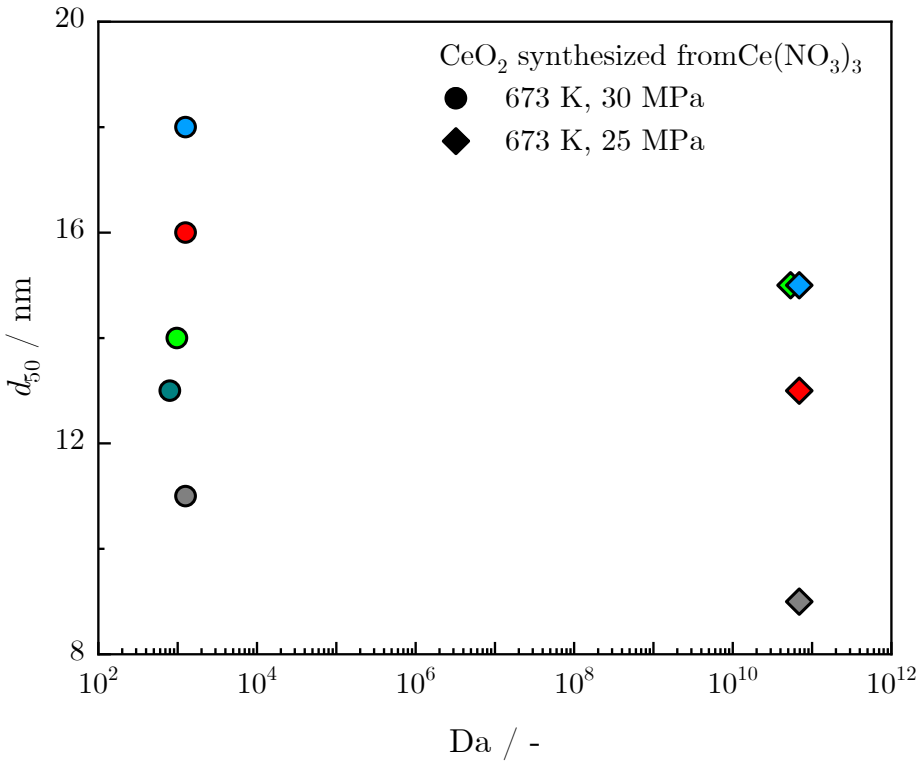

Figure 7-12: Trend of the median particle size d_{50} as a function of Da for different pressures p of 25 MPa and 30 MPa. The colors are equal to the different salt concentrations c_{salt} of 0.005 mol dm^{-3}, 0.05 mol dm^{-3} and 0.15 mol dm^{-3}, and the total mass flows $\dot{m}_3$ between 35 g min^{-1} and 55 g min^{-1}.

The drastic increase of Da is due to the strong dependence of the rate constant k on the pressure in the supercritical region. The decrease of the pressure p leads to a further reduction in the dielectric constant ε and an increase of the rate constant k. The rise of Da of 7 orders of magnitude leads to a decrease of the median particle size d_{50}. For these significant differences in the values of Da, it is not suitable to compare the values for the pressures p between 25 MPa and 30 MPa. Furthermore, it cannot be used to explain the median particle size d_{50} in relation with τ_r and τ_m. However, for lower values, as shown in Figure 7-11 Da is beneficial for determining the influence of each characteristic time.

7.3 Experiments with cerium(III)sulfate-octahydrate

$Ce(NO_3)_3$ was used as a precursor for the experiments to determine the influence of the process conditions on the relating median particle size d_{50} and shape. Next to this examination, the impact of the change of the anion was also an important aspect. For this reason, $Ce_2(SO_4)_3$ was chosen to determine this effect. In general, $Ce_2(SO_4)_3$ has the same cation with the same atomic number, but differs in the anion leading to a different solubility behavior compared to $Ce(NO_3)_3$. With increasing temperature, the solubility is rising. This is the typical type 1 behavior (compare section 2.1.2) with a good solubility for low temperatures and relatively higher solubility in the supercritical region than type 2 salts.

In contrast, $Ce_2(SO_4)_3$ has a different solubility behavior than $Ce(NO_3)_3$. Typically, the solubility of salts in H_2O increases with increasing temperature. For certain salts, it decreases with increasing temperature. This is also the case for $Ce_2(SO_4)_3$ caused by the exothermic solubility behavior. The influence of this aspect on the formation of ceria nanoparticles is described in this section. As the precursor is changed from $Ce(NO_3)_3$ to $Ce_2(SO_4)_3$, both the solubility and the kinetic behavior are changing. The kinetic approach of Aoki et al. [28] cannot be applied to $Ce_2(SO_4)_3$. In literature, no kinetic data have been provided so far. Anyway, the influence of the change of the anion was determined with this metal salt. The low solubility leads to the assumption of synthesizing ceria nanoparticles with lower mixing temperatures T_3 than $Ce(NO_3)_3$. The aim was to make the CHTS process more economically friendly due to the high required electrical heating power for hot temperatures.

At first, experiments with a mixing temperature T_3 of 673 K were carried out. The relating process conditions pressure p, the total mass flow $\dot{m}_3$, the mixing ratio a and the salt concentration c_{salt} were equal to the experiments with $Ce(NO_3)_3$. Due to the different solubility behavior and the unknown kinetics, it was unclear if ceria nanoparticles were formed with these supercritical process conditions. For the first experiments, no formed ceria nanoparticles in the suspension recovered from the CHTS plant could be obtained after the experiments, even for higher salt concentrations c_{salt}. It was suspected that smaller nanoparticles get formed due to the lower solubility of $Ce_2(SO_4)_3$ over the whole range compared to $Ce(NO_3)_3$. Both the solubility and the kinetic behavior between both metal salts show a large discrepancy. As mentioned above, $Ce(NO_3)_3$ showed large values for the rate constant at supercritical mixing temperatures of 673 K and a low solubility. It was proposed, that $Ce_2(SO_4)_3$ could have a higher solubility at 673 K and low values for the rate constant. Adschiri et al. [94] estimated the

solubility of CuO for a constant pressure of 28 MPa as a function of the temperature T. Around the critical point of water, the solubility is decreasing. In contrast, in the supercritical region, it is increasing again. This could also be the case for $Ce_2(SO_4)_3$, and no particle formation occurs due to that phenomenon. Furthermore, the rate constant could be low in the supercritical region, leading to no reaction even for the high temperatures. Therefore, the mixing temperature T_3 was decreased to a nearcritical mixing temperature T_3 of 573 K. For the use of $Ce(NO_3)_3$, the median particle size d_{50} increased with decreasing temperature, and the PSD became narrower. Figure 7-13 shows the summarized results for the first experiments performed with $Ce_2(SO_4)_3$:

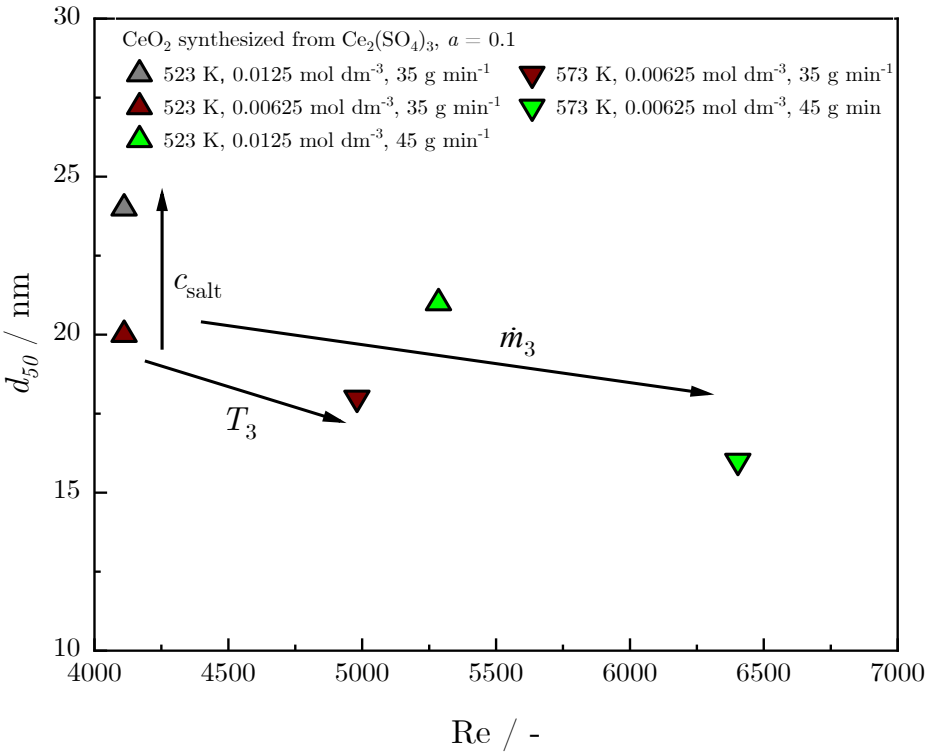

Figure 7-13: Median particle size d_{50} as a function of Re for the experiments carried out with $Ce_2(SO_4)_3$ as a precursor. The pressure p was kept constant at 30 MPa. The mixing temperature T_3 was varied between 523 K and 573 K, and the total mass flow $\dot{m}_3$ was varied between 35 g min^{-1} and 55 g min^{-1} with a constant mixing ratio a of 0.1. The salt concentration c_{salt} was varied between 0.00625 mol dm^{-3} and 0.0125 mol dm^{-3}.

As shown for the experiments with $Ce(NO_3)_3$ as a precursor, the results for $Ce_2(SO_4)_3$ are illustrated dependent on the different process conditions mixing temperature T_3, total mass flow $\dot{m}_3$ and salt concentration c_{salt}. In general, similar phenomena as for $Ce(NO_3)_3$ are detectable. The difference here is the mixing temperature T_3. With $Ce_2(SO_4)_3$ as a precursor, temperatures of 523 K are already sufficient to form ceria nanoparticles. For this mixing temperature, no particles were detectable with $Ce(NO_3)_3$ as a precursor. The median particle size d_{50} is increasing with increasing salt concentration c_{salt} at constant Re. For 523 K, the

median particle size d_{50} is slightly increasing with increasing total mass flow $\dot{m}_3$. This is in contrast to the results shown for $Ce(NO_3)_3$. The effects of potential clogging during the particle formation could be used to explain the trend. For a mixing temperature T_3 of 573 K, the median particle size d_{50} is decreasing with increasing total mass flow $\dot{m}_3$. A decrease in the mixing temperature T_3 leads to an increase in the median particle size d_{50} as also shown for $Ce(NO_3)_3$. Another important aspect is the comparison of both metal salt precursors at constant process conditions for the further decrease of the median particle size d_{50}. Figure 7-14 illustrates the median particle size d_{50} as a function of Re (left side) and the respecting PSDs (right side):

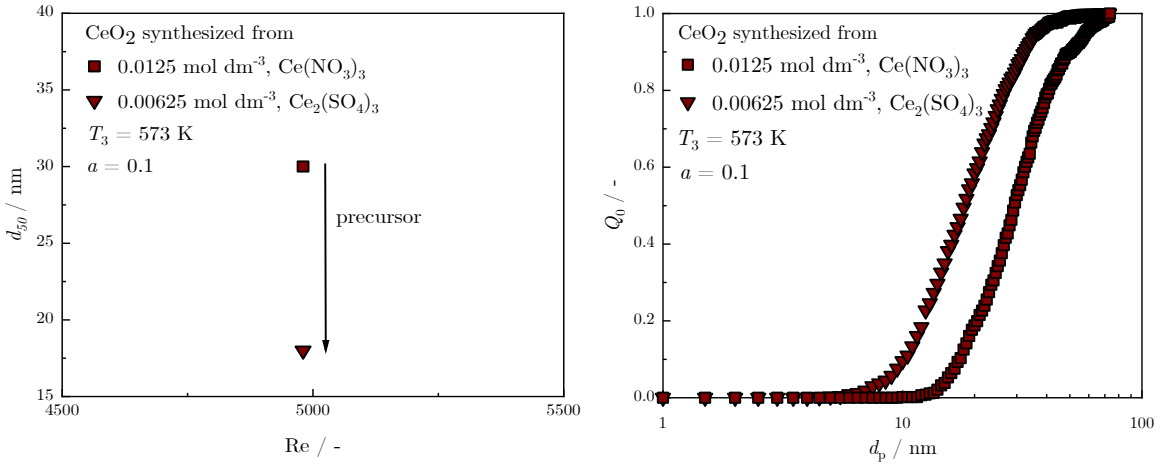

Figure 7-14: Median particle size d_{50} for a constant value of Re and different metal salts as a precursor on the left side for a constant mixing temperature T_3 of 573 K. Both the pressure p and the total mass flow $\dot{m}_3$ were kept constant at 30 MPa and 35 g min^{-1}, respectively. The mixing ratio a and the salt concentration c_{salt} were set to 0.1 mol dm^{-3} and 0.0125 mol dm^{-3} and equally to the amount of cerium to 0.00625 mol dm^{-3}. The relating PSD for both experiments is shown on the right side.

The change of the metal salt as a precursor from $Ce(NO_3)_3$ to $Ce_2(SO_4)_3$ leads to a decrease in the median particle size d_{50} for a constant nearcritical mixing temperature T_3 of 573 K from 30 nm ($\Delta = 1.04$) to 18 nm ($\Delta = 1.12$). Typical median particle sizes for $Ce(NO_3)_3$ at 573 K are in range of 30 nm to 50 nm. With supercritical mixing temperatures T_3 of 673 K, smaller ceria nanoparticles were producible. With $Ce_2(SO_4)_3$, it was possible to synthesize nanoparticles with median particle sizes below 20 nm at nearcritical conditions. The width of the PSD for both experiments was nearly equal but lower than for most of the experiments performed with $Ce(NO_3)_3$ at supercritical conditions. The use of $Ce_2(SO_4)_3$ enabled the decrease of the median particle size d_{50} below 20 nm with lower temperatures than for the use of $Ce(NO_3)_3$ as a precursor. Lowering the mixing temperature decreases the required heating energy and thus increasing the sustainability of the process. For this high temperature, an exceptionally high amount of electrical energy must be provided. Figure 11-5 shows that a cooling unit was installed in the cold metal salt solution line right before the mixing unit. The first experiments carried out with $Ce_2(SO_4)_3$ showed the problem of clogging the mixer and the tube in front of it. Due to the decreasing solubility of $Ce_2(SO_4)_3$ with increasing temperature, particle formation

takes place at certain low temperatures. Due to heat conduction, the hot mixer inside the insulation housing in combination with the heating unit around the T-junctions, heated the cold metal salt solution tube in front of the mixer. Here, the temperature of the cold metal salt solution was increased, leading to the start of the reaction and the resulting particle formation before the cold metal salt solution was mixed up with the hot near- / supercritical water stream at the mixing point. For this reason and the better control of the temperature of the cold metal salt solution, the above-mentioned cooling unit was constructed and installed. This optimization solved the problem related to the particle formation in front of the mixer. Another problem was the fast particle formation due to the low solubility of $Ce_2(SO_4)_3$ at elevated temperatures. The problem of the clogging of the mixer depended on the used salt concentration c_{salt}. First experiments were carried out with respecting salt concentrations according to the experiments with $Ce(NO_3)_3$. This led to rapid clogging of the mixer, and it had to be cleaned and reassembled in the CHTS plant. This was time-consuming and elaborately. For this reason, a case study of the salt concentration c_{salt} was performed. Starting at the concentration where the clogging occurred, it was decreased to values till no clogging occurred and still particles were formed. This concentration resulted in values between 0.00625 mol dm^{-3} and 0.0125 mol dm^{-3}. These values were used for all further experiments with this precursor, as previously shown. After examining the influence of the single process conditions on the median particle size d_{50} for the precursors, the results were unified. Figure 7-15 shows the comparison of the results of both precursors $Ce(NO_3)_3$ and $Ce_2(SO_4)_3$ used for the particle formation:

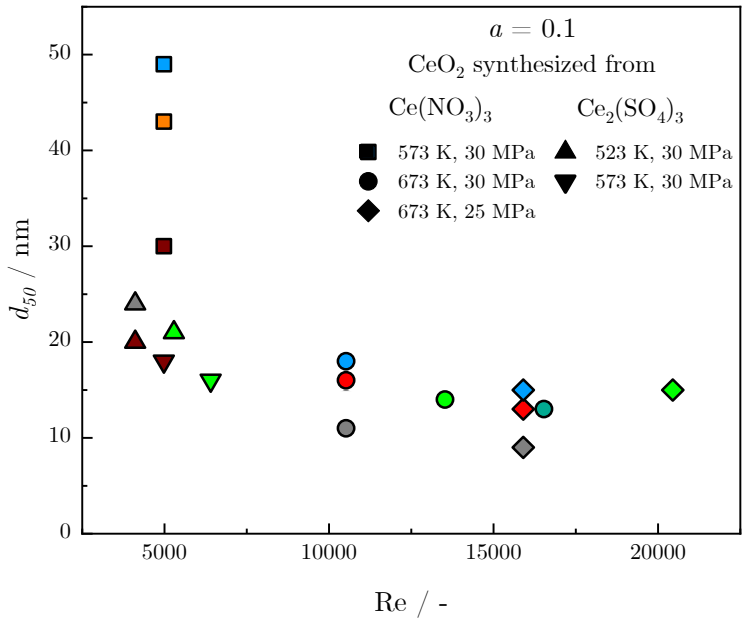

Figure 7-15: Comparison of the median particle diameter d_{50} as a function of Re for $Ce(NO_3)_3$ and $Ce_2(SO_4)_3$ used as precursors for the particle formation experiments. For both the pressure p, the mixing temperature T_3, the total mass flow $\dot{m}_3$ and the salt concentration were varied. The mixing ratio a was kept constant at 0.1.

In general, using $Ce_2(SO_4)_3$ as a precursor lead to the decrease of the median particle size d_{50} for constant nearcritical process conditions (p = 30 MPa, T_3 = 573 K, $\dot{m}_3$ = 35 g min^{-1}, a = 0.1) compared to $Ce(NO_3)_3$. Regarding Figure 7-5, the results with $Ce_2(SO_4)_3$ as precursor fit to the trend of the results examined with $Ce(NO_3)_3$. Especially the range with low values of Re showed a gap between the experiments carried out at 573 K and 673 K. The experiments with $Ce_2(SO_4)_3$ filled the gap of Re in the range of 5000. For the particle formation with mixing temperatures below 573 K, the precursor is changed to $Ce_2(SO_4)_3$. For the more complex handling during the particle formation experiments due to the low solubility and fast clogging of the mixer, $Ce_2(SO_4)_3$ was only used for low salt concentrations c_{salt}. A graph of the median particle size d_{50} as a function of the mean residence time τ is found in Appendix chapter 7.

Even though the decrease in the median particle size d_{50} at lower mixing temperatures, the disadvantages outweighed these findings. The limitation to low salt concentrations leads to the formation of less nanoparticles. The duration of the experiments and the feed volume of the metal salt solution increase what increases the heating energy. The low concentration of particles inside the product suspension requires intensified preparation steps. Due to these problems during the particle formation with $Ce_2(SO_4)_3$, another metal salt was selected for particle formation experiments. The results of these experiments are described in the following section.

7.4 Experiments with cerium(III)acetate

Cerium(III)acetate ($Ce(CH_3COO)_3$) was used as third metal salt to examine the influence of the process conditions and the change of the anion on the resulting median particle size d_{50} and the relating shape. This precursor was also used to examine the influence of the process conditions on the relating median particle size d_{50} and the shape of the resulting ceria nanoparticles. Based on the experiments with $Ce(NO_3)_3$, a salt concentration c_{salt} of 0.05 mol dm^{-3} was chosen for the first experiments to compare the results from both precursors. The mixing temperature T_3 varied from 673 K to lower near- and subcritical mixing temperatures of 573 K, 523 K, 473 K, and 423 K. Figure 7-16 visualizes the results of the experiments with different mixing temperatures T_3 at a constant total mass flow of 35 g min^{-1}:

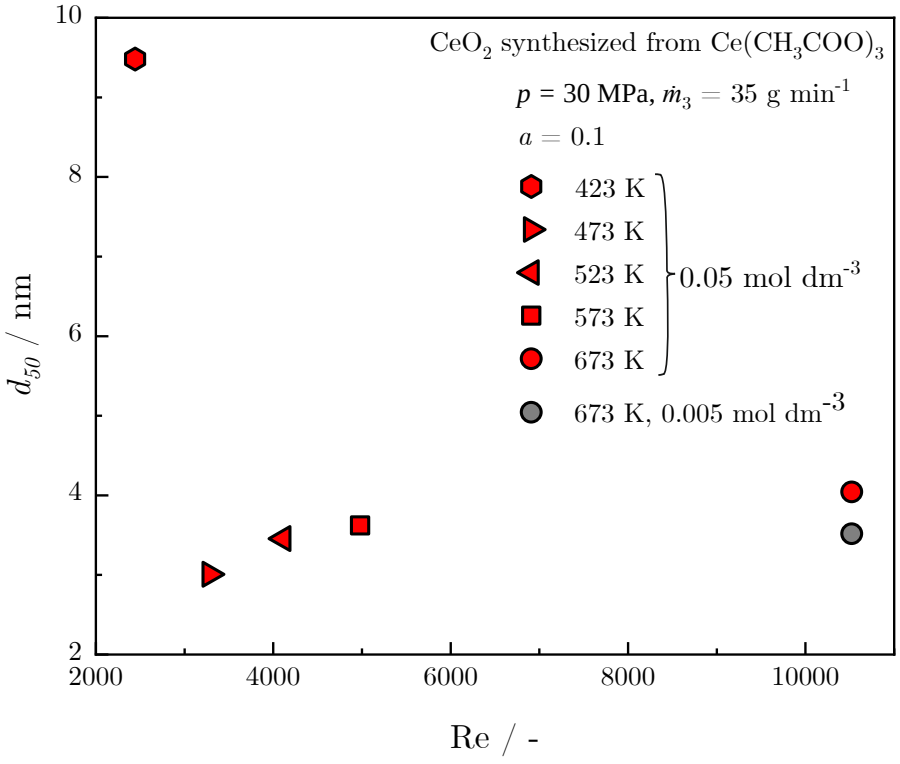

Figure 7-16: Median particle size d_{50} as a function of Re for different mixing temperatures T_3 and salt concentrations c_{salt} for stable process conditions of the pressure p and the mixing ratio a. For the experiments, $Ce(CH_3COO)_3$ was used as a precursor.

In general, the median particle size d_{50} is decreasing with increasing Re. The values are in the range between 2.6 nm and 9.5 nm, and with the use of $Ce(CH_3COO)_3$, d_{50} is further decreased compared to the other metal salts $Ce(NO_3)_3$ and $Ce_2(SO_4)_3$ for the near- and supercritical mixing temperatures. At first, the impact of the salt concentration c_{salt} on the resulting particle size was observed according to the other before used metal salts. As determined from the experiments with $Ce(NO_3)_3$ and $Ce_2(SO_4)_3$, the median particle size d_{50} is increasing with increasing salt concentration c_{salt}. This effect was detectable for all three metal salts. In addition to the influence of the salt concentration c_{salt}, the effect of the change of the mixing temperature T_3 was investigated. In general, the particle formation occured even for lower temperatures like 423 K compared to 573 K for $Ce(NO_3)_3$ and 523 K for $Ce_2(SO_4)_3$.

The use of $Ce(CH_3COO)_3$ as precursor decreased the median particle size d_{50} by a factor of 4 from 16 nm to 4 nm for mixing temperatures T_3 of 673 K. For a mixing temperature T_3 of 573 K, it was further decreased by a factor of 12 from 43 nm to 3.6 nm. However, the trend is similar to the one shown in Figure 7-5, with slight differences for the lower mixing temperatures T_3. Temperatures of 473 K result in the smallest values of the median particle size d_{50} with 3 nm. For temperatures of 423 K and 523 K, the size is increasing to 9.5 nm and 3.5 nm, respectively. The mixing temperature of 473 K results in the optimal value for synthesizing the smallest ceria nanoparticles produced within this work. For the temperatures of 573 K and 673

K, the median particle size d_{50} is slightly increasing. This is in contrast to the experiments carried out with $Ce(NO_3)_3$ and $Ce_2(SO_4)_3$. For $Ce(NO_3)_3$, experiments with 673 K showed the smallest particle sizes, whereas for $Ce_2(SO_4)_3$, no nanoparticles were obtained at that temperature. The median particle size d_{50} decreases with increasing mixing temperature from 423 K to 473 K. Above 473 K, it slightly increases with increasing temperature up to 673 K. The general decrease of the median particle size d_{50} with the change of the precursor allows the flexible tuning of the size not only by the variation of the process conditions. Another important fact in terms of using $Ce(CH_3COO)_3$ as a precursor is the width of the resulting PSD. The experiments with $Ce(NO_3)_3$ showed a relatively broad PSD in the supercritical range and a homogeneous one in the nearcritical region. The experiments performed with $Ce_2(SO_4)_3$ showed a similar PSD to $Ce(NO_3)_3$. The ceria nanoparticles synthesized with $Ce(CH_3COO)_3$ show a narrow PSD over the whole temperature range. This aspect leads, in combination with the small size, to the formation of uniform ceria nanoparticles. The synthesis of uniform nanoparticles is required for further applications of the particles in catalysis or other technically related fields. Figure 7-17 shows a PSD and TEM images of produced ceria nanoparticles with $Ce(CH_3COO)_3$ as a precursor for two different mixing temperatures:

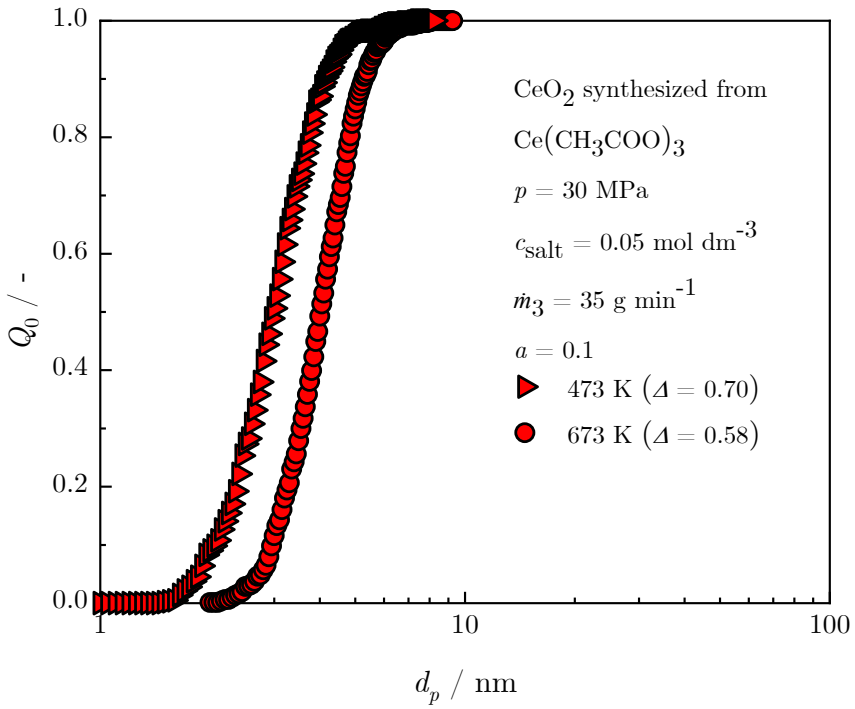

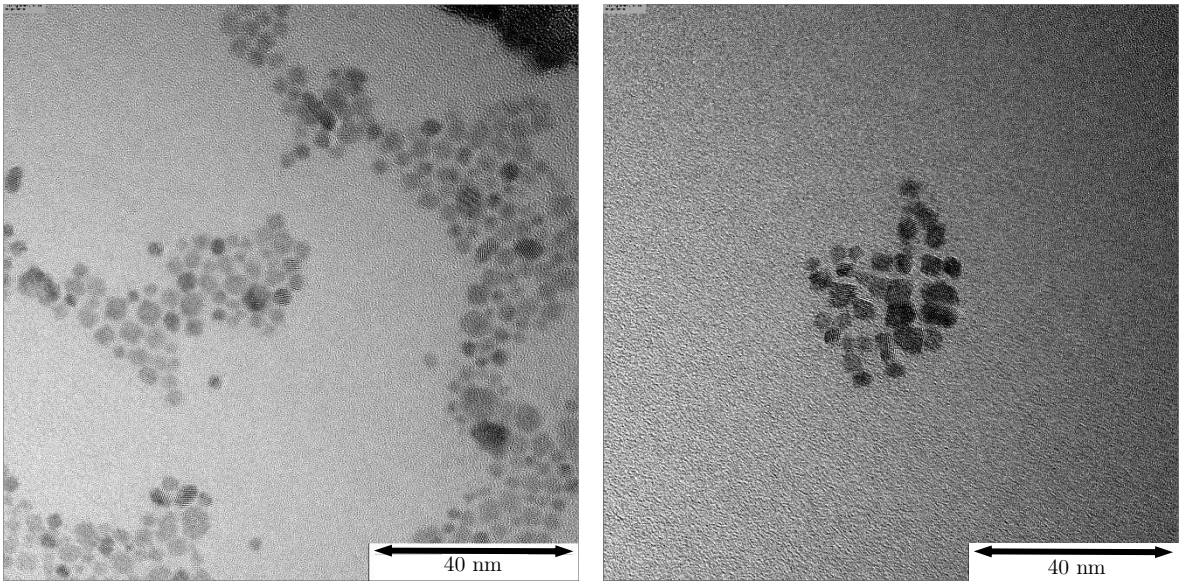

Figure 7-17: PSD of two experiments with different mixing temperature T_3 and constant process conditions, and TEM images of the synthesized ceria nanoparticles with $Ce(CH_3COO)_3$ as a precursor and different mixing temperatures T_3 (473 K left side, 673 K right side). The other process conditions were kept constant at p = 30 MPa, $\dot{m}_3$ = 35 g min^{-1}, a = 0.1 and c_{salt} = 0.05 mol dm^{-3}.

The small size compared to the nanoparticles produced with the other metal salts as precursors is visible through the scale bar. The nanoparticles were further analyzed with EDX to see the formation of CeO_2. Here, PXRD was not suitable due to remaining $Ce(CH_3COO)_3$ salt after the drying of the nanoparticles. The synthesized ceria nanoparticles show an octahedron shape and a uniform particle size with a median particle size d_{50} of 3 nm (T_3 = 473 K, left side) and 4 nm (T_3 = 673 K, right side). The small size of the particles is related to the low solubility of $Ce(CH_3COO)_3$ at elevated temperatures with the respecting high supersaturations and a high nucleation rate. The homogeneous PSD of the ceria nanoparticles is explainable with a low rate constant in general. The combination of these two effects results in the formation of homogeneous small-sized nanoparticles. It is supposed that the rate constant reaches its highest value at around 473 K or the solubility is the lowest at that temperature. Both effects lead to the formation of the smallest nanoparticles for all the performed experiments. This means that the rate constant is increasing from 423 K to 473 K and decreasing for rising temperatures up to 523 K, 573 K, and 673 K. Next to that, the solubility of $Ce(CH_3COO)_3$ in near- / supercritical water could further decrease with increasing temperature from 423 K to 473 K. After passing that temperature, the solubility increases again for the elevated temperatures up to 673 K. These results show that a control of the chemical reaction is possible, and the mixing of both, the hot near- / supercritical water stream with the cold aqueous metal salt solution, has a particular influence on the relating particle size. Therefore, further experiments with the variation of the total mass flow $\dot{m}_3$ from 35 g min^{-1} to 45 g min^{-1} and 55 g min^{-1} were carried out according to the previous experiments with $Ce(NO_3)_3$ and $Ce_2(SO_4)_3$. The following images will explain the dependence of the median particle size d_{50} on the total mass flow $\dot{m}_3$ for the

different mixing temperatures T_3. Figure 7-18 shows the results for the variation of the temperature between 423 K, 473 K, and 573 K:

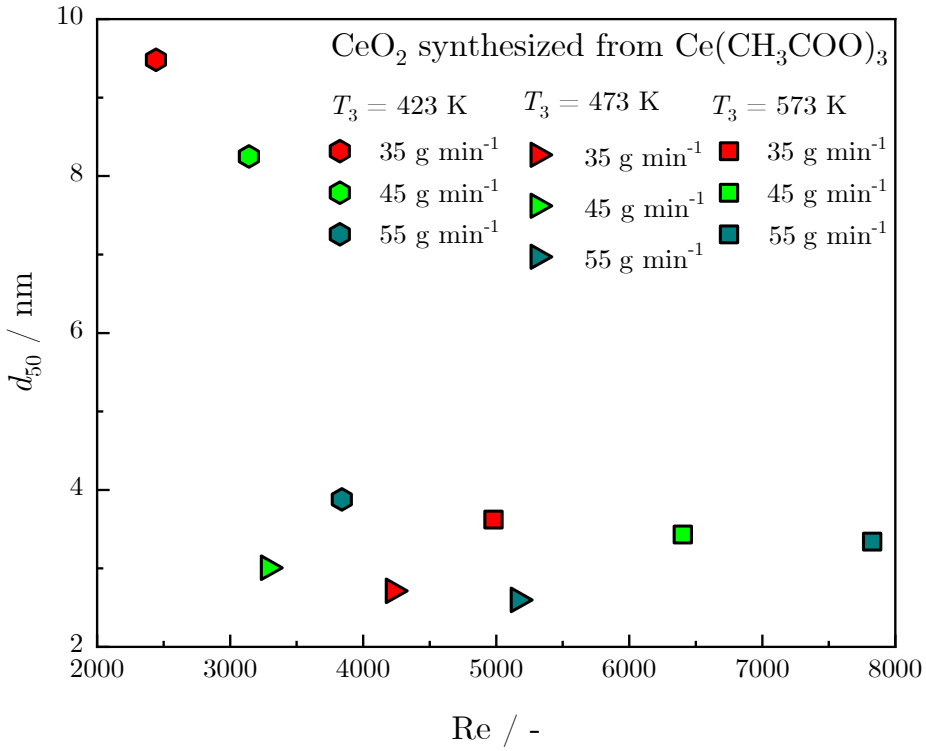

Figure 7-18: Comparison of the median particle size d_{50} as a function of Re for different mixing temperatures T_3 of 423 K, 473 K, and 573 K at constant process conditions of p = 30 MPa, a = 0.1, and c_{salt} = 0.05 mol dm^{-3}.

In principle, the values of Re are increasing with increasing mixing temperature T_3 due to the decrease of the water density ρ (compare equation (7-1)), an increase of the mean velocity v_3 and the decrease of the mean residence time τ. For all three mixing temperatures T_3, the median particle size d_{50} is decreasing with increasing total mass flow $\dot{m}_3$. These results are according to the results of the experiments performed with $Ce(NO_3)_3$. Therefore, the highest temperatures of 673 K with the respecting shortest mean residence time τ lead to the formation of the smallest ceria nanoparticles with $Ce(NO_3)_3$ as a precursor. In Figure 7-18, the mean residence time τ differs for a total mass flow $\dot{m}_3$ of 35 g min^{-1} from 1.9 s (423 K) to 0.73 s (673 K). Even though for the doubled time of the mean residence time τ the nanoparticles show smaller sizes for a mixing temperature T_3 of 473 K compared to 673 K. The solubility and kinetic effects are overwhelming the impact of the reduction of the mean residence time τ. The mean residence time τ dependent on the median particle size $d_{50,}$ is not comparable between both metal salts. Even though considering the mean residence time τ and its influence on the particle size for the single metal salt is valid. The median particle size d_{50} as a function of Re for the different mixing temperatures T_3 of 523 K and 673 K is represented in Figure 7-19:

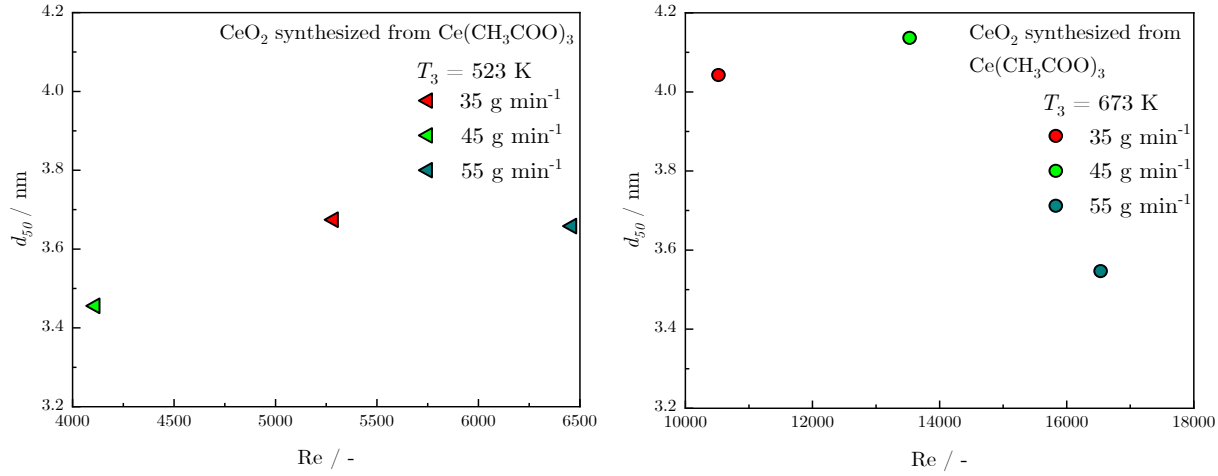

Figure 7-19: Comparison of the median particle size d_{50} as a function of Re for different mixing temperatures T_3 of 523 K and 673 K at constant process conditions of p = 30 MPa, a = 0.1, and c_{salt} = 0.05 mol dm^{-3}.

The trends of the median particle size d_{50} with the total mass flow variation differ from those shown in Figure 7-5. The particle size is not decreasing with increasing total mass flow $\dot{m}_3$. Nevertheless, the deviation between the single-particle sizes is slight. Regarding the results for the other temperatures, the differences are marginal for 523 K. For 673 K, the particle size for a total mass flow $\dot{m}_3$ of 45 g min^{-1} is more significant than for the other values. The size for a total mass flow $\dot{m}_3$ of 55 g min^{-1} fits the trend of the other mixing temperatures.

In general, the increase of the total mass flow $\dot{m}_3$ leads to a further decrease of the resulting particle size d_{50} for a broad range of mixing temperatures in the near- / supercritical region. Regarding the results for 523 K and 673 K and the slight deviation of the median particle sizes, the effect can be neglected. Especially the representation of the median particle size d_{50} as a function of Re for all performed experiments with $Ce(CH_3COO)_3$ as a precursor, the deviation is shown in Figure 7-16 are compensated. The general trend is shown in Figure 7-20:

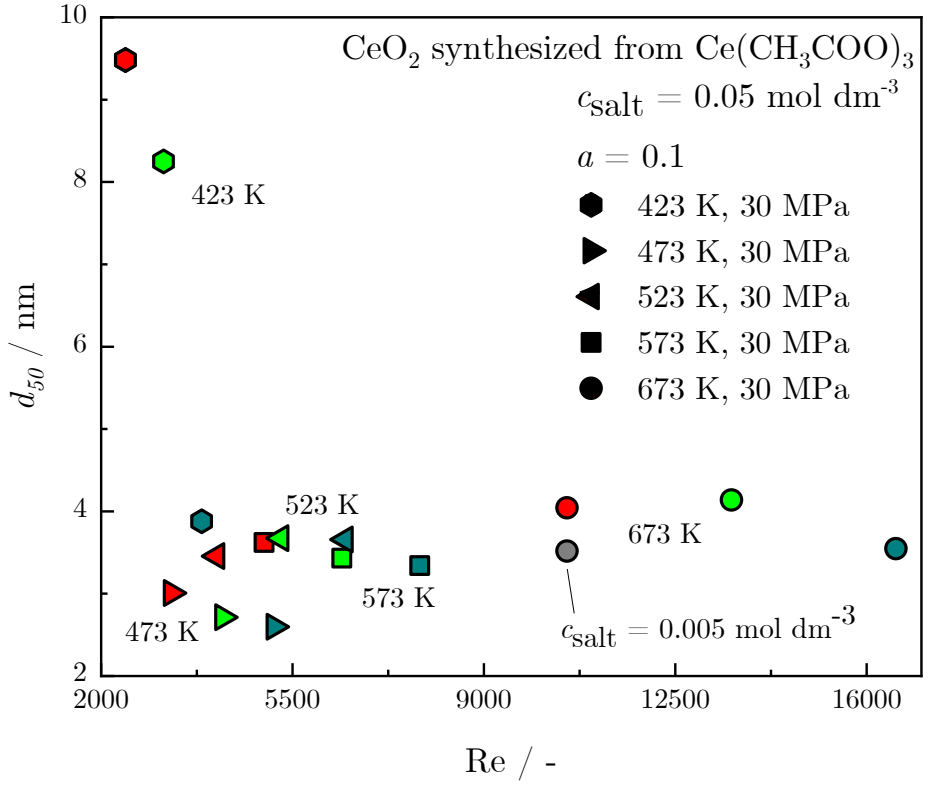

Figure 7-20: Overview of the performed experiments with $Ce(CH_3COO)_3$ as a precursor as a trend of the median particle size d_{50} as a function of Re for different mixing temperatures T_3, total mass flows, and salt concentrations c_{salt} between 0.005 mol dm^{-3} (grey circle) and 0.05 mol dm^{-3} (other colored symbols), $\dot{m}_3$ of 35 g min^{-1}, 45 g min^{-1}, and 55 g min^{-1} at constant process conditions of p = 30 MPa and a = 0.1.

The median particle size d_{50} decreases with increasing Re, as for the other used metal salts $Ce(NO_3)_3$ and $Ce_2(SO_4)_3$. The minimum of the median particle size d_{50} is reached at mixing temperatures T_3 of 473 K, a total mass flow $\dot{m}_3$ of 55 g min^{-1} and a value of Re below 5500. 2.6 nm is the smallest size of ceria nanoparticles synthesized in this work, with a width of 0.73. With increasing mixing temperature T_3, the median particle size d_{50} is slightly increasing up to 673 K. The smallest particle sizes with $Ce(CH_3COO)_3$ as precursor are below 10 nm.

7.5 Experiments with impedance spectroscopy (IS)

For the potential future control of the nanoparticle synthesis with impedance spectroscopy measurements, first experiments were carried out. The two measuring points within the CHTS plant (one in the cold metal salt tube and one in front of the back pressure regulator) were characterized and tested. Therefore, two ceramic tubes (compare section 4.2.5) with attached aluminum electrodes were integrated into the plant. At first, stability tests with both ceramic tubes were carried out what is shown in Figure 7-21.

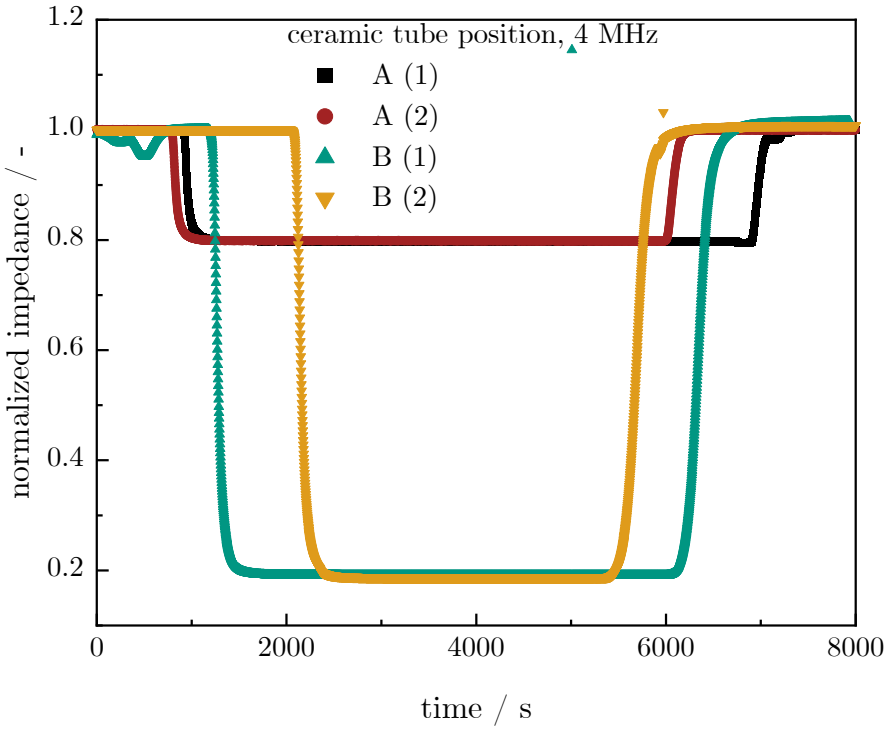

Figure 7-21: Influence of the location of the measuring point inside the CHTS plant [152], measured at ambient pressure and temperature, c_{salt} = 0.015 mol dm^{-3}, reprinted with permission from Wiley.

Four experiments were performed, two for each measuring point ((1) and (2) in Figure 7-21). The black and the red trend show the impedance at measuring point A, whereas the green and the yellow trend show the impedance for measuring point B (compare Figure 4-1). The trends of the impedance were normalized with the value of the impedance for deionized water. At first, deionized water was pumped through the CHTS plant including the measuring points. Once a stable signal for the impedance was detected, the flow was changed from water to a 0.015 mol dm^{-3} $Ce(NO_3)_3$ solution. As the salt solution reached the ceramic tube with the electrodes, the impedance decreased through an increase of the conductivity. The tubes and fittings of the CHTS plant lead to a delayed decrease due to back-mixing effects. As the impedance was stable over a longer period of time, the flow was changed to deionized water again. Here, the back-mixing effects were also responsible for the delayed increase of the impedance. The results showed that the impedance was stable and suitable for the control of the reaction. Comparing the increase after switching to deionized water it lasts longer for the green and the yellow trend. This is caused by the position of the measuring point B. It is located at the outlet of CHTS plant whereas further components and longer tubes are passed. The slight decrease of the green trend after 500 s is caused by remaining salt solution inside the tubes what was then detected at measuring point B. This is also affected by uncertainties of the measurement. For the two measurements at measuring point B an error of 1.6% was detected.

Next to the stability of the impedance during the experiment, the influence of the formed ceria nanoparticles on the impedance was also of interest. Therefore, an experiment with suspended ceria nanoparticles in deionized water, and a 0.01 mol dm^{-3} $Ce(NO_3)_3$ solution including ceria nanoparticles was performed. Figure 7-22 shows the results for the influence of the ceria nanoparticles on the impedance:

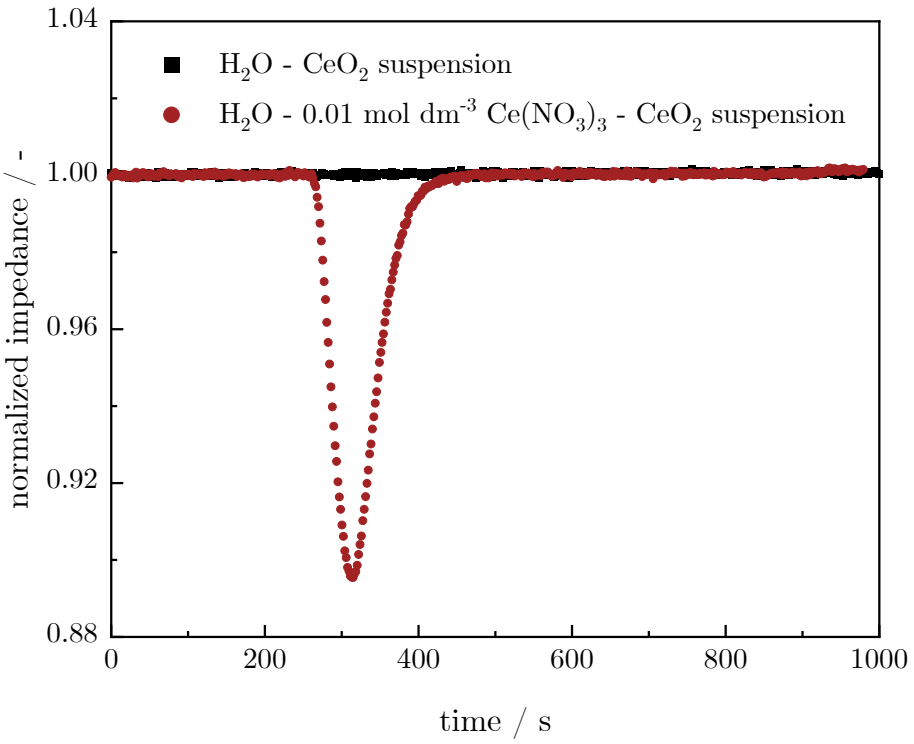

Figure 7-22: Influence of ceria nanoparticles on the trend of the impedance [152], measured at ambient pressure and temperature, reprinted with permission from Wiley.

The experiments were carried out as the previous stability tests. First, deionized water was pumped through the CHTS plant and then the flow was changed. The black trend shows that the impedance is stable over time for the ceria containing deionized water. For the $Ce(NO_3)_3$ containing suspension, the impedance is decreasing after changing the flow. This suspension represented a partially reacted product suspension. These two trends show that the impedance is influenced by the concentration of $Ce(NO_3)_3$ and not by the ceria nanoparticles. The experiments show the applicability of the impedance. The conversion is determined with the concentrations from both measuring points determined with a calibration curve. Impedance spectroscopy represents a promising measuring technique for future experiments.

In addition to the experimental work, theoretical studies in terms of CFD simulations were performed. The results of both experiments and simulations are compared and used for the optimization of the CHTS process. In the next chapter, the results for the CFD simulations of the CHTS process are presented and described.

8. Simulation results

During the ongoing experiments with different precursors, theoretical studies with CFD simulations were carried out. The designed CFD models were firstly checked with specific tests. Then the models realized in the CHTS plant (Counter- and Straight setup) were validated with experimentally determined mixing temperatures T_3. The results for the tests, the validation of the models and the theoretical mixing experiments are shown in Appendix chapter 8. The thermal and the velocity fields were analyzed in the following step. Based on that, the residence time distributions (RTD) were calculated. In a final step, the reaction occurring during the CHTS process was simulated and used for the process optimization. All these steps are described in detail in the following sections. Partial work was performed by Ponusamy [153].

8.1 Simulation of the thermal and velocity fields

In this section, the thermal and velocity fields of the designed model with the Counter setup inside the CHTS plant are analyzed and described in detail. Thermal and velocity fields of the other models are found in Appendix chapter 8.

8.1.1 Counter model

First, the following images show and describe the influence of the above-mentioned process conditions on the occurring effects at the mixing point. The images are split into an overview of the mixing unit (left side) and a more accurate view of the mixing point (right side).

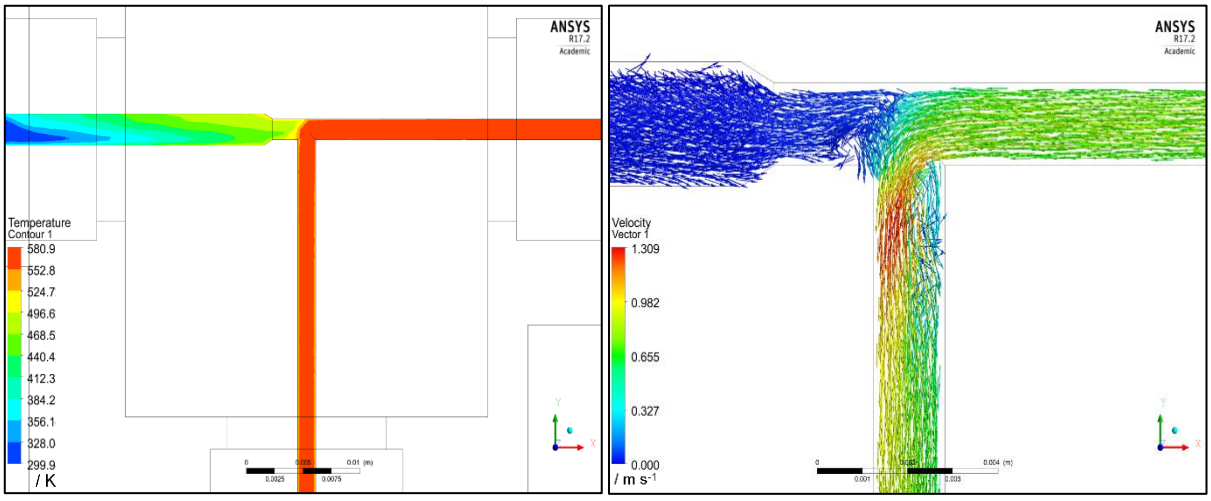

Figure 8-1: Thermal field as an overview of the mixing unit (left side) and the velocity field right at the mixing point (right side). The process conditions set to a pressure p of 25 MPa, a hot water temperature T_2 of 573 K, a total mass flow $\dot{m}_3$ of 35 g min^{-1} and a mixing ratio a of 0.05 [153].

The profiles shown in Figure 8-1 are directly compared to the profiles shown in Figure 8-2:

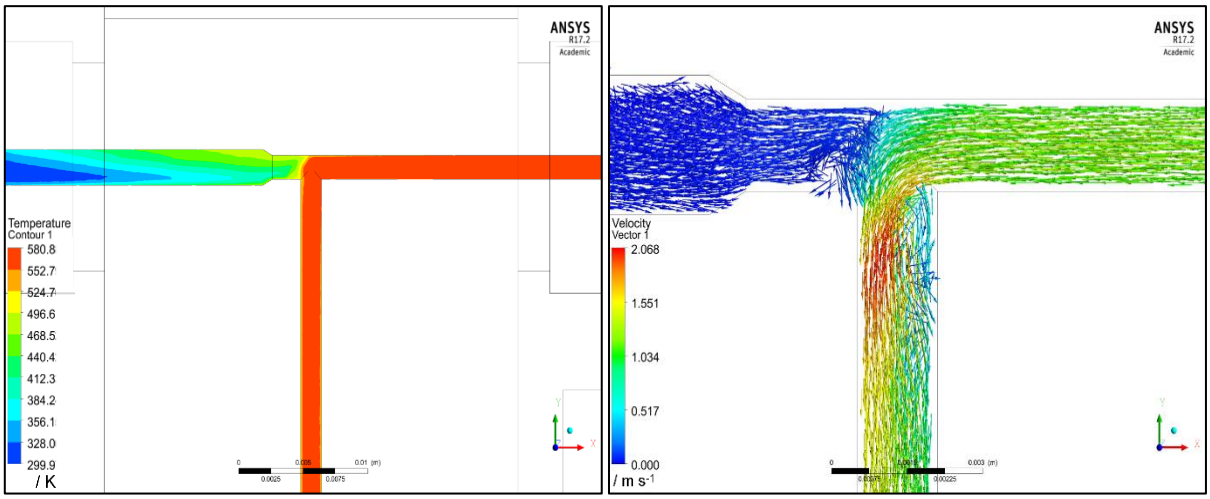

Figure 8-2: Thermal field as an overview of the mixing unit (left side) and the velocity field right at the mixing point (right side). The process conditions set to a pressure p of 25 MPa, a hot water temperature T_2 of 573 K, a total mass flow $\dot{m}_3$ of 55 g min^{-1} and a mixing ratio a of 0.05 [153].

The increase of the total mass flow $\dot{m}_3$ from 35 g min^{-1} to 55 g min^{-1} shown in Figure 8-1 and Figure 8-2, leads to a difference in the velocity field. This increases the flow velocity of the mixing stream v_3 and the maximum velocity. In both images, two vortices are developing before the mixing point in the cold water line and right after the mixing point. In the cold tube, a small vortex is formed, whereby a large one is obtained after the mixing point. The size of both vortices is the same for both total mass flows $\dot{m}_3$ as same as the ratio between the total mass flows of 35 g min^{-1} and 55 g min^{-1} and the respecting flow velocities v_3 (1.31 m s^{-1} and 2.07 m s^{-1}). Next to the velocity field, the thermal field is analyzed. Both profiles are nearly similar, although the temperature of the cold water stream $\dot{m}_1$ is lower at the inlet for the higher total mass flow of 55 g min^{-1} than the lower one. The change of the total mass flow $\dot{m}_3$ has no significant influence on either the thermal field or the size of the vortices. Nevertheless, the flow velocity of the mixing stream v_3 is increased with increasing total mass flow $\dot{m}_3$ and resulting in a decrease of the mean residence time τ.

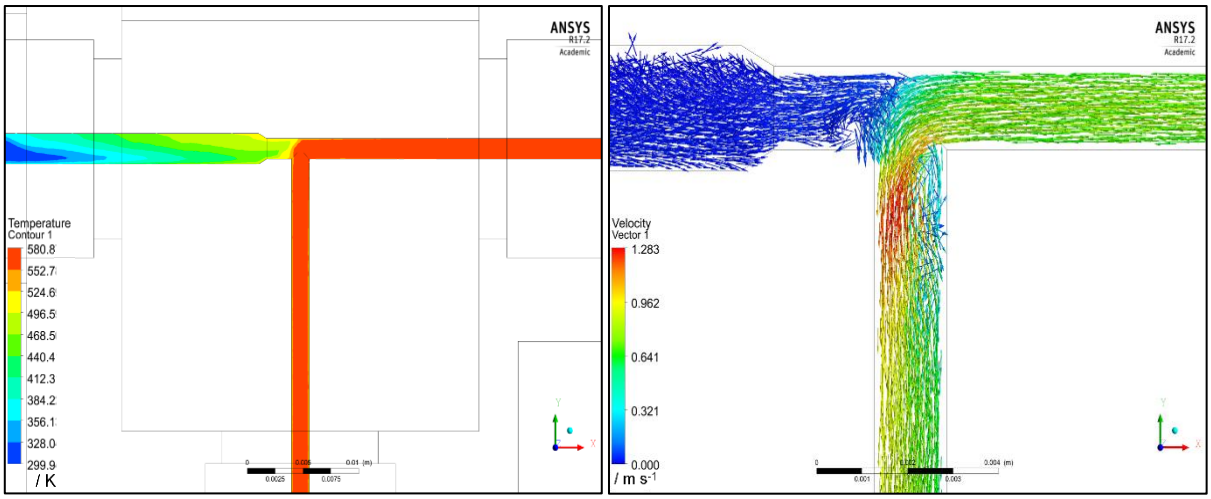

Figure 8-3: Thermal field as an overview of the mixing unit (left side) and the velocity field right at the mixing point (right side). The process conditions set to a pressure p of 35 MPa, a hot water temperature T_2 of 573 K, a total mass flow $\dot{m}_3$ of 35 g min^{-1} and a mixing ratio a of 0.05 [153].

The thermal and velocity fields are shown in Figure 8-3 for the subcritical state ($T_2 = 573$ K) and compared to fields with supercritical process conditions ($T_2 = 673$ K) shown in Figure 8-4:

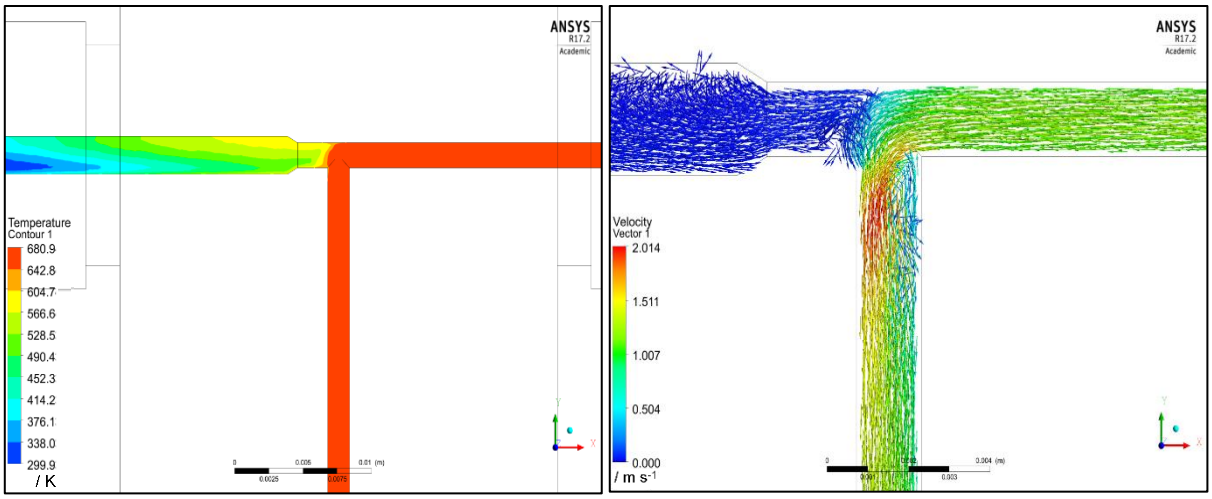

Figure 8-4: Thermal field as an overview of the mixing unit (left side) and the velocity field right at the mixing point (right side). The process conditions t set to a pressure p of 35 MPa, a hot water temperature T_2 of 673 K, a total mass flow $\dot{m}_3$ of 35 g min^{-1} and a mixing ratio a of 0.05 [153].

As the comparison of used total mass flow $\dot{m}_3$ in the previous figures, the effect of the hot water temperature T_2 was investigated. Regarding the thermal field, an increase of T_2 leads to changes in the temperature distribution. The temperatures of the cold water stream $\dot{m}_1$ in front of the mixing point are higher in Figure 8-4 compared to Figure 8-3. On the one hand, the higher temperature results in a more significant temperature difference between the cold and the hot water stream $\dot{m}_2$. This leads to improved heat transfer inside the mixer (mixing unit) and the faster heating of the cold water stream $\dot{m}_1$ at a constant total mass flow $\dot{m}_3$. On the other hand, the hot water stream dives deeper into the cold water stream $\dot{m}_1$ which is also increasing the

respecting temperature. The temperature distribution around the mixing point is more homogeneous for the supercritical temperature of $T_2 = 673$ K. The temperature distribution and the velocity field are influenced by T_2. The higher temperature results in a decrease of the density ρ which increases the flow velocity of the mixing stream v_3. The maximum velocity is increasing by a factor of 1.56 from 1.28 m s^{-1} to 2 m s^{-1}. Next to that increase, the velocity field is not changing in its nature. Two vortices appear in front of the mixing point of the cold water stream $\dot{m}_1$ and right after the mixing point. Both the total mass flow $\dot{m}_3$ and the hot water temperature T_2 have specific effects on the thermal and velocity fields. The variation of the pressure p and its impact on both fields are visualized in Figure 8-5 and Figure 8-6:

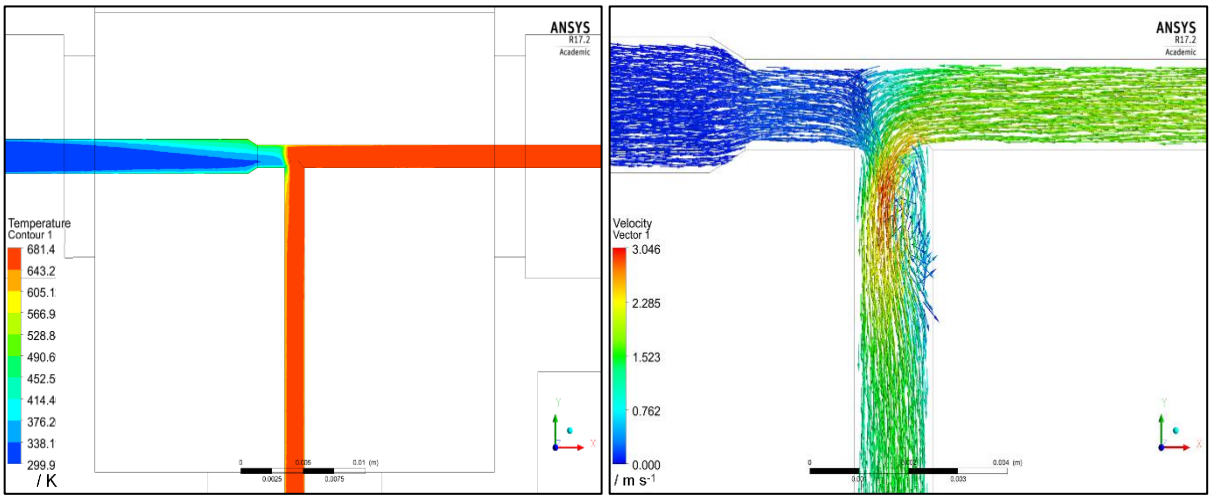

Figure 8-5: Thermal field as an overview of the mixing unit (left side) and the velocity field right at the mixing point (right side). The process conditions set to a pressure p of 25 MPa, a hot water temperature T_2 of 673 K, a total mass flow $\dot{m}_3$ of 35 g min^{-1} and a mixing ratio a of 0.35 [153].

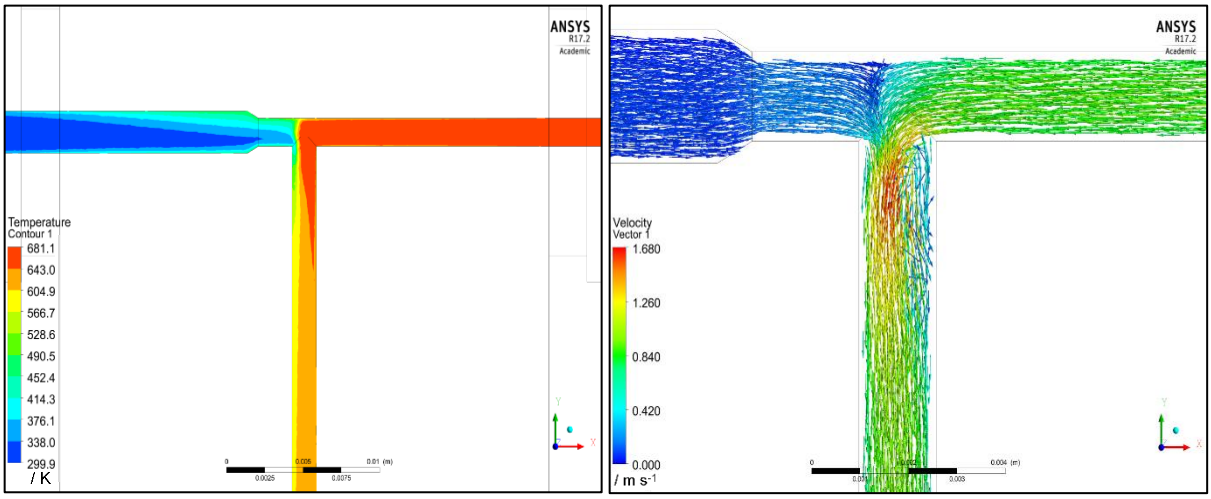

Figure 8-6: Thermal field as an overview of the mixing unit (left side) and the velocity field right at the mixing point (right side). The process conditions set to a pressure p of 35 MPa, a hot water temperature T_2 of 673 K, a total mass flow $\dot{m}_3$ of 35 g min^{-1} and a mixing ratio a of 0.35 [153].

Due to the low influence of the pressure p on the thermal and the velocity fields in the near-critical region, no drastic change in these would be noticeable (compare Figure 8-1 and Figure 8-3). However, in the supercritical area, the enthalpy h depends on the pressure p. Due to the high value of the enthalpy h for a pressure p of 25 MPa and a hot water temperature, T_2 of 673 K (2576.7 kJ kg^{-1}) compared to a pressure p of 35 MPa and the same temperature (1986.1 kJ kg^{-1}), the thermal field is more homogeneous for the lower pressure p. This is even the case for a high mixing ratio a of 0.35. The temperature reaches the maximum of the hot water temperature T_2 over the cross-section of the tube. The cold water stream $\dot{m}_1$ has no particular influence on the hot water stream and the resulting mixing temperature T_3. In contrast, with increasing pressure p from 25 MPa to 35 MPa, the enthalpy h decreases. The influence of the cold water stream $\dot{m}_1$ is increasing, and the temperature distribution after the mixing point gets broader, and the mixing temperature T_3 is decreasing. Regarding these results, a lower pressure p of 25 MPa leads to homogeneous temperatures over the whole cross-section of the tube, even for higher mixing ratios a. However, running the plant closer to the critical pressure (e.g. 25 MPa), requires more energy and a more powerful heating unit. In comparison to the velocity field, similar trends are obtainable. In contrast to the previously shown results with the variation of the total mass flow $\dot{m}_3$ and the hot water temperature T_3, only one vortex is forming right after the mixing point for both pressures p. The decrease of the pressure p leads to a reduction of the density ρ and an increase of the flow velocity of the mixing stream v_3.

The influence of the increase of the mixing ratio a from 0.05 to 0.35 is visualized in Figure 8-4 and Figure 8-6. For the lower value of the mixing ratio a of 0.05, the amount of the cold water stream $\dot{m}_1$ is low compared to the higher mixing ratio of 0.35. This enables the hot water stream to dive deeply into the cold water stream $\dot{m}_1$ which leads to the formation of a hot temperature zone within the cold water tube next to the mixing point. An increase of the mixing ratio a from 0.05 to 0.35 (compare Figure 8-6) requires a higher cold mass flow $\dot{m}_1$. This affects the interaction between both streams, and no further deep dive of the hot water stream $\dot{m}_2$ is obtainable. Furthermore, the increase leads to the formation of an inhomogeneous temperature profile of the mixing stream with lower mixing temperatures T_3 than the hot water stream temperature T_2. For a value of 0.35, the vortex in the cold part next to the mixing point disappears. A reason for this is the increasing flow velocity of the cold water stream $\dot{m}_1$. This is accompanied with a decrease in the flow velocity of the mixing stream v_3. The simulation results for the Straight model are described in Appendix chapter 8 D: Straight model.

The change in the total mass flow $\dot{m}_3$ from 35 g min^{-1} to 55 g min^{-1} affect the velocity field more than the thermal field. This was due to the proportional increase of the cold and the hot water stream at a constant mixing ratio a. Due to this, the intensive enthalpy h remained constant resulting in a similar temperature profile. The increase of the total mass flow $\dot{m}_3$ up to 55 g min^{-1} decreases the size of the hot zone in front of the mixing point. The probability of the formed ceria nanoparticles remaining and deposition at the tube wall is lowered for the later particle formation experiments. In general, the maximum velocities of the simulations differ for each designed model. The values are found in Appendix chapter 8 G: Maximum

velocities for different total mass flows and locations of the vortices. The increase of the total mass flow $\dot{m}_3$ results in an increased heating and mixing rate and lower residence times τ. This leads to the formation of smaller nanoparticles due to less time for particle growth. The effect of the residence time is discussed in the next section. The influence of the hot water temperature T_2 on the thermal and velocity fields is explainable with the decrease of the density with increasing temperature. The difference in density increases the buoyancy effect affecting the physics of the mixing. The buoyancy convection results in the formation of a circular flow and the formation of vortices. The sizes of the vortices for the different models are pretty similar. Next to the formation of these vortices right at the mixing point at the left side where the cold stream enters, vortices are formed through flow instabilities. These are located at the point where the direction of the hot water is changed due to the mixer. The bend of the hot water stream causes large pressure gradients, which favor flow instabilities. These vortices develop for all models if the hot water stream is bent. Just for the Straight models, no vortex is formed. The formed vortices located inside the mixer are summarized in G: Maximum velocities for different total mass flows and locations of the vortices. The vortices may have a negative influence on the residence time for the increase of the temperature from 573 K to 673 K. The circulation of the nanoparticles inside the vortices could enlarge the residence time τ and lead to further growth of them. This is in contrast to the decrease of the density ρ and an increase of the flow velocity v_3. The density effect surpasses the vortex effect and results in a decrease of the residence time τ for increasing temperatures. The pressure p also affects the thermal and velocity profiles. As already explained, the enthalpy h is increasing with decreasing pressure from 35 MPa to 25 MPa. This leads to higher heating rates and a lower impact of the cold water stream entering the mixer at lower pressure. The lower density decreases the residence time τ. At last, the effect of the mixing ratio a was investigated. For the lower mixing ratio, a of 0.05, the affection of the cold water stream through the hot water stream was more significant than the higher one of 0.35. This increases the buoyancy convection. An increase leads to the domination of the forced convection over the buoyancy convection. This results in no formation of circular flows. A higher value of a further decreases the mixing temperature T_3.

8.2 Residence time distribution (RTD)

Based on the thermal and velocity fields simulation, the RTD curves were simulated and are discussed in the following. For the simulations, six sets of process conditions were chosen. These are summarized in Table 8-1. The simulation of the RTD is essential for the description of the phenomena during particle formation experiments for the mean residence time τ.

Table 8-1: Used process conditions to simulate the RTD curves for the Counter model and calculated mean residence time (equation (7-3) and respected volume of the mixer and reactor tube of 1.185 10^{-6} m^3).

set	p / MPa	$\dot{m}_3$ / g min^{-1}	T_2 / K	a / -	τ_{calc} / s
1	25	35	573	0.05	1.51
2	25	55	573	0.05	0.96
3	35	35	573	0.05	1.54
4	35	35	673	0.05	0.97
5	25	35	673	0.35	0.34
6	35	35	673	0.35	0.97

The simulations of the RTD curves were carried out according to the method described in section 5.2.3 for all models. The results next to the Counter model are found in H: RTD curves for the Straight, Bending and Y-30 models. The values shown in Table 8-1 were selected to compare the influence of the single process conditions on the resulting RTD. Figure 8-7 shows the results of the simulated RTD curves for the Counter model based on the simulations of the thermal and the velocity fields with the tracer injected at the inlet of the hot water stream:

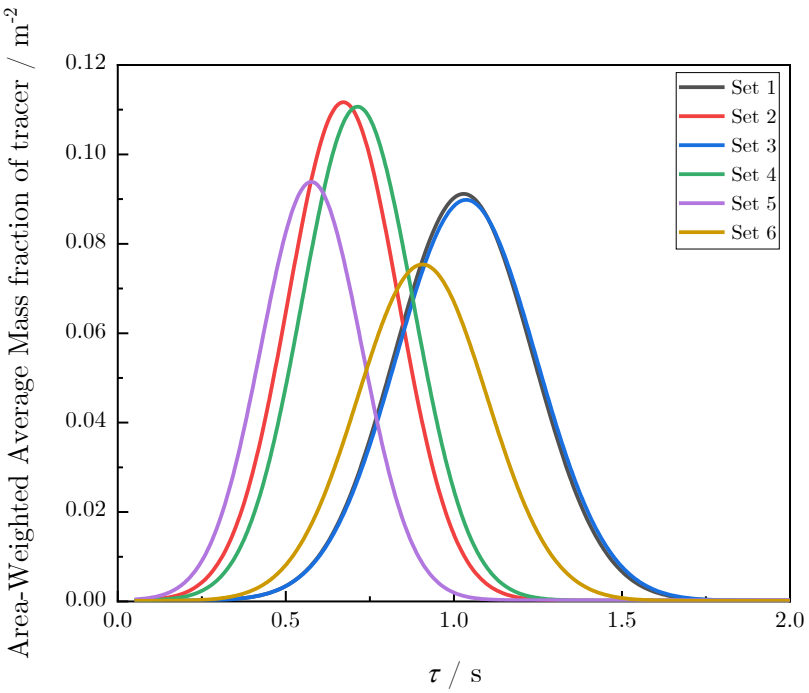

Figure 8-7: Trend of the Area weighted average mass fraction of tracer as a function of the mean residence time τ representing the RTD curve for different process conditions with the Counter model and the injection of the tracer from the inlet of the hot water stream [153].

The results of the RTD curves show the influence of the different process conditions on the mean residence time τ. The residence time was calculated according to equation (7-3) from the mixing point to the inlet of the cooler respecting the volume of the used tubes ($1.185\ 10^{-6}$ m^3). The simulation of the RTD was then compared to the calculated values shown in Table 8-1. In general, the simulated values of the RTD fit to the mean residence times τ. Set 1 and Set 3 show the variation of the pressure p and its influence on the RTD for a nearcritical hot water temperature T_2 of 573 K. Regarding the pressure dependence of the density ρ in the nearcritical region, the values are showing no considerable difference between 25 MPa and 35 MPa ($\Delta\rho = 14.69$ kg m^{-3}). This aspect indicates that the variation in the pressure p has no significant effect on the RTD. In contrast, the variation of the pressure p in the supercritical region for temperatures of 673 K has a particular impact. The difference in both densities between 25 MPa and 35 MPa equals to 192.49 kg m^{-3}. The lower density ρ for a pressure of 25 MPa leads to an increase in the flow velocity of the mixing stream v_3 compared to a pressure of 35 MPa. This has a direct influence and leads to a shift to shorter residence times τ. The variation of the hot water temperature T_2 has the same effect on the RTD as the change in the pressure from 35 MPa to 25 MPa. Set 3 and Set 4 show this influence (compare Table 8-1). An increase of T_2 from 573 K to 673 K leads to a decrease of the density ρ, an increase of the flow velocity v_3 and a shift of the RTD to shorter residence times τ. Set 1 and 2 represent the influence of the change of the total mass flow $\dot{m}_3$ from 35 g min^{-1} to 55 g min^{-1}. Both the pressure p and the hot water temperature T_2 decrease the residence time τ. Finally, the influence of the mixing ratio a on the RTD was analyzed. This is visible through sets 4 and set 6. Since the tracer explained in section 5.2.3 is injected at the inlet of the hot water stream, the mixing ratio directly influences the RTD. An increase of the mixing ratio a from 0.05 to 0.35 results in a decrease in the flow velocity v_2 and an increase of the residence times τ.

The location of the injection of the tracer has a particular effect on the RTD curves. The injection at the inlet of the hot water stream represents the mean residence time τ in good accordance with the mixing stream. The injection of the tracer at the inlet of the cold water stream is illustrated in Figure 8-8:

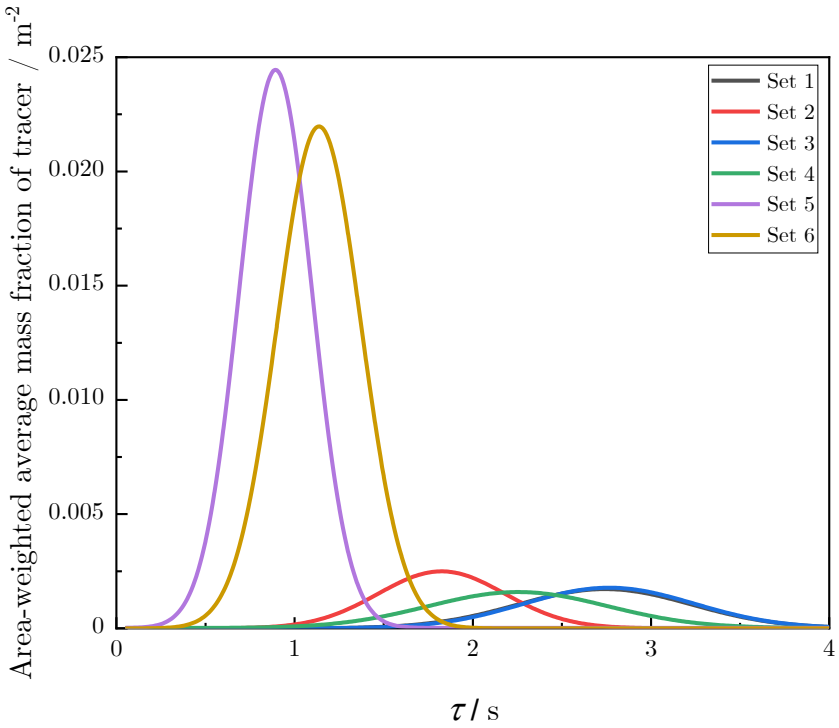

Figure 8-8: Trend of the Area weighted average mass fraction of tracer as a function of the mean residence time τ representing the RTD curve for different process conditions with the Counter model and the injection of the tracer from the inlet of the cold water stream [153].

In contrast to the tracer injection at the inlet of the hot water stream, the RTD curves show a different nature for the injection of the tracer at the inlet of the cold water stream. As the mean residence times τ fit to the calculated values for the hot inlet, the deviation is significant for the cold inlet. This is due to the low mixing ratios a used in the single simulations. A mixing ratio a of 0.05 for a total mass flow $\dot{m}_3$ of 35 g min^{-1} and a pressure of 30 MPa shows a flow velocity of 0.0137 m s^{-1}. This leads to an increase in the mean residence time τ. It takes more time until the cold flow is mixed up with the hot water stream and accelerated to the mean flow velocity v_3. Increasing the mixing ratio a from 0.05 to 0.35 leads to an increase in the flow velocity of the cold water stream v_1 up to 0.074 m s^{-1}. Due to this, the RTD curves for the Sets 5 and 6 are shifted to shorter residence times τ. Anyhow, the previously described effects in Figure 8-7 are also visible for the injection at the inlet of the cold stream. An increase of both the hot water temperature T_2 from 573 K to 673 K and the total mass flow $\dot{m}_3$ from 35 g min^{-1} to 55 g min^{-1} is also shifting the RTD curves to shorter residence times τ. Anyhow, the simulated values are not representative and comparable to the calculated mean residence times τ. Therefore, the simulated RTD curves with the injection at the hot inlet are considered for further analyses.

8.3 Simulation of the reaction

After successfully simulating the thermal and velocity fields and the RTD, the occurring reaction during the CHTS process was considered and analyzed. The UDF described in section 5.2.2 was extended by the kinetic approach for the reaction of $Ce(NO_3)_3$ to CeO_2. Due to the fast hydrolysis, the two reactions were combined to a global reaction shown in section 2.2 (compare equation (2-34)). First, the profiles of the dielectric constant ε were simulated to locate spatial differences inside the mixer and the reaction tube. Then, the influence of the process conditions on the concentration profiles for the educts and products was investigated. This was performed with the simulation of the reaction for experiments described in section 7.2 with the CHTS plant. Finally, a case study of the variation of the mixing ratio a was performed to optimize the process and identify the best process conditions regarding the particle size and especially the PSD.

8.3.1 Simulation of the profiles of the dielectric constant

Due to the strong dependence of the rate constant k on the dielectric constant ε, the profile over the mixer and reaction tube is of interest. The knowledge of ε inside the hot zone of the mixing unit directly shows the quality of the used process conditions for the later particle formation and the relating PSD. In general, the dielectric constant ε is tunable with the variation of the pressure p and the temperature of the hot water stream T_2. Figure 8-9 shows the profile of the dielectric constant ε in the mixer for two different pressures p and a supercritical hot water temperature T_2 of 673 K for the Counter model:

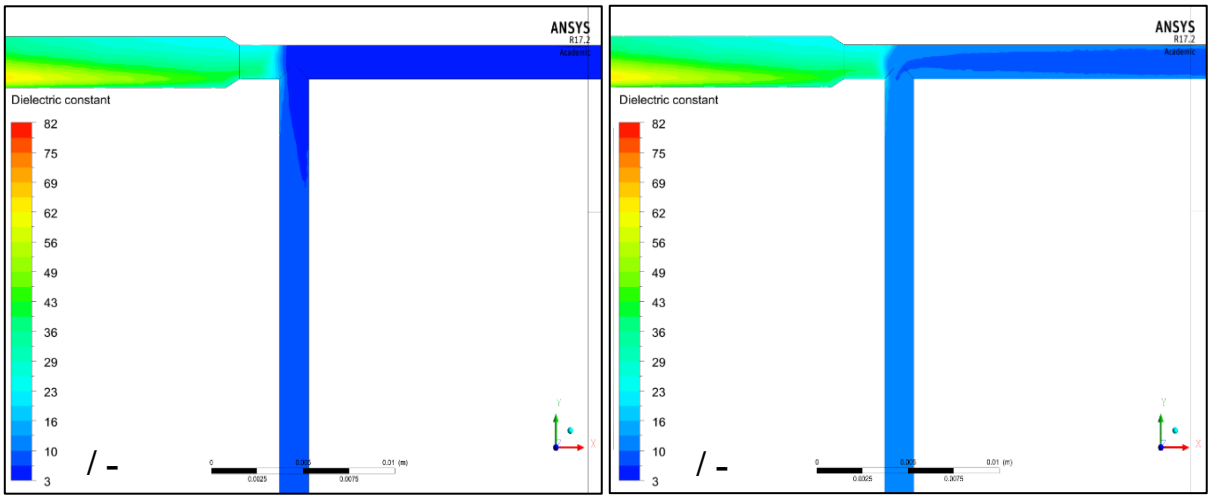

Figure 8-9: Profiles of the dielectric constant ε inside the mixing unit for different pressures p. The hot water temperature T_2 equals to 673 K, the total mass flow $\dot{m}_3$ to 35 g min^{-1} and the mixing ratio a to 0.1. The pressure p was set to 25 MPa (left side) and 35 MPa (right side).

The dielectric constant ε is a function of the pressure p and the temperature T (compare section 2.2, Figure 2-7). With increasing pressure from 25 MPa to 35 MPa, the density ρ is also growing. The density ρ and the dielectric constant ε are proportional. In addition to that,

ε is rising from 2.51 to 8.94 from 25 MPa to 35 MPa. It is directly shown in Figure 8-9. For the lower pressure of 25 MPa, the profile shows lower values for ε after the mixing point than those with 35 MPa. Furthermore, the value of ε is at the minimum right at the mixing point. Due to the penetration of the cold water stream, ε slightly increases with increasing distance from the mixing point. For a pressure p of 35 MPa, there is an inhomogeneous profile of ε in front of the mixing point in the tube of the hot water stream. At the mixing point, the cold water stream affects the hot water stream and ε. After the mixing point, a homogeneous distribution of ε is obtainable. The increase of ε with the pressure p results in a lower rate constant k (compare equation (2-35)). This information is essential for explaining the resulting particle size and the related PSD for the experiments. After comparing the influence of the pressure p on the dielectric constant ε, the impact of the hot water temperature T_2 was investigated. Figure 8-10 shows the results of the simulation of the dielectric constant ε for near- and supercritical hot water temperatures:

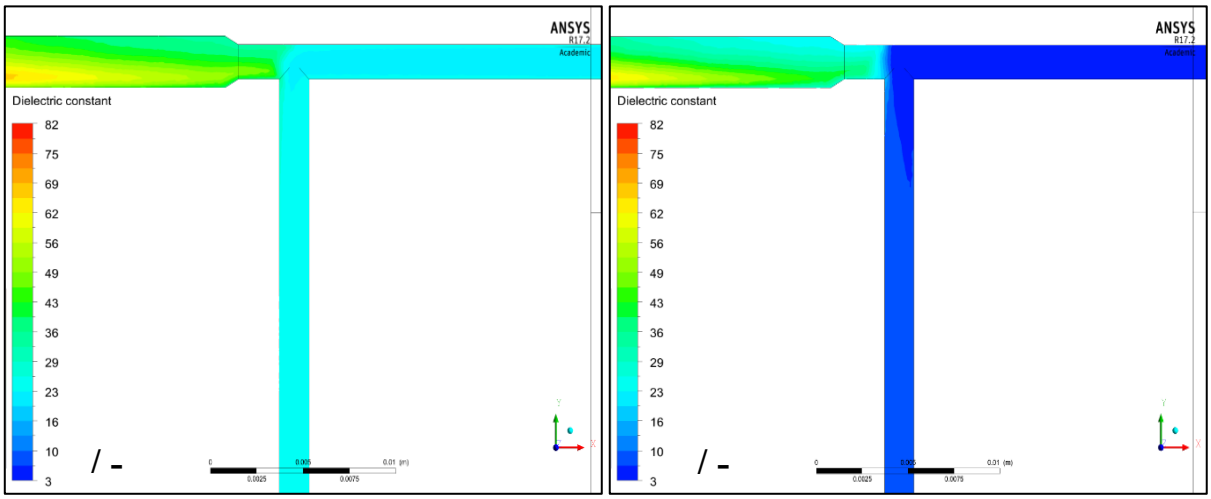

Figure 8-10: Profiles of the dielectric constant ε inside the mixing unit for different temperatures T. The pressure p equals to 25 MPa, the total mass flow $\dot{m}_3$ to 35 g min^{-1} and the mixing ratio a to 0.1. The hot water temperature T_2 was set to 573 K (left side) and 673 K (right side).

The influence of the hot water temperature T_2 on the dielectric constant ε at constant process conditions is drastic. The minimum value of ε for 573 K is around 21.5. This is approximately 8.6 times higher compared to the value of ε for 673 K and 25 MPa. The profile shows a homogeneous distribution of ε. Right at the mixing point, the values of ε for the cold and the hot water stream become equal. Due to the high value of ε for 573 K compared to 673 K, the rate constant k is decreased (compare Figure 2-8), and the solubility of $Ce(NO_3)_3$ increased. This results in a slower reaction and a lower nucleation rate. Besides that, the mean residence time is increased (compare Figure 8-7).

The profiles of the dielectric constant are important for the explanation of the rate constant and the solubility equilibria. Based on that knowledge, the concentration profiles of the educt ($Ce(NO_3)_3$), the products (CeO_2, HNO_3, and H_2), and the bulk phase (water) were simulated.

8.3.2 Simulations of the reaction with real process conditions

The simulations were carried out with process conditions according to the first particle formation experiments with the CHTS plant and $Ce(NO_3)_3$ as a precursor. The investigated process conditions are listed in Table 7-1. For these, the influence of variating the process conditions on the nature of the concentration profiles is analyzed. Figure 8-11 shows the single concentration profiles of all involved species with the process conditions for the second particle formation experiment (exp. no. 2, Table 7-1): The following simulations are described with the concentration profiles of $Ce(NO_3)_3$ and CeO_2. The other concentration profiles can be found in Appendix chapter 8.

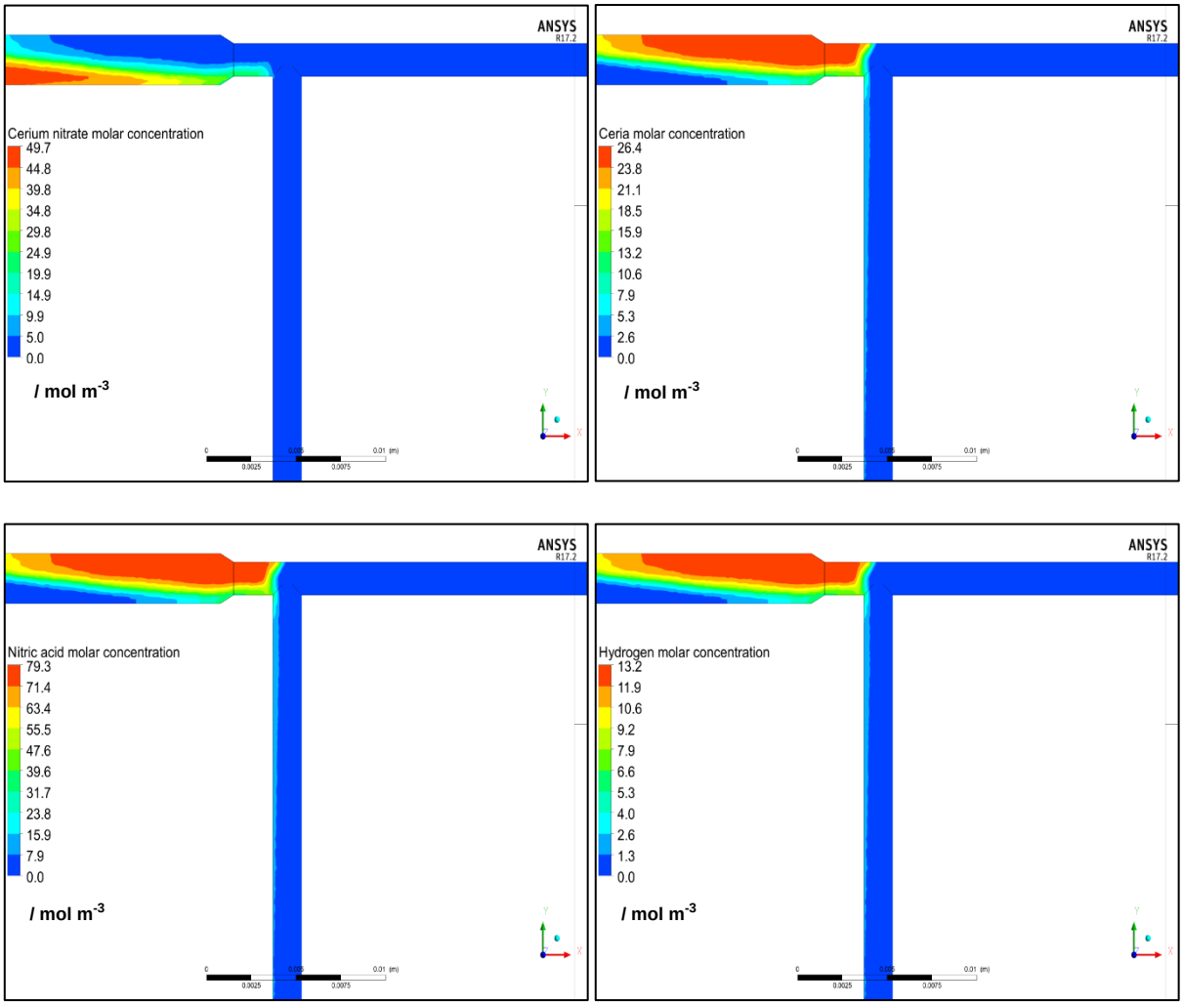

Figure 8-11: Concentration profiles of the used educts and products ($Ce(NO_3)_3$ on the left top side, CeO_2 at the top right side, HNO_3 at the bottom left side, and H_2 at the bottom right side) inside the mixing unit. The pressure p was set to 30 MPa, the hot stream temperature T_2 to 673 K, the total mass flow $\dot{m}_3$ to 35 g min^{-1} and the mixing ratio a to 0.1. The salt concentration c_{salt} was adjusted to 0.05 mol dm^{-3}.

The 0.05 mol dm^{-3} $Ce(NO_3)_3$ solution is injected at the inlet on the cold stream. The adjustment of the correct salt concentration c_{salt} is shown with the maximum value of the legend of 49.7 mol m^{-3} what equals to 0.05 mol dm^{-3}. With an increasing length from the inlet of the cold

stream, the concentration profile of the $Ce(NO_3)_3$ solution is changing. Right after the inlet, the reaction occurs at the top part of the tube. At the bottom part of the tube, the reaction occurs later, right before the mixing point. The start of the reaction is visible through the change in the concentration of $Ce(NO_3)$. The counterpart of the concentration profile of $Ce(NO_3)_3$ is shown with the concentration profiles of CeO_2, HNO_3, and H_2. The reaction occurs, and $Ce(NO_3)_3$ reacts with H_2O to the products in combination with water as the bulk phase. It is visible that the reaction happens in front of the mixing point where the highest concentrations of the product species are present. After the mixing point, the CeO_2 is diluted from the hot water stream. This means that no further CeO_2 is produced after the mixing point and in the reaction tube. A high conversion is assumed. In addition to the concentration profiles of the involved species, the profile of the mass fraction of water is also important for the reaction. Figure 8-12 shows the mass fraction profile of water inside the mixing unit. Due to the reaction in the liquid phase, H_2O acts as a solvent.

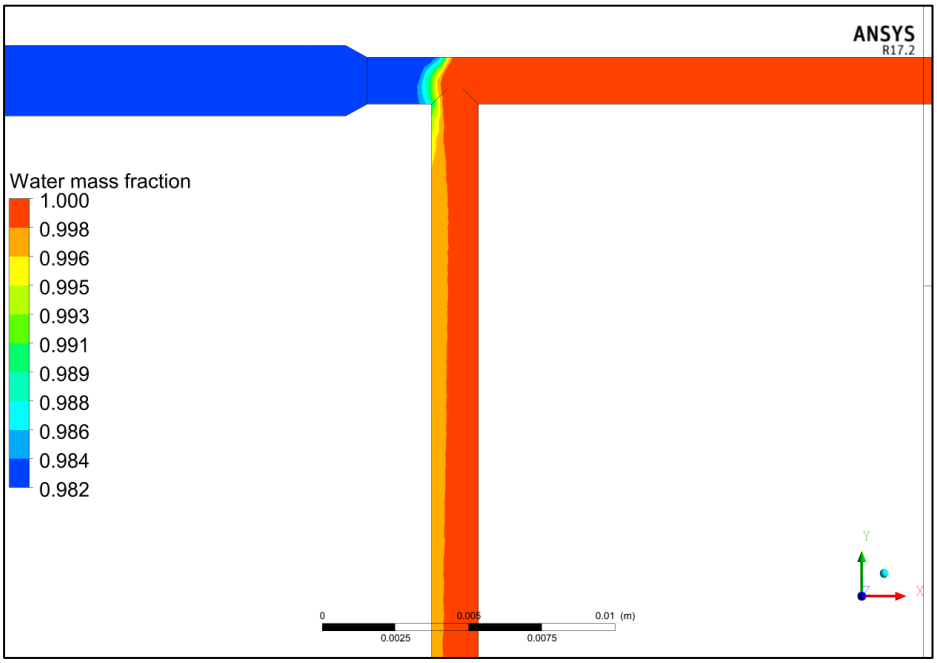

Figure 8-12: Mass fraction profile of H_2O inside the mixer for a pressure p of 30 MPa, a hot stream temperature T_2 of 673 K, a total mass flow $\dot{m}_3$ of 35 g min^{-1} and a mixing ratio a of 0.1. The salt concentration c_{salt} was adjusted to 0.05 mol dm^{-3}.

Figure 8-11 shows the reaction location in the cold stream in front of the mixing point, where the mass fraction of H_2O is lowered. This follows the occurring reaction where $Ce(NO_3)_3$ reacts with H_2O to CeO_2, HNO_3, and H_2. The dilution process of CeO_2 after the mixing point is even more precise (Figure 8-12) compared to the image in Figure 8-11 on the top right side. The mass fraction of H_2O is lowered at the left part of the tube after the mixing point where CeO_2 is present. For the mass fraction, the composition of the reaction mixture is known at each point inside the mixing unit. Furthermore, the simulation of the reaction is validated with the summation of the mass fractions. Due to the mass conversation, the summary of all mass

fractions of the species involved needs to result in a value of 1. The mass fractions of the other species are shown in the following image:

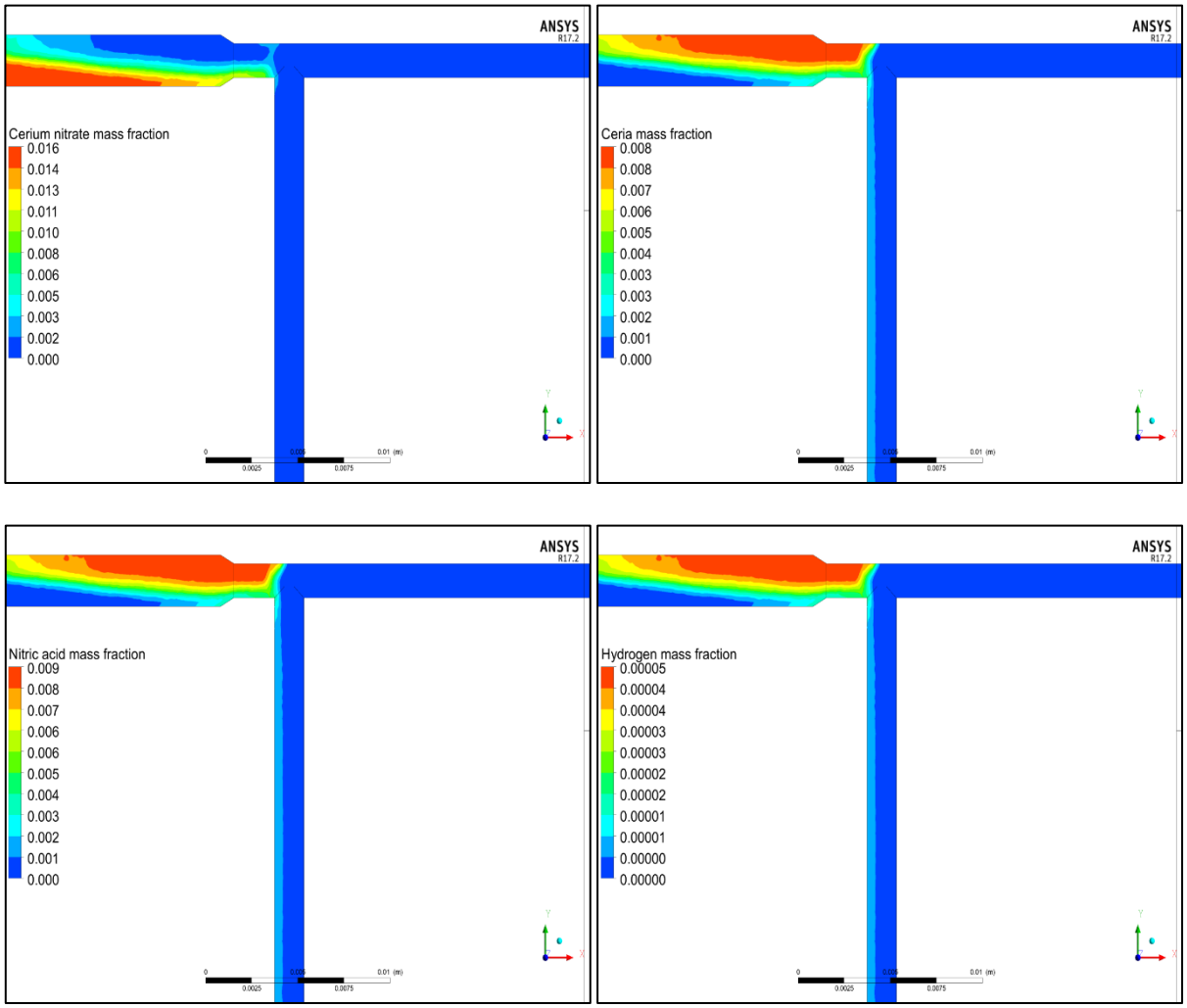

Figure 8-13: Mass fraction profiles of the used educts and products ($Ce(NO_3)_3$ on the left top side, CeO_2 at the top right side, HNO_3 at the bottom left side, and H_2 at the bottom right side) inside the mixing unit. The pressure p was set to 30 MPa, the hot stream temperature T_2 to 673 K, the total mass flow $\dot{m}_3$ to 35 g min^{-1} and the mixing ratio a to 0.1. The salt concentration c_{salt} was adjusted to 0.05 mol dm^{-3}.

The mass fractions of the additional simulations are found in Appendix chapter 8. The summation of the single mass fractions shown in Figure 8-12 and Figure 8-13 equals to 1, which leads to the assumption that the simulations of the reaction show the correct results. As a next step, further simulations are used to analyze the influence of the process conditions on the reaction and the concentration profiles. The concentration profiles of exp. no. 1 and 3, 4, and 5 (compare Table 7-1) are also shown in Appendix chapter 8.

After the investigation of the influence of both the salt concentration c_{salt}, and the total mass flow $\dot{m}_3$, the effect of the hot water temperature T_3 on the reaction was analyzed. Figure 8-14 shows the results of the simulations of the exp. no. 6 (compare Table 7-1) for a nearcritical hot

water temperature T_2 of 573 K and a salt concentration c_{salt} of 0.05 mol dm^{-3}. The concentration profiles for experiments 7, and 8 and the related discussion are found in Appendix chapter 8.

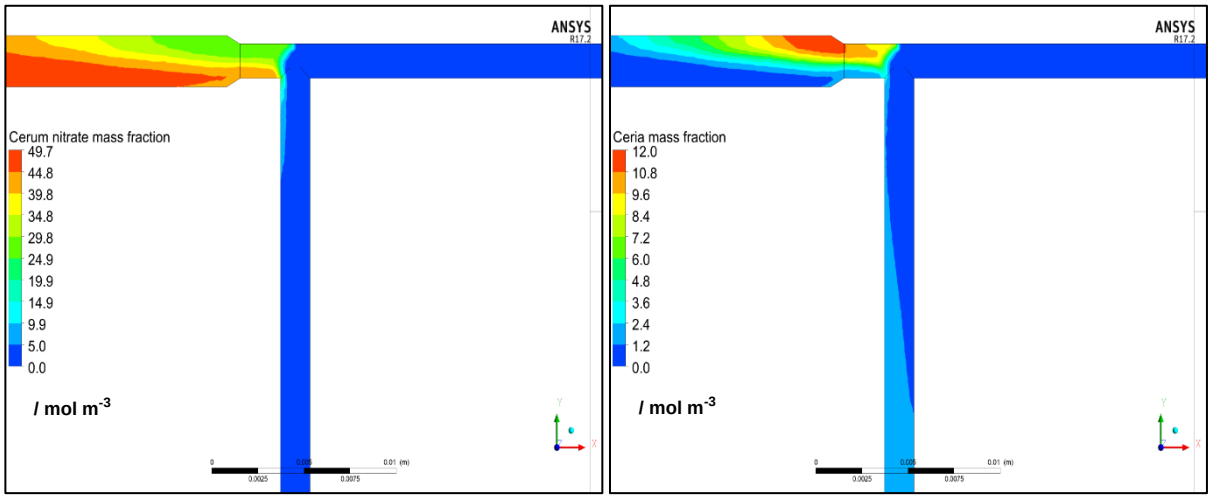

Figure 8-14: Concentration profiles of the used educts and products ($Ce(NO_3)_3$ on the left side, and CeO_2 on the right side) inside the mixing unit. The pressure p was set to 30 MPa, the hot stream temperature T_2 to 573 K, the total mass flow $\dot{m}_3$ to 35 g min^{-1} and the mixing ratio a to 0.1. The salt concentration c_{salt} was adjusted to 0.05 mol dm^{-3}.

In contrast to the simulations with 673 K, the concentration of $Ce(NO_3)_3$ is not significantly lowered after the mixing point. This indicates that the reaction is still occurring for the lower temperature of 573 K, even after mixing up the cold aqueous metal salt solution with the hot water stream. This is further clarified by the presence of CeO_2 in the reaction tube after the mixing point. The reaction is still running after the mixing point. The low rate constant k at temperatures of 573 K compared to the values at 673 K leads to the ongoing reaction after the mixing point. With increasing salt concentration c_{salt}, the effect grows, and more CeO_2 is present in the reaction tube. The above-shown results of the simulations showed the influence of the salt concentration c_{salt}, the total mass flow $\dot{m}_3$ and the hot water temperature T_2 on the concentration profiles for the species involved in the reaction (compare Appendix chapter 8). The simulations and the experiments were carried out at a constant pressure p of 30 MPa. As previously described, p strongly affects the rate constant k (compare section 2.2, Figure 2-8). Therefore, a simulation of exp. no. 30 was carried out with the respecting process conditions at 25 MPa (compare Table 7-1). The influence of the pressure p and the salt concentration c_{salt} on the concentration profiles was obtained. The concentration profiles of the experiments 31, and 34 and the related discussion can be found in Appendix chapter 8.

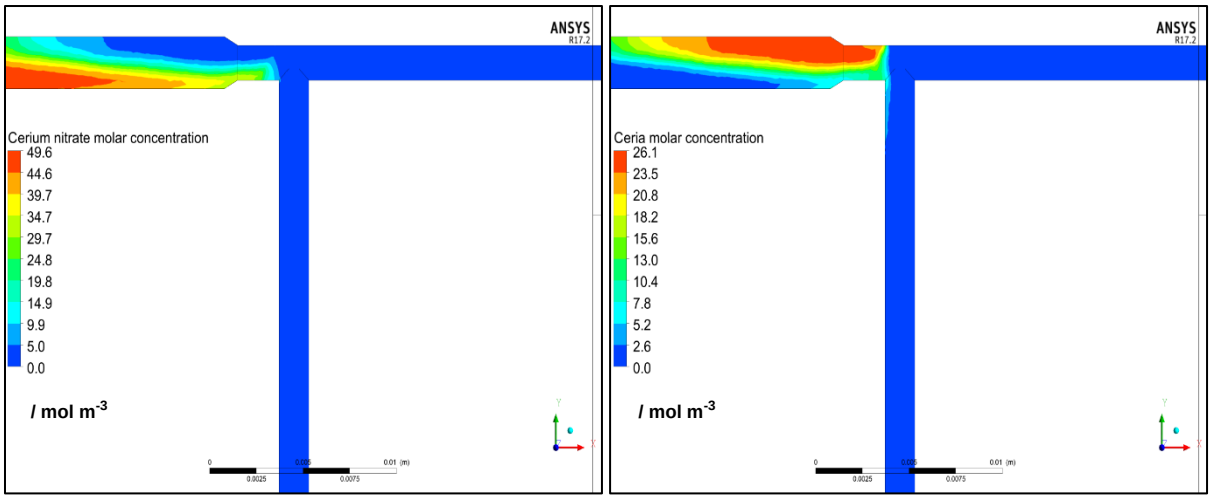

Figure 8-15: Concentration profiles of the used educts and products ($Ce(NO_3)_3$ on the left side, and CeO_2 on the right side) inside the mixing unit. The pressure p was set to 25 MPa, the hot stream temperature T_2 to 673 K, the total mass flow $\dot{m}_3$ to 35 g min^{-1} and the mixing ratio a to 0.1. The salt concentration c_{salt} was adjusted to 0.05 mol dm^{-3}.

Compared to Figure 8-11, the reaction starts earlier for 25 MPa in the tube of the cold stream. This is due to the higher amount of required energy for the heating of the hot water stream. Furthermore, the influence of the cold stream is lowered due to the higher enthalpy h for 25 MPa compared to 30 MPa. The other parts of the concentration profiles look similar to the pressure of 30 MPa. The produced CeO_2 is also directly diluted at the mixing point. This leads to the assumption that the conversion nearly completed at the mixing point.

The simulations of the concentration profiles for all species involved were carried out with the process conditions of the experiments. The results explain the underlying phenomena of the particle formation. All simulations show the start of the reaction in front of the mixing point. This aspect is of interest for a potential clogging of the mixer or the quality of the resulting PSD of the formed CeO_2 nanoparticles. Ideally, the reaction should start right at the mixing point after mixing the cold and the hot water stream. Mixing ratios a between 0.05 and 0.1 showed a start of the reaction in front of the mixing point in the tube of the cold stream (573 K and 673 K). Therefore, a case study was performed with simulations of the reactions for different mixing ratios to optimize the CHTS process. The theoretical case study led to the optimal value for the mixing ratio a of 0.35. The respecting concentration profiles are illustrated in Figure 8-16:

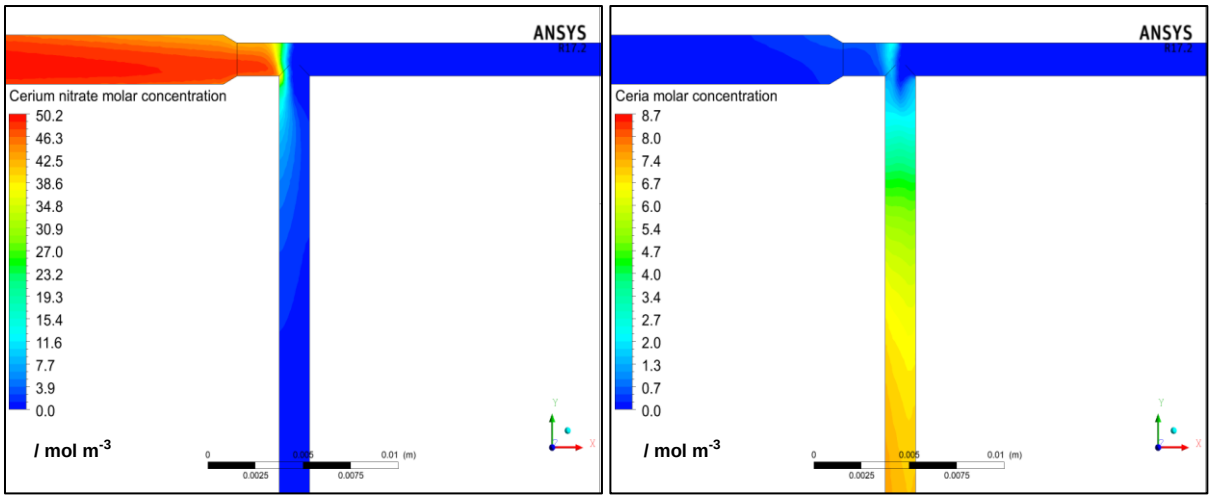

Figure 8-16: Concentration profiles of $Ce(NO_3)_3$ (left side) and CeO_2 (right side) for a pressure p of 30 MPa, a hot water temperature T_2 of 673 K, a total mass flow $\dot{m}_3$ of 35 g min^{-1}, a salt concentration c_{salt} of 0.05 mol dm$^{-3,}$ and a mixing ratio a of 0.35 [154].

An increase of the mixing ratio from 0.05 / 0.1 to 0.35 resulted in a shift of the start of the reaction. For lower values of a, the reaction occurred at the inlet of the cold aqueous metal salt solution due to heating the cold stream through high temperatures of the stainless-steel T-junction. For the increase to values of 0.35, the cold stream $\dot{m}_1$ is increased. This increases the flow velocity of the cold stream v_1. This interaction of both streams is enlarged and leads to a decrease in the mixing temperature T_3. The required temperature for the start of the reaction is reached close to the mixing point. These effects result in the shift of the reaction to the mixing point and the formation of CeO_2 after mixing. The location of the reaction may explain the difference in the resulting PSD shown in Figure 7-6. Once the reaction takes place in front of the mixing point for the supercritical temperatures of 673 K, the nanoparticles are instantly formed. The respecting residence time is changed due to the stagnation point in front of the mixing point. For the nearcritical temperature of 573 K, the reaction also occurs in front of the mixing point. However, the rate constant k is low, resulting in a slow reaction and increased particle growth. By increasing the mixing ratio a from 0.05 to 0.35, the width of the PSD for the supercritical temperatures of 673 K could be decreased to form more homogeneous nanoparticles with these high temperatures.

Based on the above-shown results, the simulations were carried out first to see the influence of the process conditions on the thermal and velocity field. After that, the RTD curves were simulated and analyzed concerning the impact on the mean residence time τ. Based on the thermal and velocity fields simulations, the reactions were simulated with the reaction kinetics for the formation of CeO_2 from $Ce(NO_3)_3$. The main effects were analyzed, and the process optimization was carried out to shift the start of the reaction from the left side (tube of the cold stream) of the mixer to the mixing point. These new findings were used to explain the different widths of the resulting PSDs from the experiments carried out with the CHTS plant.

9. Summary and outlook

In this work the formation of metal-oxide nanoparticles with the CHTS was investigated.

First, the estimation of the metal salt solubility was considered as it is an important topic for the modeling of the CHTS process. Therefore, the r-HKF and the SAA model were applied and implemented to calculate the equilibrium constants of the single reactions occurring during a dissolution process of a metal salt. The implemented models were validated with literature data of the equilibrium constants for NaCl. The solubility was estimated based on the calculation of the ionic strength with an iterative calculation method using different activity coefficient models. With this routine, the solubility of different metal salts was estimated. The trends were then compared to classify the metal salts either into type 1 or type 2. The estimated solubility of three different metal salts was then validated with experimental values.

For the experimental investigation a lab-scale pilot plant was constructed, build up, and optimized for the CHTS of metal-oxide nanoparticles. It was dimensioned up to a maximum pressure p of 38 MPa, a maximum temperature T of 773 K, and a total mass flow $\dot{m}_3$ of 4.8 kg h^{-1} (80 g min^{-1}). The variable design of the reaction zone enabled the easy assembly of different reactors and mixers. After the setup, the plant was characterized through mixing experiments with pure water.

The main experimental goal of this work was the investigation of the influence of the different process conditions (p, T, $\dot{m}_3$, c_{salt}) on the relating size and shape of the ceria nanoparticles. The influence of metal salt precursors ($Ce(NO_3)_3$, $Ce_2(SO_4)_3$ and $Ce(CH_3COO)_3$) was analyzed. to determine the effect of the variation of the anion.

The first experiments showed that the experimental data published in literature were reproducible with the CHTS plant. The synthesized nanoparticles were analyzed with TEM and PXRD. The PXRD analysis showed all reflections of CeO_2 what guaranteed that ceria nanoparticles were formed during the experiments. In further experiments, the salt concentration c_{salt}, and the total mass flow $\dot{m}_3$ were varied. The increase of the salt concentration resulted in an increase of the particle size. The increase of the total mass flow led to shorter residence times of the nanoparticles inside the hot reaction zone of the plant. In addition to that, experiments with nearcritical temperatures of 573 K were performed. For lower temperatures, no particle formation was obtainable. With increasing temperature, the median particle size was decreasing due to the increase of the rate constant and the decrease of the dielectric constant. This effect was also obtainable with the reduction of the pressure from 30 MPa to 25 MPa. This resulted in a further decrease in the median particle size. To investigate the effect of the variation of the anion, $Ce_2(SO_4)_3$ and $Ce(CH_3COO)_3$ were chosen for the following particle formation experiments. $Ce_2(SO_4)_3$ as a precursor resulted in a decrease in the median particle size at constant process conditions. The comparison was carried out at a temperature of 573 K, and the median particle sizes were around 18 nm. Even for lower temperatures of 523 K, ceria nanoparticles were formed. With the change of the metal salt, the

CHTS process required less energy, decreasing the required heating power. On the other hand, the low solubility of $Ce_2(SO_4)_3$ led to instant clogging of the mixer and the whole mixing unit. The mixing setup was changed from the Counter to the Straight configuration. Clogging was prevented due to the penetration of the cold stream into the hot stream at a 90° angle sideways. With $Ce(CH_3COO)_3$ as a precursor, even lower temperatures than 523 K were used to synthesize ceria nanoparticles. The examination of the influence of the process conditions on the median particle size fits to the results with $Ce(NO_3)_3$ for the increase of the total mass flow and the variation of the salt concentration. The change of the metal salt as a precursor from $Ce(NO_3)_3$ to $Ce_2(SO_4)_3$ and $Ce(CH_3COO)_3$ led to a steady decrease of the median particle size. The synthesized nanoparticles with $Ce(CH_3COO)_3$ showed the smallest median particle size with the most homogeneous particles. With the variation of the process conditions pressure, temperature, total mass flow, and salt concentration combined with the change of the metal salt as a precursor, the median particle size and the related PSD were tunable. Changing the precursor from $Ce(NO_3)_3$ to $Ce(CH_3COO)_3$ lead to a decrease of the mixing temperature of 200 K.

In addition, two ceramic tubes were integrated into the CHTS plant for the performance of impedance spectroscopy measurements. Experiments were carried out to study the stability and the change of the impedance over time. The influence of ceria nanoparticles was obtained through experiments with deionized water, a ceria suspension and a ceria suspension containing $Ce(NO_3)_3$. The impedance remained constant for the ceria suspension, whereas the impedance decreased for the $Ce(NO_3)_3$ containing suspension. These results in combination with the stability tests show that the impedance spectroscopy is suitable for the determination of the conversion during particle formation experiments.

The experimental work was supported by a theoretical investigation of the CHTS process with CFD simulations. Therefore, 3D CAD models were designed with different mixing setups and implemented into ANSYS Fluent®. The models were meshed after designing the CAD models. The Counter model and the Straight model were validated with experimentally determined values of the mixing temperature measured with the CHTS plant. The mean error for both models was in a reasonable range. Based on the simulation of the thermal and the velocity fields, the simulation of the RTD was carried out. The influence of the single process conditions on the RTD was examined and related to the phenomena during the particle formation experiments. Beyond the analysis of both the fields and the RTDs, the reaction from $Ce(NO_3)_3$ to CeO_2 was investigated. The field of the dielectric constant for water was analyzed as a function of pressure and temperature. After that, the thermal and velocity fields simulations were used and extended by the reaction. The kinetic behavior relating the rate constant k with the dielectric constant within a Born type equation was also applied with a UDF. The influence of the process conditions on the reaction was investigated. Beyond that, a case study of the mixing ratio was carried out to identify the best operation conditions regarding the particle size and the related PSD. A value of 0.35 for the mixing ratio led to reaction at the mixing point and was used for further simulations.

For future works concerning the estimation of the metal salt solubility, more experimental data are required to calculate the equilibrium constants with the r-HKF model. With more experimental data, further reactions during the dissolving process can be examined, which increases the iterative calculation's accuracy. This would enable the correct calculation of the equilibrium constants of the CeO_2 system. The CeO_2 solubility would then be estimated through the summation of the single molalities of the involved species and the simulation of the particle formation.

For the experimental setup of the CHTS plant, a magnetic valve for a better control of the pressure could be installed in a further optimization step. In addition, the heating power should be enlarged to optimize the heating of higher total mass flows than 3.3 kg h^{-1} in the future. The influence of the residence time on the quality and the median particle size could be obtained in the future with an elongated reaction tube. The CHTS plant was prepared with a variable extension of the reaction tube (compare section 4.3). The variation of the residence time allows the investigation of the kinetic behavior of other metal salts. Furthermore, another tube connection for the surface modification of the metal-oxide nanoparticles was implemented. In the future, the synthesis of several types of metal-oxide nanoparticles is possible. The preparations allow the formation of organic surface modified, metal doped and clickable metal-oxide nanoparticles. Concerning EIS, further investigations are required to set up an impedance system for the in situ control of the CHTS process.

Regarding the simulation of the reaction, kinetic data of $Ce(NO_3)_3$ from literature were applied. For $Ce_2(SO_4)_3$ and $Ce(CH_3COO)_3$ no kinetic data are available. In terms of further possible future works, the solubility of ceria for elevated pressures and temperatures needs to be estimated as already mentioned above.

The simulation of the particle formation could be realistic in the future after the estimation of the ceria solubility at elevated pressures and temperatures. The supersaturation at given pressure and temperature is then calculated with the estimated solubility. Based on these values, it is possible to either calculate the nucleation rate or the growth rate. This is realized in combination with a population balance module in ANSYS Fluent®. The particle size distribution is then shown as a profile inside the mixer and the reaction tube and in a relating PSD.

10. References

[1] T. Adschiri, K. Kanazawa, K. Arai; *Rapid and Continuous Hydrothermal Crystallization of Metal Oxide Particles in Supercritical Water*, Journal of American Ceramic Society 4 (1992) 1019–1022.

[2] I. Prigogine, S. A. Rice; *Advances in Chemical Physics*, John Wiley & Sons, Hoboken (1967).

[3] H. C. Helgeson, D. H. Kirkham, G. C. Flowers; *Theoretical prediction of the thermodynamic behavior of aqueous electrolytes by high pressures and temperatures: IV, Calculation of activity coefficients, osmotic coefficients, and apparent molal and standard and relative partial molal properties to 600°C and 5kb*, American Journal of Science 281, 10 (1981) 1249–1516.

[4] K. Sue, T. Adschiri, K. Arai; *Predictive Model for Equilibrium Constants of Aqueous Inorganic Species at Subcritical and Supercritical Conditions*, Industrial & Engineering Chemistry Research 41, 13 (2002) 3298–3306.

[5] T. Noguchi, K. Matsui, N. M. Islam, Y. Hakuta, H. Hayashi; *Rapid synthesis of γ-Al_2O_3 nanoparticles in supercritical water by continuous hydrothermal flow reaction system*, The Journal of Supercritical Fluids 46, 2 (2008) 129–136.

[6] Y. Roig, S. Marre, T. Cardinal, C. Aymonier; *Synthesis of Exciton Luminescent ZnO Nanocrystals Using Continuous Supercritical Microfluidics*, Angewandte Chemie 123, 50 (2011) 12277–12280.

[7] K. Sue, K. Murata, K. Kimura, K. Arai; *Continuous synthesis of zinc oxide nanoparticles in supercritical water*, Green Chemistry 5, 5 (2003) 659–662.

[8] K. Sue, S. Kawasaki, M. Suzuki, Y. Hakuta, H. Hayashi, K. Arai, Y. Takebayashi, S. Yoda, T. Furuya; *Continuous hydrothermal synthesis of Fe_2O_3, NiO, and CuO nanoparticles by superrapid heating using a T-type micro mixer at 673 K and 30 MPa*, Chemical Engineering Journal 166, 3 (2011) 947–953.

[9] Y. Hao, A. S. Teja; *Continuous hydrothermal crystallization of α-Fe_2O_3 and Co_3O_4 nanoparticles*, Journal of Materials Research 18, 2 (2003) 415–422.

[10] T. Sato, K. Sue, W. Suzuki, M. Suzuki, K. Matsui, Y. Hakuta, H. Hayashi, K. Arai, S. Kawasaki, A. Kawai-Nakamura, T. Hiaki; *Rapid and Continuous Production of Ferrite Nanoparticles by Hydrothermal Synthesis at 673 K and 30 MPa*, Industrial & Engineering Chemistry Research 47, 6 (2008) 1855–1860.

[11] M. Daschner de Tercero, C. Röder, U. Fehrenbacher, U. Teipel, M. Türk; *Continuous supercritical hydrothermal synthesis of iron oxide nanoparticle dispersions and their characterization*, Journal of Nanoparticle Research 16, 4 (2014) 1–27.

[12] B. Palanisamy, B. Paul; *Continuous flow synthesis of ceria nanoparticles using static T-mixers*, Chemical Engineering Science 78 (2012) 46–52.

[13] Y. Hakuta, S. Onai, H. Terayama, T. Adschiri, K. Arai; *Production of Ultra-fine Ceria Particles by Hydrothermal Synthesis Under Supercritical Conditions*, Journal of Materials Science Letters 17 (1998) 1211–1213.

[14] S. Kawasaki, Y. Xiuyi, K. Sue, Y. Hakuta, A. Suzuki, K. Arai; *Continuous supercritical hydrothermal synthesis of controlled size and highly crystalline anatase TiO_2 nanoparticles*, The Journal of Supercritical Fluids 50, 3 (2009) 276–282.

[15] L. J. Cote, A. S. Teja, A. P. Wilkinson, Z. Zhang; *Continuous hydrothermal synthesis of $CoFe_2O_4$ nanoparticles*, Fluid Phase Equilibria 210, 2 (2003) 307–317.

[16] S.-A. Hong, S. J. Kim, K. Y. Chung, M.-S. Chun, B. G. Lee, J. Kim; *Continuous synthesis of lithium iron phosphate ($LiFePO_4$) nanoparticles in supercritical water: Effect of mixing tee*, The Journal of Supercritical Fluids 73 (2013) 70–79.

[17] T. Sasaki, S. Ohara, T. Naka, J. Vejpravova, V. Sechovsky, M. Umetsu, S. Takami, B. Jeyadevan, T. Adschiri; *Continuous synthesis of fine $MgFe_2O_4$ nanoparticles by supercritical hydrothermal reaction*, The Journal of Supercritical Fluids 53, 1-3 (2010) 92–94.

[18] E. Lester, P. Blood, J. Denyer, D. Giddings, B. Azzopardi, M. Poliakoff; *Reaction engineering: The supercritical water hydrothermal synthesis of nano-particles*, The Journal of Supercritical Fluids 37, 2 (2006) 209–214.

[19] S. Takami, K. Sugioka, K. Ozawa, T. Tsukada, T. Adschiri, K. Sugimoto, N. Takenaka, Y. Saito; *In-situ neutron tomography on mixing behavior of supercritical water and room temperature water in a tubular flow reactor*, Physics Procedia 69 (2015) 564–569.

[20] S. Marre, Y. Roig, C. Aymonier; *Supercritical microfluidics: Opportunities in flow-through chemistry and materials science*, The Journal of Supercritical Fluids 66 (2012) 251–264.

[21] H. Jensen, M. Bremholm, R. P. Nielsen, K. D. Joensen, J. S. Pedersen, H. Birkedal, Y.-S. Chen, J. Almer, E. G. Søgaard, S. B. Iversen, B. B. Iversen; *In Situ High-Energy Synchrotron Radiation Study of Sol-Gel Nanoparticle Formation in Supercritical Fluids*, Angewandte Chemie (International ed. in English) 46, 7 (2007) 1113–1116.

[22] M. Bremholm, J. Becker-Christensen, B. B. Iversen; *High-Pressure, High-Temperature Formation of Phase-Pure Monoclinic Zirconia Nanocrystals Studied by Time-Resolved in situ Synchrotron X-Ray Diffraction*, Advanced Materials 21, 35 (2009) 3572–3575.

[23] M. Bremholm, M. Felicissimo, B. Iversen, B; *Time-Resolved In Situ Synchrotron X-ray Study and Large-Scale Production of Magnetite Nanoparticles in Supercritical Water*, Angewandte Chemie 121, 26 (2009) 4882–4885.

[24] N. Lock, M. Christensen, K. M. Ø. Jensen, B. B. Iversen; *Rapid One-Step Low-Temperature Synthesis of Nanocrystalline γ-Al_2O_3*, Angewandte Chemie 123, 31 (2011) 7183–7185.

[25] S. Marre, A. Adamo, S. Basak, C. Aymonier, K. F. Jensen; *Design and Packaging of Microreactors for High Pressure and High Temperature Applications*, Industrial & Engineering Chemistry Research 49, 22 (2010) 11310–11320.

[26] D. Rangappa, S. Ohara, M. Umetsu, T. Naka, T. Adschiri; *Synthesis, characterization and organic modification of copper manganese oxide nanocrystals under supercritical water*, The Journal of Supercritical Fluids 44, 3 (2008) 441–445.

[27] M. Daschner de Tercero; *Near-critical and supercritical hydrothermal flow synthesis of metal oxide nanoparticles and hybrid metal oxide nanoparticles presenting clickable anchors*, PhD Thesis, Karlsruhe Institute of Technology (KIT), KIT Scientific Publishing (2014).

[28] N. Aoki, A. Sato, H. Sasaki, A.-A. Litwinowicz, G. Seong, T. Aida, D. Hojo, S. Takami, T. Adschiri; *Kinetics study to identify reaction-controlled conditions for supercritical hydrothermal nanoparticle synthesis with flow-type reactors*, The Journal of Supercritical Fluids 110 (2016) 161–166.

[29] K. Stephan, P. Stephan, F. Mayinger, K. Schaber; *Thermodynamik*: Grundlagen und technische Anwendungen; Band 1: Einstoffsysteme, Springer, Berlin, Heidelberg (2009).

[30] R. E. Dickerson; *Molecular Thermodynamics*, W. A. Benjamin, New York (1969).

[31] F. Cansell, C. Aymonier, A. Loppinet-Serani; *Review on materials science and supercritical fluids*, Current Opinion in Solid State and Materials Science 7, 4-5 (2003) 331–340.

[32] S. Müller, M. Türk; *Production of supported gold and gold–silver nanoparticles by supercritical fluid reactive deposition: Effect of substrate properties*, The Journal of Supercritical Fluids 96 (2015) 287–297.

[33] P. Chattopadhyay, R. B. Gupta; *Supercritical CO_2 Based Production of Magnetically Responsive Micro- and Nanoparticles for Drug Targeting*, Industrial & Engineering Chemistry Research 41, 24 (2002) 6049–6058.

[34] P. Chattopadhyay, R. B. Gupta; *Production of Drug Nanoparticles of Controllable Size using Supercritical Fluid Antisolvent Technique with Enhanced Mass Transfer*, Proceedings of the 6th International Symposium of Supercritical Fluids 3 (2003) 1617–1622.

[35] M. J. Meziani, H. W. Rollins, L. F. Allard, Y.-P. Sun; *Protein-Protected Nanoparticles from Rapid Expansion of Supercritical Solution into Aqueous Solution*, The Journal of Physical Chemistry B 106, 43 (2002) 11178–11182.

[36] H. Hayashi, K. Torii; *Hydrothermal synthesis of titania photocatalyst under subcritical and supercritical water conditions*, Journal of Materials Chemistry 12 (2002) 3671–3676.

[37] T. Wang, R. L. Smith, H. Inomata, K. Arai; *Reactive phase behavior of aluminum nitrate in high temperature and supercritical water*, Hydrometallurgy 65, 2-3 (2002) 159–175.

[38] R. Viswanathan, R. B. Gupta; *Formation of zinc oxide nanoparticles in supercritical water*, The Journal of Supercritical Fluids 27, 2 (2003) 187–193.

[39] M. Türk; *Design metalloxidischer Nanopartikel mittels kontinuierlicher hydrothermaler Synthese: Status und Ausblick*, Chemie Ingenieur Technik 90, 4 (2018) 436–442.

[40] S. E. Humphris, G. Thompson; *Hydrothermal alteration of oceanic basalts by seawater*, Geochimica et Cosmochimica Acta 42, 1 (1978) 107–125.

[41] P. E. Savage, S. Gopalan, T. I. Mizan, C. J. Martino, E. E. Brock; *Reactions at supercritical conditions: Applications and fundamentals*, AIChE Journal 41, 7 (1995) 1723–1778.

[42] H. E. Barner, C. Y. Huang, T. Johnson, G. Jacobs, M. A. Martch, W. R. Killilea; *Supercritical water oxidation: An emerging technology*, Journal of Hazardous Materials 31, 1 (1992) 1–17.

[43] Y. Hakuta, H. Hayashi, K. Arai; *Fine particle formation using supercritical fluids*, Current Opinion in Solid State and Materials Science 7, 4-5 (2003) 341–351.

[44] C. Aymonier, A. Loppinet-Serani, H. Reverón, Y. Garrabos, F. Cansell; *Review of supercritical fluids in inorganic materials science*, The Journal of Supercritical Fluids 38, 2 (2006) 242–251.

[45] T. Adschiri; *Supercritical Hydrothermal Synthesis of Organic–Inorganic Hybrid Nanoparticles*, Chemistry Letters 36, 10 (2007) 1188–1193.

[46] A. Loppinet-Serani, C. Aymonier, F. Cansell; *Supercritical water for environmental technologies*, Journal of Chemical Technology & Biotechnology 85, 5 (2010) 583–589.

[47] M. Türk; *Particle Formation with Supercritical Fluids: Challenges and Limitations*, Supercritical Fluid Science and Technology 6, Elsevier, Amsterdam (2014).

[48] H. Weingärtner, E. U. Franck; *Überkritisches Wasser als Lösungsmittel*, Angewandte Chemie 117, 18 (2005) 2730–2752.

[49] N. Matubayasi, C. Wakai, M. Nakahara; *NMR Study of Water Structure in Super- and Subcritical Conditions*, Physical Review Letters 78, 13 (1997) 2573–2576.

[50] E. U. Franck, K. Roth; *Infra-red absorption of HDO in water at high pressures and temperatures*, Discussions of the Faraday Society 43 (1967) 108.

[51] A. G. Kalinichev; *Universality of hydrogen bond distributions in liquid and supercritical water*, Journal of Molecular Liquids 241 (2017) 1038–1043.

[52] A. Kruse, E. Dinjus; *Hot compressed water as reaction medium and reactant: Properties and synthesis reactions*, The Journal of Supercritical Fluids 39, 3 (2007) 362–380.

[53] E. W. Lemmon, M. L. Huber, M. O. McLinden; *Reference Fluid Thermodynamic and Transport Properties (REFPROP). NIST Standard Reference Database 23*, NIST (2013).

[54] W. Wagner, A. Pruß; *The IAPWS Formulation 1995 for the Thermodynamic Properties of Ordinary Water Substance for General and Scientific Use*, Journal of Physical and Chemical Reference Data 31, 2 (2002) 387–535.

[55] J. Kestin, J. V. Sengers, B. Kamgar-Parsi, J. M. H. L. Sengers; *Thermophysical Properties of Fluid H_2O*, Journal of Physical and Chemical Reference Data 13, 1 (1984) 175–183.

[56] J. W. Johnson, D. Norton; *Critical phenomena in hydrothermal systems: state, thermodynamic, electrostatic, and transport properties of H_2O in the critical region*, American Journal of Science 291, 6 (1991) 541–648.

[57] W. L. Marshall, E. U. Franck; *Ion Product of Water Substance, 0-1000 °C, 1-10000 Bars, New International Formulation and Its Background*, Journal of Physical and Chemical Reference Data 10, 2 (1981) 295–304.

[58] M. Hohm; *Inbetriebnahme einer Anlage zur kontinuierlichen hydrothermalen Synthese von metalloxidischen Nanopartikeln*, Master's thesis, Karlsruhe Institute of Technology (KIT), Karlsruhe (2018).

[59] G. Brunner; *Supercritical process technology related to energy and future directions – An introduction*, The Journal of Supercritical Fluids 96 (2015) 11–20.

[60] T. Voisin, A. Erriguible, D. Ballenghien, D. Mateos, A. Kunegel, F. Cansell, C. Aymonier; *Solubility of inorganic salts in sub- and supercritical hydrothermal environment: Application to SCWO processes*, The Journal of Supercritical Fluids 120 (2017) 18–31.

[61] G. Brunner; *Near critical and supercritical water. Part I. Hydrolytic and hydrothermal processes*, The Journal of Supercritical Fluids 47, 3 (2009) 373–381.

[62] G. Brunner; *Hydrothermal and Supercritical Water Processes*, Supercritical Fluid Science and Technology 5, Elsevier Science, Burlington (2014).

[63] M. Luckas, J. Krissmann; *Thermodynamik der Elektrolytlösungen*: *Eine Einheitliche Darstellung der Berechnung Komplexer Gleichgewichte,* Springer, Berlin, Heidelberg (2001).

[64] P. H. van Konynenburg; *Critical lines and phase equilibria in binary van der Waals mixtures*, Philosophical Transactions of the Royal Society of London, Series A, Mathematical and Physical Sciences 298, 1442 (1980) 495–540.

[65] F. J. Armellini, J. W. Tester; *Experimental methods for studying salt nucleation and growth from supercritical water*, The Journal of Supercritical Fluids 4, 4 (1991) 254–264.

[66] W. L. Marshall; *Water and its solutions at high temperature and high pressure*, Chemistry 48 (1975) 6–12.

[67] V. M. Valyashko; *Hydrothermal Properties of Materials: Experimental Data on Aqueous Phase Equilibria and Solution Properties at Elevated Temperatures and Pressures*, Wiley, Chichester (2008).

[68] D. L. Reger, S. R. Goode, E. E. Mercer; *Chemistry: Principles and Practice*, Saunders College Pub, Fort Worth (1997).

[69] W. J. Moore.; *Grundlagen der Physikalischen Chemie*, W. De Gruyter, Berlin, New York (1990).

[70] J. C. Tanger, H. C. Helgeson; *Calculation of the thermodynamic and transport properties of aqueous species at high pressures and temperatures: Revised equations of state for the*

standard partial molal properties of ions and electrolytes, American Journal of Science 288, 1 (1988) 19–98.

[71] E. L. Shock, H. C. Helgeson; *Calculation of the thermodynamic and transport properties of aqueous species at high pressures and temperatures: Correlation algorithms for ionic species and equation of state predictions to 5 kb and 1000°C*, Geochimica et Cosmochimica Acta 52, 8 (1988) 2009–2036.

[72] E. L. Shock, E. H. Oelkers, J. W. Johnson, D. A. Sverjensky, H. C. Helgeson; *Calculation of the thermodynamic properties of aqueous species at high pressures and temperatures. Effective electrostatic radii, dissociation constants and standard partial molal properties to 1000 °C and 5 kbar*, Journal of the Chemical Society, Faraday Transactions 88, 6 (1992) 803–826.

[73] M. S. Gruszkiewicz, R. H. Wood; *Conductance of Dilute LiCl, NaCl, NaBr, and CsBr Solutions in Supercritical Water Using a Flow Conductance Cell*, The Journal of Physical Chemistry B 101, 33 (1997) 6549–6559.

[74] P. C. Ho, D. A. Palmer, R. E. Mesmer; *Electrical conductivity measurements of aqueous sodium chloride solutions to 600 °C and 300 MPa*, Journal of Solution Chemistry 23, 9 (1994) 997–1018.

[75] P. C. Ho, H. Bianchi, D. A. Palmer, R. H. Wood; *Conductivity of Dilute Aqueous Electrolyte Solutions at High Temperatures and Pressures Using a Flow Cell*, Journal of Solution Chemistry 29, 3 (2000) 217–235.

[76] P. C. Ho, D. A. Palmer; *Ion association of dilute aqueous sodium hydroxide solutions to 600 °C and 300 MPa by conductance measurements*, Journal of Solution Chemistry 25, 8 (1996) 711–729.

[77] F. Masoodiyeh, M. R. Mozdianfard, J. Karimi-Sabet; *Solubility estimation of inorganic salts in supercritical water*, The Journal of Chemical Thermodynamics 78 (2014) 260–268.

[78] A. Rabenau; *The Role of Hydrothermal Synthesis in Preparative Chemistry*, Angewandte Chemie (International ed. in English) 24, 12 (1985) 1026–1040.

[79] G. Spezia; *La pressione è chimicamente inattiva nella solubilità e ricostituzione del quarzo*, Atti della Reale Accademia delle scienze di Torino 40 (1905) 254–262.

[80] K. Byrappa, T. Adschiri; *Hydrothermal technology for nanotechnology*, Progress in Crystal Growth and Characterization of Materials 53, 2 (2007) 117–166.

[81] J. A. Darr, J. Zhang, N. M. Makwana, X. Weng; *Continuous Hydrothermal Synthesis of Inorganic Nanoparticles: Applications and Future Directions*, Chemical Reviews 117, 17 (2017) 11125–11238.

[82] H. P. Klug, L. E. Alexander; *X-Ray Diffraction Procedures*: *For Polycrystalline and Amorphous Materials*, Wiley, New York (1974).

[83] T. Adschiri, Y. Hakuta, K. Sue, K. Arai; *Hydrothermal synthesis of metal oxide nanoparticles at supercritical conditions*, Journal of Nanoparticle Research 3 (2001) 227–235.

[84] D. W. Matson, J. C. Linehan, R. M. Bean; *Ultrafine iron oxide powders generated using a flow-through hydrothermal process*, Materials Letters 14, 4 (1992) 222–226.

[85] T. Adschiri, Y.-W. Lee, M. Goto, S. Takami; *Green materials synthesis with supercritical water*, Green Chemistry 13, 6 (2011) 1380–1390.

[86] http://hcc.hanwha.co.kr/eng/; (accessed 13.07.2022).

[87] C. Aymonier, G. Philippot, A. Erriguible, S. Marre; *Playing with chemistry in supercritical solvents and the associated technologies for advanced materials by design*, The Journal of Supercritical Fluids 134 (2018) 184–196.

[88] F. Cansell, C. Aymonier; *Design of functional nanostructured materials using supercritical fluids*, The Journal of Supercritical Fluids 47, 3 (2009) 508–516.

[89] H. Hayashi, Y. Hakuta; *Hydrothermal Synthesis of Metal Oxide Nanoparticles in Supercritical Water*, Materials 3, 7 (2010) 3794–3817.

[90] J. Sierra-Pallares, T. Huddle, J. García-Serna, E. Alonso, F. Mato, I. Shvets, O. Luebben, M. J. Cocero, E. Lester; *Understanding bottom-up continuous hydrothermal synthesis of nanoparticles using empirical measurement and computational simulation*, Nano Research 9, 11 (2016) 3377–3387.

[91] T. Adschiri, A. Yoko; *Supercritical fluids for nanotechnology*, The Journal of Supercritical Fluids 134 (2018) 167–175.

[92] S. Kawasaki, K. Sue, R. Ookawara, Y. Wakashima, A. Suzuki, Y. Hakuta, K. Arai; *Engineering study of continuous supercritical hydrothermal method using a T-shaped mixer*, The Journal of Supercritical Fluids 54, 1 (2010) 96–102.

[93] Verein deutscher Ingenieure VDI e.V; *VDI-Wärmeatlas*, Springer-Verlag, 10. Auflage, Berlin, Heidelberg (2006).

[94] T. Adschiri, Y. Hakuta, K. Arai; *Hydrothermal Synthesis of Metal Oxide Fine Particles at Supercritical Conditions*, Industrial & Engineering Chemistry Research 39, 12 (2000) 4901–4907.

[95] P. G. Debenedetti; *Homogeneous nucleation in supercritical fluids*, AIChE Journal 36, 9 (1990) 1289–1298.

[96] M. Türk; *Influence of thermodynamic behaviour and solute properties on homogeneous nucleation in supercritical solutions*, The Journal of Supercritical Fluids 18, 3 (2000) 169–184.

[97] R. Becker, W. Döring; *Kinetische Behandlung der Keimbildung in übersättigten Dämpfen*, Annalen der Physik 416, 8 (1935) 719–752.

[98] M. Volmer; *Kinetik der Phasenbildung*, T. Steinkopff, Leipzig (1939).

[99] J. W. Mullin; *Crystallisation*, Butterworth Heinemann, Oxford, UK (2001).

[100] K. Sue, M. Suzuki, K. Arai, T. Ohashi, H. Ura, K. Matsui, Y. Hakuta, H. Hayashi, M. Watanabe, T. Hiaki; *Size-controlled synthesis of metal oxide nanoparticles with a flow-through supercritical water method*, Green Chemistry 8, 7 (2006) 634–638.

[101] U. T. Lam, R. Mammucari, K. Suzuki, N. R. Foster; *Processing of Iron Oxide Nanoparticles by Supercritical Fluids*, Industrial & Engineering Chemistry Research 47, 3 (2008) 599–614.

[102] C. Slostowski, S. Marre, J.-M. Bassat, C. Aymonier; *Synthesis of cerium oxide-based nanostructures in near- and supercritical fluids*, The Journal of Supercritical Fluids 84 (2013) 89–97.

[103] C. Schüßler, M. Hohm, M. Türk; *Near- and supercritical hydrothermal flow synthesis of CeO_2 nanoparticles*, 12th International Symposium on Supercritical Fluids, 22-25 April 2018, Antibes, France, http://www.supflu2018.fr/pdf/OM06.pdf.

[104] K. Sugioka, K. Ozawa, M. Kubo, T. Tsukada, S. Takami, T. Adschiri, K. Sugimoto, N. Takenaka, Y. Saito; *Relationship between size distribution of synthesized nanoparticles and flow and thermal fields in a flow-type reactor for supercritical hydrothermal synthesis*, The Journal of Supercritical Fluids 109 (2016) 43–50.

[105] Y.-P. Sun; *Supercritical Fluid Technology in Materials Science and Engineering: Syntheses, Properties, and Applications*, Dekker, New York, Basel (2002).

[106] M. Daschner de Tercero, M. Bruns, I. G. Martínez, M. Türk, U. Fehrenbacher, S. Jennewein, L. Barner; *Continuous Hydrothermal Synthesis of In Situ Functionalized Iron Oxide Nanoparticles: A General Strategy to Produce Metal Oxide Nanoparticles With Clickable Anchors*, Particle & Particle Systems Characterization 30, 3 (2013) 229–234.

[107] M. Daschner de Tercero, I. G. Martínez, M. Herrmann, M. Bruns, C. Kübel, S. Jennewein, U. Fehrenbacher, L. Barner, M. Türk; *Synthesis of in situ functionalized iron oxide nanoparticles presenting alkyne groups via a continuous process using near-critical and supercritical water*, The Journal of Supercritical Fluids 82 (2013) 83–95.

[108] N. K. V. Nadimpalli, R. Bandyopadhyaya, V. Runkana; *A coupled CFD-PBM and thermodynamic analysis of continuous supercritical hydrothermal synthesis of nanoparticles*, The Journal of Supercritical Fluids 136 (2018) 164–179.

[109] E. S. Amis, J. F. Hinton; *Solvent Effects on Chemical Phenomena*, Academic Press, New York (1973).

[110] M. Uematsu, E. U. Franck; *Static Dielectric Constant of Water and Steam*, Journal of Physical and Chemical Reference Data 9, 4 (1980) 1291–1306.

[111] E. Lester, P. J. Blood, J. P. Denyer, B. J. Azzopardi, J. Li, M. Poliakoff; *Impact of reactor geometry on continuous hydrothermal synthesis mixing*, Materials Research Innovations 14, 1 (2010) 19–26.

[112] E. Lester, G. Aksomaityte, J. Li, S. Gomez, J. Gonzalez-Gonzalez, M. Poliakoff; *Controlled continuous hydrothermal synthesis of cobalt oxide (Co_3O_4) nanoparticles*, Progress in Crystal Growth and Characterization of Materials 58, 1 (2012) 3–13.

[113] K. Sue, T. Sato, S. Kawasaki, Y. Takebayashi, S. Yoda, T. Furuya, T. Hiaki; *Continuous Hydrothermal Synthesis of Fe_2O_3 Nanoparticles Using a Central Collision-Type Micromixer for Rapid and Homogeneous Nucleation at 673 K and 30 MPa*, Industrial & Engineering Chemistry Research 49, 18 (2010) 8841–8846.

[114] J. Sierra-Pallares, T. Huddle, E. Alonso, F. A. Mato, J. García-Serna, M. J. Cocero, E. Lester; *Prediction of residence time distributions in supercritical hydrothermal reactors working at low Reynolds numbers*, Chemical Engineering Journal 299 (2016) 373–385.

[115] L. Zhou, S. Wang, D. Xu, Y. Guo; *Impact of Mixing for the Production of CuO Nanoparticles in Supercritical Hydrothermal Synthesis*, Industrial & Engineering Chemistry Research 53, 1 (2013) 481–493.

[116] C. J. Tighe, R. I. Gruar, C. Y. Ma, T. Mahmud, X. Z. Wang, J. A. Darr; *Investigation of counter-current mixing in a continuous hydrothermal flow reactor*, The Journal of Supercritical Fluids 62 (2012) 165–172.

[117] T. Aizawa, Y. Masuda, K. Minami, M. Kanakubo, H. Nanjo, R. L. Smith; *Direct observation of channel-tee mixing of high-temperature and high-pressure water*, The Journal of Supercritical Fluids 43, 2 (2007) 222–227.

[118] S. Takami, K. Sugioka, T. Tsukada, T. Adschiri, K. Sugimoto, N. Takenaka, Y. Saito; *Neutron radiography on tubular flow reactor for hydrothermal synthesis: In situ monitoring of mixing behavior of supercritical water and room-temperature water*, The Journal of Supercritical Fluids 63 (2012) 46–51.

[119] R. E. Shannon; *Introduction to the art and science of simulation*, IEEE Winter Simulation Conference, Washington, DC, USA (1998) 7–14.

[120] M. Chen, Y. Cai, T. Mahmud, J. A. Darr, X. Z. Wang; *Modelling and simulation of continuous hydrothermal flow synthesis process for nano-materials manufacture*, The Journal of Supercritical Fluids 59 (2011) 131–139.

[121] N. Lümmen, B. Kvamme; *Kinetics of NaCl nucleation in supercritical water investigated by molecular dynamics simulations*, Physical Chemistry Chemical Physics 9, 25 (2007) 3251–3260.

[122] H. G. Weller, G. Tabor, H. Jasak, C. Fureby; *A tensorial approach to computational continuum mechanics using object-oriented techniques*, Journal of Computational Physics 12, 6 (1998) 620-631.

[123] J. Tu; *Computational fluid dynamics*: *A practical approach*, Butterworth-Heinemann (2018).

[124] J. H. Ferziger, M. Perić, R. L. Street; *Computational Methods for Fluid Dynamics*, Springer, Berlin, Heidelberg (2020).

[125] T. Ahmad, S. L. Plee, J. P. Myers; *Fluent User's Guide* (2016).

[126] T. J. Baker; *Fluent Meshing User's Guide* (2013).

[127] A. Leybros, R. Piolet, M. Ariane, H. Muhr, F. Bernard, F. Demoisson; *CFD simulation of ZnO nanoparticle precipitation in a supercritical water synthesis reactor*, The Journal of Supercritical Fluids 70 (2012) 17–26.

[128] B. Abramzon and W. A. Sirignano; *Fluent Theory Guide* (2016).

[129] D. R. Lide; *CRC Handbook of Chemistry and Physics*, CRC Press (2010).

[130] A. Trovarelli; *Catalytic Properties of Ceria and CeO_2 - Containing Materials*, Catalysis Reviews 38, 4 (1996) 439–520.

[131] S. Deshpande, S. Patil, S. V. Kuchibhatla, S. Seal; *Size dependency variation in lattice parameter and valency states in nanocrystalline cerium oxide*, Applied Physics Letters 87, 13 (2005) 133113.

[132] W. J. Stark; *Nanopartikel in biologischen Systemen*, Angewandte Chemie 123, 6 (2011) 1276–1293.

[133] I. Celardo, J. Z. Pedersen, E. Traversa, L. Ghibelli; *Pharmacological potential of cerium oxide nanoparticles*, Nanoscale 3, 4 (2011) 1411–1420.

[134] C. K. Kim, T. Kim, I.-Y. Choi, M. Soh; *Ceria Nanoparticles that can Protect against Ischemic Stroke*, Angewandte Chemie (International ed. in English) 51, 44 (2012) 11039–11043.

[135] C. L. Allen, U. Bayraktutan; *Oxidative Stress and Its Role in the Pathogenesis of Ischaemic Stroke*, International Journal of Stroke: Official Journal of the International Stroke Society 4, 6 (2009) 461–470.

[136] R. Sabia, H. J. Stevens; *Performance Characterization of Cerium Oxide Abrasives for Chemical-Mechanical Polishing of Glass*, Machining Science and Technology 4, 2 (2000) 235–251.

[137] A. Trovarelli, P. Fornasiero; *Catalysis by Ceria and Related Materials*, Catalytic science series 12, Imperial College Press, London, Singapore (2013).

[138] V. K. Pecharsky and P. Y. Zavalij; *Fundamentals of Powder Diffraction and Structural Characterization of Materials*, Springer, New York (2009).

[139] J. M. Zuo, J. C. H. Spence; *Advanced Transmission Electron Microscopy: Imaging and Diffraction in Nanoscience*, Springer, New York (2017).

[140] D. Ende, K.-M. Mangold; *Impedanzspektroskopie*, Chemie in unserer Zeit 27, 3 (1993) 134–140.

[141] E. Barsoukov, J. R. Macdonald; *Impedance Spectroscopy*, Wiley-Interscience, Hoboken (2005).

[142] S. Kawasaki, T. Oe, S. Itoh, A. Suzuki, K. Sue, K. Arai; *Flow characteristics of aqueous salt solutions for applications in supercritical water oxidation*, The Journal of Supercritical Fluids 42, 2 (2007) 241–254.

[143] C. Y. Ma, M. Chen, X. Z. Wang; *Modelling and Simulation of Counter-Current and Confined Jet Reactors for Hydrothermal Synthesis of Nano-Materials*, Chemical Engineering Science 109 (2014) 26–37.

[144] Promat; *Promasil®-1000, -1000P, -1100_ Technical Data Sheet - English*, https://www.promat.com/siteassets/industry/downloads/technical-data-sheets-tds/calcium-silicates/eng/promat-promasil-1000-1000p-1100-product-data-sheet.pdf?v=49cca6/Download (accessed April 2018).

[145] J. Sierra-Pallares, E. Alonso, I. Montequi, M. J. Cocero; *Particle diameter prediction in supercritical nanoparticle synthesis using three-dimensional CFD simulations: Validation for anatase titanium dioxide production*, Chemical Engineering Science 64, 13 (2009) 3051–3059.

[146] http://www.periodensystem-online.de/index.php?el=58&id=compound&cpid=1231 (accessed 02.09.2021).

[147] M. Zürn; *Theoretische Untersuchung des Löslichkeitsverhaltens von Metallsalzen in nahe- oder überkritischem Wasser mit Hilfe unterschiedlicher Modelle*, Master's thesis, Karlsruhe Institute of Techology (KIT), Karlsruhe (2020).

[148] S. Sawamura, N. Egoshi, Y. Setoguchi, H. Matsuo; *Solubility of sodium chloride in water under high pressure*, Fluid Phase Equilibria 254, 1-2 (2007) 158–162.

[149] I. Leusbrock, S. J. Metz, G. Rexwinkel, G. F. Versteeg; *Solubility of 1:1 Alkali Nitrates and Chlorides in Near-Critical and Supercritical Water*, Journal of Chemical & Engineering Data 54, 12 (2009) 3215–3223.

[150] I. Leusbrock, S. J. Metz, G. Rexwinkel, G. F. Versteeg; *The solubility of magnesium chloride and calcium chloride in near-critical and supercritical water*, The Journal of Supercritical Fluids 53, 1-3 (2010) 17–24.

[151] S. N. Rogak, P. Teshima; *Deposition of sodium sulfate in a heated flow of supercritical water*, AIChE Journal 45, 2 (1999) 240–247.

[152] C. Schüßler, M. Zürn, T. Hanemann, M. Türk; *Überwachung der kontinuierlichen hydrothermalen Synthese mittels Impedanzspektroskopie*, Chemie Ingenieur Technik 94, 3 (2022) 281–288.

[153] SK. Ponusamy; *Theoretical study of the mixing behavior during continuous hydrothermal synthesis (CHTS) of metal oxide nanoparticles*, Master's thesis, Karlsruhe Institute of Technology (KIT), Karlsruhe (2018).

[154] E. Heil; *Untersuchungen zum Löslichkeitsverhalten von Metallsalzen und Metalloxiden in nahe- und überkritischem Wasser*, Bachelor's thesis, Karlsruhe Institute of Technology (KIT), Karlsruhe (2021).

[155] M. Born; *Volumen und Hydratationswärme der Ionen*, Zeitschrift für Physik 1, 1 (1920) 45–48.

[156] A. Goel; *Simulation of the particle formation during continuous hydrothermal synthesis (CHTS) of metal oxide nanoparticles*, Master's thesis, Karlsruhe Institute of Technology (KIT), Karlsruhe (2020).

11.Appendix

Appendix chapter 2

A: Calculation of the ion product of water

For the calculation of the dimensionless ion product K_W^*, the following equation, according to Marshall et al., was applied for the water phase [57]:

$$\log K_W^* = A + \frac{B}{T} + \frac{C}{T^2} + \frac{D}{T^2} + (E + \frac{F}{T} + \frac{G}{T^2}) \log \rho_w^* \quad (2\text{-}36)$$

The calculation is based on the following parameters [57] and the notification of the variables:

A = -4.098

B = -3245.2 K

C = 2.2362 · 10^5 K^2

D = -3.984 · 10^7 K^3

E = 13.957

F = -1262.3 K

G = 8.5641 · 10^5 K^2

K_W^* = K_W / (mol kg^{-1})^2

ρ_w^* = ρ_w / g cm^{-3}

B: r-HKF model

$$\Delta\bar{G}^{\circ}_{\mathrm{n},i} = -S^{\circ}_{p_{\mathrm{r}},T_{\mathrm{r}}}(T-T_{\mathrm{r}}) - c_1\left[T\ln\left(\frac{T}{T_{\mathrm{r}}}\right) - T + T_{\mathrm{r}}\right]$$

$$-c_2\left\{\left[\left(\frac{1}{T-\Theta_{hkf}}\right)-\left(\frac{1}{T_{\mathrm{r}}-\Theta_{hkf}}\right)\right]\left(\frac{\Theta_{hkf}-T}{\Theta_{hkf}}\right)-\frac{T}{{\Theta_{hkf}}^2}\ln\left[\frac{T_{\mathrm{r}}(T-\Theta_{hkf})}{T(T_{\mathrm{r}}-\Theta_{hkf})}\right]\right\}$$

$$+a_1(p-p_{\mathrm{r}})+a_2\ln\left(\frac{\Psi+p}{\Psi+p_{\mathrm{r}}}\right)+\left(\frac{1}{T-\Theta_{hkf}}\right)\left[a_3(p-p_{\mathrm{r}})+a_4\ln\left(\frac{\Psi+p}{\Psi+p_{\mathrm{r}}}\right)\right] \quad (2\text{-}4\text{-}1)$$

$$\Delta\bar{G}^{\circ}_{\mathrm{s},i} = \omega_{p,T}\left(\frac{1}{\varepsilon_{P,T}}-1\right)-\omega_{P_{\mathrm{r}},T_{\mathrm{r}}}\left(\frac{1}{\varepsilon_{p_{\mathrm{r}},T_{\mathrm{r}}}}-1\right) + \omega_{p_{\mathrm{r}},T_{\mathrm{r}}}Y_{p_{\mathrm{r}},T_{\mathrm{r}}}(T-T_{\mathrm{r}}) \quad (2\text{-}4\text{-}2)$$

The parameter η_{HKF} is calculated through the Avogadro number and the elemental charge and results in 6.94657 10^{-5} J mol^{-1}. z and r_{e,p_r,T_r} represent the charge of the ion and the effective electrostatic ionic radius of the involved ions. The ionic radius is the summation of the crystal radius and the radius change due to pressure and temperature variation. It is defined as follows:

$$r_{e,p_{\mathrm{r}},T_{\mathrm{r}}} = r_x + |z|k_z \quad (2\text{-}5\text{-}1)$$

r_x represents the crystal ionic radius. k_z equals to 0 in terms of anions and 0.94 for cations, according to the HKF model [3]. Next to ionic species, neutral or non-ionic species, the Born coefficient is a constant value of -12.552 kJ mol^{-1}. This value is defined within the r-HKF model and is independent of pressure and temperature [70].

The parameters a'_{g}, a''_{g}, a'''_{g}, b'_{g}, b''_{g} and b'''_{g} shown in Table 11-1 are used for fitting the temperatures and densities in the supercritical region. The temperature is considered in °C:

$$a_{\mathrm{g}} = a'_{\mathrm{g}} + a''_{\mathrm{g}}T + a'''_{\mathrm{g}}T^2 \quad (2\text{-}6\text{-}1)$$

$$b_{\mathrm{g}} = b'_{\mathrm{g}} + b''_{\mathrm{g}}T + b'''_{\mathrm{g}}T^2 \quad (2\text{-}6\text{-}2)$$

Table 11-1: Used parameters for the calculation of a_g and b_g for the g - function, according to [72]:

parameter	
a'_g / Å	-2.037662
a''_g / Å K^{-1}	-5.747000 ·10^{-3}
a'''_g / Å K^{-2}	-6.557892 · 10^{-6}
b'_g / -	6.107361
b''_g / K^{-1}	-1.074377 · 10^{-2}
b'''_g / K^{-2}	1.268343 · 10^{-5}

They aimed a better description of the pressure and temperature dependency of the effective electrostatic radius. The three other regions are shown in Figure 11-1:

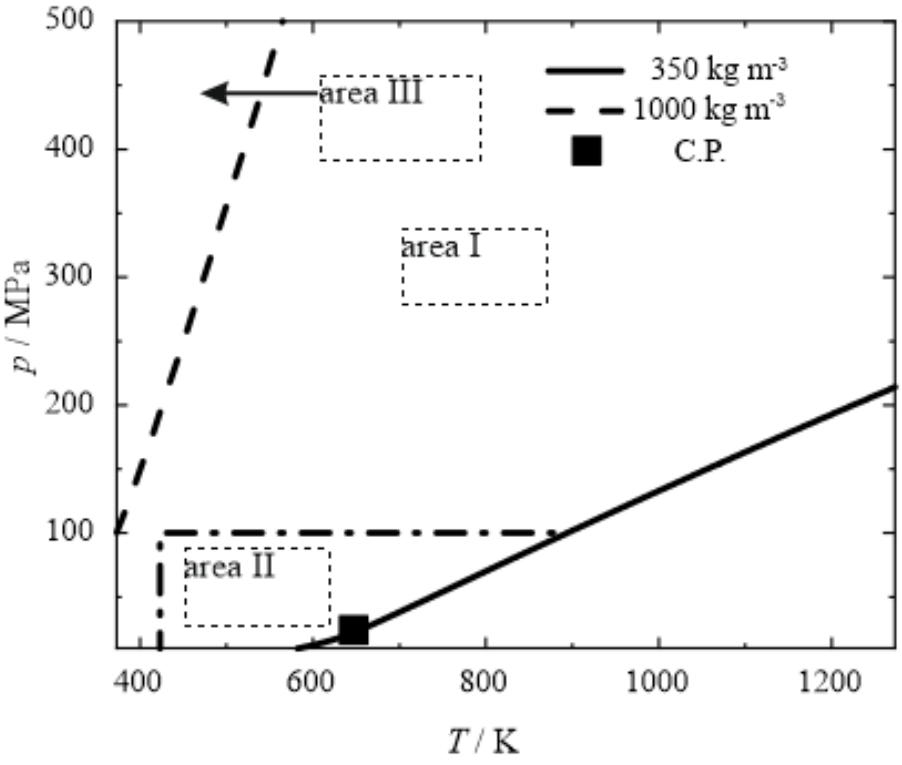

Figure 11-1: Pressure – temperature diagram for water with areas for the g - function, according to [72].

For area I, the g - function is calculated according to equation (2-6), (2-6-1), and (2-6-2). Area II is for temperatures over 423 K, pressures below 100 MPa and densities lower than 0.35 g · cm^{-3}. The term for the g - function is then extended by a pressure and temperature-dependent part $f(P,T)$ and described as follows:

$$g = a_{\mathrm{g}}(1.0 - \rho^{*})^{b_{\mathrm{g}}} - f(p,T) \tag{2-6-3}$$

$$f(p,T) = \left[\left(\frac{T-155}{300}\right)^{4,8} + c_{\mathrm{g},1}\left(\frac{T-155}{300}\right)^{16}\right]\left[c_{\mathrm{g},2}(1000-p)^3 + c_{\mathrm{g},3}(1000-p)^4\right] \tag{2-6-4}$$

Both the parameters $c_{\mathrm{g},1}$ - $c_{\mathrm{g},3}$ are shown by Shock et al. [72] in Table 11-2:

Table 11-2: Parameters used for calculating the pressure and temperature-dependent part $f(P,T)$ of the g – function, according to [72].

parameter	
$c_{\mathrm{g},1}$ / K	$3.66666 \cdot 10^{-16}$
$c_{\mathrm{g},2}$ / Å bar^{-3}	$-1.504956 \cdot 10^{-10}$
$c_{\mathrm{g},3}$ / Å bar^{-4}	$5.01799 \cdot 10^{-14}$

Area III is valid for densities larger than 1 g cm^{-3}. In this region, the g - function is neglectable and set to 0.

C: SAA model

$\Delta\bar{G}^{\circ}_{T_{\mathrm{r}},\rho_{\mathrm{r}}}$ and $\Delta\bar{G}^{\circ}$ are defined as the change in the Gibbs free energy of reaction at the reference state and the difference in the Gibbs free energy of reaction at the reference state to a state of given temperature and density. $\Delta\bar{G}^{\circ}$ can be divided into two parts $\Delta\bar{G}^{\circ}_{\mathrm{s}}$ and $\Delta\bar{G}^{\circ}_{\mathrm{res}}$ which describe either the electrostatic interaction between solute and solvent and the non-electrostatic interactions between solid and solvent or solvent - solvent. The new arrangement of the solvent molecules is also included in this part:

$$\Delta\bar{G}^{\circ} = \Delta\bar{G}^{\circ}_{\mathrm{s}}(T_{\mathrm{r}},\rho_{\mathrm{r}} \rightarrow T,\rho) + \Delta\bar{G}^{\circ}_{\mathrm{res}}(T_{\mathrm{r}},\rho_{\mathrm{r}} \rightarrow T,\rho) \tag{2-7-1}$$

with

$$\Delta\bar{G}^{\circ}_{\mathrm{s}} = \omega_{T,\rho}\left(\frac{1}{\varepsilon_{T,\rho}} - 1\right) - \omega_{T_{\mathrm{r}},\rho_{\mathrm{r}}}\left(\frac{1}{\varepsilon_{T_{\mathrm{r}},\rho_{\mathrm{r}}}} - 1\right) \tag{2-7-2}$$

The formulation of $\Delta\bar{G}^{\circ}_{\mathrm{s}}$ is according to the theory of Born [155] with $\omega_{T_{\mathrm{r}},\rho_{\mathrm{r}}}$ and $\omega_{T,\rho}$ previously described in section with either the Born coefficient for the reference state or at given temperature and pressure. Concerning the different areas of the g - function and the related calculation rules, it is neglectable in the temperature range of 298 K to 873 K. The g - function for the reference state equals to 0 and $\omega_{T,\rho}$ becomes constant:

$$\Delta\bar{G}_{\mathrm{s}}^{\circ} = \omega_{T_{\mathrm{r}},\rho_{\mathrm{r}}}\left(\frac{1}{\varepsilon_{T,\rho_{\mathrm{r}}}} - \frac{1}{\varepsilon_{T_{\mathrm{r}},\rho_{\mathrm{r}}}}\right) \tag{2-7-3}$$

According to Johnson et al. [56], the dielectric constant is calculated as already described in section 2.1.1. The empirical part of the r-HKF model is adapted. Either the temperature of the reference state T_{r} at reference density ρ_{r} is changed to a specific temperature, and the reference density ρ_{r} is changed to a certain density at a specific temperature. Both of these modifications are described in the following.

As already mentioned, the equilibrium constant K_i can be defined with a van't Hoff approach. For a constant density, the equilibrium constant $\ln K_{T,\rho}$ can be related to the temperature what is also valid around the critical point.

$$\ln K_{T,\rho_{\mathrm{r}}} = -\frac{\Delta\bar{G}_{T,\rho_{\mathrm{r}}}}{RT} = -\frac{\Delta\bar{G}^{\circ}_{T_{\mathrm{r}},\rho_{\mathrm{r}}}}{RT_{\mathrm{r}}} - \frac{\Delta\bar{H}^{\circ}_{T,\rho_{\mathrm{r}}}}{R}\left(\frac{1}{T} - \frac{1}{T_{\mathrm{r}}}\right) \tag{2-7-4}$$

The Gibbs free energy of formation at the reference state $\Delta\bar{G}^{\circ}_{T_{\mathrm{r}},\rho_{\mathrm{r}}}$ is calculated with literature data of the metal salts and the species involved in the reaction. For many species, data are provided in databases. Once the values are not found, they are calculated with the Gibbs free energy of formation and the relating Gibbs free entropy. The enthalpy of formation at given temperature and reference density $\Delta\bar{H}^{\circ}_{T,\rho_{\mathrm{r}}}$ is determined as follows:

$$-\frac{\Delta\bar{H}^{\circ}_{T,\rho_{\mathrm{r}}}}{R}\left(\frac{1}{T'} - \frac{1}{T_{\mathrm{r}}}\right) = \ln\frac{K_{T'}}{K_{T_{\mathrm{r}}}} \tag{2-7-5}$$

$\Delta\bar{H}^{\circ}_{T,\rho_{\mathrm{r}}}$ is a constant that correlates the reference temperature T_{r} with a temperature T' below 373 K. Both equilibrium constants $K_{T'}$ and $K_{T_{\mathrm{r}}}$ need to be calculated. $K_{T_{\mathrm{r}}}$ is determined according to equation (2-7) and $K_{T'}$ is evaluated with $T' = 50$ °C and according to:

$$\ln K_{T'} = \ln K_{T_{\mathrm{r}}} - \frac{\Delta\bar{H}^{\circ}_{T_{\mathrm{r}},\rho_{\mathrm{r}}}}{R}\left(\frac{1}{T'} - \frac{1}{T_{\mathrm{r}}}\right) + \frac{\Delta\bar{C}^{\circ}_{p\,T_{\mathrm{r}},\rho_{\mathrm{r}}}}{R}\left(\ln\frac{T'}{T_{\mathrm{r}}} + \frac{T_r}{T'} - 1\right) \tag{2-7-6}$$

The combination of equations (2-7) (2-7-2), (2-7-3), and (2-7-4) equals to:

$$-\frac{\Delta\bar{G}_{\mathrm{res}}}{RT} = -\frac{\Delta\bar{H}^{\circ}_{T,\rho_{\mathrm{r}}}}{R}\left(\frac{1}{T} - \frac{1}{T_{\mathrm{r}}}\right) + \frac{\Delta\bar{G}^{\circ}_{T_{\mathrm{r}},\rho_{\mathrm{r}}}}{R}\left(\frac{1}{T} - \frac{1}{T_{\mathrm{r}}}\right) + \frac{\alpha\Delta\omega_{T_{\mathrm{r}},\rho_{\mathrm{r}}}(T - T_{\mathrm{r}})}{RT}$$

$$= -\frac{\Delta\bar{H}^{\circ}_{T,\rho_{\mathrm{r}}} - \Delta\bar{G}^{\circ}_{T_{\mathrm{r}},\rho_{\mathrm{r}}} + \alpha\Delta\omega_{T_{\mathrm{r}},\rho_{\mathrm{r}}}T_{\mathrm{r}}}{R}\left(\frac{1}{T} - \frac{1}{T_{\mathrm{r}}}\right) \tag{2-7-7}$$

with $\alpha = 6.385\ 10^{-5}\ \mathrm{K}^{-1}$ [4]. The parameters are derived from equation (2-7-3) and the relationship between dielectric constants at reference conditions and a given temperature. A linear function of the temperature fits to describe this relation:

$$\frac{1}{\varepsilon_{T,\rho_r}} - \frac{1}{\varepsilon_{T_r,\rho_r}} = \alpha(T - T_r) \tag{2-7-8}$$

The combination of equations (2-7-3) and (2-7-7) provides the function for the equilibrium constant K_{T,ρ_r} at given temperature and reference density:

$$\ln K_{T,\rho_r} = -\frac{\Delta\bar{G}_{T,\rho_r}}{RT} = -\frac{\Delta\bar{G}^{\circ}_{T_r,\rho_r}}{RT_r} - \frac{\Delta\bar{H}^{\circ}_{T,\rho_r} + \alpha\Delta\omega_{T_r,\rho_r}T_r}{R}\left(\frac{1}{T} - \frac{1}{T_r}\right)$$

$$-\frac{\Delta\omega_{T,\rho_r}}{RT}\left(\frac{1}{\varepsilon_{T,\rho_r}} - 1\right) + \frac{\Delta\omega_{T_r,\rho_r}}{RT}\left(\frac{1}{\varepsilon_{T_r,\rho_r}} - 1\right) \tag{2-7-9}$$

Next to the derived function for K_{T,ρ_r}, the influence of the density on $\Delta\bar{G}^{\circ}_s$ is investigated. Both the dielectric constant and the Born coefficient are replaced from the reference state to a specific state. A comparison of literature data with equation (2-7-9) implements the influence on the non-electrostatic interactions. For the NaCl system, present literature data favors it for this investigation. The following function shows the density dependence of the non-electrostatic interactions while changing from reference to a specific density:

$$\ln K_{T,\rho,\mathrm{lit}} - \ln K_{T,\rho} = -\frac{\beta(1-\rho^*)^{2/3}}{R}\left(\frac{1}{T} - \frac{1}{T_r}\right) \tag{2-7-10}$$

D: Activity coefficient models

Debye-Hückel-Davies equation:

The parameters A_M and I_M and z_j represent the Debye – Hückel parameter, the ionic strength and the charge of the ion. A_M is a function of the solvent density $\rho_{solv}(T)$, the dielectric constant $\varepsilon(T)$ and the temperature [69]:

$$A_M(T) = \frac{1}{\ln 10}\sqrt{2\cdot 10^3 \pi N_A \rho_{solv}(T)}\left(\frac{e^2}{4\pi\varepsilon_0\,\varepsilon(T)\,k\,T}\right)^{\frac{3}{2}}$$

$$\approx \frac{1.8248\cdot 10^6\sqrt{\rho_{solv}}}{(T\varepsilon)^{3/2}} \tag{2-11-1}$$

Furthermore, N_A, e and k represent the Avogadro number, the elemental charge and the Boltzmann constant. The ionic strength is a function of the concentration of each concerning species and their corresponding charge:

$$I_m = \frac{1}{2}\sum_i m_i z_i^2 \tag{2-11-2}$$

Bromley equation:

The calculation of the activity coefficients with the Bromley model is defined with two parameters F_a and F_c with a temperature-dependent parameter B^*_{ca} with values in literature [63]. The indices a and c represent either the anion and the cation.

$$F_a = \sum_c B^*_{ca}\, z^2_{ca} m_c \tag{2-12-1}$$

$$F_c = \sum_a B^*_{ca}\, z^2_{ca} m_a \tag{2-12-2}$$

and

$$z_{ca} = \frac{1}{2}(|z_c| + |z_a|) \tag{2-12-3}$$

$$B^*_{ca} = \frac{(0.06 + 0.6B_{ca})|z_c z_a|}{\left(1 + \frac{1{,}5I_{\mathrm{m}}}{|z_c z_a|}\right)^2} + B_{ca} \tag{2-12-4}$$

E: General equations

The first equation of the NS-equations is the continuity equation:

$$\frac{\partial \rho}{\partial t} + \nabla \cdot (\rho \vec{v}) = S_{\mathrm{m}} \tag{2-37}$$

Within that equation, ρ describes the fluid density, $\vec{v}$ the velocity vector and S_{m} an external source term. The second equation as the momentum conservation equation, is defined as the follows:

$$\frac{\partial}{\partial t}(\rho \vec{v}) + \nabla \cdot (\rho \vec{v} \vec{v}) = -\nabla p + \nabla \cdot \bar{\bar{\tau}} + \rho \vec{g} + \vec{F} \tag{2-38}$$

Here, p and $\bar{\bar{\tau}}$ represent the static pressure and the stress tensor whereas $\rho \vec{g}$ and $\vec{F}$ stand for the gravitational and the external body force. Within the equation, $\bar{\bar{\tau}}$ is described as:

$$\bar{\bar{\tau}} = \mu \left[(\nabla \vec{v} + \nabla \vec{v}^T) - \frac{2}{3} \nabla \vec{v}\, I \right] \tag{2-39}$$

The parameters μ and I_v are the molar viscosity and the combination of the unit tensor with the volume dilation. The third equation of the NS-equations is the energy equation. It is required for the simulation of the thermal field based on the heat transfer theory, which is implemented into ANSYS Fluent® [128]:

$$\frac{\partial}{\partial t}(\rho E) + \nabla \cdot (\vec{v}(\rho E + p)) = \nabla \cdot \left(k_{eff}\nabla T - \sum_j h_j \vec{J}_j + \left(\bar{\bar{\tau}}_{eff} \cdot \vec{v}\right)\right) + S_h \tag{2-40}$$

The energy equation requires the parameters k_{eff}, $\vec{J}_j$ and S_h. k_{eff} is defined as the summation of k_t and k_T, where k_T depends on the used turbulence model for the simulation. $\vec{J}_j$ and S_h represent the diffusion flux and the heat sources, including the heat of chemical reactions. The energy transfer caused by conduction, species diffusion, and viscous dissipation is represented by the three terms on the right side of the equation. Next to these parameters, the factor E is defined as a function of the specific enthalpy h:

$$E = h - \frac{p}{\rho} + \frac{v^2}{2} \tag{2-41}$$

Besides the NS-equations, a turbulence model has to be chosen to describe the turbulent flow. There, two crucial models are mostly taken, the semi-empirical standard or the realizable k - ε model. The standard k - ε model is built up from the transport equations of the kinetic energy k and dissipation rate ε_t. The equations for the kinetic energy and the dissipation rate are obtained from the original equation or theoretically with less accuracy. It is assumed that the flow behavior is fully turbulent. Secondly, the molecular viscosity and its effects are negligible. Based on the standard model, the realizable model was developed as a modification. This model provides advantages to the standard model and deviates into two general aspects. The turbulent viscosity is newly defined, and the transport equation for the dissipation rate is obtained from an exact equation. One great advantage of the realizable model compared to the standard is the accordance of the model with the theory and physics of turbulent flows. The equation of the realizable k - ε model is defined as follows:

$$\frac{\partial}{\partial t}(\rho k_t) + \frac{\partial}{\partial x_j}(\rho k_t u_j) = \frac{\partial}{\partial x_j}\left[\left(\mu + \frac{\mu_t}{\sigma_{k_t}}\right)\frac{\partial k_t}{\partial x_j}\right] + G_k + G_b - \rho\varepsilon - Y_M + S_{k_t} \tag{2-42}$$

Herein $\rho\varepsilon_t$ can be written as:

$$\frac{\partial}{\partial t}(\rho\varepsilon_t) + \frac{\partial}{\partial x_j}(\rho\varepsilon_t u_j) = \frac{\partial}{\partial x_j}\left[\left(\mu + \frac{\mu_t}{\sigma_\varepsilon}\right)\frac{\partial\varepsilon_t}{\partial x_j}\right] + \rho C_1 S_{\varepsilon_t} - \rho C_2 \frac{{\varepsilon_t}^2}{k_t + \sqrt{v\,\varepsilon_t}}$$

$$+ C_{1\varepsilon_t}\frac{\varepsilon_t}{k_t} C_{3\varepsilon_t} G_b + S_{\varepsilon_t} \tag{2-43}$$

with

$$C_1 = \max\left[0.43, \frac{\eta}{\eta+5}\right],\ \eta = S\frac{k_t}{\varepsilon_t}, S = \sqrt{2S_{ij}S_{ij}}. \tag{2-44}$$

G_k, G_b, Y_M represent the parameters for the generation of the turbulent kinetic energy initiated by mean velocity gradients, the formation of turbulent kinetic energy caused by buoyancy effects, and the amount of fluctuating dilatation to the total dissipation rate in compressible turbulence. The parameters $C_{1\varepsilon_t}, C_2$ and either σ_{k_t} or σ_{ε_t} represent two constants and the turbulent Prandtl number for both, the kinetic energy k_t and the dissipation rate ε_t. S_{k_t} and S_{ε_t} describe user-defined source terms according to S_m in equation (2-37).

The previously formulated equations describe the physics for the simulation of the thermal and velocity fields. Another equation needs to be used to simulate the residence time distribution (RTD) and the reaction. The species transport equation are defined as follows [128]:

$$\frac{\partial}{\partial t}\left(\alpha_p \rho_p Y_p^i\right) + \nabla\cdot\left(\alpha_p \rho_p \overrightarrow{v_p} Y_p^i\right) = -\nabla\cdot\alpha_p J_p^i + \alpha_p R_p^i + R_h \tag{2-45}$$

Within this equation, the parameters J_p^i, R_p^i, and R_h stand for the mass transfer rate and the rate for the homogeneous and the heterogeneous reaction. For the homogeneous reaction, another species transport equation is used and solved for the i^{th} species. Here, the convection-diffusion is defined as a conservation equation [128]:

$$\frac{\partial}{\partial t}(\rho Y_i) + \nabla\cdot(\rho\vec{v}Y_i) = -\nabla\cdot\vec{J_i} + R_i + S_i \tag{2-46}$$

with R_i and S_i as the net production rate during the occurring chemical reaction and the creation rate due to adding of the dispersed phase of the species i th species.

Appendix chapter 3

A: PXRD

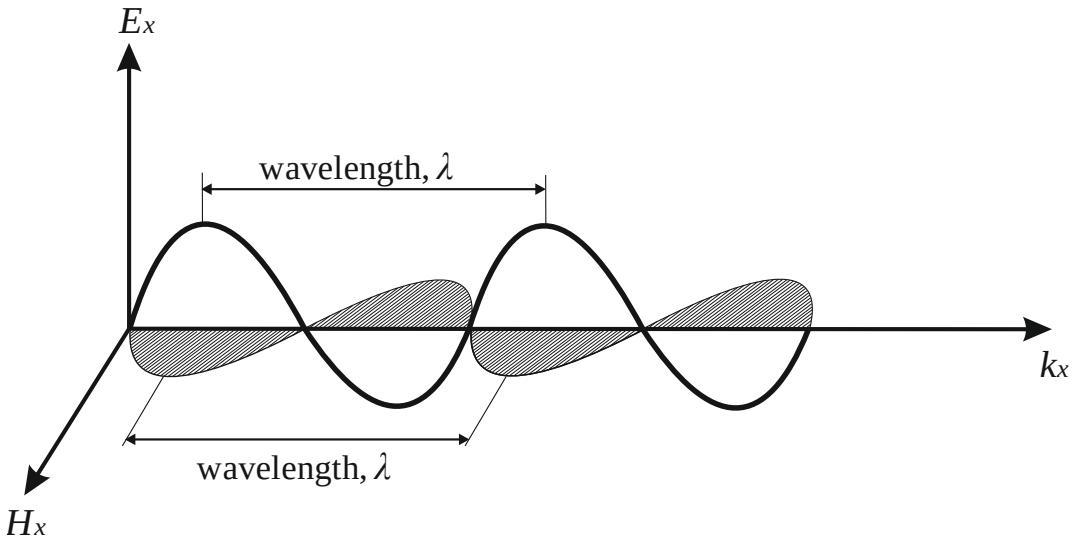

Figure 11-2: Illustration of an electromagnetic wave. The characteristic value of the wavelength λ represents the distance between two crests of the wave. λ is valid for both the electric and the magnetic fraction.

Regarding the diffraction related to X-rays, several processes need to be considered: coherent scattering, incoherent, or Compton scattering and absorption. The relation between crystals and X-rays is of great complexity. X-rays are emitted in conventional so-called X-ray tubes, which show low efficiency in a synchrotron where high-energy electrons are used. For the application of the X-rays concerning the analysis of crystal structures, the Braggs' law relates the diffraction angle, the wavelength, and the interplanar spacing:

$$n\lambda = 2d_{hkl}\sin\Theta_{hkl} \tag{3-2}$$

with n as the order of reflection, the angle Θ and the diameter of the unit cell d_{hkl} with hkl representing the planes. The Bragg's law is the primary law for analyzing crystal structures with X-rays and is imaged in Figure 11-3:

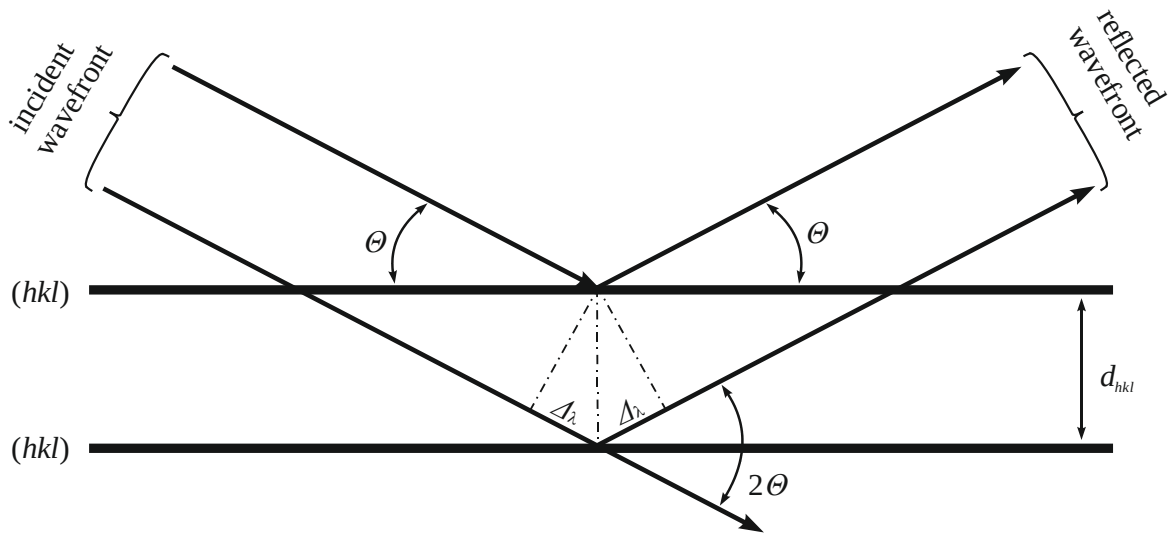

Figure 11-3: Sketch of the Braggs' law, two incident waves with a wavelength λ hitting two planes (hkl) with the angle Θ. The planes have a distance of d_{hkl}. The waves are reflected after hitting the planes.

The two parallel waves hit the two planes (*hkl*) and are reflected with the same angle Θ. The difference in the distance between the two waves after the reflection is represented by Δ_λ. It is defined as $\Delta_\lambda = d_{hkl}\ sin\,\Theta$. This causes constructive interferences with the total length of $2\,\Delta = n\,\lambda$. The reflected X-rays are collected by a detector as characteristic peaks summarized in a diffractogram. As far as enough planes are detectable, the Bragg's law is appropriate. The Bragg's law describes the reflection of an ideal single crystal emitting non-ideal interreference. Mainly, small particles are analyzed as powders consisting of small polycrystalline particles. The Braggs' law is limited for small sizes of the particles. With decreasing size of the particles in the nanometer range, the resulting diffraction peaks get broader, the so-called peak broadening. It occurs due to imperfections in the crystal and the instrument. For this, the Scherrer equation was developed. It enables the estimation of the crystallite size due to the peak broadening and the analysis of a single characteristic peak:

$$\beta_{hkl} = \frac{K_S \lambda}{L_{hkl} cos\theta} \tag{3-3}$$

with β_{hkl} representing the angular width, K_S as a scale factor, depending on the particle shape and L_{hkl} as the crystallite size. For the case of a perfect sphere, K represents the value of 0.89, and for cubes, 0.94. In general, it is roundabout 1.

Commercial apparatus or synchrotrons determine and analyze the particles with PXRD experiments. The powders are prepared on a carrier or in a thin glass capillary. The detector is a crucial component of the PXRD apparatus. It is used to record the diffraction intensities as a function of the angle. The above-mentioned characteristic peaks and the peak broadening effects are used to analyze the examined material. Next to the Scherrer equation, a more complex whole pattern fitting is possible.

The particles synthesized within this work were prepared and analyzed with PXRD measurements. Therefore, a diffractometer STADI-MP, STOE (Institute for Inorganic Chemistry, Karlsruhe Institute of Technology, Germany) was used. It was operated at 40 kV and 40 mA with a copper Kα radiation and a Mythen1K detector. A monochromator made of curved Germanium was further used. The obtained diffractograms were compared to reference peaks for CeO_2 from the Inorganic Crystal Structure Database (ICSD) to get the examined phases of the produced particles.

B: TEM

A TEM microscope consists of specific components like the electron source, a condenser lens, an objective lens, an intermediate lens, and a projector lens. The lenses are of a magnetic type instead of glass lenses built in optical microscopes. The final image of the sample (located in between condenser and objective lens) is found on the screen after the projector lens. The electron beam containing housing is vacuumed to prevent the electron beam from scattering with air molecules. TEM is often coupled with further analyzing methods like EDX. This is used for the analysis of the examined samples regarding their content of elements. Figure 11-4 illustrates a standard TEM system as it is typically used.

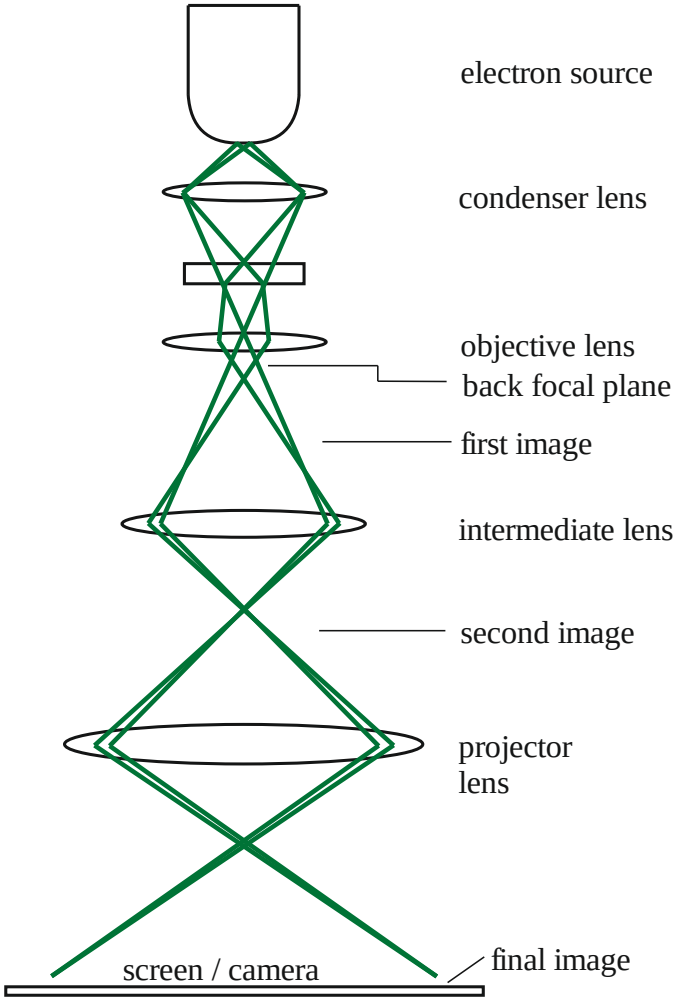

Figure 11-4: Commercial TEM system with the main components and additional attached equipment.

Appendix chapter 4

A: Detailed list of the used components for the CHTS plant

Table 11-3: Used components.

		Component	Company	Type
Pressure	indication	Digital display	WIKA	DI35
	measuring	Pressure transmitter		S-20
	measuring	Manometer		9239472
Pumps		Pneumatic HPLC pump	Knauer	HPLC-1950
		Isocratic HPLC pump		HPLC-64
Protection of the pumps		Check valve	SITEC-Sieber	720.4533
Overpressure protection		Rupture disc, p_{max} = 60 MPa		728.0600
Temperature	indication	Process controller	Eurotherm	3504
	control			
	limiter	Process controller		2116
	measuring	Thermocouple	TEC CN	Type K, class 1
			SITEC-Sieber	770.5231-7
Heating unit		Heating unit 1, 750 W	Constructed	
		Heating unit 2, 3000 W	SITEC-Sieber	Constructed
Cooling unit		Heat exchanger		Constructed
		Thermostat	Lauda, 200 W	RE212, Ra 8
			Thermo Scientific, 500 W	K35, DC 50
Mass flow measurement		Coriolis mass flow meters	Rheonik	RHE07,-015, RHM
Mass balances			Mettler Toledo	PM 6100
				AB265-S
			Mettler Toledo	
Data acquisition		Data logger	Keysight	34970A
T-junctions		Fittings, 400 MPa	SITEC-Sieber	720.1533
		Mixer, 700 MPa		720.1633
Tubing		Stainless steel, ¼" x 2.4		730.2340
		Stainless steel, ¼" x 1.6		730.2350
		Stainless steel, 3/8" x 5.2		730.1223/f
Filter		High-pressure filter, 10 µm		720.6533-10
Valves		Valve, 100 MPa		710.3310
		Valve, 200 MPa		710.4310
		Valve, 200 MPa, double		710.4350
		Back pressure regulator		710.4322

Ceramic tubes	EIS measurement	Friatec	F143-11030-00050
Insulation, $T = 1273$ K	Insulation plates, 20 mm	Promat	Promatect
Housing	Polycarbonate plates, 6mm	S-Polytec	1650

B: Process flow diagram of the CHTS plant and operation

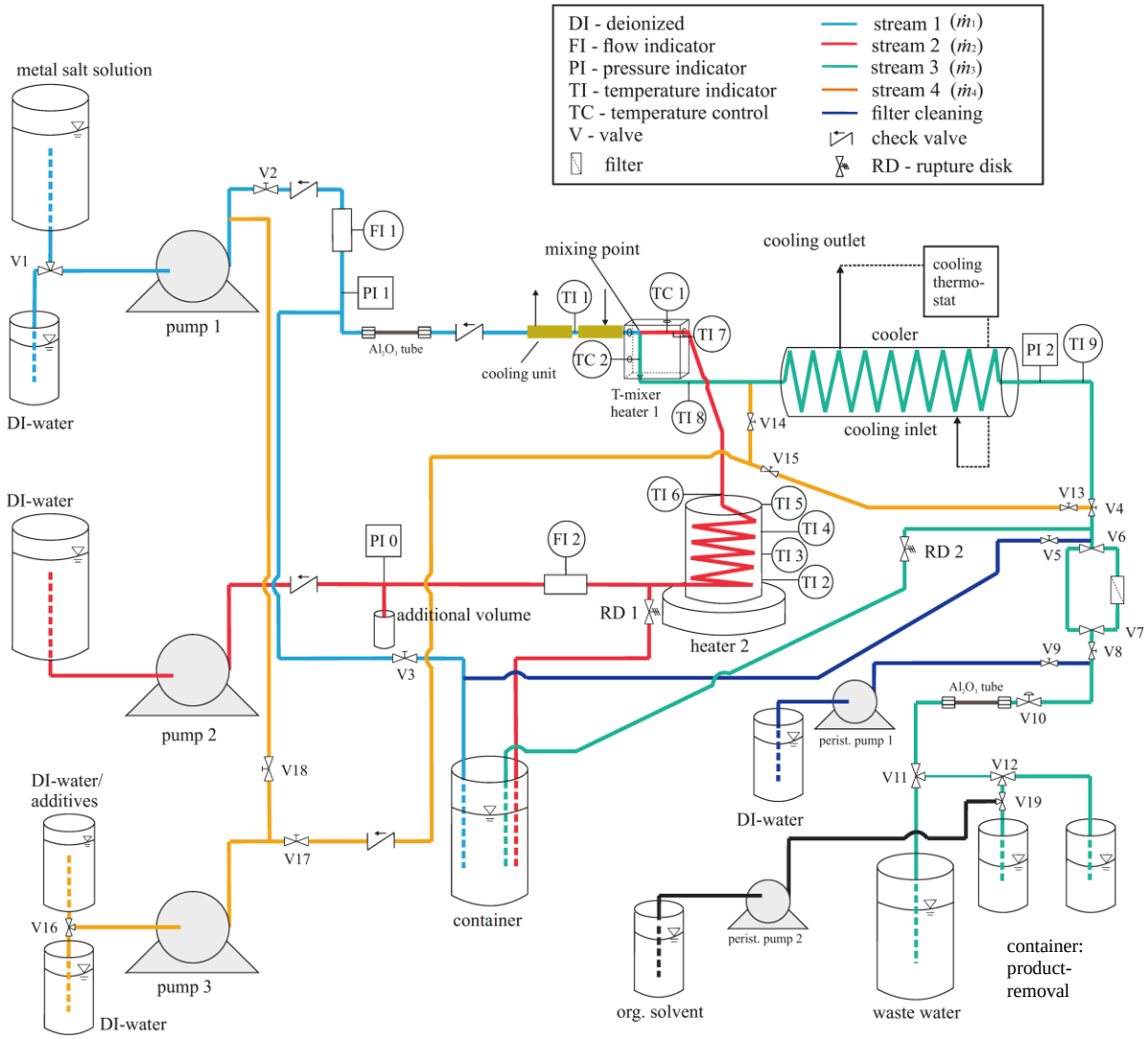

Figure 11-5: Process flow diagram of the CHTS plant including all components and measuring points.

The measuring points shown in the image were used for the determination of the temperature of the cold water or metal salt solution stream ($TI\,1,\ T_{\mathrm{salt}},\ T_1$), of the hot near- / supercritical water stream right after the heating unit ($TI\,6,\ T_{\mathrm{hot,1}}$), and right before the mixing point ($TC\,1,\ T_{\mathrm{hot,2}},\ T_2$), the mixing of the hot and the cold streams ($TC\,2,\ T_{\mathrm{mix}},\ T_3$), after the reaction tube ($TI\,8,\ T_{\mathrm{mix,2}}$) and after the cooling unit ($TI\,9,\ T_{\mathrm{cold}}$). Furthermore, the temperatures of the heating cartridges of both heating units ($TI\,7$ for heater 1 and $TI\,2$ – $TI\,5$ for heater 2) were measured.

After the construction and the setup of the CHTS plant, it was operated for characterization and experiments. In this section, the typical procedure during the operation of the plant is described. The main steps were the heating of the hot near- / supercritical water stream, the insurance of the constant temperature of the cold water / aqueous metal salt solution stream, the adjustment of the steady-state, the injection of the cold aqueous metal salt solution, the recovery of the particle suspension and the cooldown of the plant after the experiment.

1. At first, a protocol file for each experiment was created in LabVIEW. The file included the date, information about the performed experiment, the used process conditions (yearmonthday_(particle system)_pressure_temperature either of the hot water or the mixing stream_(salt concentration)_total mass flow rate_mixing ratio_cooling temperature of the cold stream).
2. The mean residence time was calculated depending on the used process conditions (density as a function of pressure and temperature). It referred to the inlet of the cold stream at the container in front of pump 1 to the outlet of the back pressure regulator. Here, the mean residence time was calculated for the cold stream (density for ambient temperature and high system's pressure) till the mixing point and from the mixing point (density at elevated temperature and high system's pressure) till the back pressure regulator.
3. The containers for either the cold and the hot water stream were filled with deionized water and degassed afterwards. Therefore, gaseous nitrogen was used for 5 minutes for the container of the cold water stream and 15 minutes for the container of the hot water stream. As recognizable in Figure 11-5, valve 1 was set to pressurize the deionized water after degassing, and valve 11 was set to carry the product stream into the container for wastewater.
4. The draft and the thermostats were started. The cooling temperature of the thermostats was set to 288 K. The pumps were started to transport both streams ($\dot{m}_1$ and $\dot{m}_2$). The total mass flow $\dot{m}_3$ and the mixing ratio a were set through the pumps (adjustment of the mass flow of pump 1) and the pneumatic pump. Then the back pressure regulator was closed slowly, and the pressure was increased with the pneumatic pump up to the desired pressure (25 – 35 MPa). Both process parameters are continuously controlled by the back pressure regulator and pump 2. Once the pressure and the total mass flow reached the steady-state, the heating unit of the hot water stream was switched on. The hot water temperature ($TC\,1,\ T_{\mathrm{hot,2}},\ T_2$) was set with the process controller, and the stream was heated till the set hot water temperature was reached. With this

procedure, mixing experiments of the cold and the hot water stream and the influence of the process conditions on the resulting mixing temperature could be carried out. Depending on the type of experiment, the prepared protocol file was started within LabVIEW to record all process parameters during the experiments.

5. For particle formation experiments, the second heating unit is switched on. The mixing temperature ($TC\,2,\ T_{\mathrm{mix}},\ T_3$) was set in the second process controller to ensure a constant temperature of the product stream. Once the steady-state was reached, the experiment for particle formation could be initiated. Therefore, the cold aqueous metal salt solution was prepared with 20 g of degassed water and the used metal salt. For the desired concentration, the metal salt (depending on the molar mass) was weighted on a fine balance (Mettler Toledo AB265-S) and mixed with the degassed water. In order to form the metal-oxide nanoparticles, valve 1 was switched to the transportation of the prepared aqueous metal salt solution.
6. During the transportation of the aqueous metal salt solution to the mixing point and the resulting particle formation with steady-state conditions, valve 11 was switched at the calculated mean residence time. The successful particle formation was visible through the turbidity of the product stream. The formed particles were recovered in glass bottles. For further production, valve 12 could be used to switch between two2 glass bottles. When the aqueous metal salt solution's prepared volume was empty, valve 1 was changed to deionized water. Once enough particle suspension was recovered, valve 11 was switched to the wastewater container again.
7. After the switch to deionized water, the turbidity decreased with increasing time. Another experimental run could be performed (other process conditions) once the turbidity disappeared and only pure deionized water left the CHTS plant.
8. Both heating units were switched off after the mixing or the particle formation experiments were carried out, and the plant was flushed with pure deionized water. Both pumps transported deionized water till the temperature of all thermocouples in the hot part of the CHTS plant measured values below 373 K. For this case, the system's pressure needed to be above the critical pressure of 22.1 MPa to ensure the liquid state of the deionized water. Once the CHTS plant was cooled down, the system's pressure was decreased to ambient pressure. The pumps were stopped, and the thermostats switched off together with the draft. The filter unit was backflushed regularly with the installed filter cleaning unit.

The functionalization stream $\dot{m}_4$ was used for different kinds of applications within the operation of the CHTS plant. In addition to the above-mentioned operating process, the functionalization stream could be used variably for different types of experimental setups.

As previously described, pump 3 was used for the functionalization stream as well as increased cold water or aqueous metal salt stream through the connection to pump 1. For functionalization, pump 3 transported either water, water with surfactants, other aqueous metal salt solutions, or organic acids. For this additional setup, deionized water was transported

by pump 3 until the steady-state of the CHTS plant was reached while heating the system. Depending on the performed experiment, valve 16 was switched from deionized water to one of the possibly before-mentioned fluids.

It was possible to dilute the resulting product suspension after the particle formation with water. Therefore, valves 14 and 18 were kept closed, and valves 13, 15, 17, and 20 were kept open. The deionized water was transported to valve 4, where it was mixed up with the particle suspension. Due to the dilution, the mean distance between the metal-oxide nanoparticles increased. Thereby, the probability of nanoparticle agglomeration decreased. For surface modification, the same setup of the functionalization line was used as the dilution of the metal-oxide nanoparticles with deionized water.

The functionalization stream enabled the production of hybrid or core-shell nanoparticles. The mixing of the produced metal-oxide nanoparticles with another cold aqueous metal salt solution after the mixing point in the reaction tube led to the formation of these nanoparticles (valve 13, 15, and 18 closed, valve 14, 17, and 20 open). The last point mentioned using organic solvents was necessary for the in situ functionalization of metal-oxide nanoparticles. Therefore, the organic acid was mixed up with the cold aqueous metal salt solution beforehand through the connection of pumps 1 and 2 (valve 13, 15, 17, and 20 closed and valve 18 open).

On the other hand, the functionalization could occur in the same setup as for the formation of hybrid or core-shell nanoparticles. This resulted in the surface modification of the metal-oxide nanoparticles and the fine dispersibility in organic solvents. Furthermore, even surface-modified metal-oxide nanoparticles for the click chemistry were synthesizable [27]. The previously described setup was also usable for quenching the product stream directly before entering the cooling unit. This led to rapid cooling and even fewer residence times within the hot reaction zone.

C: Image of the graphical surface of the LabVIEW evaluation routine

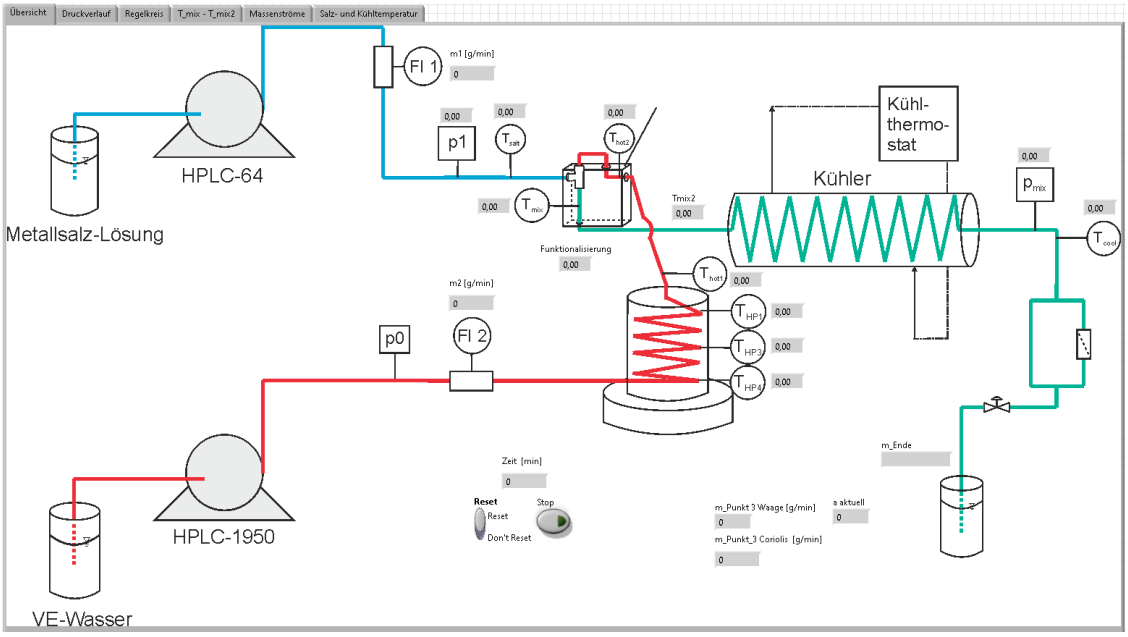

Figure 11-6: Visualization of the routine developed in LabVIEW to document the process conditions.

Appendix chapter 5

A: Designed 3D models with other mixing geometries used for the simulation

A.1 Bending setup

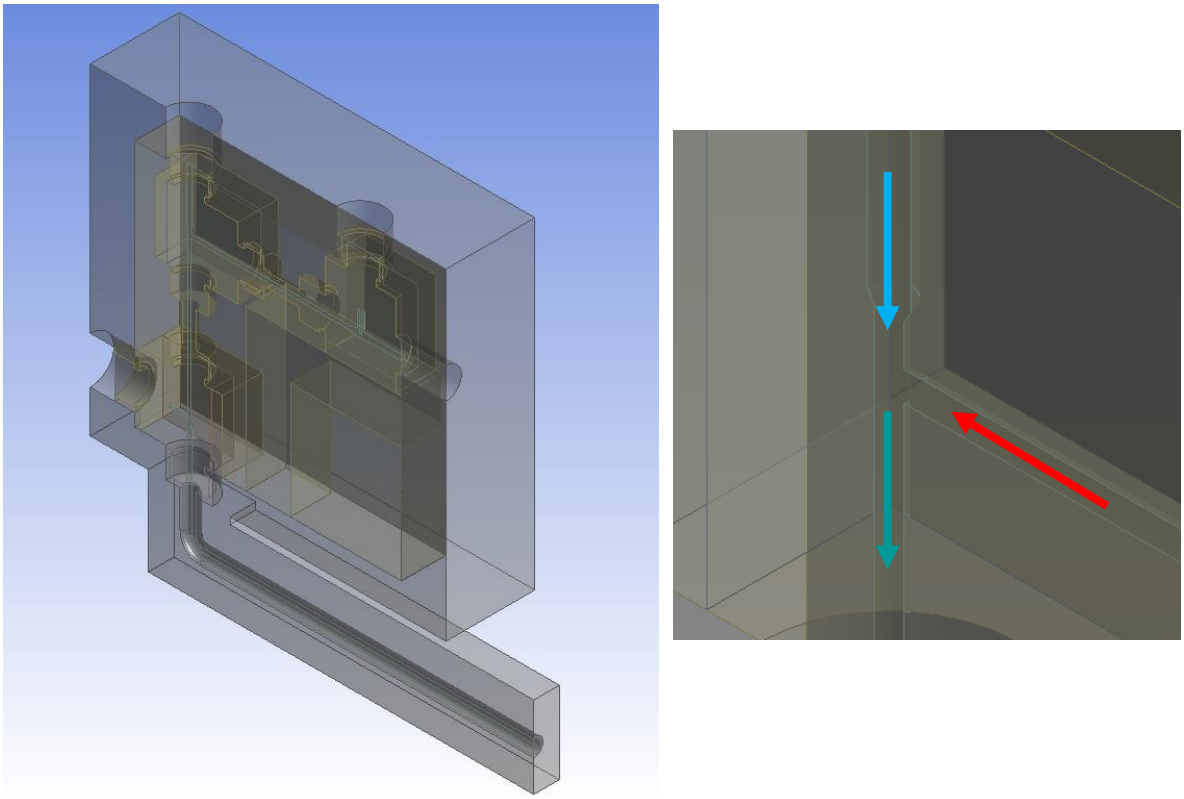

Figure 11-7: 3D model with the Bending setup [153].

A.2 Straight setup

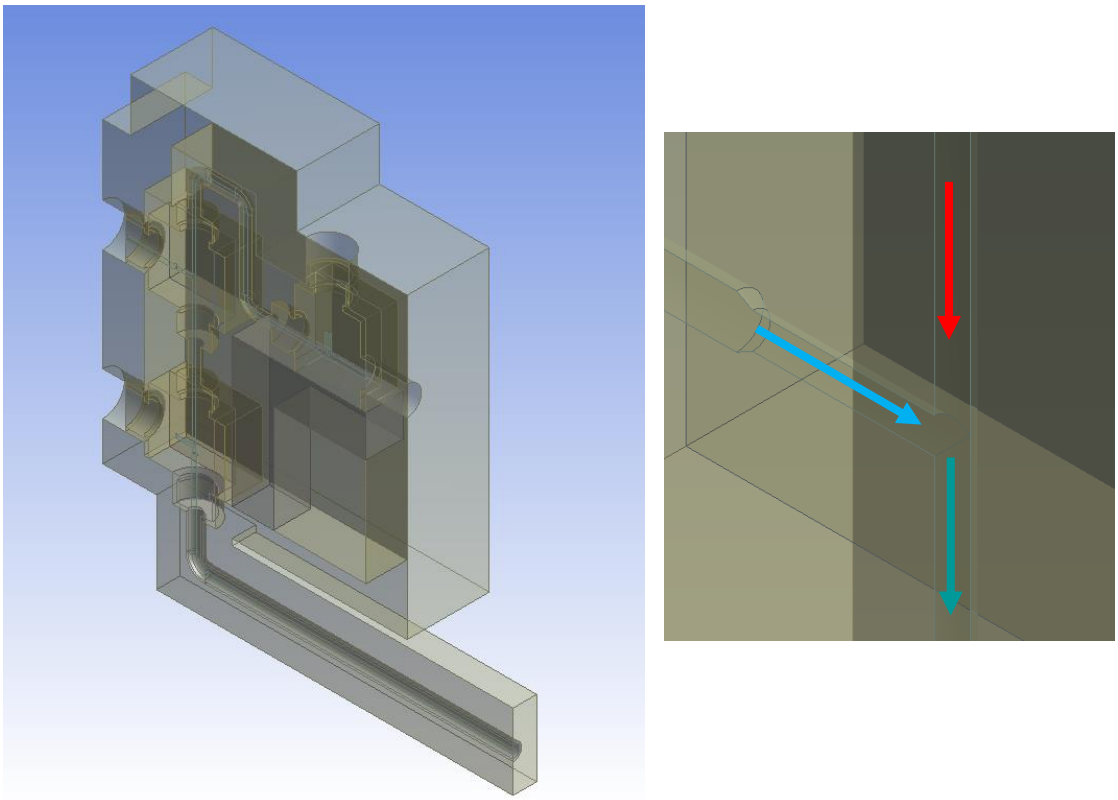

Figure 11-8: 3D model with the Straight setup [153].

A.3 Y-30 setup

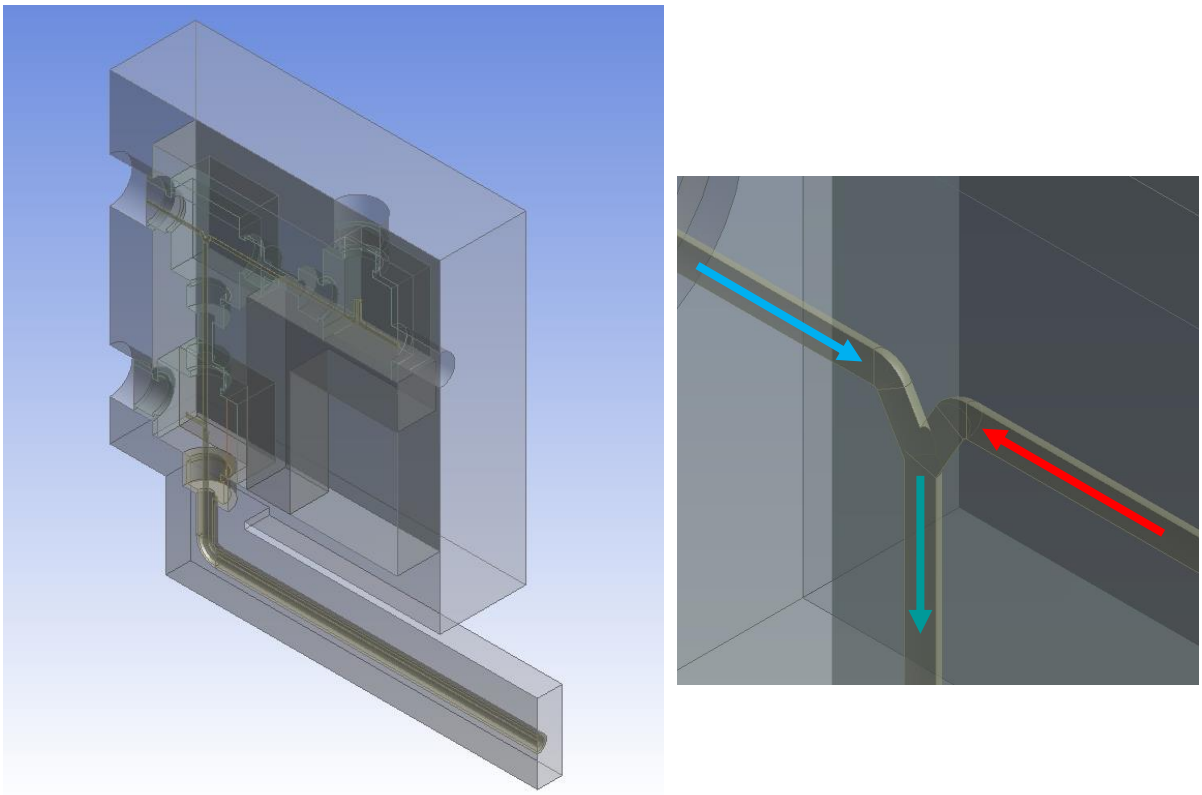

Figure 11-9: 3D model with the Y-30 setup [153].

B: Method of the simulation of the thermal and the velocity fields

Table 11-4. Different process conditions for the other designed models (Bending and Y-30)

p / MPa	$\dot{m}_3$ / g min^{-1}	T_2 / K	a / -
25	35	573	0.05; 0.20; 0.35
		673	
	55	573	
		673	
30	35	573	
		673	
	55	573	
		673	
35	35	573	
		673	
	55	573	
		673	

C: User-Defined Function (UDF) including water properties and kinetic approach

```
#include "udf.h"
DEFINE_SPECIFIC_HEAT(cp_heat_30, T, Tref, h, yi)
{
 real cp;

 if (T <= 660.)
{
    cp = (8104.8415381214 -156.3865463033 * T + 1.3052180401 * T * T
        -0.0061517586 * pow(T,3.) + 1.7911604582e-5 * pow(T, 4.)
        -3.299775792e-8 * pow(T, 5.) + 3.7572510257e-11 * pow(T, 6.)
        -2.4183344256e-14 * pow(T, 7.) + 6.7391326757e-18 * pow(T, 8.))*1000;
```

```
   *h = (8104.8415381214 * (T - Tref) - (156.3865463033/2)*(T*T - Tref*Tref) +
(1.3052180401/3)* (pow(T,3.) - pow(Tref,3.))

       - (0.0061517586/4) * (pow(T,4.)-pow(Tref,4.)) + ((1.7911604582e-5)/5) * (pow(T,5.) -
pow(Tref,5.))

       - ((3.299775792e-8)/6) * (pow(T,6.)- pow(Tref,6.)) + ((3.7572510257e-11)/7) *
(pow(T,7.)-pow(Tref,7.))

       - ((2.4183344256e-14)/8) * (pow(T,8.)-pow(Tref,8.)) + ((6.7391326757e-18)/9) *
(pow(T,9.)-pow(Tref,9.)))*1000;




}


else

{

   cp = (1.2384661082e10  -1.0732948382e8 * T  +387432.9197572286* T * T -
745.6317952621 * pow(T,3.) + 0.8069085472 * pow(T,4.)

         - 4.6555400874e-4 * pow(T,5.) + 1.1187917245e-7 * pow(T,6.))*1000;


   *h = (1.2384661082e10 * (T - 660.)  - ((1.0732948382e8) /2) * (T*T - 660.*660.) +
((387432.9197572286)/3) * (pow(T,3.) - pow(660.,3.))

       - (745.6317952621/4) * (pow(T,4.)-pow(660.,4.)) + (0.8069085472/5) *(pow(T,5.) -
pow(660.,5.)) - ((4.6555400874e-4)/6) *(pow(T,6.) - pow(660.,6.)) + ((1.1187917245e-
7)/7)*(pow(T,7.) - pow(660.,7.))


       + 8104.8415381214 * (660. - Tref) - (156.3865463033/2)*(660.*660. - Tref*Tref) +
(1.3052180401/3)* (pow(660.,3.) - pow(Tref,3.))

       - (0.0061517586/4) * (pow(660.,4.)-pow(Tref,4.)) + ((1.7911604582e-5)/5) *
(pow(660.,5.) - pow(Tref,5.))

       - ((3.299775792e-8)/6) * (pow(660.,6.)- pow(Tref,6.)) + ((3.7572510257e-11)/7) *
(pow(660.,7.)-pow(Tref,7.))

       - ((2.4183344256e-14)/8) * (pow(660.,8.)-pow(Tref,8.)) + ((6.7391326757e-18)/9) *
(pow(660.,9.)-pow(Tref,9.)))*1000;

}
```

```
return cp;
}



DEFINE_PROPERTY(therm_cond_30,cell,thread)
{
  real ktc;
  real temp = C_T(cell,thread);

  ktc = (-23573.5925737082 + 322.205845884 * temp - 1.7883460109 * temp * temp
        + 0.0052816734 * pow(temp, 3.) -8.7120029406e-6 * pow(temp, 4.)
        + 7.5859948683e-9 * pow(temp,5.) -2.7231722059e-12 * pow(temp, 6.))* 0.001;

  return ktc;
}

DEFINE_PROPERTY(density_30,cell,thread)
{
  real rho;
  real temp = C_T(cell,thread);

  rho = 147507.3619220635 -2362.1612235536 * temp + 16.1288838659 * temp * temp
        -0.0604465383 * pow(temp,3.) +  1.3431274934e-4 * pow(temp,4.)
        -1.7702425303e-7 * pow(temp,5.) + 1.2819587599e-10 * pow(temp,6.)
        -3.9369362426e-14 * pow(temp,7.);

  return rho;
```

```
}

DEFINE_PROPERTY(viscosity_30,cell,thread)
{
  real mu;
  real temp = C_T(cell,thread);

    mu = (565717.2777223417 -9021.988185464 * temp + 62.8966130101 * temp * temp
        -0.2496997663 * pow(temp,3.) + 6.1651442751e-4 * pow(temp,4.) -9.6846908534e-7 *
pow(temp,5.)
        + 9.4464435651e-10 * pow(temp,6.) -5.2286001754e-13 * pow(temp,7.) +
1.2569667873e-16 * pow(temp,8.)) * 1.e-6;
  return mu;
}
DEFINE_VR_RATE(vol_reac_rate, c, t, r, wk, yk, rate, rr_t)
{
real ci, ep, prod;
int i;

/* Calculate Arrhenius reaction rate  */

prod = 1.;

ep = (C_R(c, t)/1000) * (1. + 14.70333593 / (C_T(c, t)/298.15) + 212.8462733 / (C_T(c,
t)/298.15) - 115.4445173 + 19.55210915 * (C_T(c, t)/298.15) - 83.30347980 / (C_T(c,
t)/298.15) + 32.13240048 * (C_T(c, t)/298.15) - 6.694098645 * pow((C_T(c, t)/298.15), 2) -
37.86202045 * pow((C_T(c, t)/298.15), -2) + 68.87359646 / (C_T(c, t)/298.15) -
27.29401652) ;

for (i = 0; i < r->n_reactants; i++)
{
```

```
ci = C_R(c, t) * yk[r->reactant[i]] / wk[r->reactant[i]];

prod *= pow(ci, r->exp_reactant[i]);

}

*rate = r->A * exp(-(r->E - 4.5e5 *(1 / ep - 1 / 35.93)) /
(UNIVERSAL_GAS_CONSTANT * C_T(c, t))) * prod;


*rr_t = *rate;


/* No "return..;" value. */

}
```

Appendix chapter 6

A: Classification of typical metal salts according to Marshall and Valyashko

Table 11-5: Classification of different metal salts [66,67].

type 1 metal salt	type 2 metal salt
according to Marshall [66]	
$LiClO_4$	Li_2SO_4
NaCl, NaBr, NaI, $NaNO_3$, Na_2SeO_4	Na_2SO_4, Na_2CO_3
KCl, KBr, KI, KNO_3, $KBrO_3$, KIO_3	Na_3PO_4
K_2CrO_4, $KReO_4$	K_2SO_4
NH_4Cl, NH_4Br, $(NH_4)_2SO_4$	
$MgCl_2$, MgI_2	
$CaCl_2$	
$SrCl_2$, $SrBr_2$, $Sr(NO_3)_2$,	
$BaCl_2$, $BaBr_2$, $Ba(NO_3)_2$	
$MnCl_2$	
$FeCl_3$	
$ZnCl_2$	
$CdCl_2$, $CdBr_2$, CdI_2, $Cd(ClO_4)_2$	
$HgCl_2$	
TiCl, Ti_2SO_4	
$PbCl_2$, $PbBr_2$	

according to Valyashko [67]	
KF, RbF, CsF	LiF, NaF
LiCl, LiBr, LiI	Li_2CO_3, Na_2CO_3
NaCl, NaBr, NaI	Li_2SO_4, Na_2SO_4, K_2SO_4, $KLiSO_4$
K_2CO_3, Rb_2CO_3	Li_2SiO_3, Na_2SiO_3
Rb_2SO_4	Li_3PO_4, Na_3PO_4
Na_2SeO_4	CaF_2
K_2SiO_3	SrF_2,
K_3PO_4	BaF_2
$CaCl_2$, $CaBr_2$, CaI_2	
$SrCl_2$, $SrBr_2$	
$BaCl_2$, $BaBr_2$	

Appendix chapter 7

A: Characterization of the CHTS plant

After the construction and the setup of the pilot plant, it was characterized with preliminary experiments. Stability and heating tests were carried out to investigate the long-term stability of the process conditions depending on the used components within the plant. At first, the stability of the process conditions during the operation needed to be guaranteed. These have an enormous influence on the effects during particle formation. Therefore, mixing experiments were performed with a constant mixing ratio and variable pressures, hot stream temperatures, and total mass flows. Figure 11-10 shows the results for the long-term stability test for the before-mentioned process conditions.

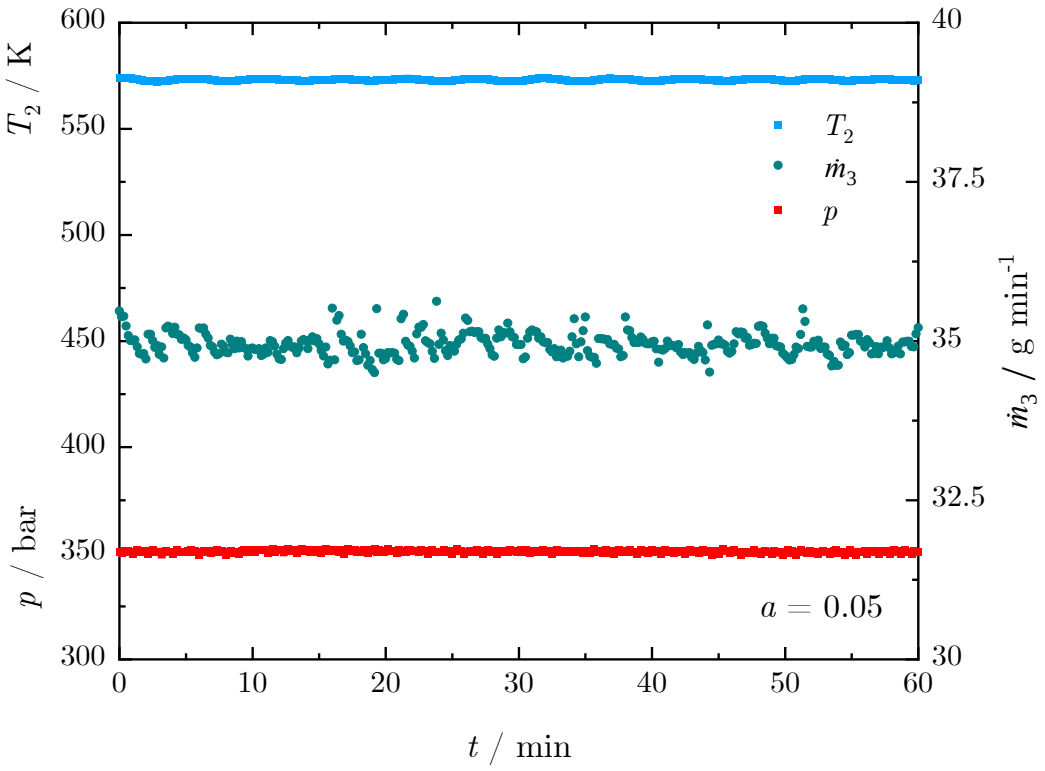

Figure 11-10: Stability test of the plant during the operation. Trends of the process conditions pressure p, hot stream temperature T_2 and total mass flow $\dot{m}_3$ as a function of the experimental time t.

The above-shown results were carried out for a pressure p of 35 MPa (shown as 350 bar for better scaling of the results), a hot stream temperature T_2 of 573 K, and a total mass flow $\dot{m}_3$ of 35 g min^{-1}. Both the pressure and the hot stream temperature show constant values for 60 minutes. The total mass flow varies slightly around 35 g min^{-1}. Also, this variation is in the range of accuracy. The relative deviation for the pressure p, the hot stream temperature T_2 and the total mass flow $\dot{m}_3$ results in 0.24%, 0.03% and 0.13%. Figure 11-11 images the mean deviation:

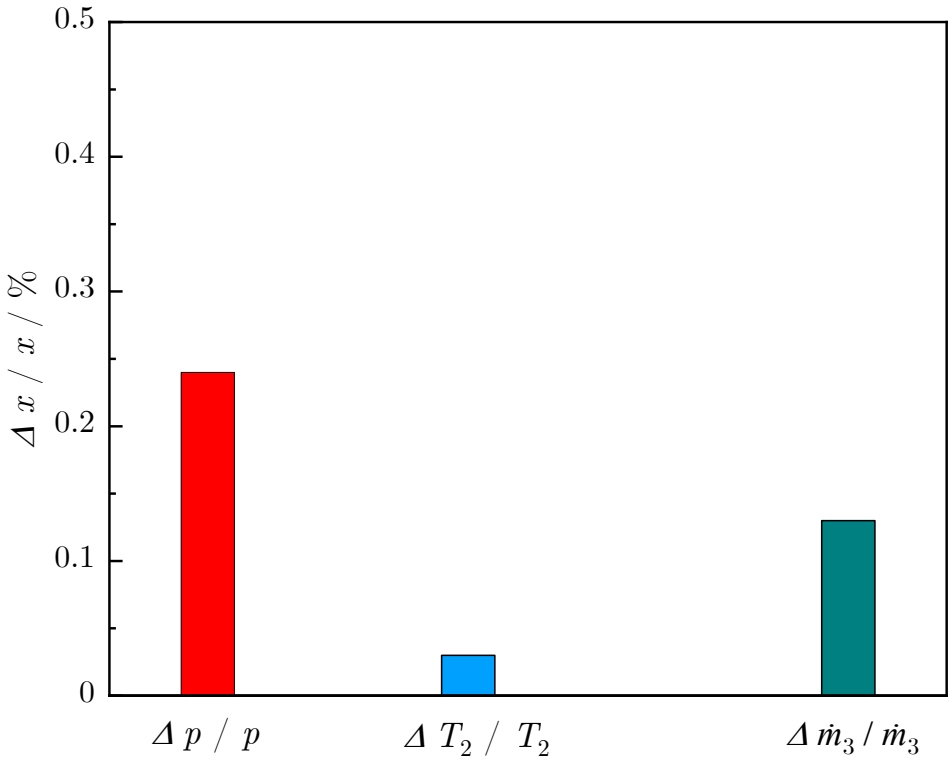

Figure 11-11: Relative deviation of the process conditions pressure p, hot stream temperature T_2, and total mass flow $\dot{m}_3$ for the stability experiments.

The results show constant values essential for the later particle size and the resulting particle size distribution. A variation in both the pressure and the temperature affects the reaction rate. A change in the total mass flow affects the particles' residence time inside the hot reaction part of the plant.

After the stability experiments, specific mixing experiments were performed for different process conditions. Beforehand, the mixer's total volume was determined by the internal diameter of the tube d_i and mixer d_m. In combination with the respecting length, the volume resulted in $1.185 \cdot 10^{-6}$ m^3. Based on that, the residence time was calculated according to the process conditions. Furthermore, the total volume of the CHTS plant was determined to calculate the mean residence time τ (compare equation (7-3)) from the inlet to the outlet before the experiments. The total mass flow $\dot{m}_3$ was kept constant at 35 g min^{-1} while the pressure p, the hot stream temperature T_2, and the mixing ratio a were varied. Both near- and supercritical temperatures were used with 573 K and 673 K. The pressure was varied between 25 MPa and 35 MPa. Figure 11-12 shows the results for the different mixing experiments:

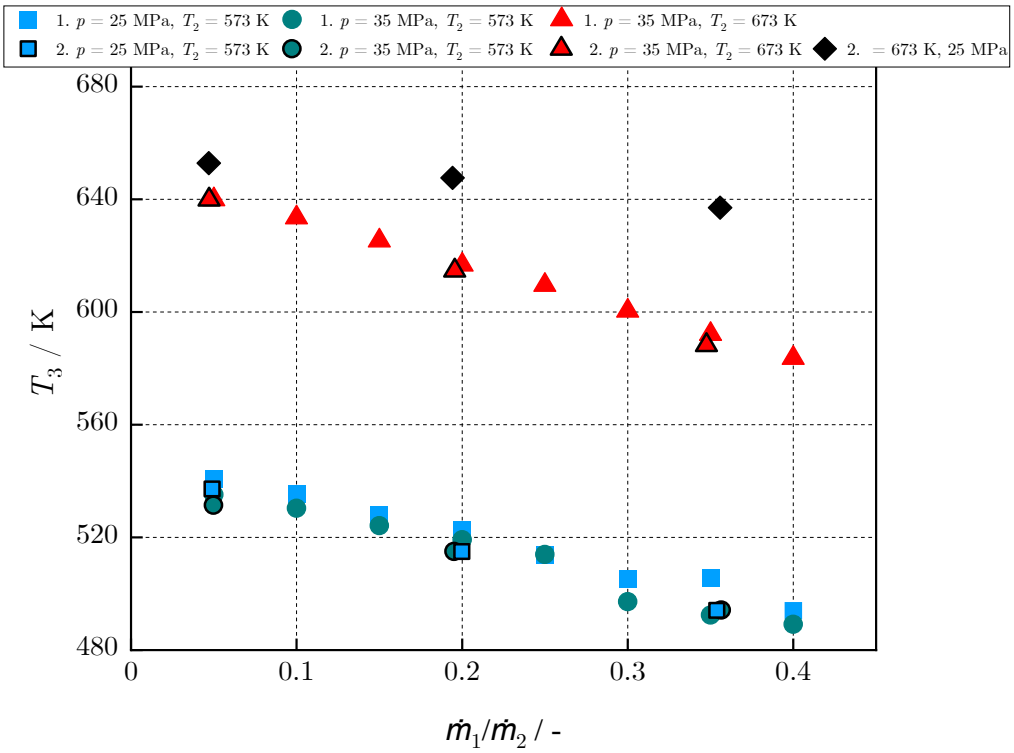

Figure 11-12: Mixing experiments for the characterization of the plant. The experiments were carried out twice (1. (full symbols) and 2. (black edged symbols)) Trend of the mixing temperature T_3 for near- and supercritical temperatures as a function of the mixing ratio a. The influence of the used supercritical pressure of 25 MPa and 35 MPa was investigated [58].

The full symbols show the first mixing experiments carried out. The black edged symbols represent the repeated experiments. These experiments were carried out four times. For all the different experiments, the mixing temperature T_3 is decreasing with increasing mixing ratio a. For the subcritical hot stream temperature T_2 of 573 K, the results for the mixing temperatures are nearly identical. Furthermore, there is no pressure dependence on the mixing temperature. The results for 25 MPa and 35 MPa show almost the same values since the specific isobaric heat capacity does not differ for temperatures below 600 K for pressures between 25 MPa and 35 MPa. On the other hand, the trends for the supercritical hot stream temperature T_2 of 673 K differ from 25 MPa to 35 MPa. For the lower pressure of 25 MPa, the mixing temperature is higher than for 35 MPa. This difference in the mixing temperature is explained by the pressure dependency of the enthalpy in the supercritical region. In Figure 2-4, the enthalpy is increasing linearly in the subcritical range up to 650 K. For a hot stream temperature of 673 K, the enthalpy is around 1.3 times higher for a pressure of 25 MPa than for 35 MPa. This leads to a higher energy amount of the hot stream. The cold stream's impact is lowered, which leads to a higher mixing temperature T_3 compared to the higher pressure of 35 MPa. The slope of the values for 35 MPa is around three times larger than the slope of the results for 25 MPa. This effect is explained by the derivation of the energy balance around the mixing unit (compare equation (2-21)). The immense value of the specific isobaric heat capacity in the range between 600 K and 673 K for the lower pressure of 25 MPa results in a more

downward slope $\left(\frac{dT_3}{da}\right)$. Furthermore, the difference between the values of the mixing temperatures for 25 MPa and 35 MPa is increasing with increasing mixing ratio. The results of the mixing experiments concerning the increasing enthalpy with decreasing pressures also show that the required heating power of the heating unit is increasing with decreasing pressure from 35 MPa to 25 MPa. The results show that the experimentally determined mixing temperatures are reproducible. With that, the single process conditions like pressure, temperature, and mass flows are adjustable. In combination with the before mentioned stability experiments, the stability of the CHTS plant can be guaranteed.

B: Median particle size d_{50} as a function of the residence time $\boldsymbol{\tau}$

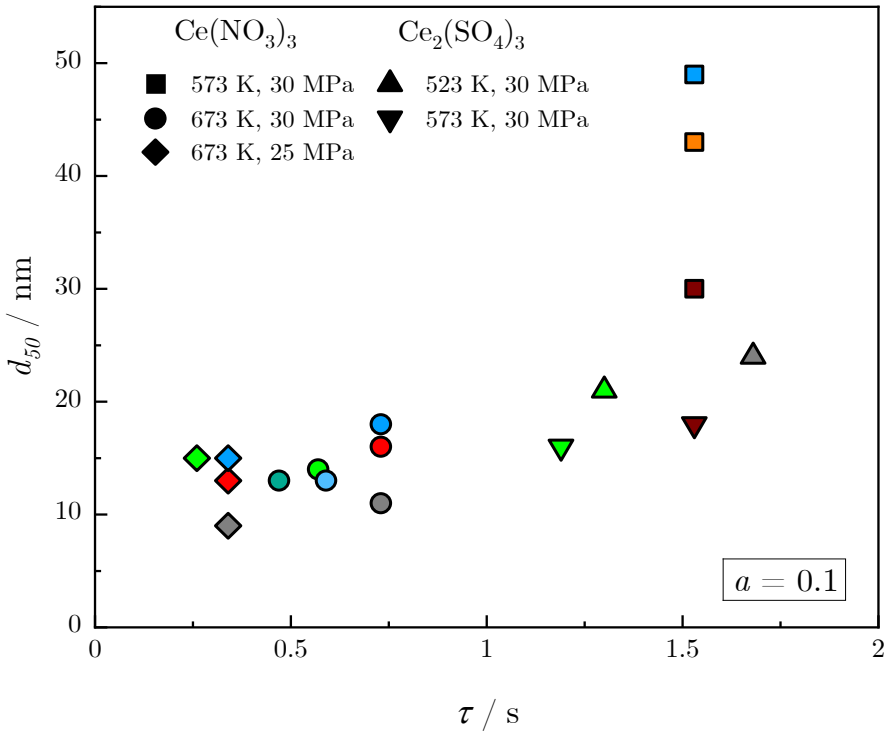

Figure 11-13: Median particle size d_{50} as a function of the mean residence time τ for given process conditions and $Ce(NO_3)_3$ and $Ce_2(SO_4)_3$ as precursors and a mixing ratio a of 0.1.

Appendix chapter 8

A: Preliminary work

After the CAD models of the relating mixing units were constructed and meshed (compare section 5.1), specific tests were carried out. The quality of the models was checked with a mesh independency test, a convergence test, and a turbulent intensity test. The meshed models were tested with different cell sizes. Figure 11-14 shows the results for the mesh independency test for different cell sizes of 0.1 mm and 0.2 mm for all the designed models and the used boundary conditions explained in section 5.1.1:

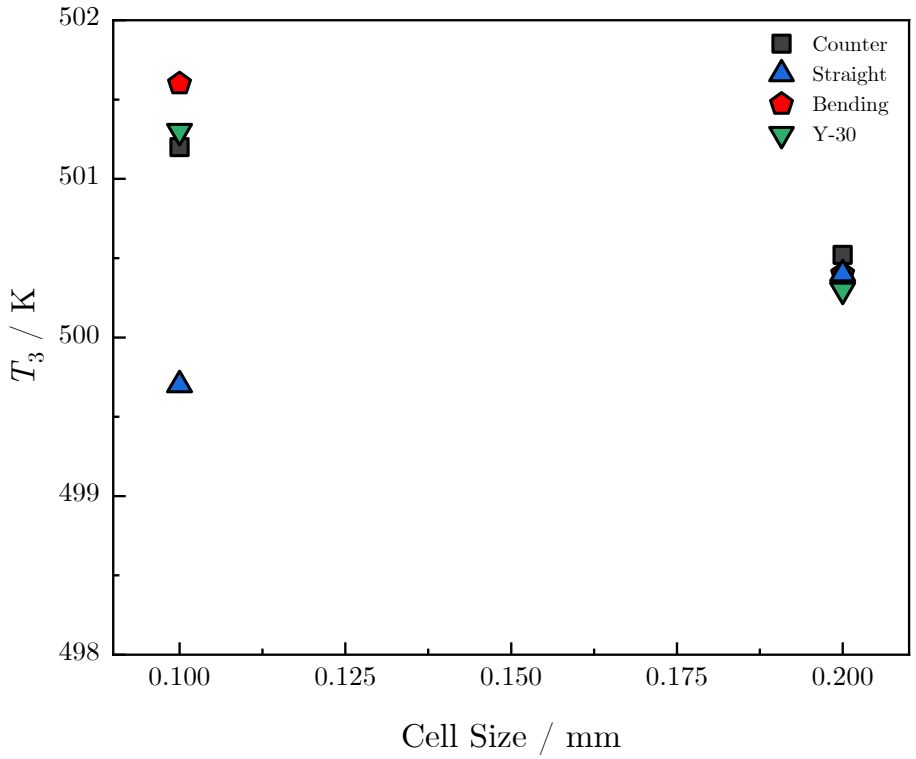

Figure 11-14: Determination of the influence of the mesh's related cell size (0.1 mm and 0.2 mm) on the mixing temperature T_3. The test was carried out for each designed model (Counter, Straight, Bending setup, and Y-30 mixer) [153].

The simulations regarding the influence of the cell size on the mixing temperature T_3 were carried out for the above-mentioned designed models. Especially the Straight setup was firstly designed with another arrangement of the tubes between the T-junctions. In the later phase of the work, the Straight setup was realized in the CHTS plant. The realization in the plant and the previously designed model with the Straight configuration were different. So, the developed Straight model was modified to depict it as it was assembled in the CHTS plant (compare Figure 5-1, right side). Due to the experiences of the former models, the tests were not carried out for the Straight model. In general, the differences of the resulting mixing temperatures T_3 from the simulations between a cell size of 0.1 mm and 0.2 mm, respectively, and the models

themselves are minor. Decreasing the cell size from 0.2 mm to 0.1 mm led to an increase of the computational time of a factor of 6. For the other tests and the further simulations, a cell size of 0.2 mm was used. Only the Bending and the Y-30 model achieved the lower values of the set residuals (compare section 5.1.1) in the convergence test. There, the difference of the mixing temperature T_3 was around ±1 K for the previous set and the new convergence criteria. Due to these results, the standard convergence criteria were used for all the other designed models of the Counter and Straight models. The turbulent intensity test led to the assumption that the results of the use of 5% of the turbulent intensity were nearly equal to the results for 10%. It was found out that the use of 10% of the turbulent intensity led to a more stable simulation. The experiences from the preliminary tests for the designed models resulted in the assumptions of a cell size of 0.2 mm, the standard convergence criteria, and 10% of the turbulent intensity for all performed simulations.

B: Validation of the models

The models were validated for the application of the models and the later comparison with the experimental work. Regarding the realization in the CHTS plant, only the Counter model and the Straight model were validated with experimentally determined values of the mixing temperature T_3. The other designed models were not validated due to the complexity of the manufacturing of the mixers. Anyhow, the simulations of the mixing temperature T_3 were carried out for the other models for later comparison. The simulations of the mixing temperature T_3 for the validation of both models were performed according to Table 5-1. Figure 11-15 visualizes the comparison between the experimental values and the mixing temperatures determined from the simulations for the Counter model:

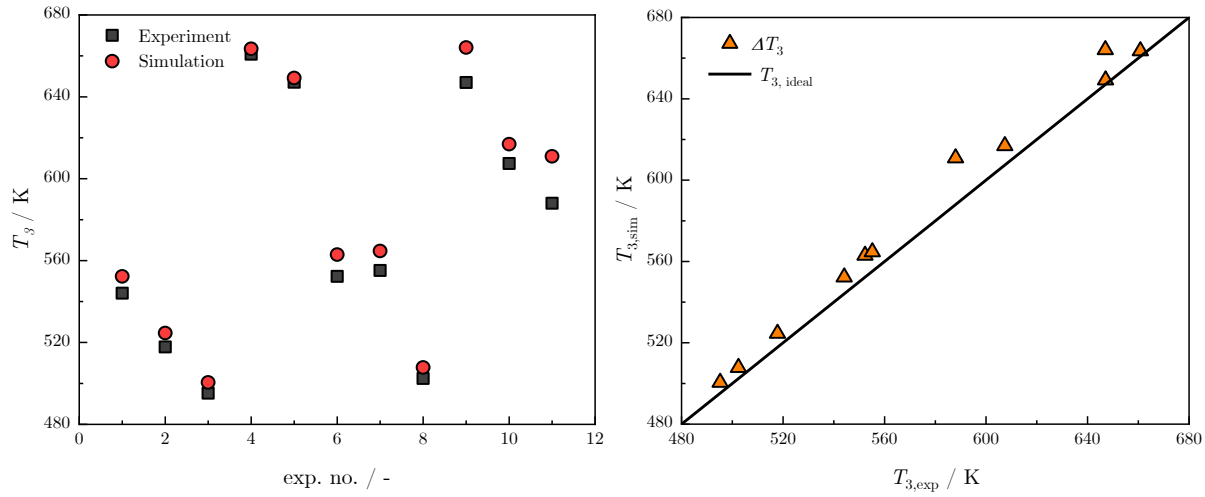

Figure 11-15: Comparison of the experimental and the simulation values of the mixing temperature T_3 for eleven different experiments (left side) of the Counter model and parity plot of the mixing temperature T_3 determined from simulations and experiments (right side).

The differences between the experimental and the simulation data are shown on the left side. Nearly all experiments show a difference of values less than 10 K. The experiment with the slightest deviation is experiment 5 with 2.1 K. In contrast to that, experiment 11 delivers the largest one with 22.9 K. Concerning the tolerance value of the used thermocouples of ± 2 K, the difference is negligible. In combination with the complexity of the models, the simulation results show high quality and accuracy. The mean relative error results in 1.55% for all the carried-out experiments and simulations. As for the Counter model, the experimentally determined mixing temperature T_3 was also compared with simulations of the Straight model for the validation (compare Table 5-1). Figure 11-16 shows the results of the validation for the Straight model:

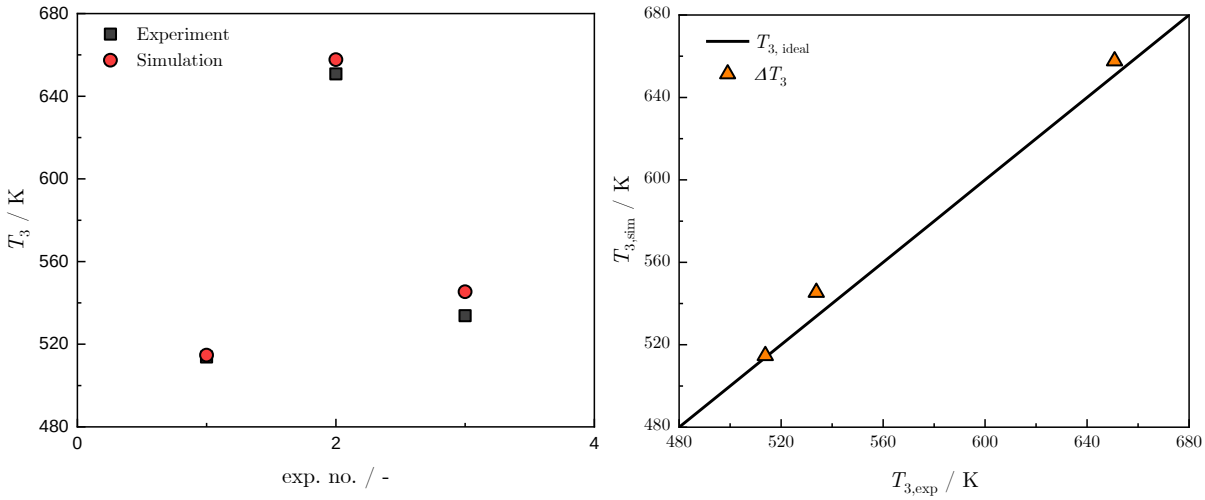

Figure 11-16: Comparison of three experimental and simulation results for the mixing temperature T_3 for the Straight model validation (left side). Parity plot of the differences of both the experimental and simulation values (right side).

For the Straight model, the differences between the experimental and simulation results are low, and the simulations show good accuracy in the way as the Counter model. The mean relative error equals to 1.14%. The first experiment shows the lowest deviation of 0.9 K. The other experiments show a variation of either 6.9 K and 11.6 K. For the accuracy limits, all three experiments are within the range. Both the Counter and the Straight model show good results regarding the validation experiments. The successful validation led to the use of the models for future simulations. Based on this, the other designed models were assumed as modeled correctly, even with the lack of experimental data for the validation.

C: Simulation of the mixing experiments

C1: Counter model

The results of the experimental determination of the mixing temperatures T_3 shown in Figure 11-12 were checked with simulations for the Counter model for different pressures p, total mass flows $\dot{m}_3$ and mixing ratios a. Based on the different process conditions, the simulations were performed. The influence of the process conditions pressure p, hot water temperature T_2, total mass flow $\dot{m}_3$ and mixing ratio a, on the resulting mixing temperature T_3 was investigated in the simulations according to the mixing experiments. Therefore, the mixing temperature T_3 is plotted as a function of the mixing ratio a for 15 simulations:

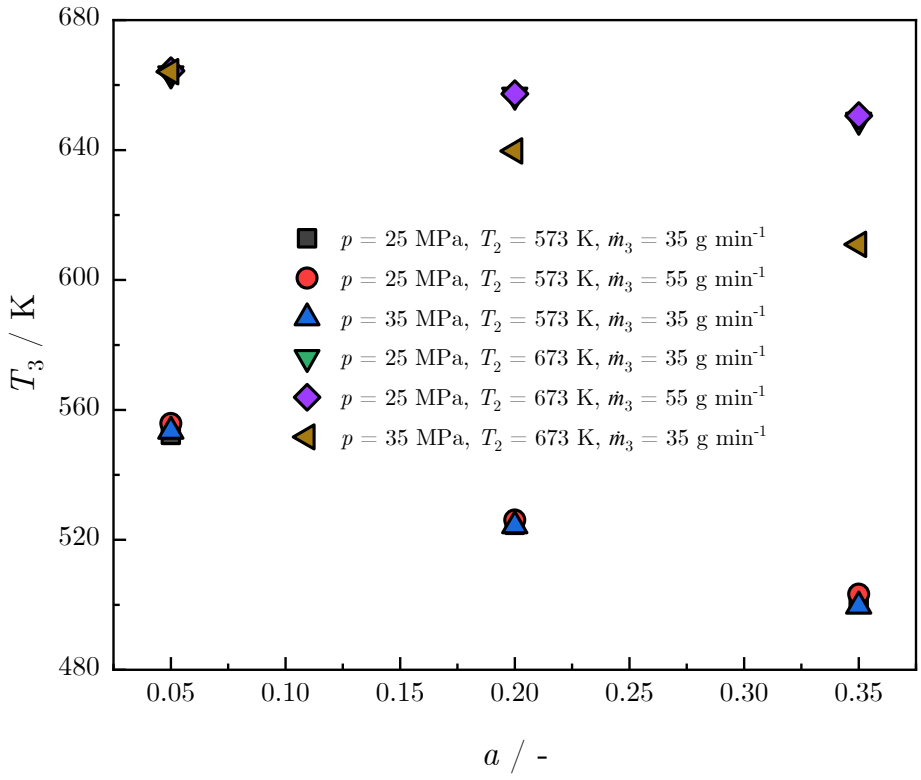

Figure 11-17: Results of the simulations of the mixing experiments for changing the process conditions p, T and $\dot{m}_3$ as a function of the mixing ratio a (Counter model) [153].

According to the experimental mixing experiments, the mixing temperature T_3 is decreasing with increasing mixing ratio a for the simulations. The same difference in the trends for near- and supercritical conditions is also obtainable. For nearcritical conditions, the pressure p has no significant effect on the mixing temperature T_3. Furthermore, the change in the total mass flow $\dot{m}_3$ has no particular effect on the simulated mixing temperature T_3. This effect is also valid for supercritical process conditions. In contrast, the pressure p significantly impacts the mixing temperature T_3 in the supercritical region. The impact of the influence of the enthalpy on the mixing stream $\dot{m}_3$ is increasing with decreasing pressure p. In general, the influence of

the process conditions on the simulated mixing temperature T_3 is comparable to the experimental results. The simulations were also carried out for the other models (Straight, Bending, and Y-30 model) and can be found in the following. Furthermore, the results with all used process conditions and the respecting models are listed in E: Used process conditions for the simulations and mixing temperature T_3. The mixing temperature T_3 and the respecting temperature distribution obtained inside the T-junction below the mixer are not affected by the mixing geometry. On the other hand, the mixing of both streams is strongly dependent on the used mixing geometry.

C2: Straight model

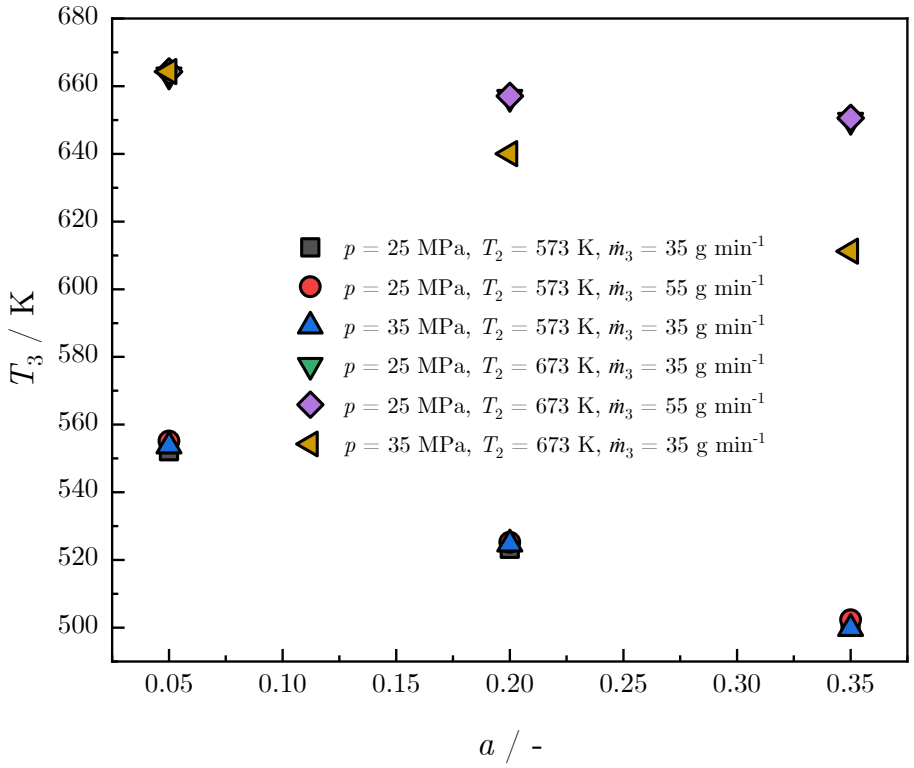

Figure 11-18: Results of the simulations of the mixing experiments for different process conditions as a function of the mixing ratio a (Straight model) [153].

C3: Bending model

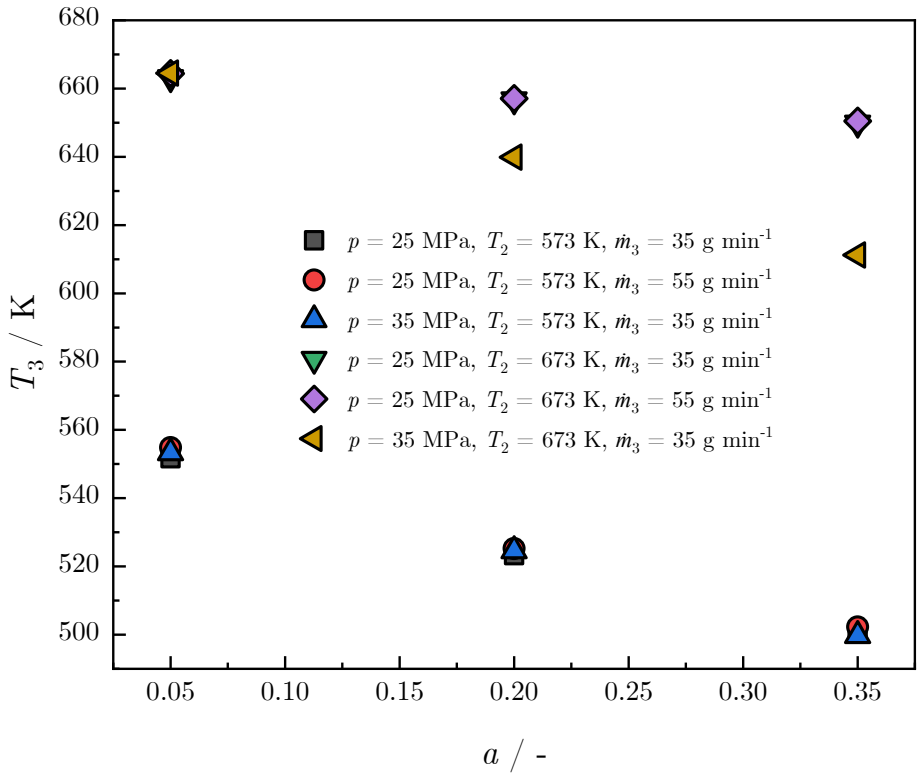

Figure 11-19: Results of the simulations of the mixing experiments for different process conditions as a function of the mixing ratio a (Bending model) [153].

C4: Y-30 model

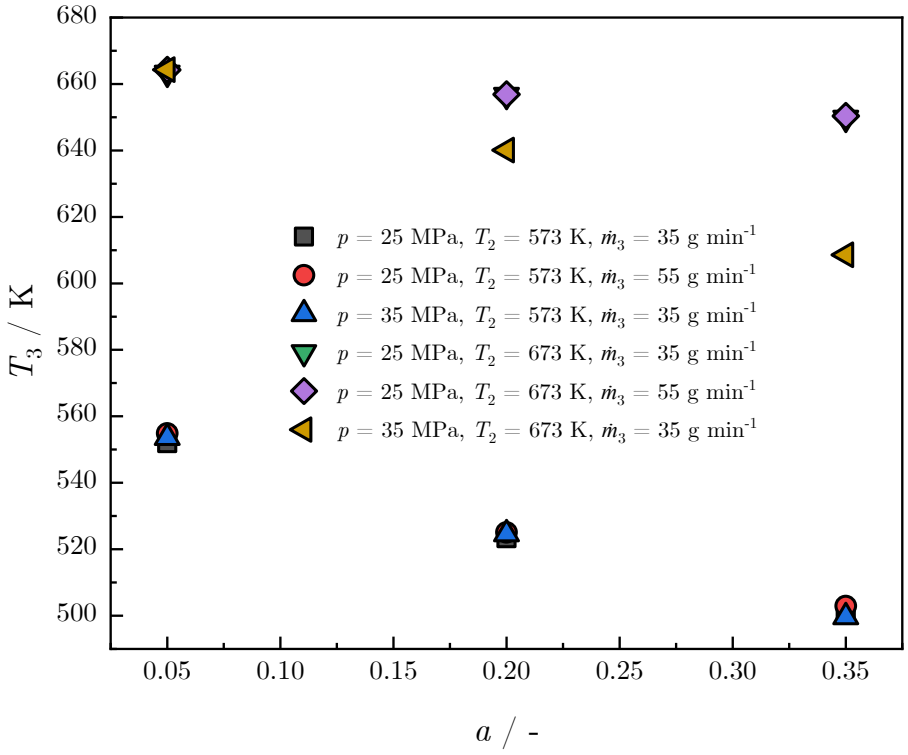

Figure 11-20: Results of the simulations of the mixing experiments for different process conditions as a function of the mixing ratio a (Y-30 model) [153].

D: Straight model

In addition to the Counter model, the results for the Straight model are shown below. The effect of the different process conditions on the thermal and velocity fields is also described similar to the Counter model. After that, the results of both models are compared.

At first, the influence of the total mass flow $\dot{m}_3$ on the resulting mixing temperature T_3 was investigated.

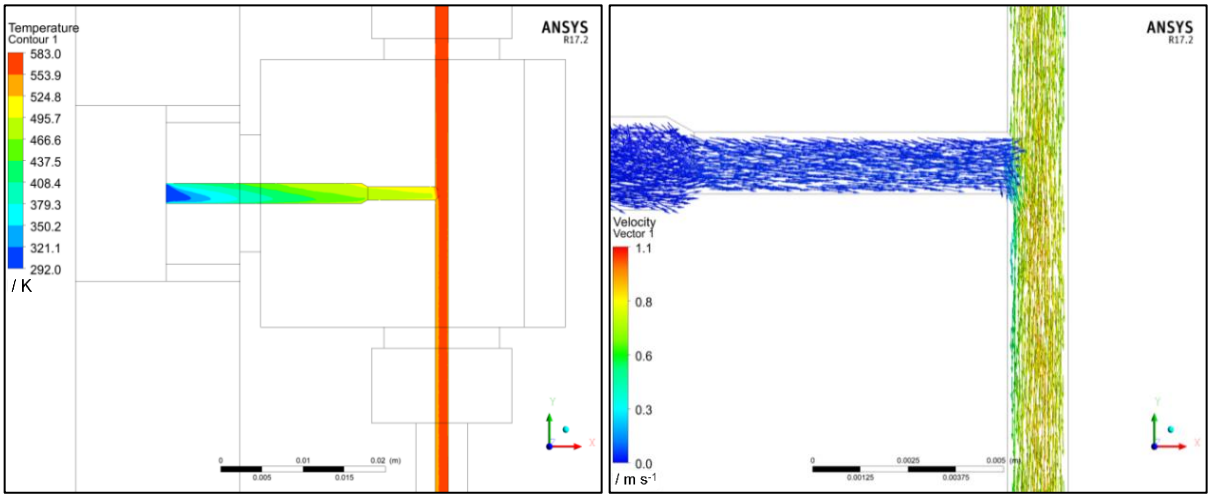

Figure 11-21: Thermal field as an overview of the mixing unit (left side) and the velocity field right at the mixing point (right side). The process conditions set to a pressure p of 25 MPa, a hot water temperature T_2 of 573 K, a total mass flow $\dot{m}_3$ of 35 g min^{-1} and a mixing ratio a of 0.05 [156].

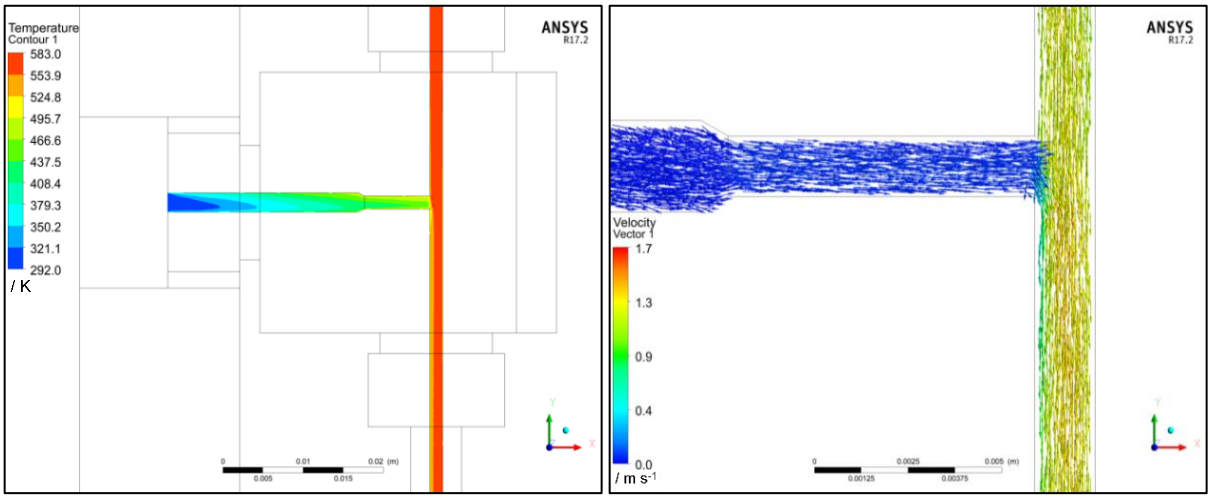

Figure 11-22: Thermal field as an overview of the mixing unit (left side) and the velocity field right at the mixing point (right side). The process conditions set to a pressure p of 25 MPa, a hot water temperature T_2 of 573 K, a total mass flow $\dot{m}_3$ of 55 g min^{-1} and a mixing ratio a of 0.05 [156].

As shown for the Counter model, the increase of the total mass flow $\dot{m}_3$ from 35 g min^{-1} to 55 g min^{-1} slightly affects the thermal field in front of the mixing point. The temperature of the cold water stream T_1 is decreased, and the cold zone enlarges. The velocity fields remain the same for the increase of the total mass flow $\dot{m}_3$ and a small vortex is formed right after the mixing point. The flow velocity of the mixing stream v_3 is decreased below the entrance of the cold water stream $\dot{m}_1$ at the left wall of the tube. The ratio of the maximum flow velocities equals to the one of the Counter model, even if the maximum flow velocity v_3 is lower for the Straight model. This is argued with the entry of the cold water stream $\dot{m}_1$ from the side instead of hitting the hot water stream $\dot{m}_2$ directly. Next to the variation of the total mass flow $\dot{m}_3$, the effect of the hot water temperature T_2 was investigated. Figure 11-23 and Figure 11-24 show the impacts:

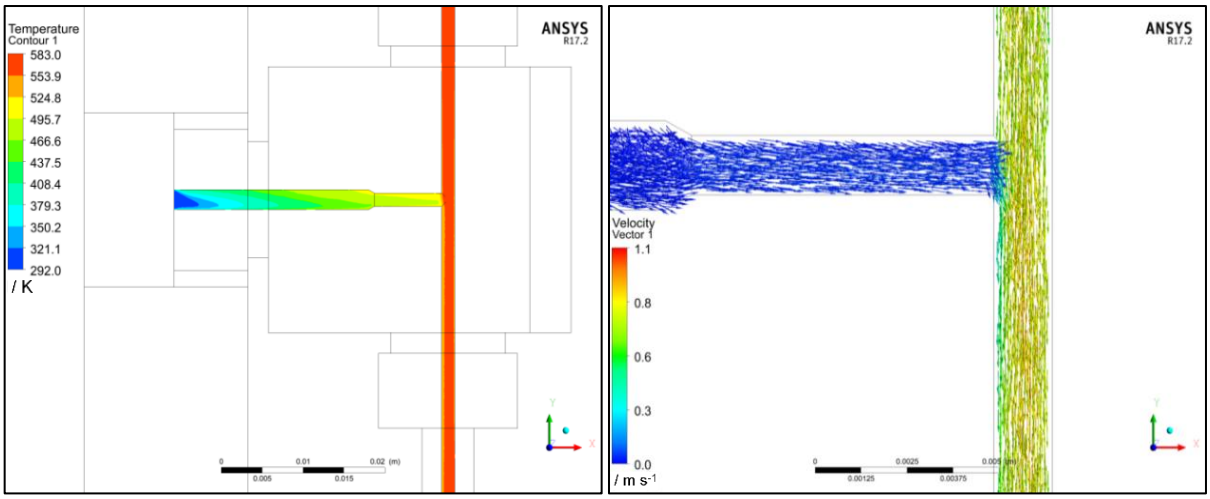

Figure 11-23: Thermal field as an overview of the mixing unit (left side) and the velocity field right at the mixing point (right side). The process conditions set to a pressure p of 35 MPa, a hot water temperature T_2 of 573 K, a total mass flow $\dot{m}_3$ of 35 g min^{-1} and a mixing ratio a of 0.05 [156].

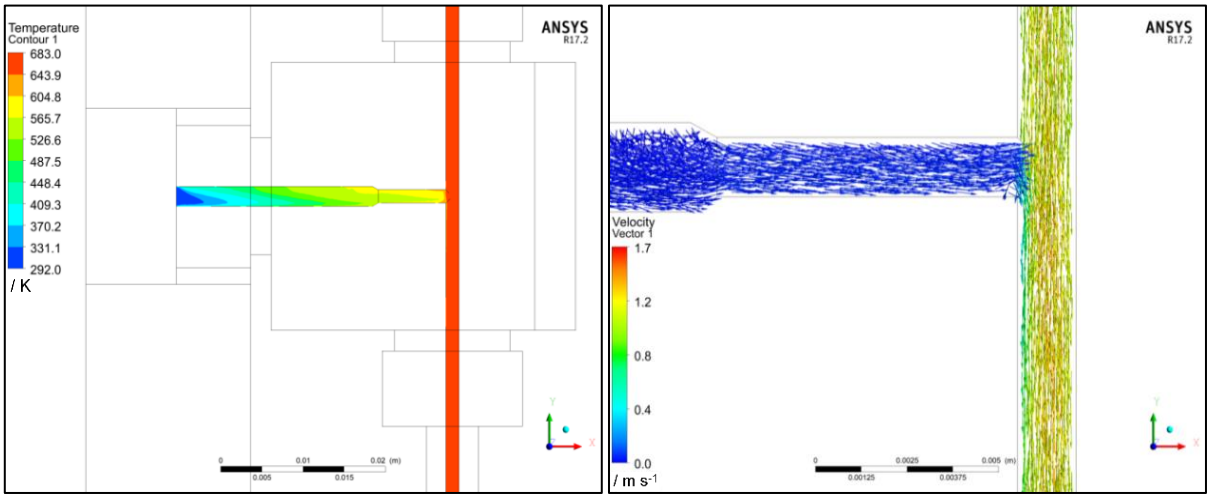

Figure 11-24: Thermal field as an overview of the mixing unit (left side) and the velocity field right at the mixing point (right side). The process conditions set to a pressure p of 35 MPa, a hot water temperature T_2 of 673 K, a total mass flow $\dot{m}_3$ of 35 g min^{-1} and a mixing ratio a of 0.05 [156].

The increase of the hot water temperature T_2 affects the temperature of the cold water stream T_1 in front of the mixing point. The temperature is increasing due to the deep dive of the hot water stream $\dot{m}_2$ into the cold water stream $\dot{m}_1$. For the lower temperature, the effect is not showing. Regarding the velocity field, the cold water stream $\dot{m}_1$ is not affecting the mixing stream $\dot{m}_3$. A small vortex is obtainable. For the higher temperature, the size of the vortex is increasing right at the mixing point. In contrast to the Straight model, only one vortex is present in the Counter model. This is a difference between both mixing configurations. Due to the decrease of the density ρ the flow velocity v_3 is increasing with increasing temperature.

The influence of the change in the pressure p was also studied for the Straight model. Figure 11-25 and Figure 11-26 show the results for the two pressures of 25 MPa and 35 MPa with constant process conditions:

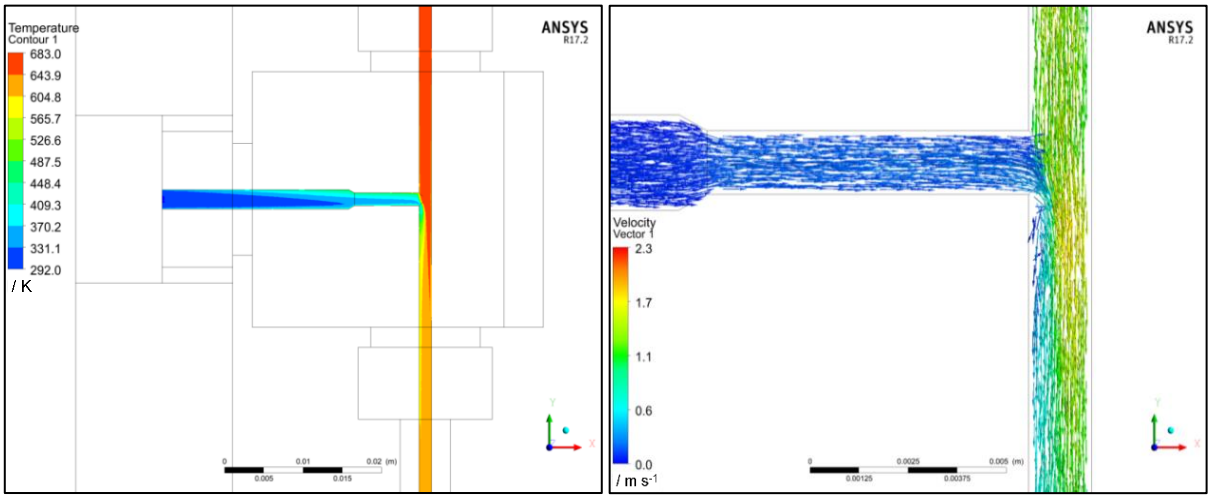

Figure 11-25: Thermal field as an overview of the mixing unit (left side) and the velocity field right at the mixing point (right side). The process conditions set to a pressure p of 25 MPa, a hot water temperature T_2 of 673 K, a total mass flow $\dot{m}_3$ of 35 g min^{-1} and a mixing ratio a of 0.35 [156].

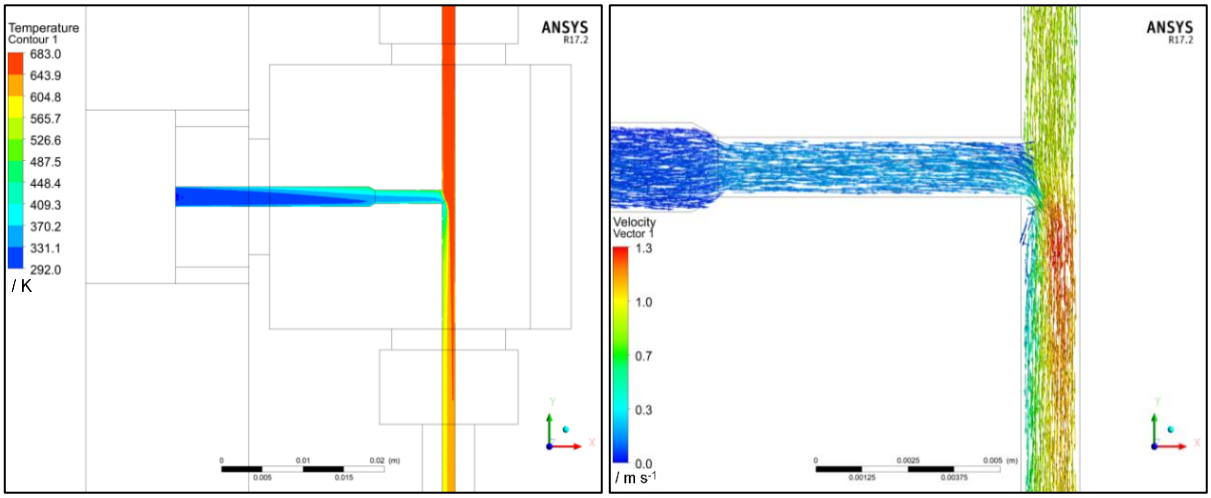

Figure 11-26: Thermal field as an overview of the mixing unit (left side) and the velocity field right at the mixing point (right side). The process conditions set to a pressure p of 35 MPa, a hot water temperature T_2 of 673 K, a total mass flow $\dot{m}_3$ of 35 g min^{-1} and a mixing ratio a of 0.35 [156].

For the lower pressure p of 25 MPa, the influence of the cold water stream $\dot{m}_1$ is decreased due to the previously mentioned high value of the enthalpy h. An increase of the pressure p to 35 MPa leads to a more significant influence of the cold water stream $\dot{m}_1$ which results in an inhomogeneous thermal profile with specific temperatures. With 25 MPa, the temperature in

the cross-section is more homogeneous. Regarding the velocity field, the flow velocity v_3 for 25 MPa is higher due to the decrease of the density ρ. The previous vortices for the other cases are not present for the supercritical temperature and the high mixing ratio. Comparing the effects of the pressure p at nearcritical conditions shows the same results for the Straight model as for the Counter model (compare Figure 11-21 and Figure 11-23). The increase of the mixing ratio a (compare Figure 11-24 and Figure 11-26) leads to the erase of the vortex appearing right after the mixing point. The hot region in the cold water stream right before the mixing point is also disappearing with an increasing mixing ratio a from 0.05 to 0.35. The flow velocity of the mixing stream v_3 is decreasing with increasing mixing ratio a.

E: Used process conditions for the simulations and mixing temperature T_3

According to [153]:

E1: Counter model

p / MPa	$\dot{m}_3$ / g/min	T_2 / K	a / -	T_3 / K
25	35	573	0.05	552.3
			0.20	524.6
			0.35	500.5
		673	0.05	663.5
			0.20	656.9
			0.35	649.2
	55	573	0.05	555.8
			0.20	526.1
			0.35	503.3
		673	0.05	664.4
			0.20	657
			0.35	650.6
30	35	573	0.05	551.8
			0.20	525.1
			0.35	500.0
		673	0.05	664.5
			0.20	642.3
			0.35	616.9
	55	573	0.05	556.6
			0.20	527.2

			0.35	503.2
		673	0.05	666.3
			0.20	644.7
			0.35	618.1
35	35	573	0.05	553.4
			0.20	524.3
			0.35	499.6
		673	0.05	664.1
			0.20	639.7
			0.35	610.9
	55	573	0.05	556.2
			0.20	526.6
			0.35	501.8
		673	0.05	665.7
			0.20	641.1
			0.35	610.9

E2: Straight model

p / MPa	$\dot{m}_3$ / g/min	T_2 / K	a / -	T_3 / K
25	35	573	0.05	552.1
			0.20	523.3
			0.35	500.4
		673	0.05	663.3
			0.20	656.7
			0.35	649.9
	55	573	0.05	555.1
			0.20	525.2
			0.35	502.3
		673	0.05	664.3
			0.20	657.1
			0.35	650.6
30	35	573	0.05	554.1
			0.20	525.3
			0.35	500.2
		673	0.05	664.8
			0.20	642.7
			0.35	616.0
	55	573	0.05	556.8
			0.20	527.3
			0.35	502.2
		673	0.05	666.6

			0.20	644.8
			0.35	618.1
35	35	573	0.05	553.7
			0.20	524.7
			0.35	499.8
		673	0.05	664.3
			0.20	640.0
			0.35	611.2
	55	573	0.05	556.1
			0.20	526.7
			0.35	501.7
		673	0.05	665.8
			0.20	642.6
			0.35	611.2

E3: Bending model

p / MPa	$\dot{m}_3$ / g/min	T_2 / K	a / -	T_3 / K
25	35	573	0.05	551.7
			0.20	523.3
			0.35	500.4
		673	0.05	663.2
			0.20	656.7
			0.35	649.9
	55	573	0.05	554.8
			0.20	525.2
			0.35	502.3
		673	0.05	664.4
			0.20	657.1
			0.35	650.5
30	35	573	0.05	553.7
			0.20	525.1
			0.35	500.2
		673	0.05	664.5
			0.20	642.4
			0.35	615.7
	55	573	0.05	557.5
			0.20	527.3
			0.35	502.3
		673	0.05	666.5

			0.20	644.7
			0.35	618.1
35	35	573	0.05	553.3
			0.20	524.6
			0.35	499.7
		673	0.05	664.5
			0.20	639.9
			0.35	611.2
	55	573	0.05	556.2
			0.20	526.8
			0.35	501.8
		673	0.05	665.7
			0.20	642.6
			0.35	610.8

E4: Y-30 model

p / MPa	$\dot{m}_3$ / g/min	T_2 / K	a / -	T_3 / K
25	35	573	0.05	551.9
			0.20	523.3
			0.35	500.3
		673	0.05	663.4
			0.20	656.7
			0.35	649.8
	55	573	0.05	554.9
			0.20	525.1
			0.35	502.9
		673	0.05	664.2
			0.20	656.9
			0.35	650.4
30	35	573	0.05	554.0
			0.20	525.2
			0.35	500.1
		673	0.05	664.8
			0.20	642.5
			0.35	615.6
	55	573	0.05	556.7
			0.20	527.2
			0.35	502.1
		673	0.05	666.5

			0.20	644.6
			0.35	617.8
35	35	573	0.05	553.5
			0.20	524.6
			0.35	499.6
		673	0.05	664.3
			0.20	640.1
			0.35	608.6
	55	573	0.05	556.4
			0.20	527.0
			0.35	501.6
		673	0.05	665.8
			0.20	642.6
			0.35	613.5

F: Thermal and velocity fields for the Bending and Y-30 models

F1: Bending model

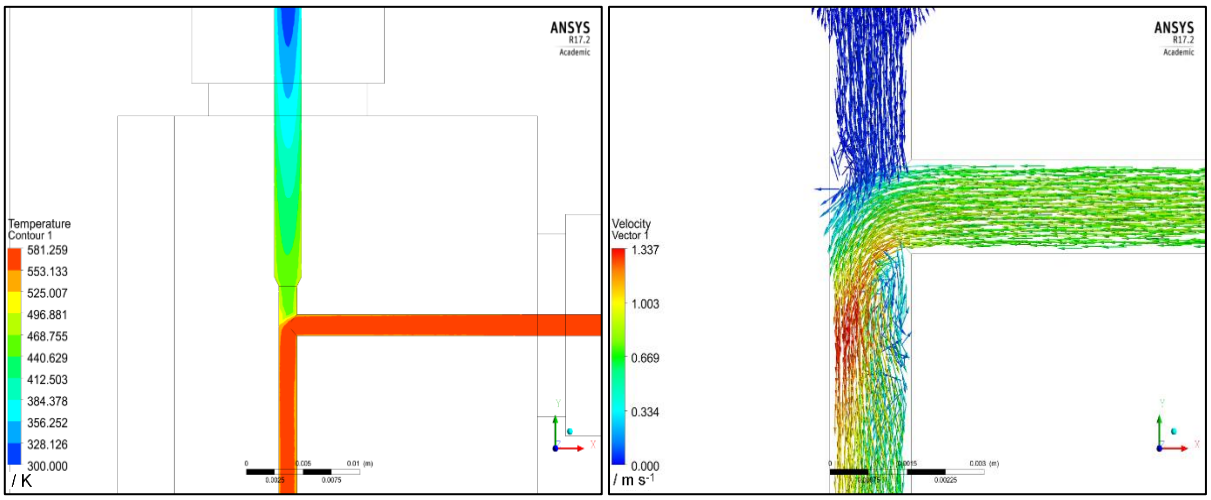

Figure 11-27: Thermal field as an overview of the mixing unit (left side) and the velocity field right at the mixing point (right side). The process conditions set to a pressure p of 25 MPa, a hot water temperature T_2 of 573 K, a total mass flow $\dot{m}_3$ of 35 g min^{-1} and a mixing ratio a of 0.05 [153].

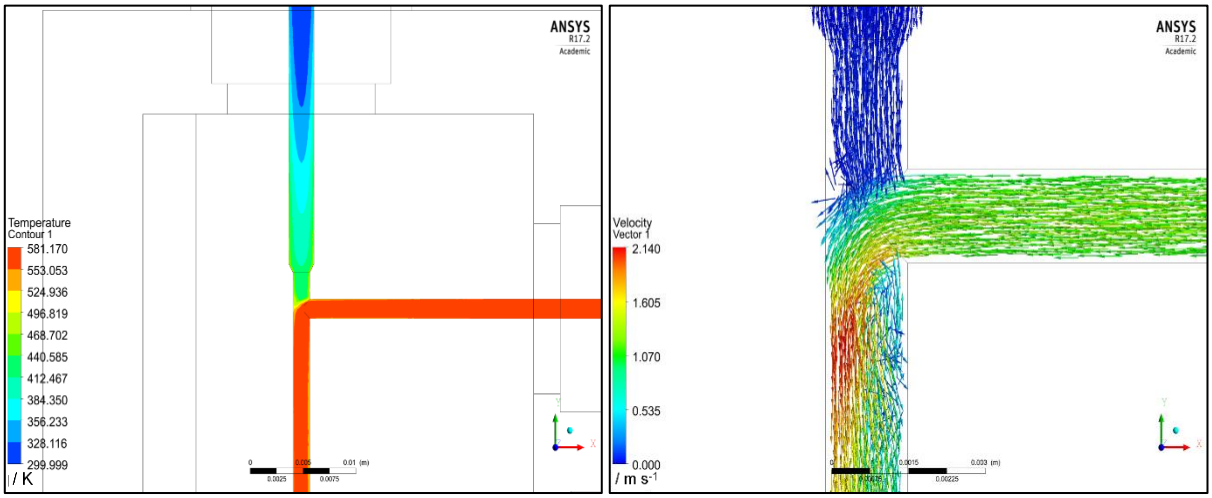

Figure 11-28: Thermal field as an overview of the mixing unit (left side) and the velocity field right at the mixing point (right side). The process conditions set to a pressure p of 25 MPa, a hot water temperature T_2 of 573 K, a total mass flow $\dot{m}_3$ of 55 g min^{-1} and a mixing ratio a of 0.05 [153].

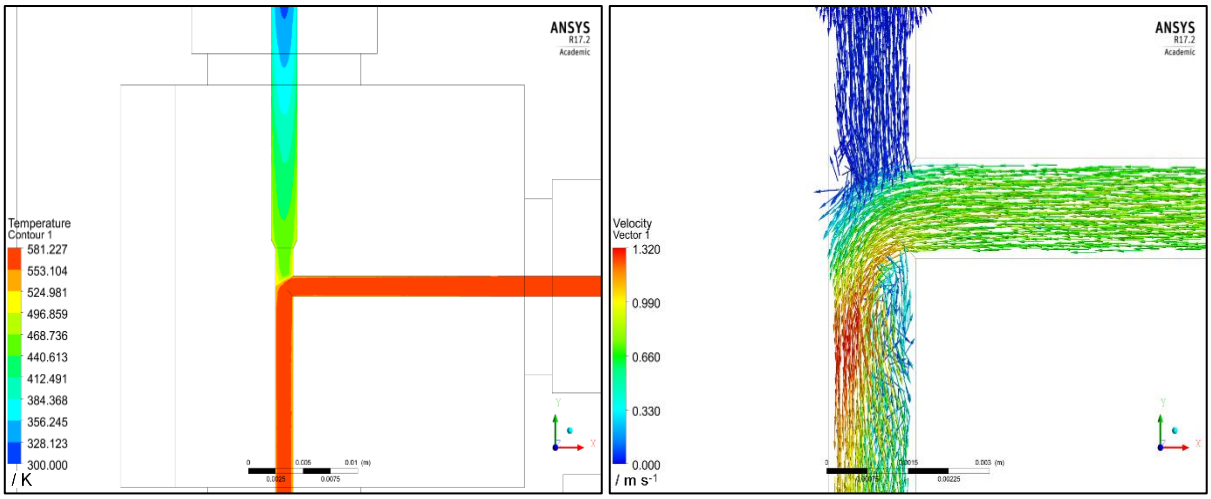

Figure 11-29: Thermal field as an overview of the mixing unit (left side) and the velocity field right at the mixing point (right side). The process conditions set to a pressure p of 35 MPa, a hot water temperature T_2 of 573 K, a total mass flow $\dot{m}_3$ of 35 g min^{-1} and a mixing ratio a of 0.05 [153].

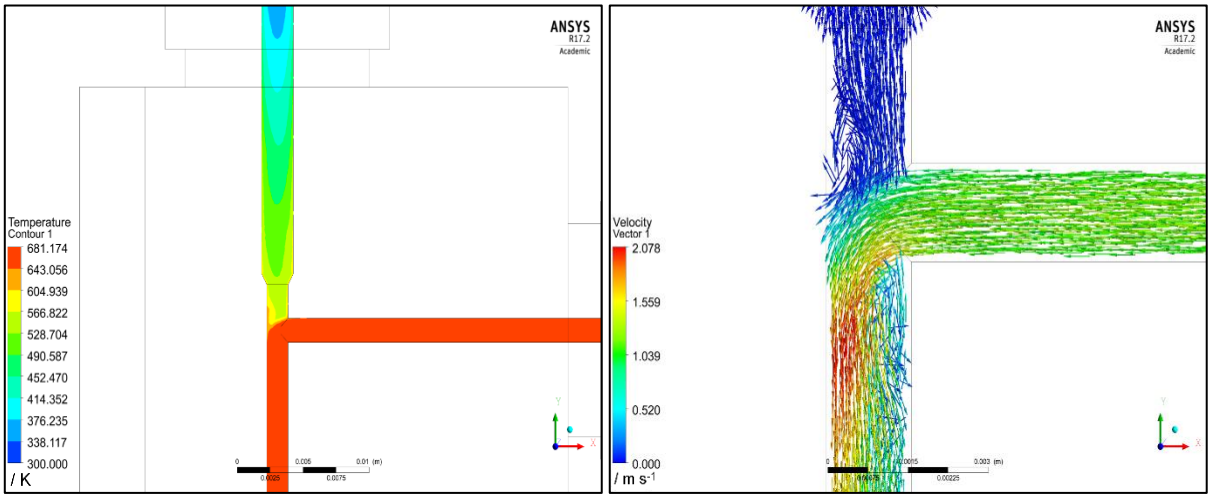

Figure 11-30: Thermal field as an overview of the mixing unit (left side) and the velocity field right at the mixing point (right side). The process conditions set to a pressure p of 35 MPa, a hot water temperature T_2 of 673 K, a total mass flow $\dot{m}_3$ of 35 g min^{-1} and a mixing ratio a of 0.05 [153].

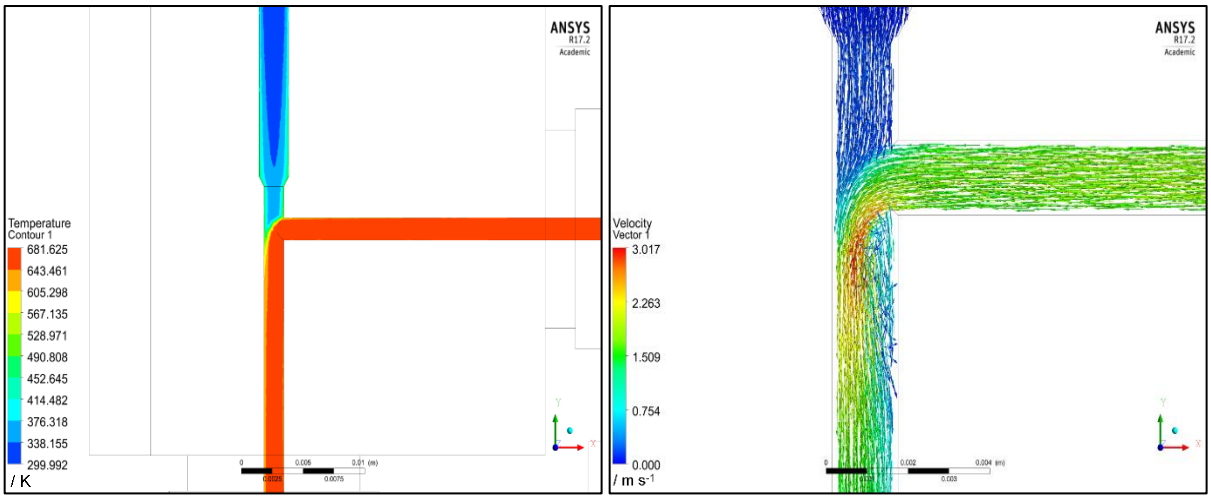

Figure 11-31: Thermal field as an overview of the mixing unit (left side) and the velocity field right at the mixing point (right side). The process conditions set to a pressure p of 25 MPa, a hot water temperature T_2 of 673 K, a total mass flow $\dot{m}_3$ of 35 g min^{-1} and a mixing ratio a of 0.35 [153].

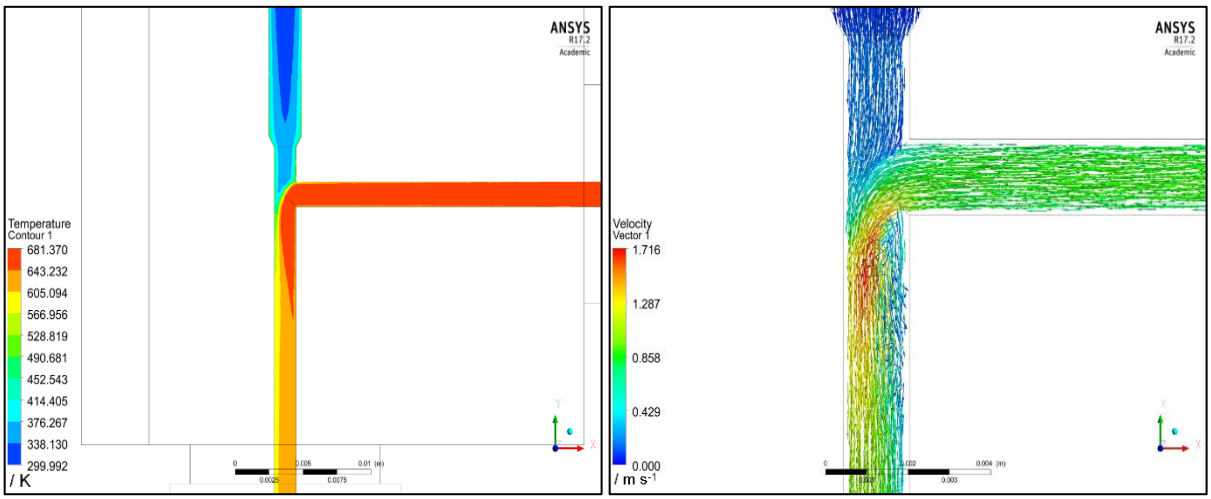

Figure 11-32: Thermal field as an overview of the mixing unit (left side) and the velocity field right at the mixing point (right side). The process conditions set to a pressure p of 35 MPa, a hot water temperature T_2 of 673 K, a total mass flow $\dot{m}_3$ of 35 g min^{-1} and a mixing ratio a of 0.35 [153].

F2: Y-30 model

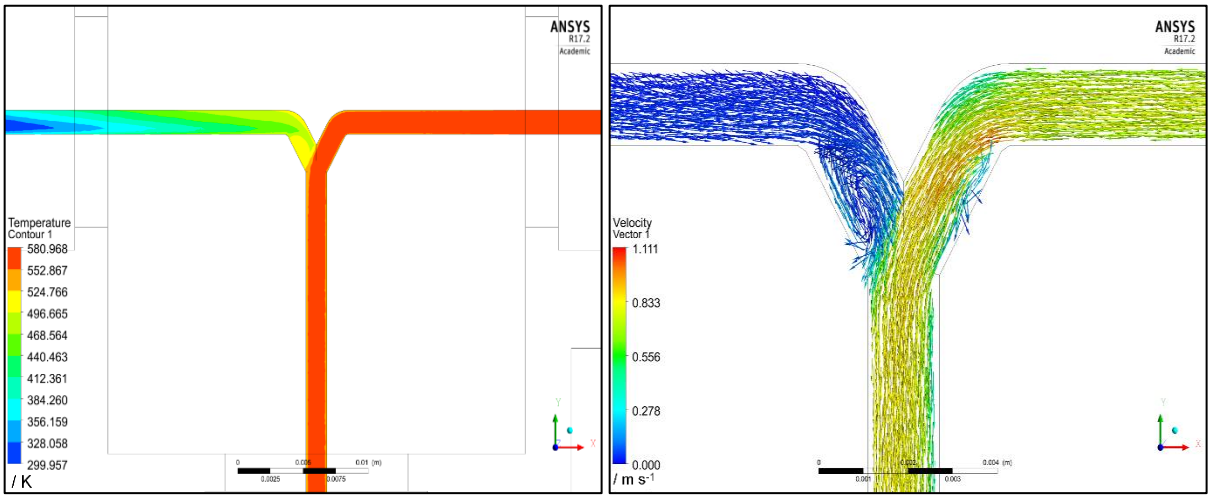

Figure 11-33: Thermal field as an overview of the mixing unit (left side) and the velocity field right at the mixing point (right side). The process conditions set to a pressure p of 25 MPa, a hot water temperature T_2 of 573 K, a total mass flow $\dot{m}_3$ of 35 g min^{-1} and a mixing ratio a of 0.05 [153].

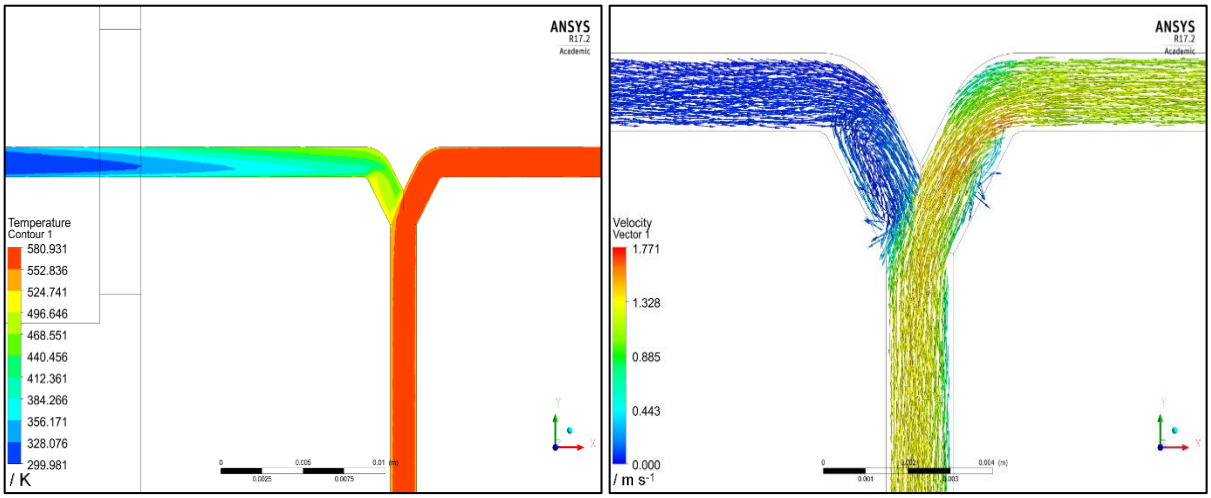

Figure 11-34: Thermal field as an overview of the mixing unit (left side) and the velocity field right at the mixing point (right side). The process conditions set to a pressure p of 25 MPa, a hot water temperature T_2 of 573 K, a total mass flow $\dot{m}_3$ of 55 g min^{-1} and a mixing ratio a of 0.05 [153].

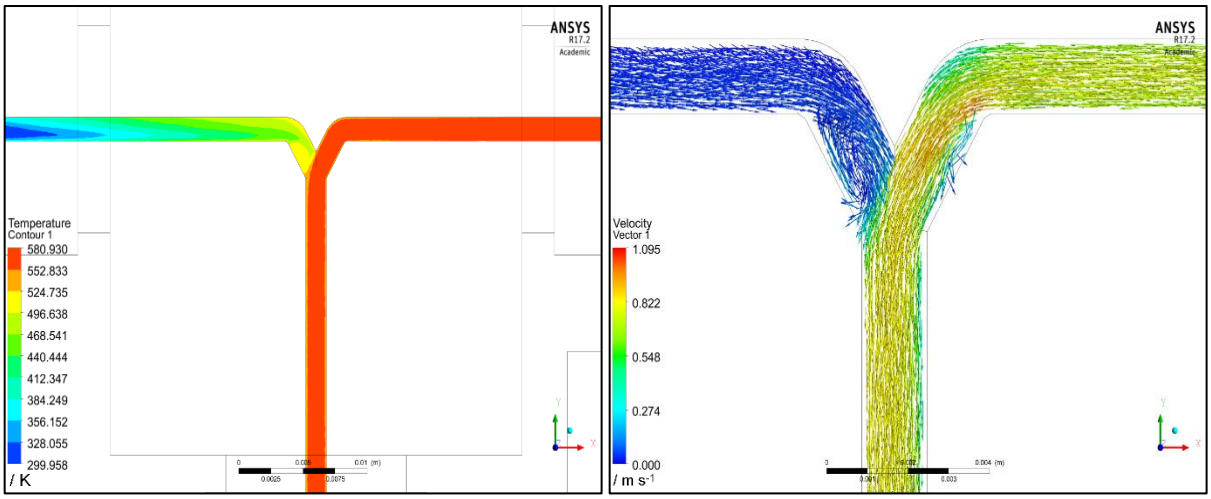

Figure 11-35: Thermal field as an overview of the mixing unit (left side) and the velocity field right at the mixing point (right side). The process conditions set to a pressure p of 35 MPa, a hot water temperature T_2 of 573 K, a total mass flow $\dot{m}_3$ of 35 g min^{-1} and a mixing ratio a of 0.05 [153].

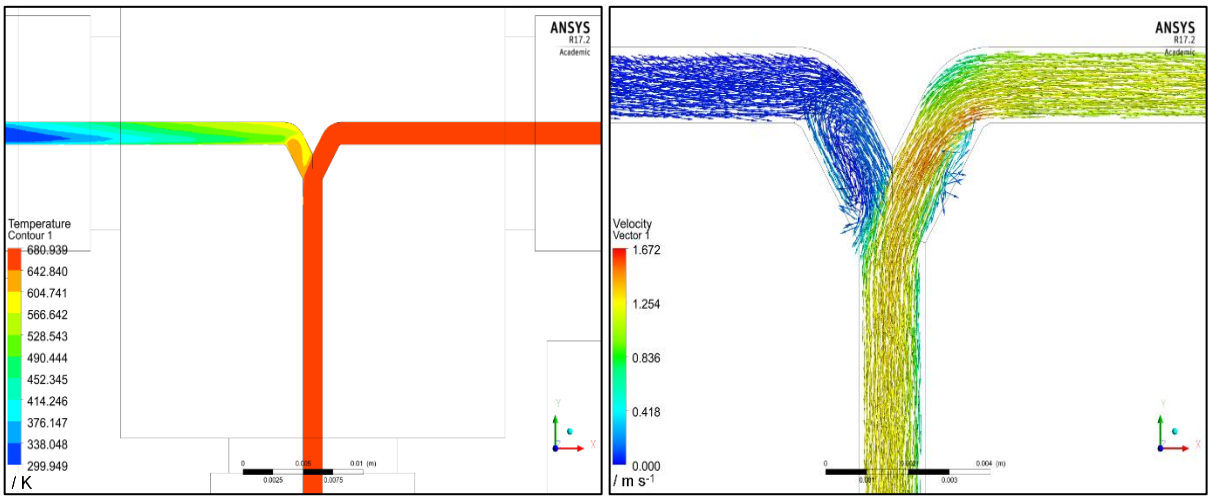

Figure 11-36: Thermal field as an overview of the mixing unit (left side) and the velocity field right at the mixing point (right side). The process conditions set to a pressure p of 35 MPa, a hot water temperature T_2 of 673 K, a total mass flow $\dot{m}_3$ of 35 g min^{-1} and a mixing ratio a of 0.05 [153].

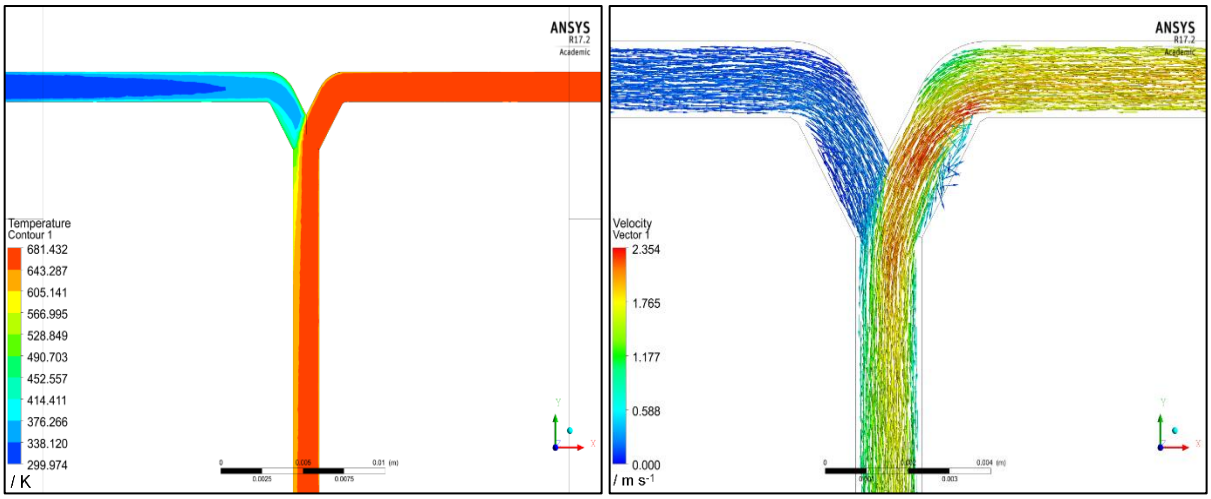

Figure 11-37: Thermal field as an overview of the mixing unit (left side) and the velocity field right at the mixing point (right side). The process conditions set to a pressure p of 25 MPa, a hot water temperature T_2 of 673 K, a total mass flow $\dot{m}_3$ of 35 g min^{-1} and a mixing ratio a of 0.35 [153].

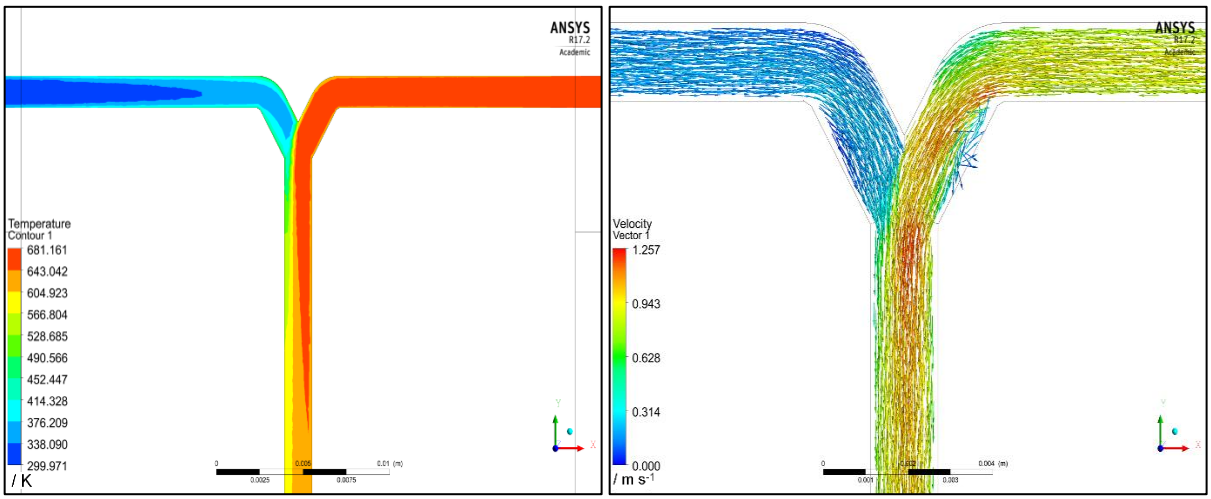

Figure 11-38: Thermal field as an overview of the mixing unit (left side) and the velocity field right at the mixing point (right side). The process conditions set to a pressure p of 35 MPa, a hot water temperature T_2 of 673 K, a total mass flow $\dot{m}_3$ of 35 g min^{-1} and a mixing ratio a of 0.35 [153].

G: Maximum velocities for different total mass flows and locations of the vortices

G1: Maximum velocities [153]

model	maximum velocity / m/s	
	case: $\dot{m}_3 = 35\,\mathrm{g/min}$	case: $\dot{m}_3 = 55\,\mathrm{g/min}$
Counter	1.37	2.07
Bending	1.34	2.14
Straight	1.08	1.71
Y-30	1.11	1.77

G2: Locations of vortices inside the mixer [153]

model	vortex location	
	vortex induced by buoyancy convection	vortex induced by flow instability
Counter	Bottom-corner of cold water stream region (horizontal pipe)	Right-side region of product stream (vertical pipe)
Bending	Top-left region of cold water stream (vertical pipe)	Bottom-right region of product stream (vertical pipe)
Straight	Bottom-corner of cold water stream region (horizontal pipe)	Absent
Y-30	Within the cold water stream's inclined pipe	Within the hot water stream's inclined pipe

H: RTD curves for the Straight, Bending and Y-30 models

H1: Straight model

In comparison to the Counter model, the Straight model was also used for the simulation of the RTD curves:

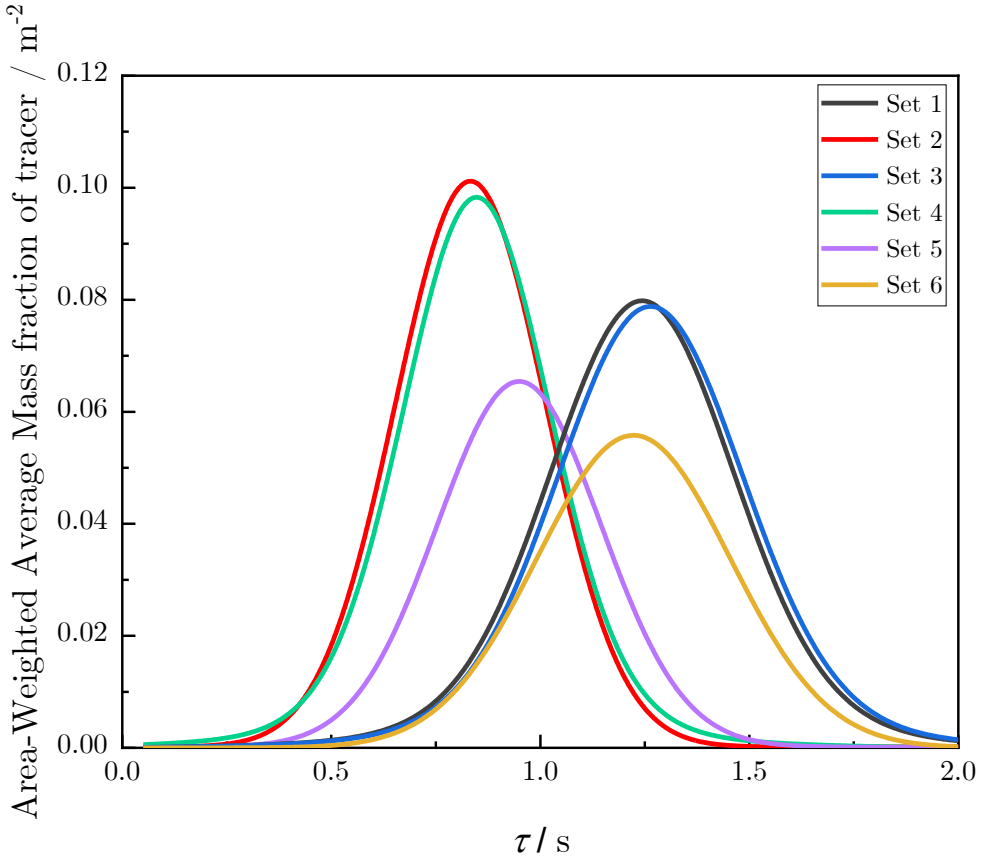

Figure 11-39: Trend of the Area weighted average mass fraction of tracer as a function of the mean residence time τ representing the RTD curve for different process conditions with the Straight model and the tracer injection from the inlet of the hot water stream [153].

In general, the RTD curves show a similar trend as the curves of the Counter model. The length of the tubes changes from the Counter model to the Straight model (compare Figure 5-1). This is the reason for the different values of the mean residence times τ. Due to this, all RTD curves are shifted to longer residence times τ. The injection of the tracer at the inlet of the cold water stream is of the same nature for the Straight model as for the Counter model. The reason for this is the constant length of the tubes before the mixer for both models. Figure 8-8 and Figure 11-40 show similar results for the tracer injection at the inlet of the cold water stream.

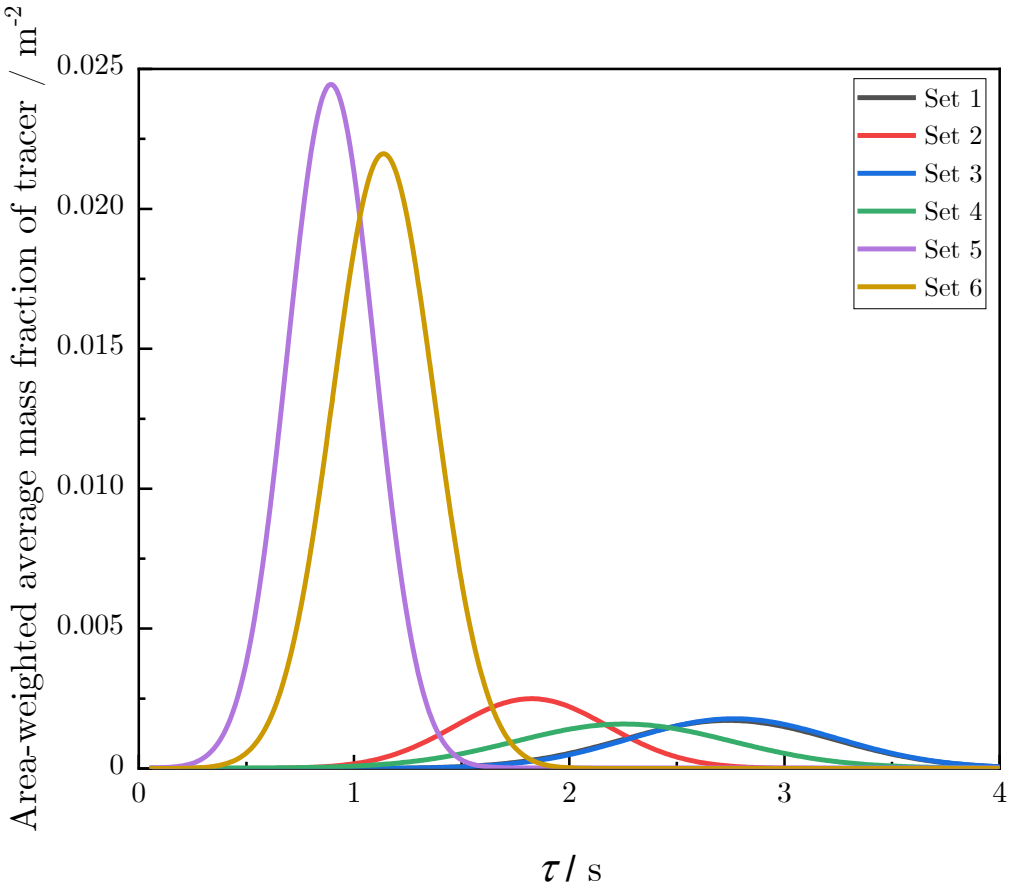

Figure 11-40: Trend of the Area weighted average mass fraction of tracer as a function of the mean residence time τ representing the RTD curve for different process conditions with the Straight model and the injection of the tracer from the inlet of the cold water stream [153].

Comparing both images shows that the simulations carried out with the models are consistent and underline the previous validation experiments.

H2: Bending model

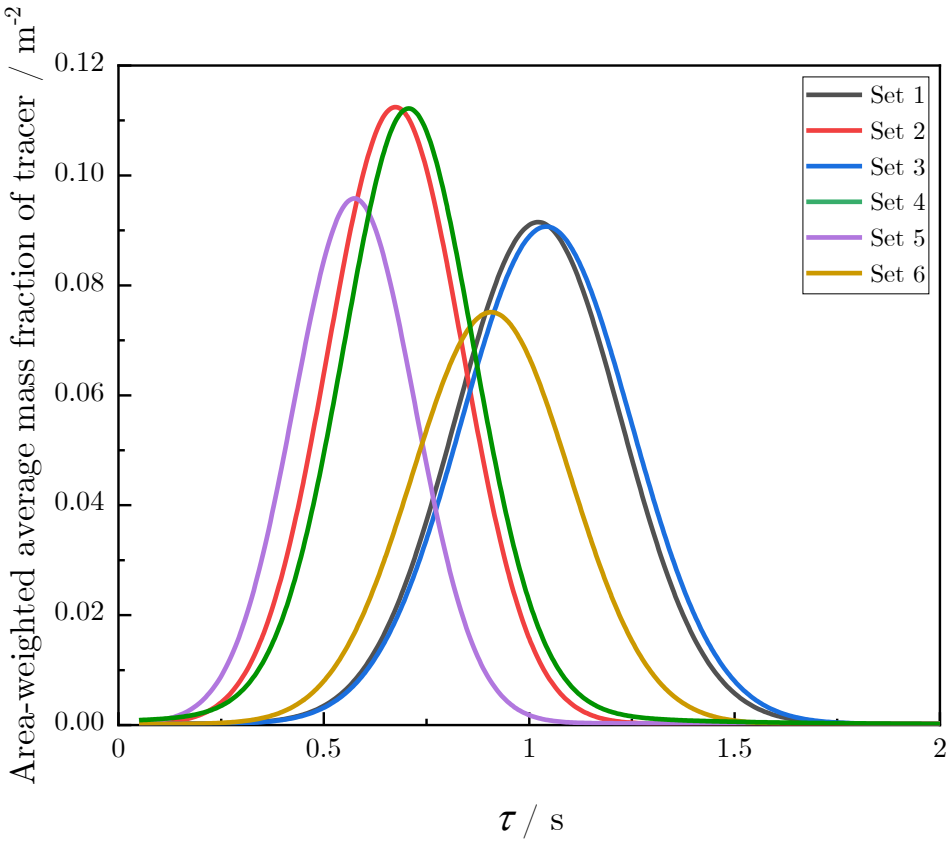

Figure 11-41: Trend of the Area weighted average mass fraction of tracer as a function of the mean residence time τ representing the RTD curve for different process conditions with the Bending model and the injection of the tracer from the inlet of the hot water stream [153].

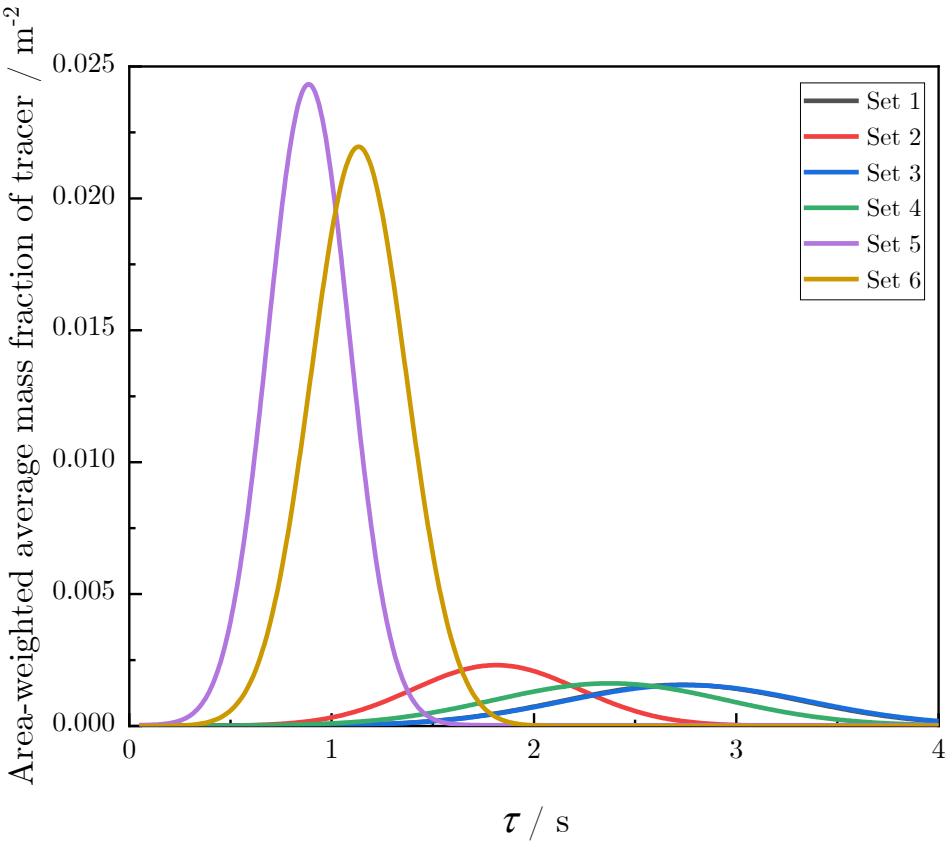

Figure 11-42: Trend of the Area weighted average mass fraction of tracer as a function of the mean residence time τ representing the RTD curve for different process conditions with the Bending model and the injection of the tracer from the inlet of the cold water stream [153].

H3: Y-30 model

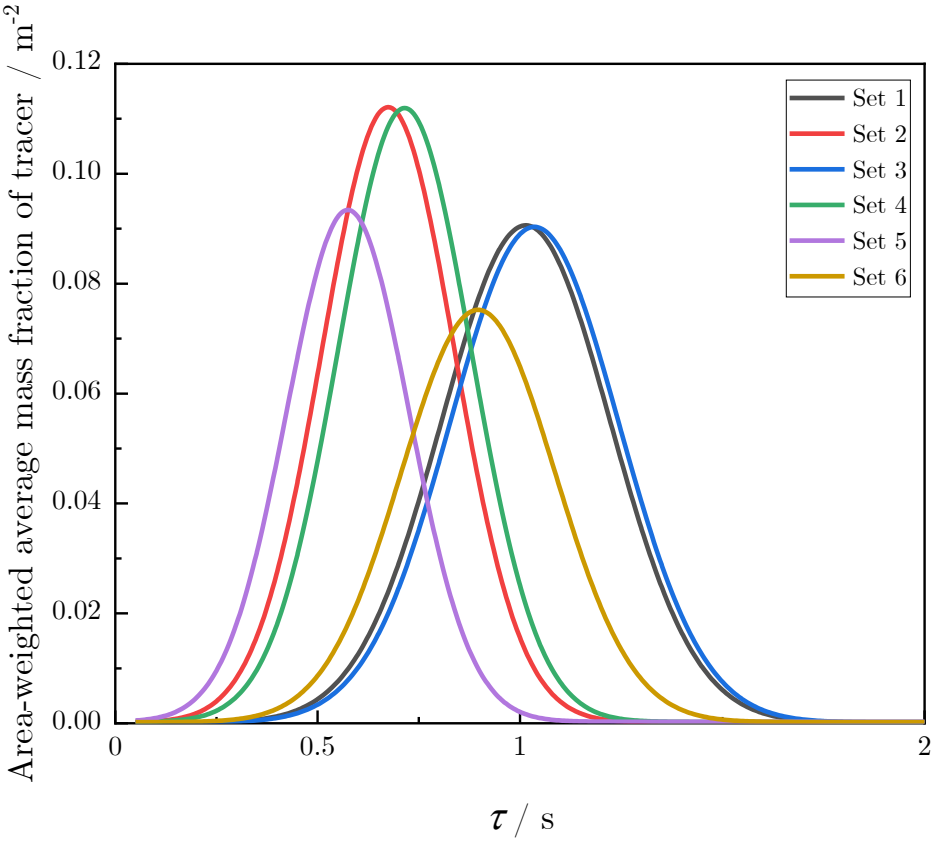

Figure 11-43: Trend of the Area weighted average mass fraction of tracer as a function of the mean residence time τ representing the RTD curve for different process conditions with the Y-30 model and the injection of the tracer from the inlet of the hot water stream [153].

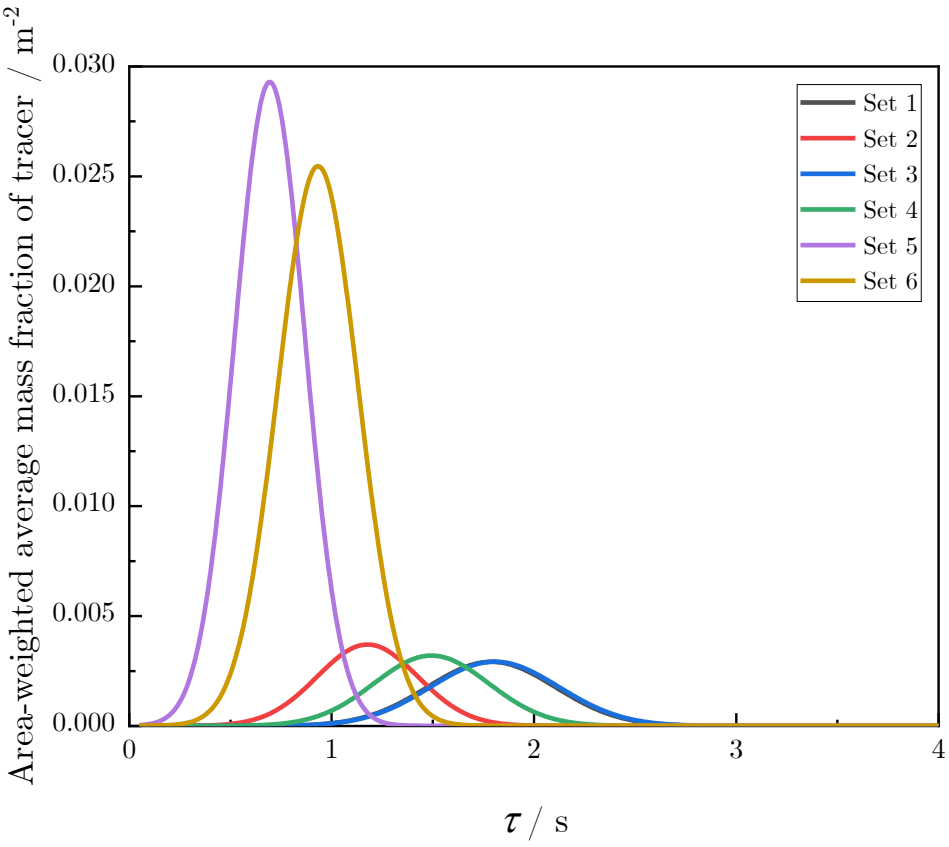

Figure 11-44: Trend of the Area weighted average mass fraction of tracer as a function of the mean residence time τ representing the RTD curve for different process conditions with the Y-30 model and the injection of the tracer from the inlet of the cold water stream [153].

I: Simulation of the reaction with process conditions used for the experiments

Figure 11-45 and Figure 11-46 show the concentration profiles of the simulation with the process conditions of the first and the third experiment (exp. no. 1 and exp. no. 3, Table 7-1) for the comparison with Figure 8-11 regarding the influence of the used salt concentration c_{salt}:

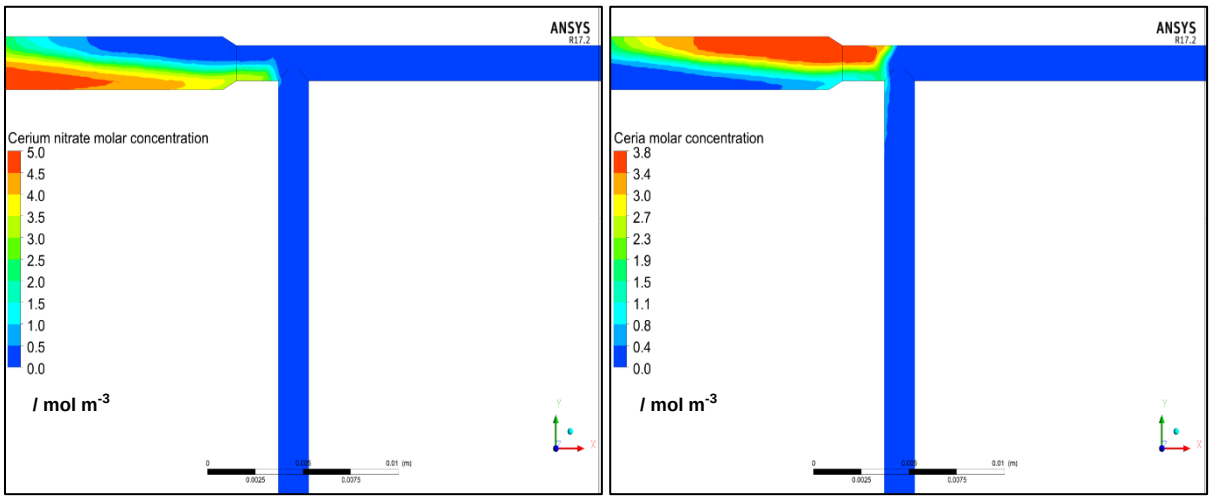

Figure 11-45: Concentration profiles of the used educts and products ($Ce(NO_3)_3$ on the left side, and CeO_2 on the right side) inside the mixing unit. The pressure p was set to 30 MPa, the hot stream temperature T_2 to 673 K, the total mass flow $\dot{m}_3$ to 35 g min^{-1} and the mixing ratio a to 0.1. The salt concentration c_{salt} was adjusted to 0.005 mol dm^{-3}.

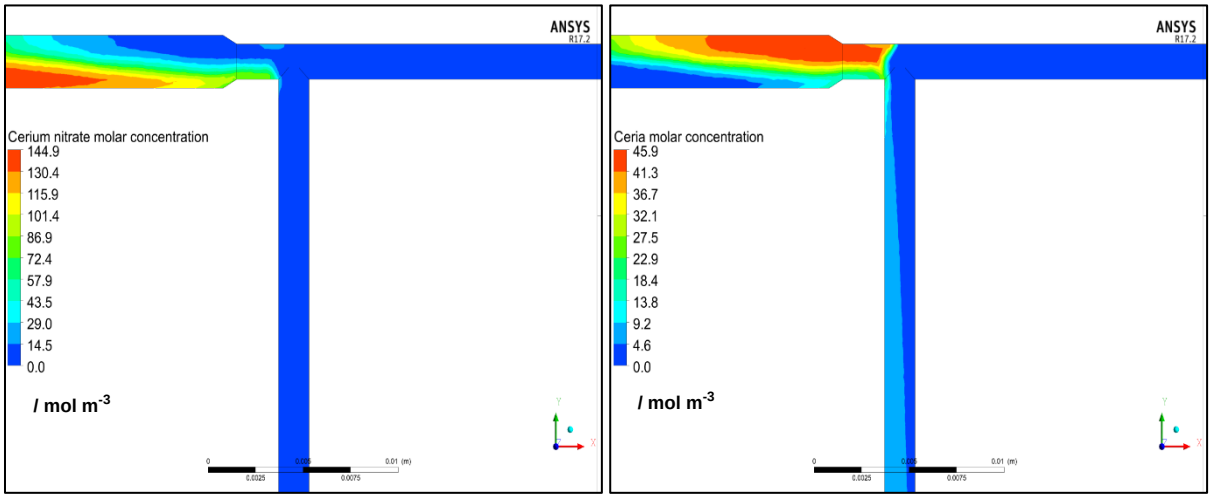

Figure 11-46: Concentration profiles of the used educts and products ($Ce(NO_3)_3$ on the left side, and CeO_2 on the right side) inside the mixing unit. The pressure p was set to 30 MPa, the hot stream temperature T_2 to 673 K, the total mass flow $\dot{m}_3$ to 35 g min^{-1} and the mixing ratio a to 0.1. The salt concentration c_{salt} was adjusted to 0.15 mol dm^{-3}.

With increasing salt concentration c_{salt}, the concentration of CeO_2 is also rising. The concentration profiles are changing with increasing salt concentration c_{salt}. A concentration of 0.005 mol dm^{-3} results in a similar profile as for 0.05 mol dm^{-3}. However, the lowest salt concentration c_{salt} shows the highest dilution effect after the mixing point. The comparison of the concentration profiles (0.05 mol dm^{-3} and 0.15 mol dm^{-3}) shows that the start of the reaction at the top part of the mixer tube is shifted to the mixing point for the higher concentration. In addition to that, the dilution effect is decreased with increasing salt concentration c_{salt}. After the mixing point, the formation of CeO_2 is still ongoing. In general, it was determined that an increase of the salt concentration c_{salt} has no specific effects on the concentration profile in front of the mixing point. Still, the dilution effect after the mixing point is lowered with increasing concentration.

Beyond the influence of the salt concentration, the effect of the change in the total mass flow $\dot{m}_3$ was investigated. Therefore, the simulations were carried out according to exp. no. 4 and 5 (compare Table 7-1) with a variation from 45 g min^{-1} and 55 g min^{-1}. Figure 11-47 and Figure 11-48 show the results of the simulations with an increasing total mass flow $\dot{m}_3$:

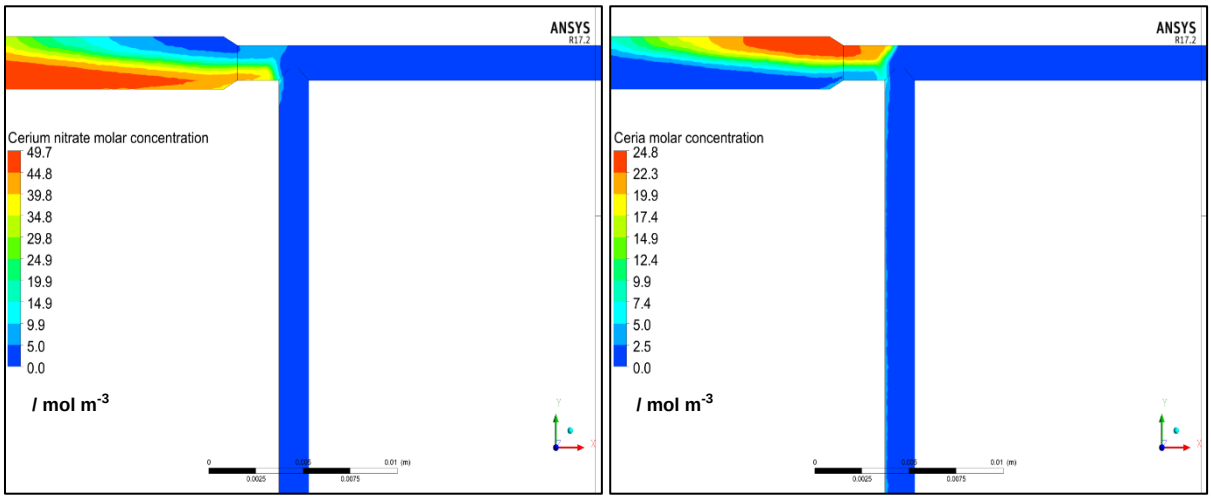

Figure 11-47: Concentration profiles of the used educts and products ($Ce(NO_3)_3$ on the left side, and CeO_2 on the right side) inside the mixing unit. The pressure p was set to 30 MPa, the hot stream temperature T_2 to 673 K, the total mass flow $\dot{m}_3$ to 45 g min^{-1} and the mixing ratio a to 0.1. The salt concentration c_{salt} was adjusted to 0.05 mol dm^{-3}.

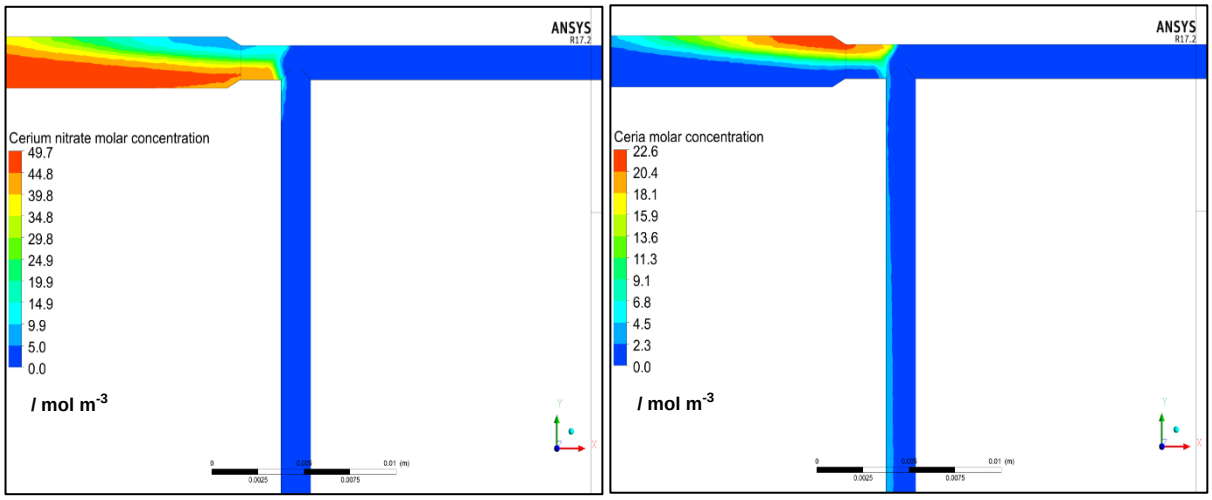

Figure 11-48: Concentration profiles of the used educts and products ($Ce(NO_3)_3$ on the left side, and CeO_2 on the right side) inside the mixing unit. The pressure p was set to 30 MPa, the hot stream temperature T_2 to 673 K, the total mass flow $\dot{m}_3$ to 55 g min^{-1} and the mixing ratio a to 0.1. The salt concentration c_{salt} was adjusted to 0.05 mol dm^{-3}.

In comparison to a total mass flow $\dot{m}_3$ of 35 g min^{-1}, the start of the reaction is shifted to the mixing point with increasing to 45 g min^{-1} and 55 g min^{-1}, respectively. However, the reaction is still occurring in front of the mixing point for these two experiments. At the mixing point, all species are mixed up with the near- / supercritical waterstream. This means that the conversion for the experiments with increased total mass flow $\dot{m}_3$ is also high, and only a small amount is produced after the mixing point. It is concluded that an increase in the total mass

flow $\dot{m}_3$ counters the early start of the reaction close to the mixing point in the tube of the cold stream.

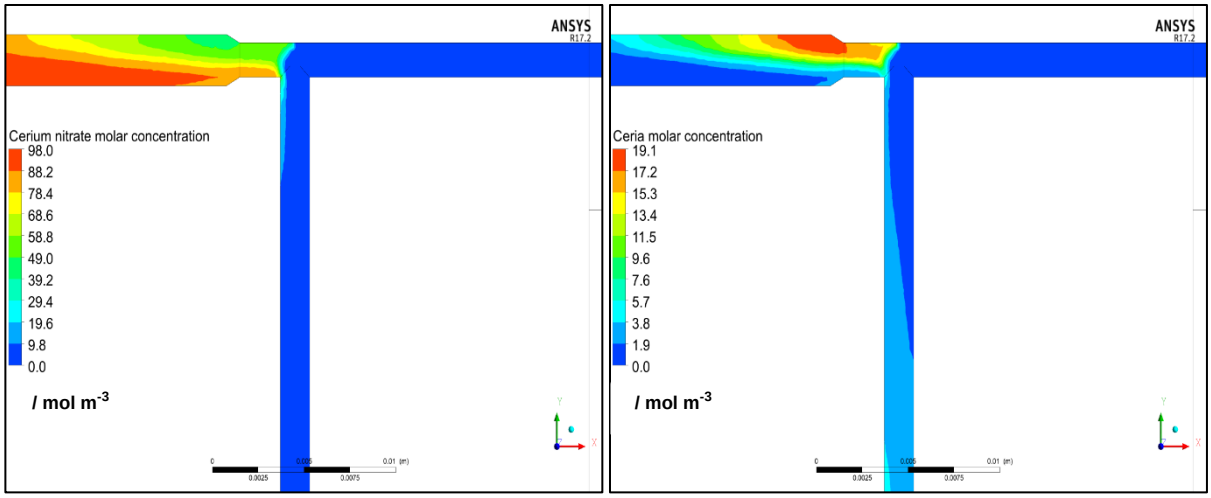

Figure 11-49: Concentration profiles of the used educts and products ($Ce(NO_3)_3$ on the left side, and CeO_2 on the right side) inside the mixing unit. The pressure p was set to 30 MPa, the hot stream temperature T_2 to 573 K, the total mass flow $\dot{m}_3$ to 35 g min^{-1} and the mixing ratio a to 0.1. The salt concentration c_{salt} was adjusted to 0.1 mol dm^{-3}.

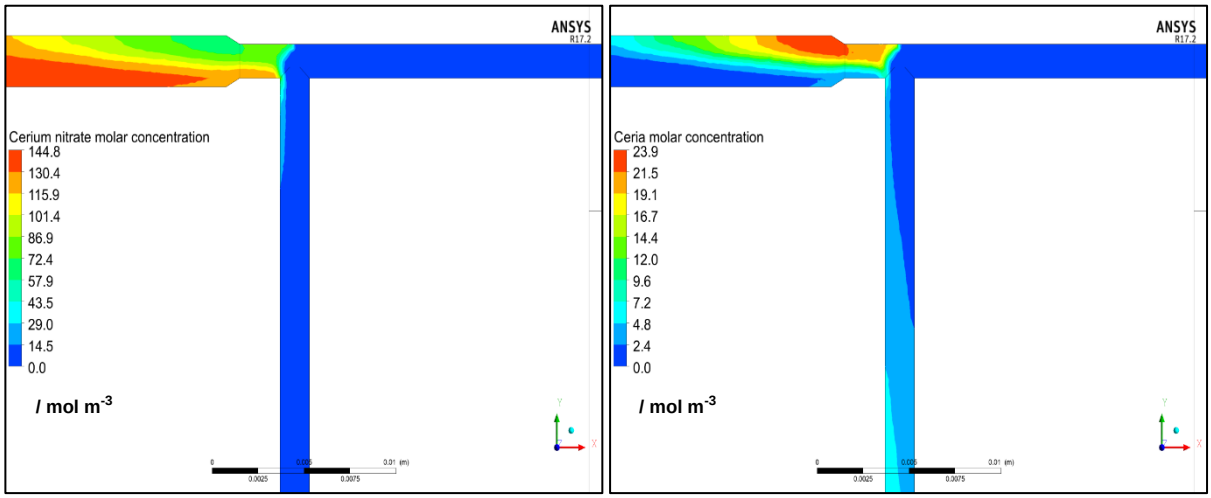

Figure 11-50: Concentration profiles of the used educts and products ($Ce(NO_3)_3$ on the left side, and CeO_2 on the right side) inside the mixing unit. The pressure p was set to 30 MPa, the hot stream temperature T_2 to 573 K, the total mass flow $\dot{m}_3$ to 35 g min^{-1} and the mixing ratio a to 0.1. The salt concentration c_{salt} was adjusted to 0.15 mol dm^{-3}.

The concentration dependence is also observed for a mixing temperature of 573 K. The change in the concentration does not affect the concentration profile in the tube of the cold part in front of the mixing point.

Figure 11-51 and Figure 11-52 show the concentration profiles for experiments 31 and 34 for 25 MPa and the variation of the salt concentration c_{salt} between 0.005 mol dm^{-3} and 0.15 mol dm^{-3}:

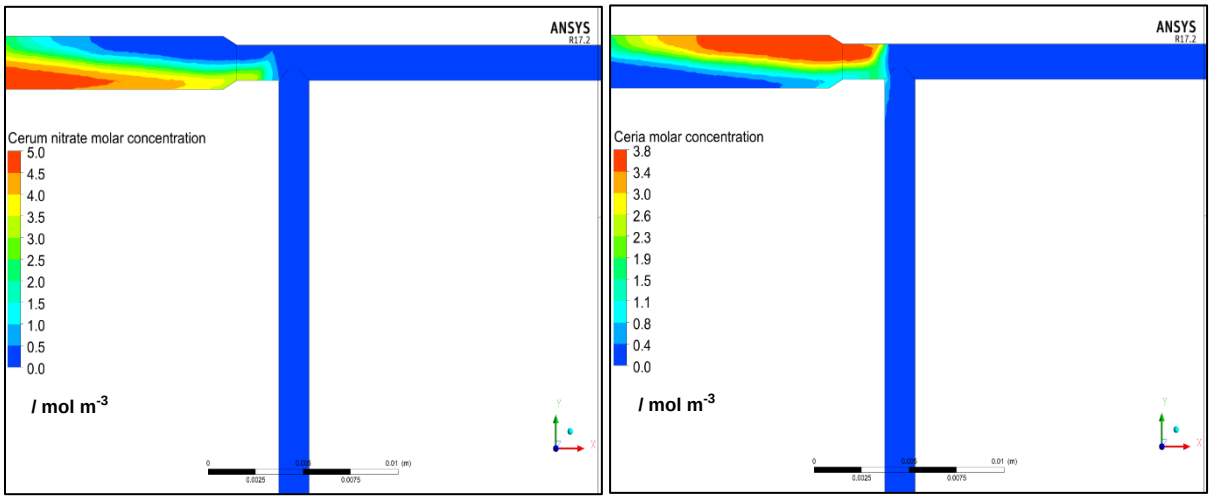

Figure 11-51: Concentration profiles of the used educts and products ($Ce(NO_3)_3$ on the left side, and CeO_2 on the right side) inside the mixing unit. The pressure p was set to 25 MPa, the hot stream temperature T_2 to 673 K, the total mass flow $\dot{m}_3$ to 35 g min^{-1} and the mixing ratio a to 0.1. The salt concentration c_{salt} was adjusted to 0.005 mol dm^{-3}.

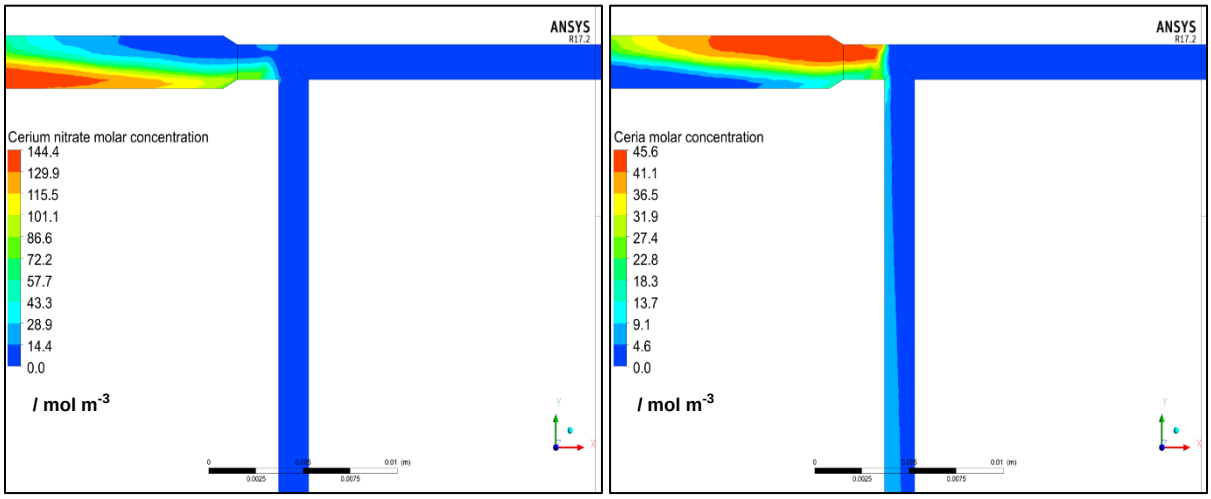

Figure 11-52: Concentration profiles of the used educts and products ($Ce(NO_3)_3$ on the left side, and CeO_2 on the right side) inside the mixing unit. The pressure p was set to 25 MPa, the hot stream temperature T_2 to 673 K, the total mass flow $\dot{m}_3$ to 35 g min^{-1} and the mixing ratio a to 0.1. The salt concentration c_{salt} was adjusted to 0.15 mol dm^{-3}.

With increasing salt concentration c_{salt}, the amount of CeO_2 is rising according to the previously described simulations. Especially for 0.15 mol dm^{-3}, CeO_2 exists in the reaction tube after the mixing unit. The maximum amount of produced CeO_2 is independent of the pressure p.

J: Concentration profiles of the simulation of the experiments

J1: exp. no. 1

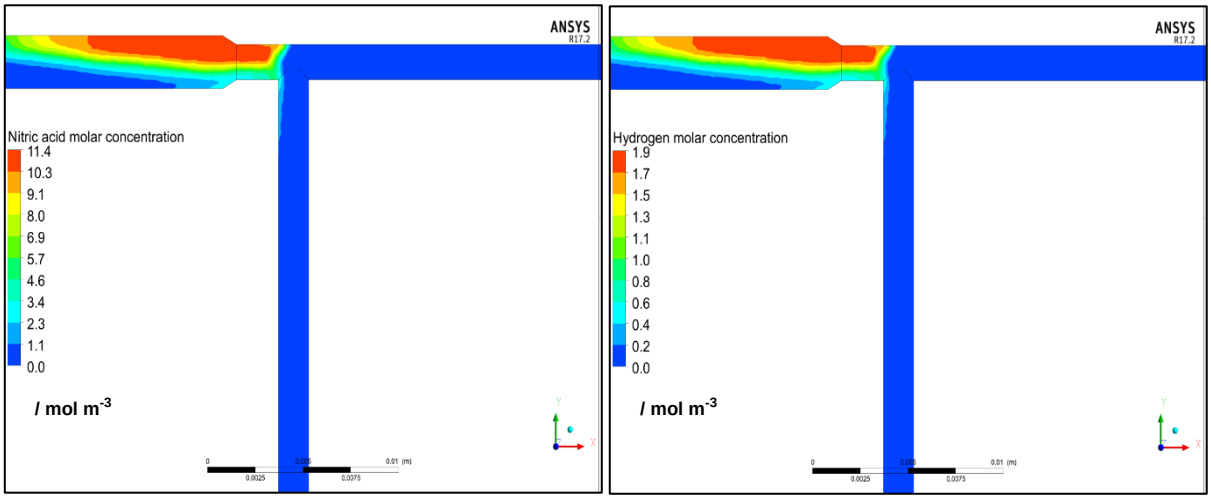

Figure 11-53: Concentration profiles of the products (HNO_3 on the left side and H_2 on the right side) inside the mixing unit. The pressure p was set to 30 MPa, the hot stream temperature T_2 to 673 K, the total mass flow $\dot{m}_3$ to 35 g min^{-1} and the mixing ratio a to 0.1. The salt concentration c_{salt} was adjusted to 0.05 mol dm^{-3}.

J2: exp. no. 2

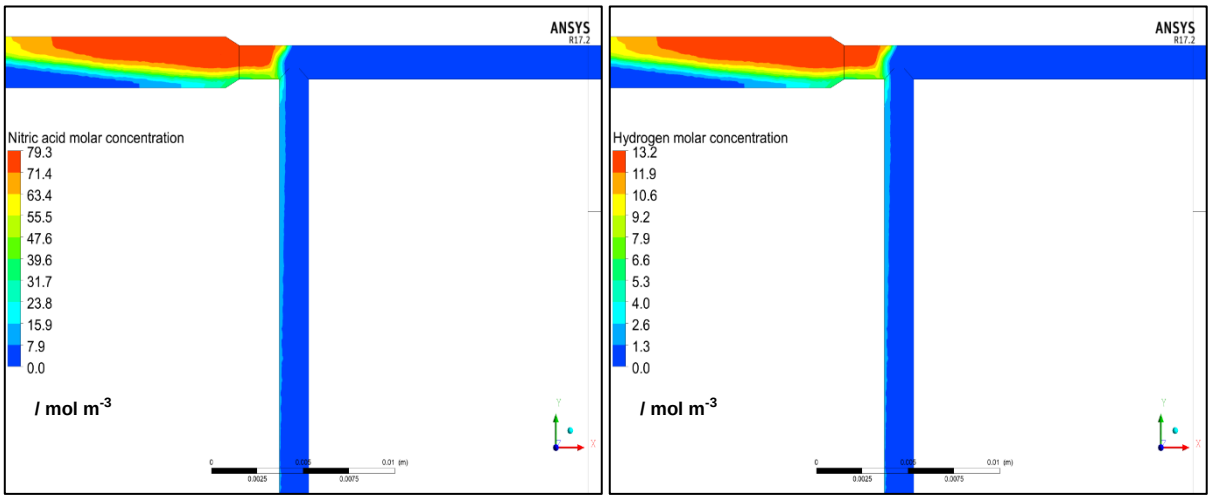

Figure 11-54: Concentration profiles of the products (HNO_3 on the left side and H_2 on the right side) inside the mixing unit. The pressure p was set to 30 MPa, the hot stream temperature T_2 to 673 K, the total mass flow $\dot{m}_3$ to 35 g min^{-1} and the mixing ratio a to 0.1. The salt concentration c_{salt} was adjusted to 0.05 mol dm^{-3}.

J3: exp. no. 3

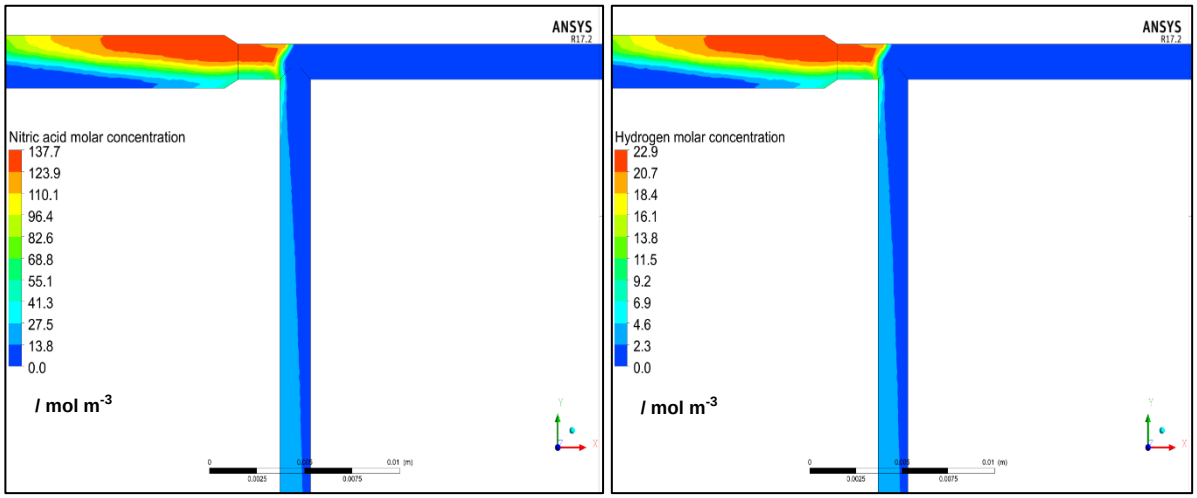

Figure 11-55: Concentration profiles of the products (HNO_3 on the left side and H_2 on the right side) inside the mixing unit. The pressure p was set to 30 MPa, the hot stream temperature T_2 to 673 K, the total mass flow $\dot{m}_3$ to 35 g min^{-1} and the mixing ratio a to 0.1. The salt concentration c_{salt} was adjusted to 0.15 mol dm^{-3}.

J4: exp. no. 4

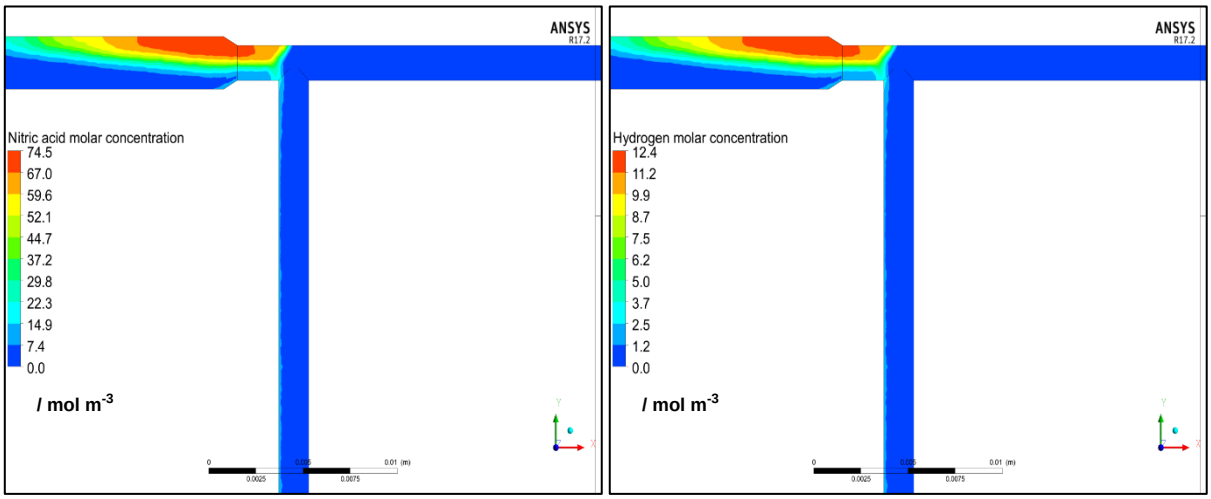

Figure 11-56: Concentration profiles of the products (HNO_3 on the left side and H_2 on the right side) inside the mixing unit. The pressure p was set to 30 MPa, the hot stream temperature T_2 to 673 K, the total mass flow $\dot{m}_3$ to 45 g min^{-1} and the mixing ratio a to 0.1. The salt concentration c_{salt} was adjusted to 0.05 mol dm^{-3}.

J5: exp no. 5

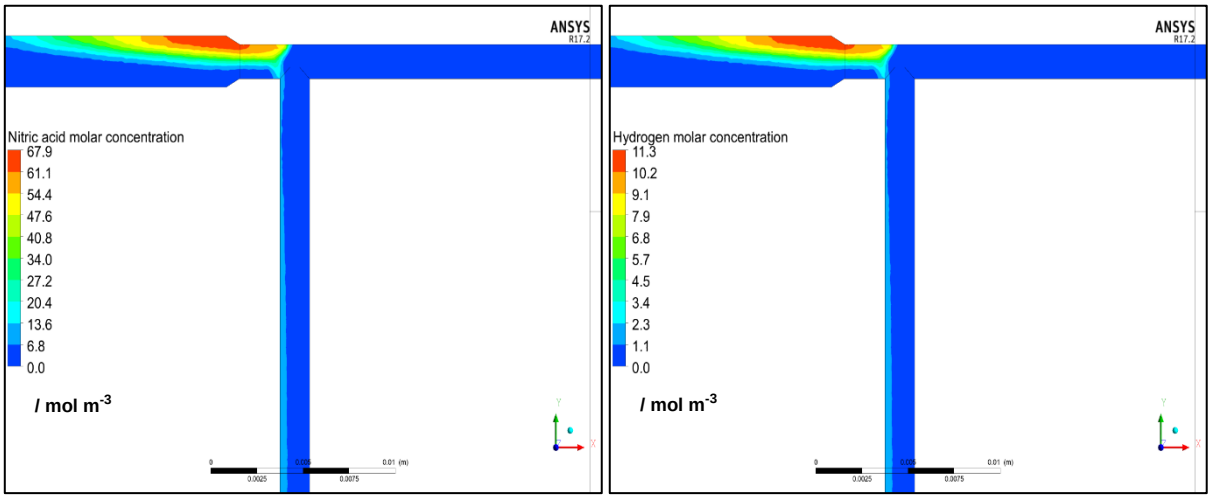

Figure 11-57: Concentration profiles of the products (HNO_3 on the left side and H_2 on the right side) inside the mixing unit. The pressure p was set to 30 MPa, the hot stream temperature T_2 to 673 K, the total mass flow $\dot{m}_3$ to 55 g min^{-1} and the mixing ratio a to 0.1. The salt concentration c_{salt} was adjusted to 0.05 mol dm^{-3}.

J6: exp. no. 6

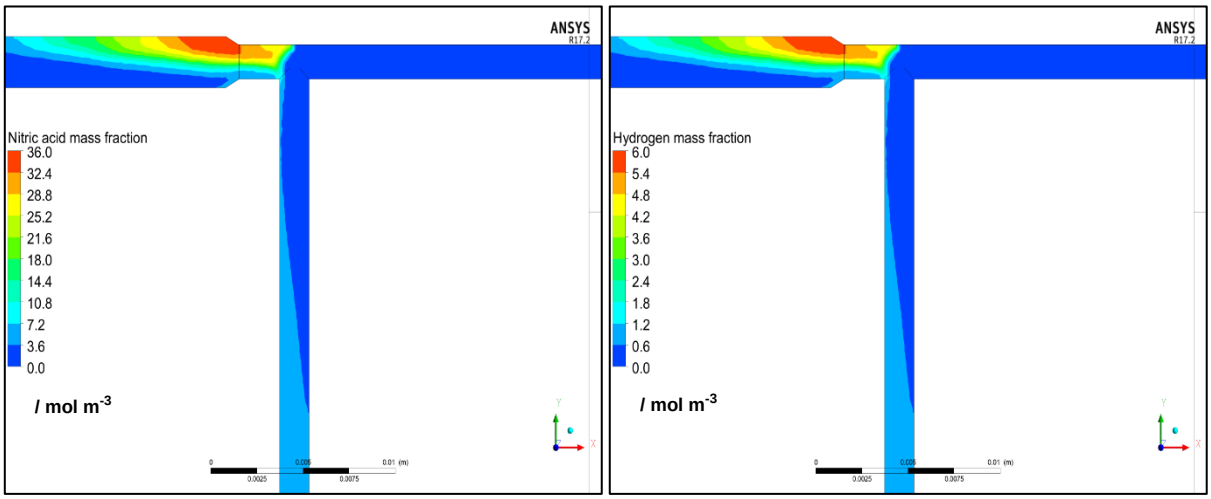

Figure 11-58: Concentration profiles of the products (HNO_3 on the left side and H_2 on the right side) inside the mixing unit. The pressure p was set to 30 MPa, the hot stream temperature T_2 to 573 K, the total mass flow $\dot{m}_3$ to 35 g min^{-1} and the mixing ratio a to 0.1. The salt concentration c_{salt} was adjusted to 0.05 mol dm^{-3}.

J7: exp. no. 7

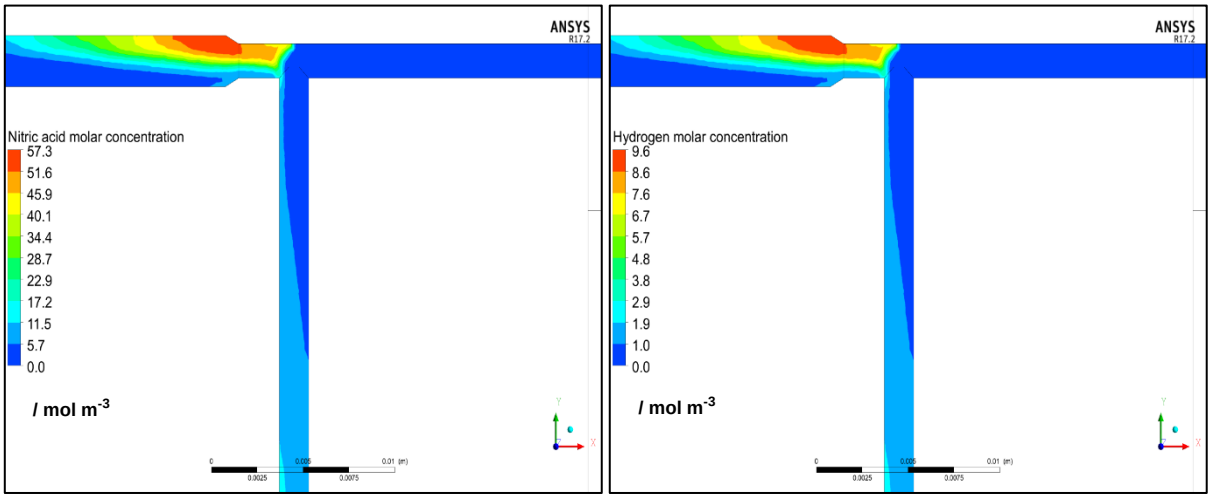

Figure 11-59: Concentration profiles of the products (HNO_3 on the left side and H_2 on the right side) inside the mixing unit. The pressure p was set to 30 MPa, the hot stream temperature T_2 to 573 K, the total mass flow $\dot{m}_3$ to 35 g min^{-1} and the mixing ratio a to 0.1. The salt concentration c_{salt} was adjusted to 0.1 mol dm^{-3}.

J8: exp. no. 8

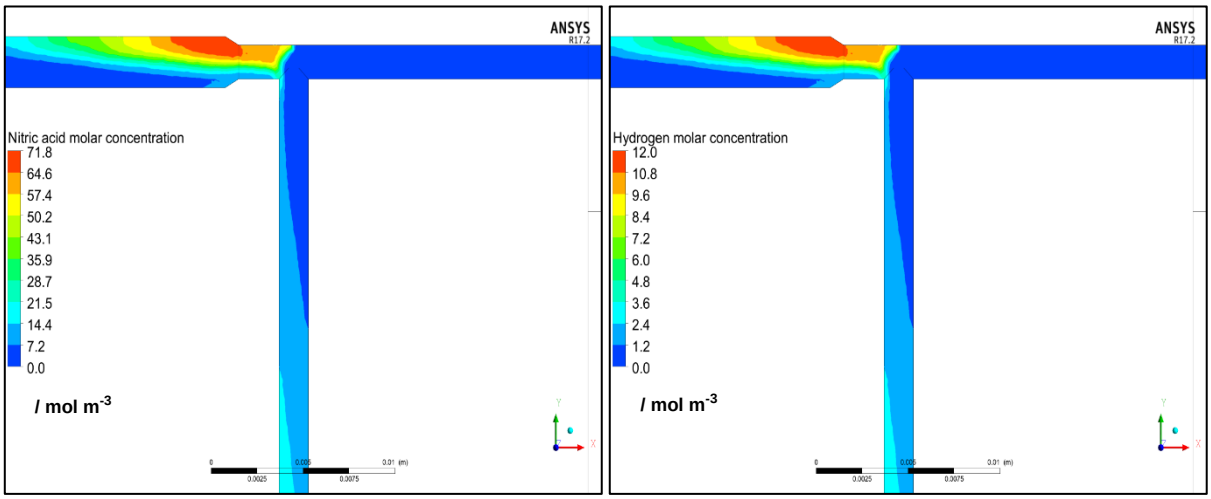

Figure 11-60: Concentration profiles of the products (HNO_3 on the left side and H_2 on the right side) inside the mixing unit. The pressure p was set to 30 MPa, the hot stream temperature T_2 to 573 K, the total mass flow $\dot{m}_3$ to 35 g min^{-1} and the mixing ratio a to 0.1. The salt concentration c_{salt} was adjusted to 0.15 mol dm^{-3}.

J9: exp. no. 30

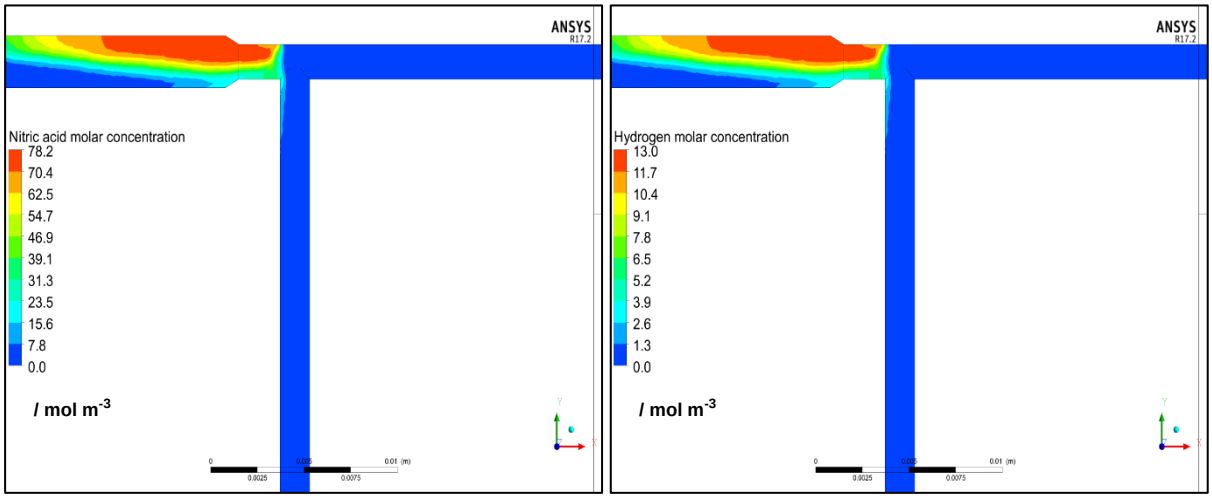

Figure 11-61: Concentration profiles of the products (HNO_3 on the left side and H_2 on the right side) inside the mixing unit. The pressure p was set to 25 MPa, the hot stream temperature T_2 to 673 K, the total mass flow $\dot{m}_3$ to 35 g min^{-1} and the mixing ratio a to 0.1. The salt concentration c_{salt} was adjusted to 0.05 mol dm^{-3}.

J10: exp. no 31

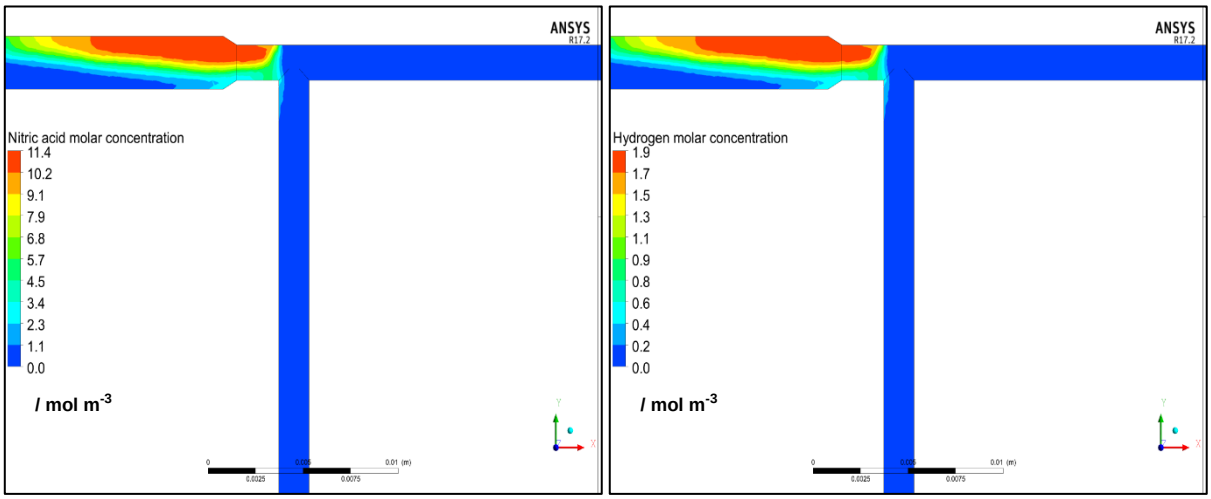

Figure 11-62: Concentration profiles of the products (HNO_3 on the left side and H_2 on the right side) inside the mixing unit. The pressure p was set to 25 MPa, the hot stream temperature T_2 to 673 K, the total mass flow $\dot{m}_3$ to 35 g min^{-1} and the mixing ratio a to 0.1. The salt concentration c_{salt} was adjusted to 0.005 mol dm^{-3}.

J11: exp. no. 34

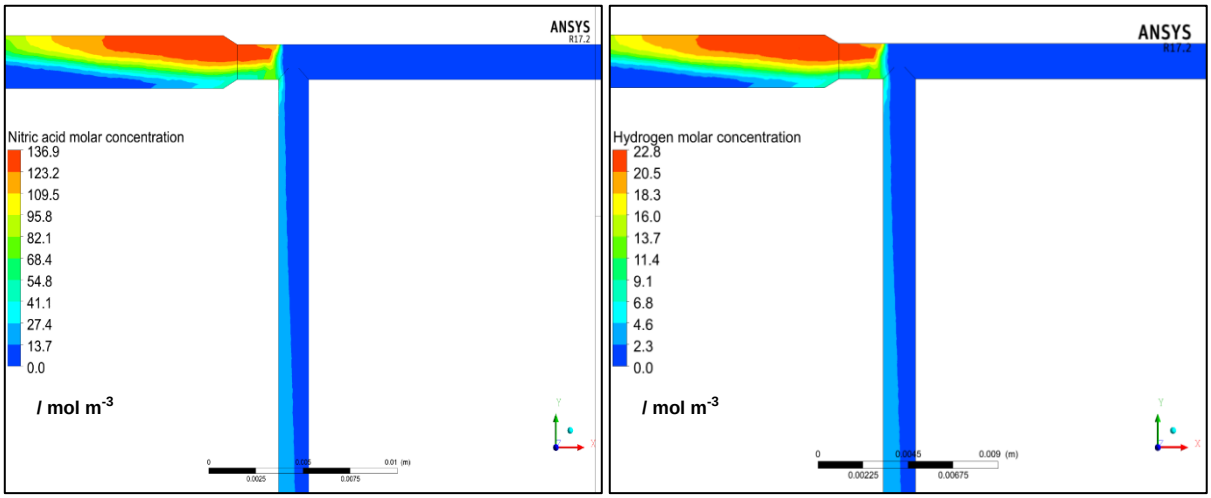

Figure 11-63: Concentration profiles of the products (HNO_3 on the left side and H_2 on the right side) inside the mixing unit. The pressure p was set to 25 MPa, the hot stream temperature T_2 to 673 K, the total mass flow $\dot{m}_3$ to 35 g min^{-1} and the mixing ratio a to 0.1. The salt concentration c_{salt} was adjusted to 0.15 mol dm^{-3}.

K: Mass fraction profiles of the simulation of the experiments

K1: exp. no. 1

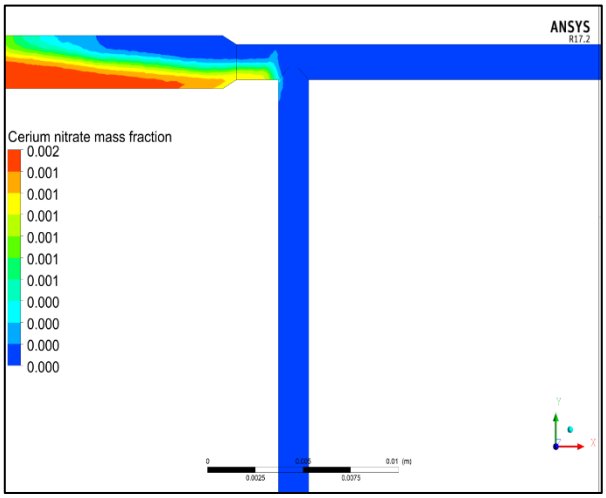

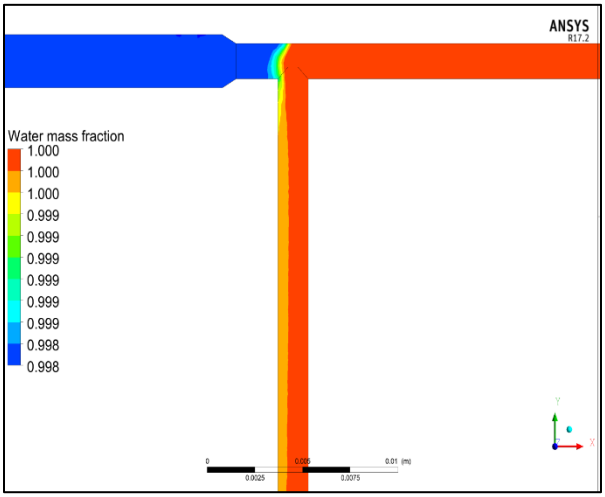

Figure 11-64: Mass fraction profiles of the used educts and products ($Ce(NO_3)_3$ on the left top side, CeO_2 at the top right side, HNO_3 at the bottom left side, and H_2 at the bottom right side) and H_2O inside the mixing unit. The pressure p was set to 30 MPa, the hot stream temperature T_2 to 673 K, the total mass flow $\dot{m}_3$ to 35 g min^{-1} and the mixing ratio a to 0.1. The salt concentration c_{salt} was adjusted to 0.005 mol dm^{-3}.

K2: exp. no. 2

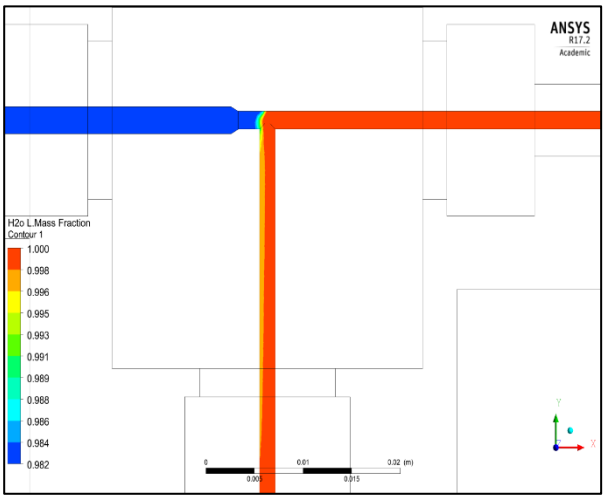

Figure 11-65: Mass fraction profile of H_2O inside the mixing unit. The pressure p was set to 30 MPa, the hot stream temperature T_2 to 673 K, the total mass flow $\dot{m}_3$ to 35 g min^{-1} and the mixing ratio a to 0.1. The salt concentration c_{salt} was adjusted to 0.05 mol dm^{-3}.

K3: exp. no. 3

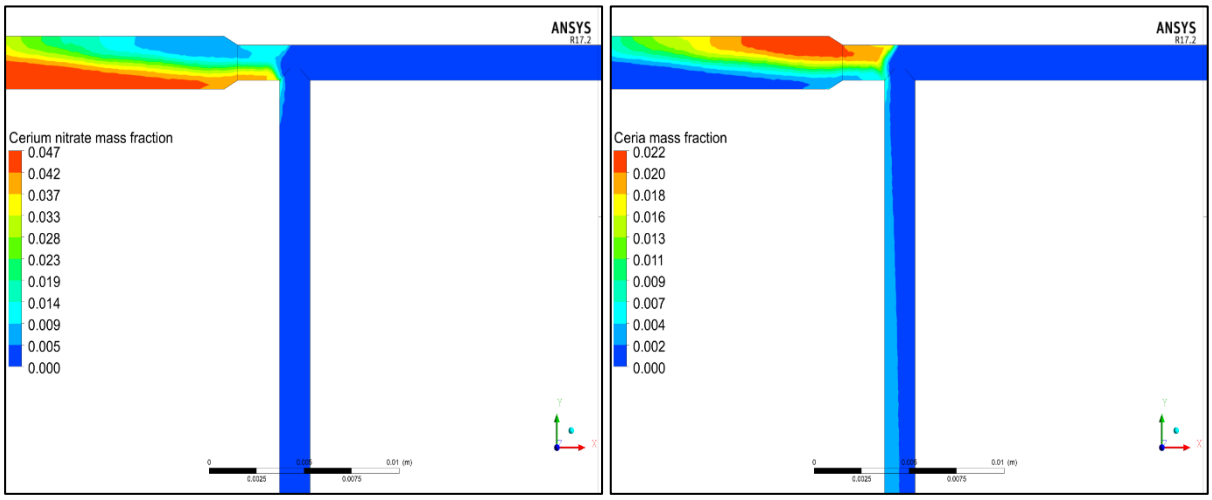

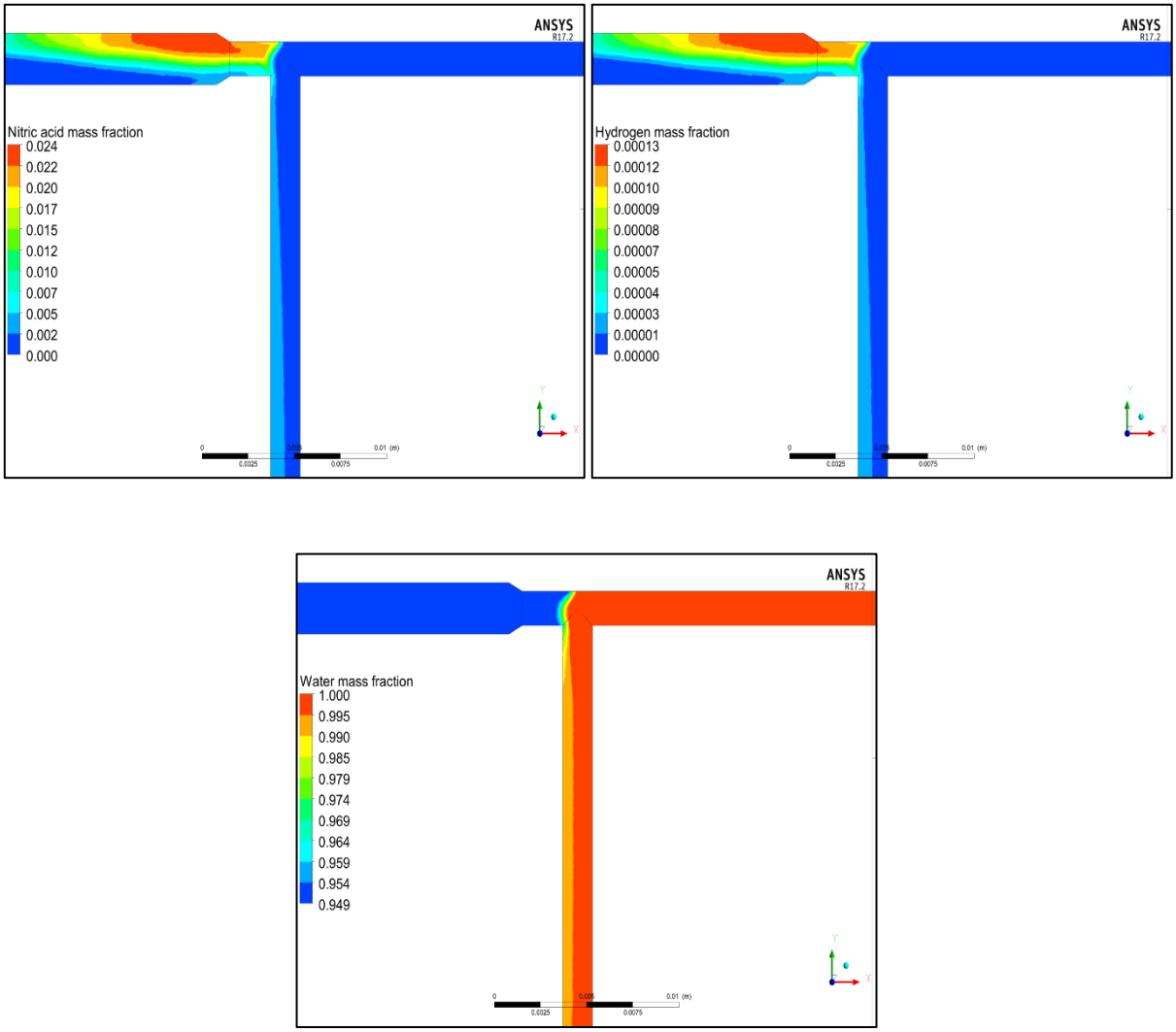

Figure 11-66: Mass fraction profiles of the used educts and products ($Ce(NO_3)_3$ on the left top side, CeO_2 at the top right side, HNO_3 at the bottom left side, and H_2 at the bottom right side) and H_2O inside the mixing unit. The pressure p was set to 30 MPa, the hot stream temperature T_2 to 673 K, the total mass flow $\dot{m}_3$ to 35 g min^{-1} and the mixing ratio a to 0.1. The salt concentration c_{salt} was adjusted to 0.15 mol dm^{-3}.

K4: exp. no. 4

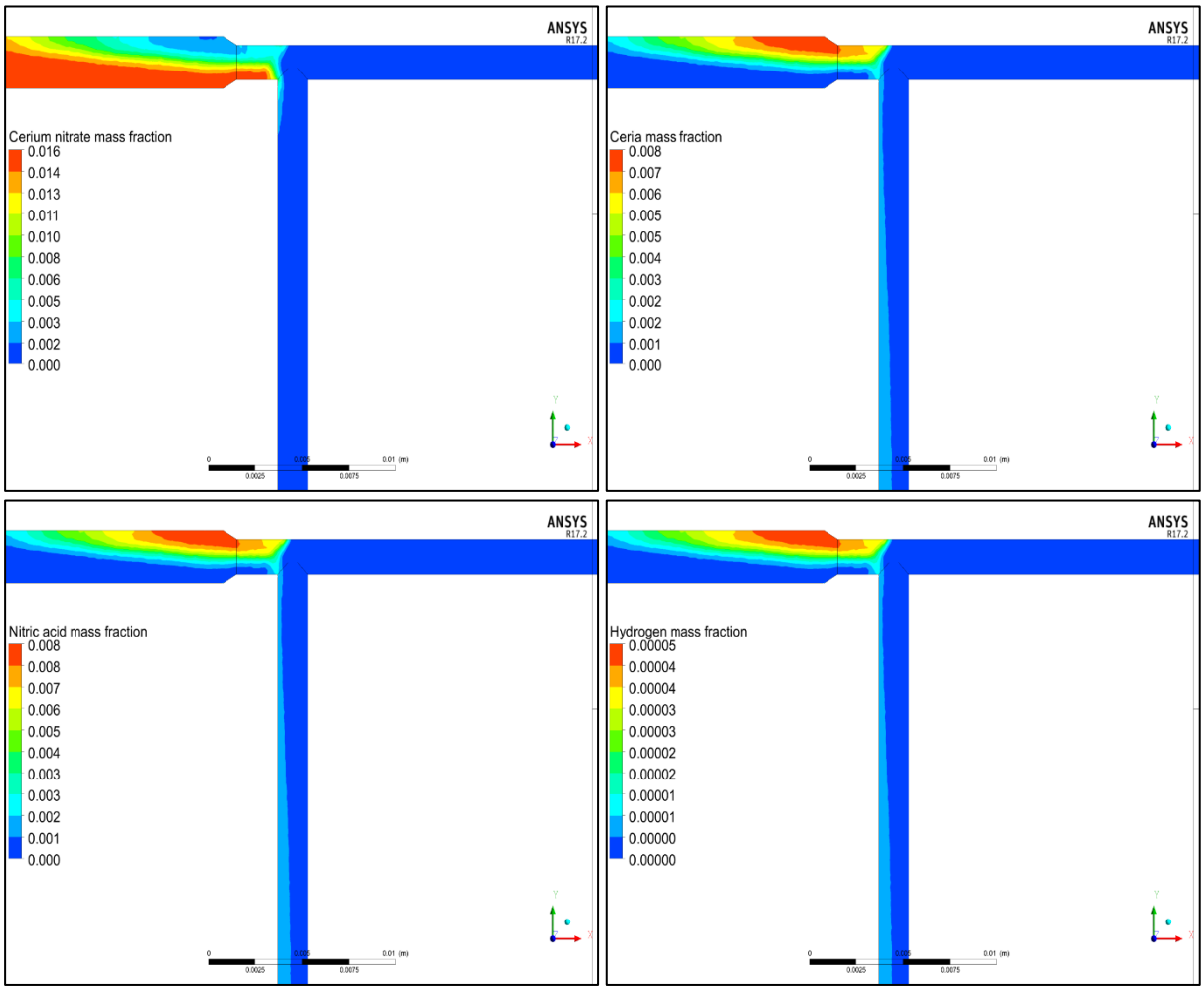
ANSYS
R17.2
Cerium nitrate mass fraction
0.016
0.014
0.013
0.011
0.010
0.008
0.006
0.005
0.003
0.002
0.000
ANSYS
R17.2
Ceria mass fraction
0.008
0.007
0.006
0.005
0.005
0.004
0.003
0.002
0.002
0.001
0.000
ANSYS
R17.2
Nitric acid mass fraction
0.008
0.008
0.007
0.006
0.005
0.004
0.003
0.003
0.002
0.001
0.000
ANSYS
R17.2
Hydrogen mass fraction
0.00005
0.00004
0.00004
0.00003
0.00003
0.00002
0.00002
0.00001
0.00001
0.00000
0.00000

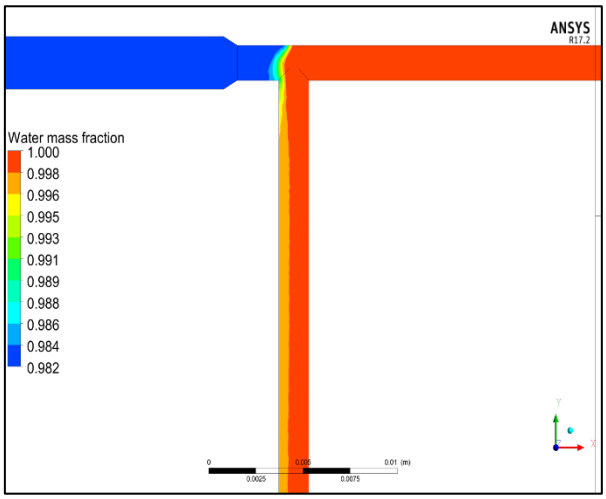

Figure 11-67: Mass fraction profiles of the used educts and products ($Ce(NO_3)_3$ on the left top side, CeO_2 at the top right side, HNO_3 at the bottom left side, and H_2 at the bottom right side) and H_2O inside the mixing unit. The pressure p was set to 30 MPa, the hot stream temperature T_2 to 673 K, the total mass flow $\dot{m}_3$ to 45 g min^{-1} and the mixing ratio a to 0.1. The salt concentration c_{salt} was adjusted to 0.05 mol dm^{-3}.

K5: exp. no. 5

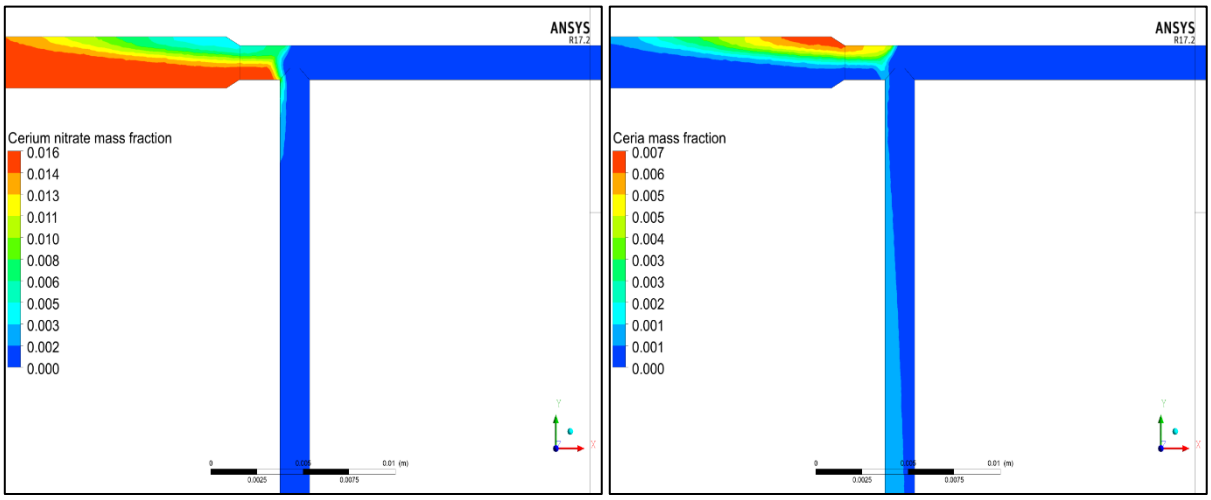

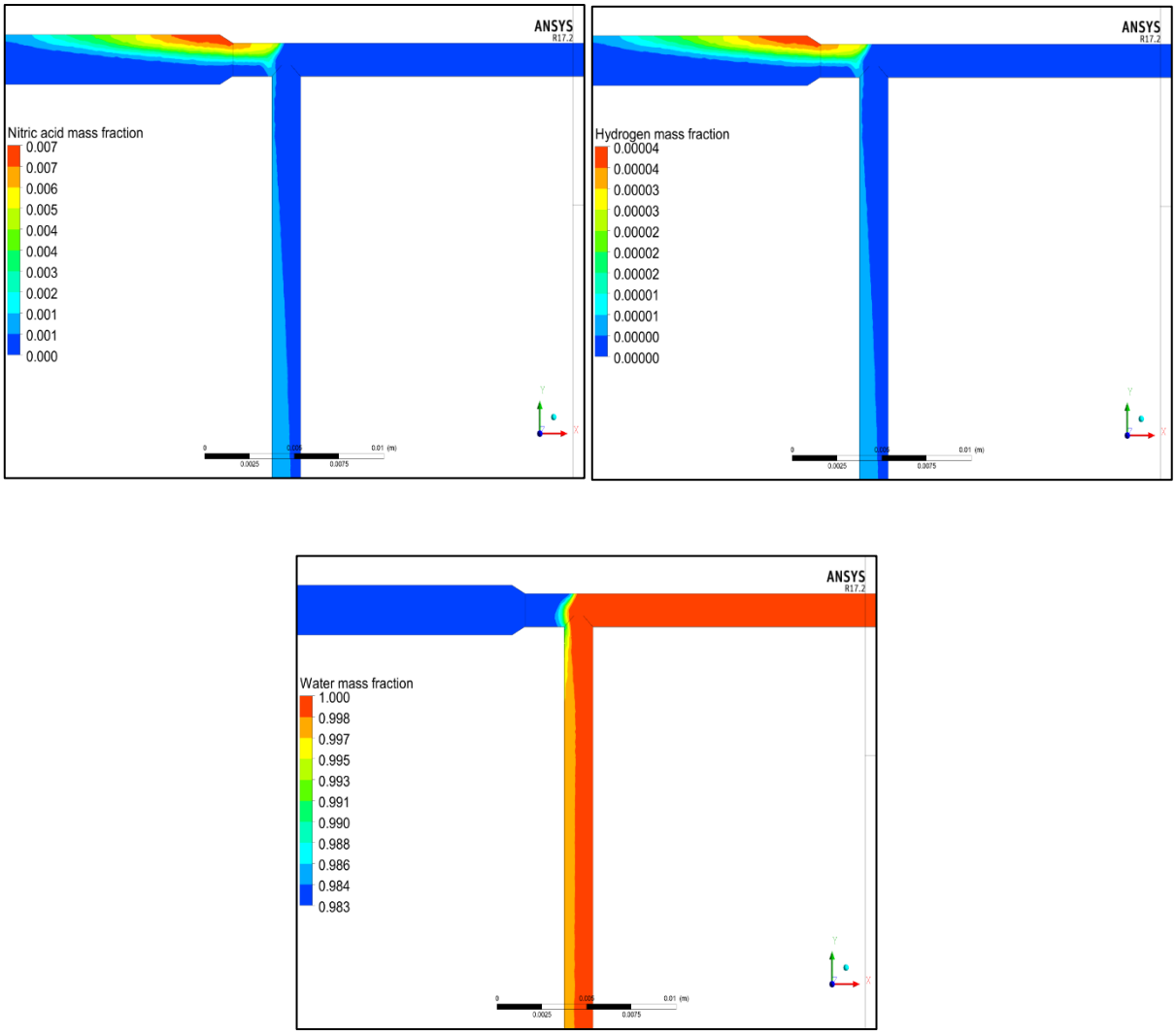

Figure 11-68: Mass fraction profiles of the used educts and products ($Ce(NO_3)_3$ on the left top side, CeO_2 at the top right side, HNO_3 at the bottom left side, and H_2 at the bottom right side) and H_2O inside the mixing unit. The pressure p was set to 30 MPa, the hot stream temperature T_2 to 673 K, the total mass flow $\dot{m}_3$ to 55 g min^{-1} and the mixing ratio a to 0.1. The salt concentration c_{salt} was adjusted to 0.05 mol dm^{-3}.

K6: exp. no. 6

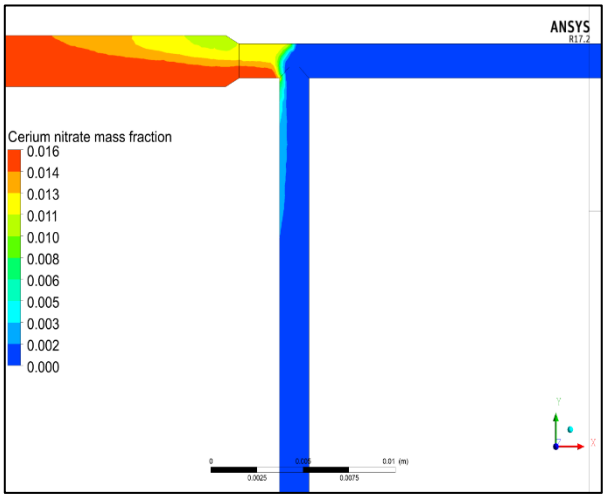
ANSYS
R17.2
Cerium nitrate mass fraction
0.016
0.014
0.013
0.011
0.010
0.008
0.006
0.005
0.003
0.002
0.000

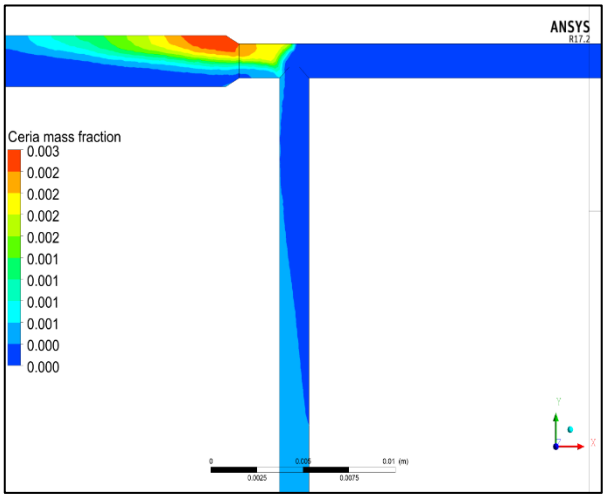
ANSYS
R17.2
Ceria mass fraction
0.003
0.002
0.002
0.002
0.002
0.001
0.001
0.001
0.001
0.000
0.000

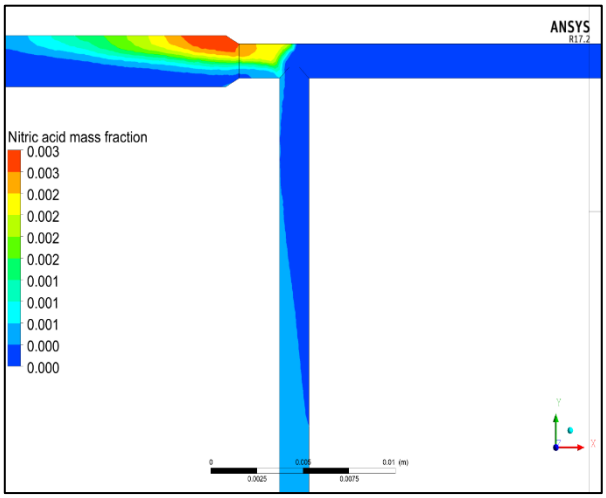
ANSYS
R17.2
Nitric acid mass fraction
0.003
0.003
0.002
0.002
0.002
0.002
0.001
0.001
0.001
0.000
0.000

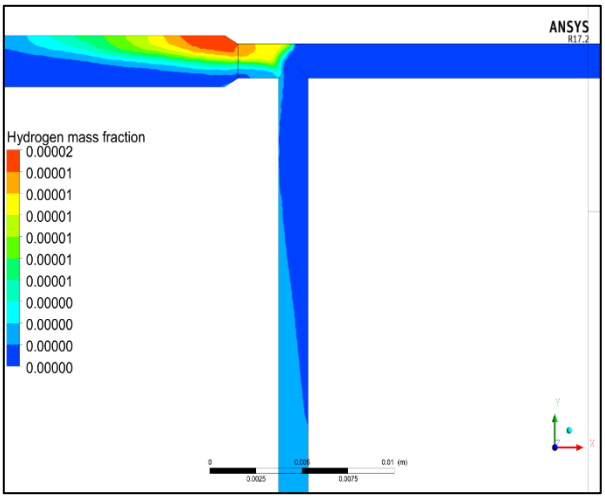
ANSYS
R17.2
Hydrogen mass fraction
0.00002
0.00001
0.00001
0.00001
0.00001
0.00001
0.00001
0.00000
0.00000
0.00000
0.00000

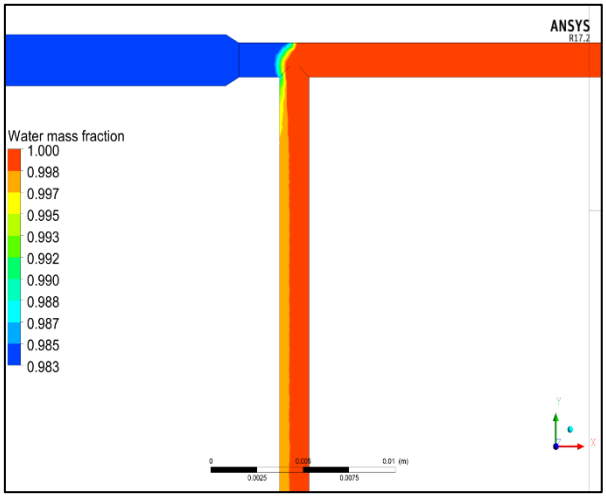
ANSYS
R17.2
Water mass fraction
1.000
0.998
0.997
0.995
0.993
0.992
0.990
0.988
0.987
0.985
0.983

Figure 11-69: Mass fraction profiles of the used educts and products ($Ce(NO_3)_3$ on the left top side, CeO_2 at the top right side, HNO_3 at the bottom left side, and H_2 at the bottom right side) and H_2O inside the mixing unit. The pressure p was set to 30 MPa, the hot stream temperature T_2 to 573 K, the total mass flow $\dot{m}_3$ to 35 g min^{-1} and the mixing ratio a to 0.1. The salt concentration c_{salt} was adjusted to 0.05 mol dm^{-3}.

K7: exp. no. 7

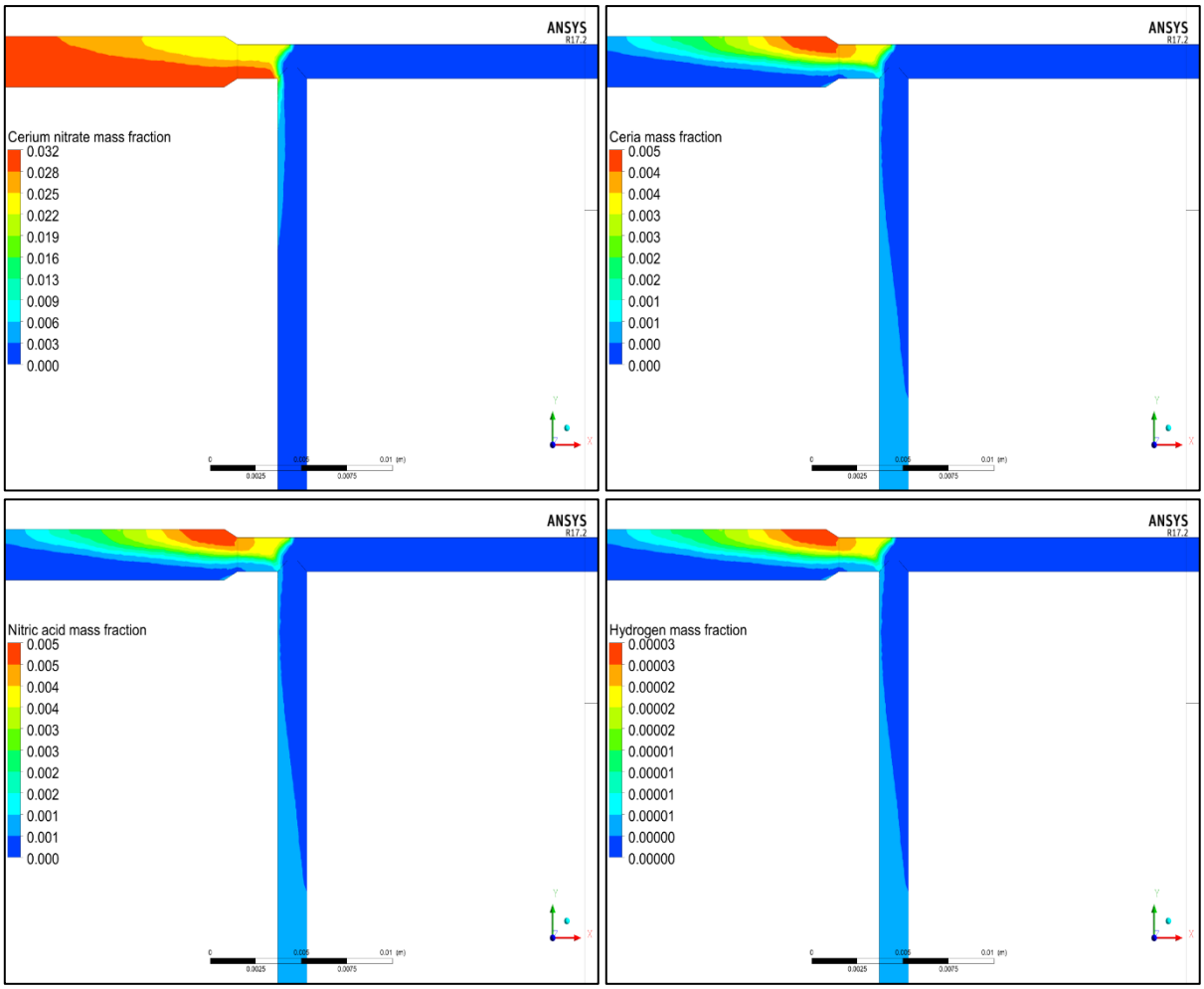

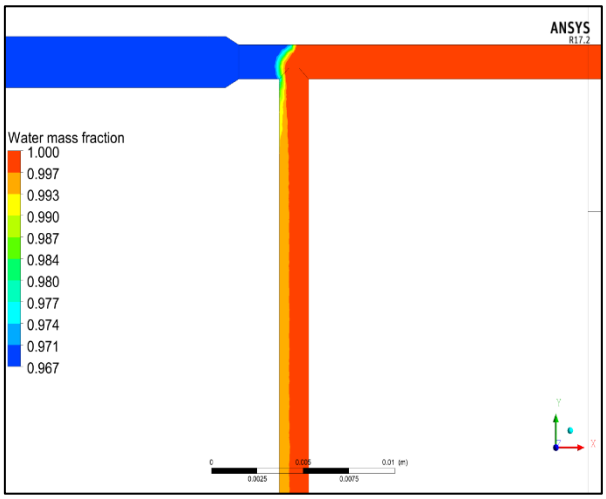

Figure 11-70: Mass fraction profiles of the used educts and products ($Ce(NO_3)_3$ on the left top side, CeO_2 at the top right side, HNO_3 at the bottom left side, and H_2 at the bottom right side) and H_2O inside the mixing unit. The pressure p was set to 30 MPa, the hot stream temperature T_2 to 573 K, the total mass flow $\dot{m}_3$ to 35 g min^{-1} and the mixing ratio a to 0.1. The salt concentration c_{salt} was adjusted to 0.1 mol dm^{-3}.

K8: exp. no. 8

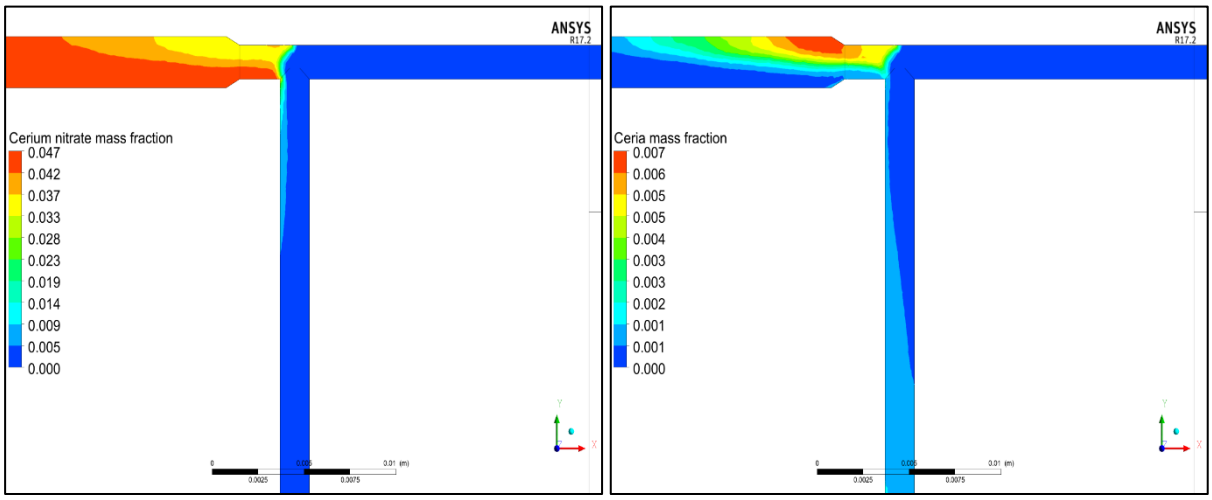

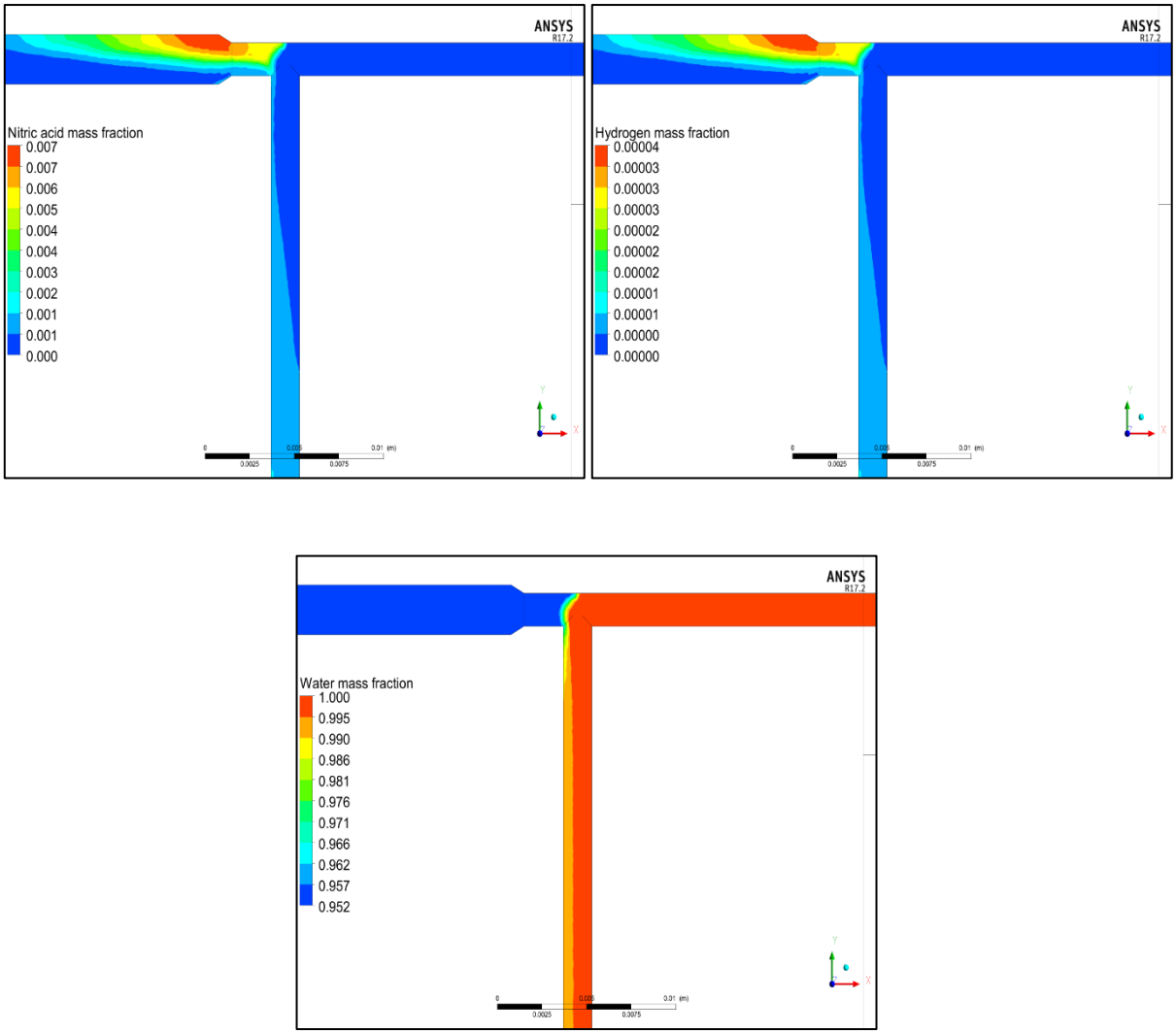

Figure 11-71: Mass fraction profiles of the used educts and products ($Ce(NO_3)_3$ on the left top side, CeO_2 at the top right side, HNO_3 at the bottom left side, and H_2 at the bottom right side) and H_2O inside the mixing unit. The pressure p was set to 30 MPa, the hot stream temperature T_2 to 573 K, the total mass flow $\dot{m}_3$ to 35 g min^{-1} and the mixing ratio a to 0.1. The salt concentration c_{salt} was adjusted to 0.15 mol dm^{-3}.

K9: exp. no. 30

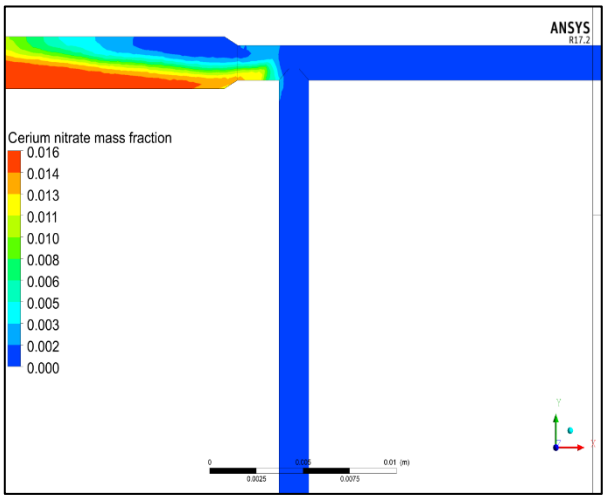
ANSYS
R17.2
Cerium nitrate mass fraction
0.016
0.014
0.013
0.011
0.010
0.008
0.006
0.005
0.003
0.002
0.000

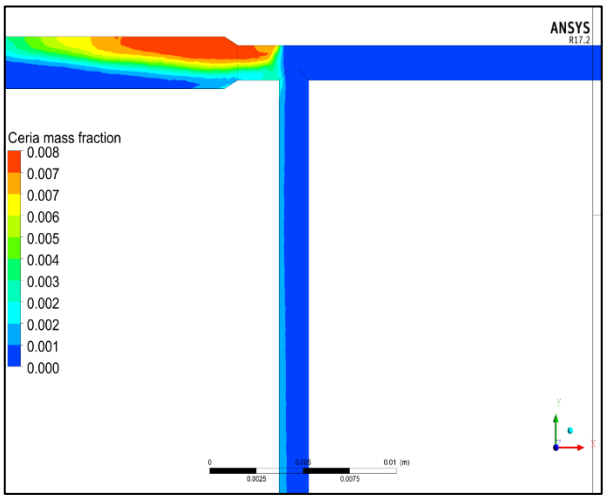
ANSYS
R17.2
Ceria mass fraction
0.008
0.007
0.007
0.006
0.005
0.004
0.003
0.002
0.002
0.001
0.000

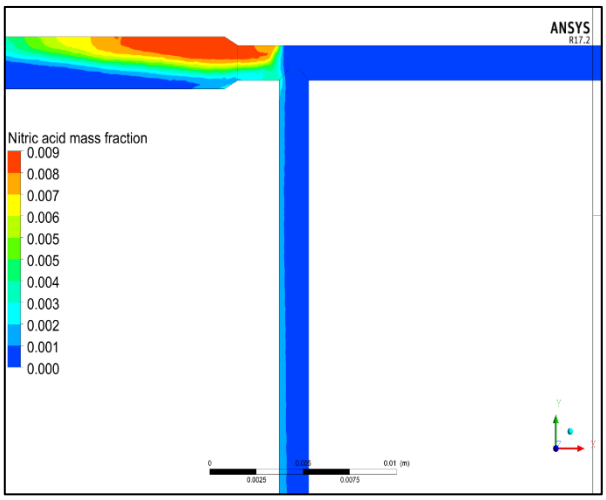
ANSYS
R17.2
Nitric acid mass fraction
0.009
0.008
0.007
0.006
0.005
0.005
0.004
0.003
0.002
0.001
0.000

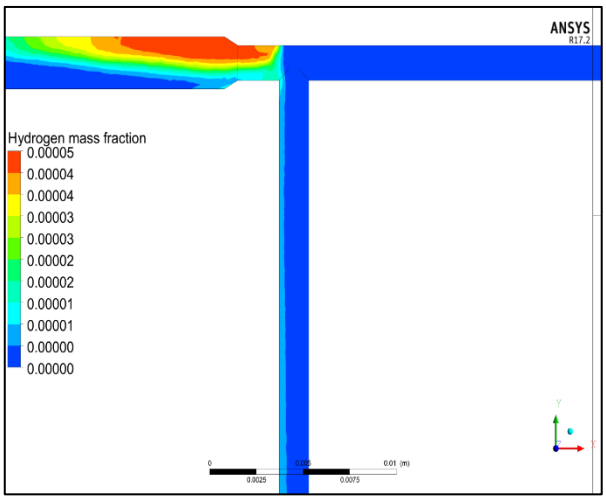
ANSYS
R17.2
Hydrogen mass fraction
0.00005
0.00004
0.00004
0.00003
0.00003
0.00002
0.00002
0.00001
0.00001
0.00000
0.00000

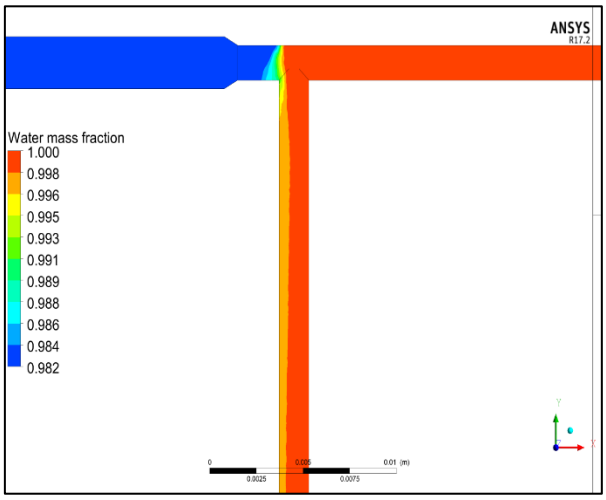
ANSYS
R17.2
Water mass fraction
1.000
0.998
0.996
0.995
0.993
0.991
0.989
0.988
0.986
0.984
0.982

Figure 11-72: Mass fraction profiles of the used educts and products ($Ce(NO_3)_3$ on the left top side, CeO_2 at the top right side, HNO_3 at the bottom left side, and H_2 at the bottom right side) and H_2O inside the mixing unit. The pressure p was set to 25 MPa, the hot stream temperature T_2 to 673 K, the total mass flow $\dot{m}_3$ to 35 g min^{-1} and the mixing ratio a to 0.1. The salt concentration c_{salt} was adjusted to 0.05 mol dm^{-3}.

K10: exp. no. 31

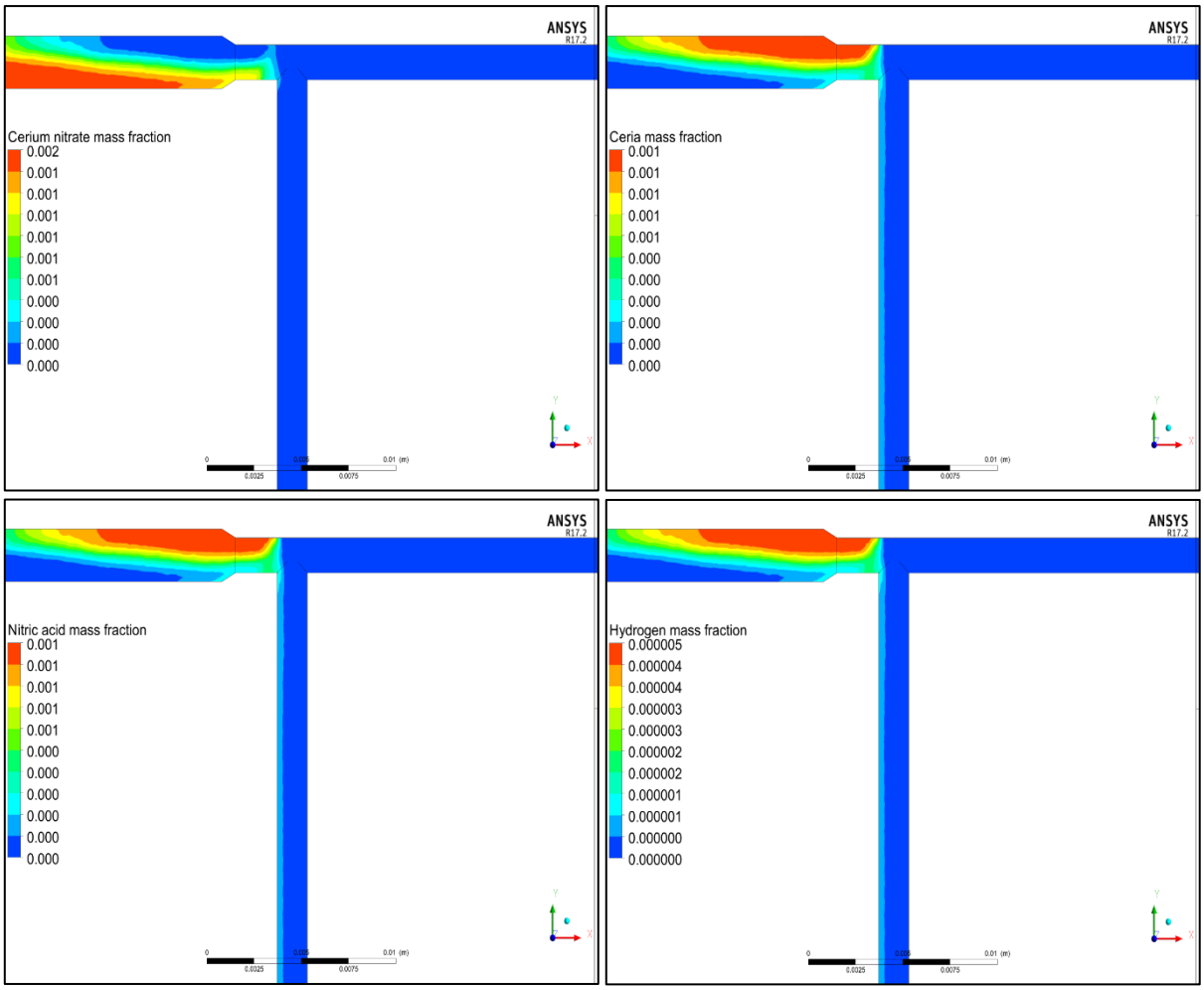

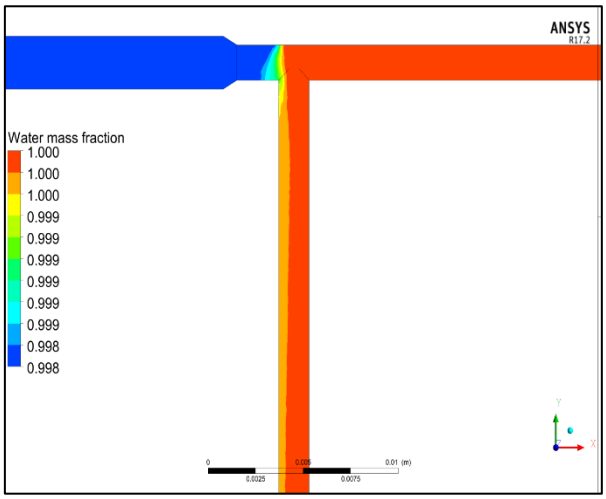

Figure 11-73: Mass fraction profiles of the used educts and products ($Ce(NO_3)_3$ on the left top side, CeO_2 at the top right side, HNO_3 at the bottom left side, and H_2 at the bottom right side) and H_2O inside the mixing unit. The pressure p was set to 25 MPa, the hot stream temperature T_2 to 673 K, the total mass flow $\dot{m}_3$ to 35 g min^{-1} and the mixing ratio a to 0.1. The salt concentration c_{salt} was adjusted to 0.005 mol dm^{-3}.

K11: exp. no 34

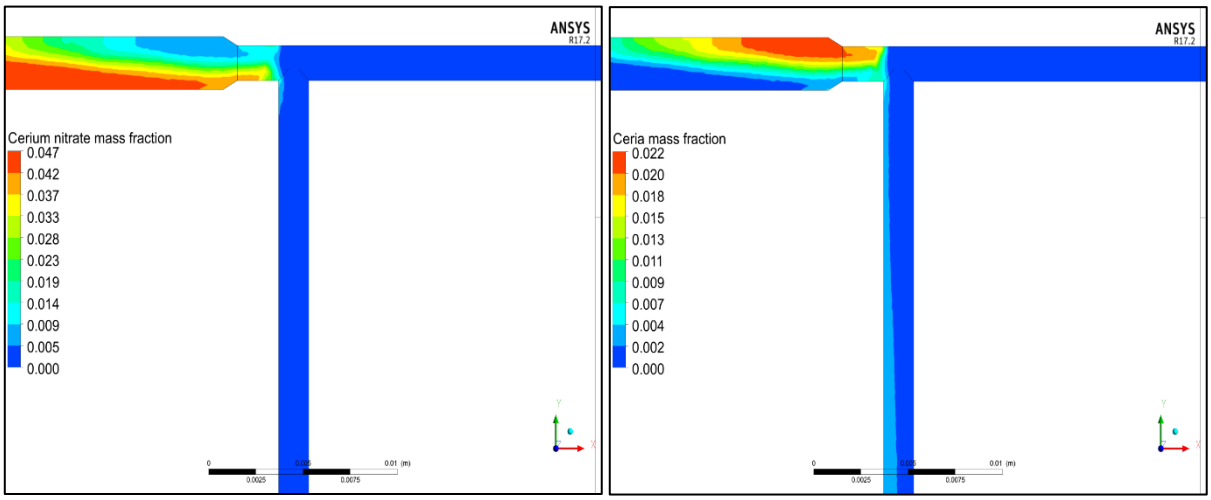

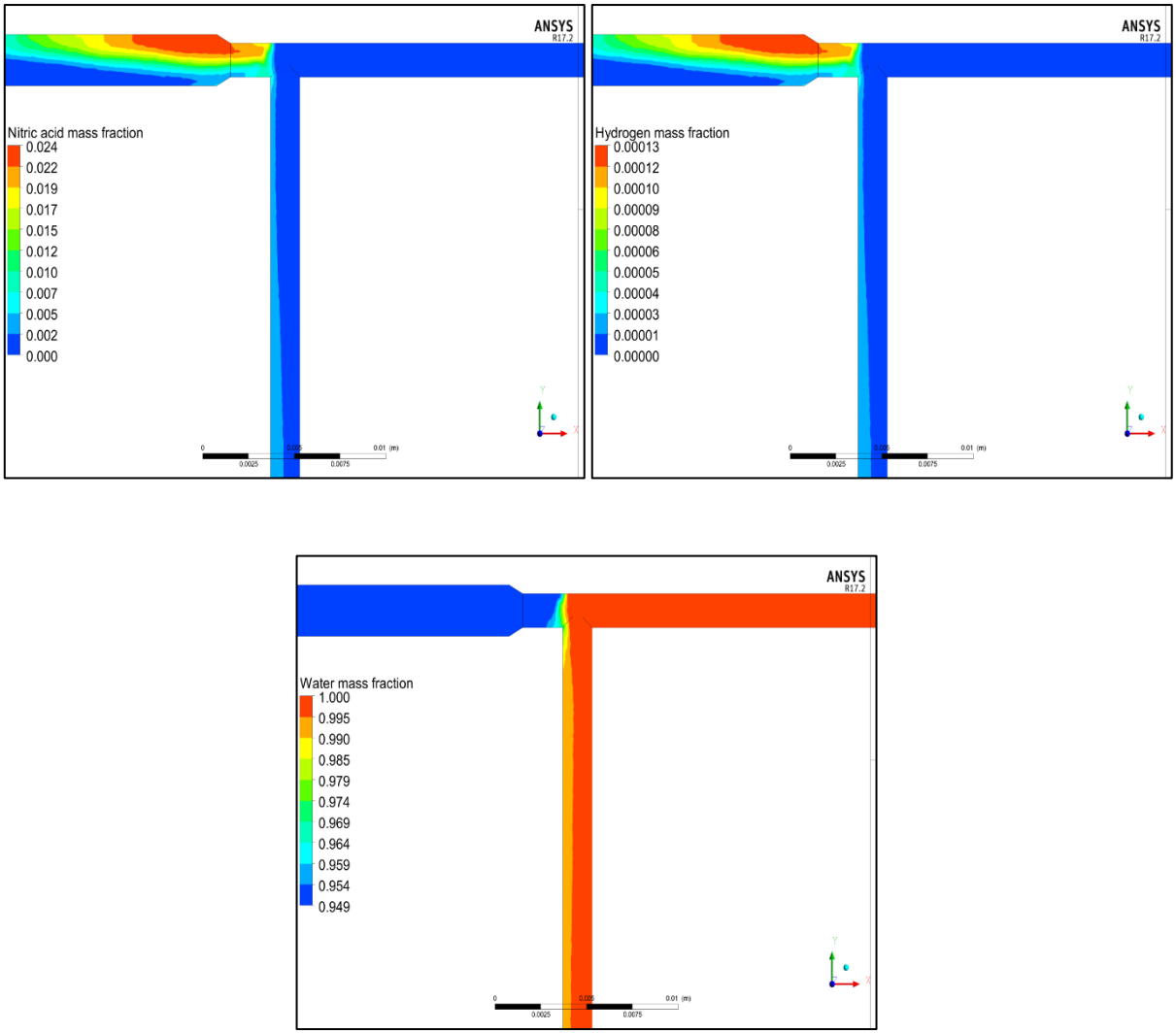

Figure 11-74: Mass fraction profiles of the used educts and products ($Ce(NO_3)_3$ on the left top side, CeO_2 at the top right side, HNO_3 at the bottom left side, and H_2 at the bottom right side) and H_2O inside the mixing unit. The pressure p was set to 25 MPa, the hot stream temperature T_2 to 673 K, the total mass flow $\dot{m}_3$ to 35 g min^{-1} and the mixing ratio a to 0.1. The salt concentration c_{salt} was adjusted to 0.15 mol dm^{-3}.